**Parametric and Numeric Design and Test of Electrical Connectors**

Von der Fakultät für Ingenieurwissenschaften, Abteilung Maschinenbau und Verfahrenstechnik der

Universität Duisburg-Essen

zur Erlangung des akademischen Grades

eines

Doktors der Ingenieurwissenschaften

Dr.-Ing.

genehmigte Dissertation

von

Abhay Rammurti Shukla
aus
Pune, Indien

Gutachter:

Prof. Dr. rer. nat. habil. Robert Martin

Prof. Dr.-Ing. Jian Song

Prof. Dr.-Ing. Dr. h.c. Dieter Schramm

Tag der mündlichen Prüfung: 25.04.2024

**DOI:** 10.17185/duepublico/81939
**URN:** urn:nbn:de:hbz:465-20240528-135129-7

# Acknowledgement

I would like to thank Precision Engineering Laboratory, Ostwestfalen-Lippe University of Applied Sciences and Arts where I was employed as a research assistant and a Ph.D. student while writing this thesis. I would like to express my gratitude to Graduiertenzentrum TH OWL for providing the financial support to enable the completion of my thesis.

This endeavor would not have been possible without Prof. Dr.-Ing. Jian Song from Ostwestfalen-Lippe University of Applied Sciences and Arts. I would like to express my gratitude to him for giving me an opportunity to write my Ph.D. thesis at Precision Engineering Laboratory, valuable advice, support and willingness to guide me through this journey as my doctoral supervisor.

I am extremely grateful to Prof. Dr. rer. nat. habil. Robert Martin from University of Duisburg-Essen for accepting the task of being doctoral supervisor of my Ph.D. thesis and giving valuable suggestions and comments on my thesis.

I am thankful to Prof. Dr.-Ing. Dr. h.c. Dieter Schramm for accepting the task of reviewing this work and giving valuable comments.

I am also thankful to Dr.-Ing Sascha Nolte and Mr. Tobias Langer from Weidmüller Interface GmbH & Co. KG for kind support of my work, especially in the parametric optimization of electrical connectors.

I would like to thank all my colleagues at Precision Engineering Laboratory for the pleasant and productive environment, support in conducting experiments and valuable suggestions. I would like to thank my Master student Roman Probst for his excellent work and assistance especially in conducting statistical analysis.

A very special thanks to my family Bhagwan, Jalpana Shukla, Rammurti Shukla, Mamta, Madhuri, Kaushal and Brunda for their care and love.

Abhay Shukla, Lemgo, April 2024

# Abstract

The electrical connectors are a significant component of the system and system performance is directly influenced by the ability of electrical connectors to conduct required signals and current throughout the designed life. The overall performance of an electrical connector can be gauged with respect to its structural, thermal and electrical performances which in turn are interrelated. Therefore, designing an electrical connector for a given application is a challenging task and the need for its miniaturization in order to be accommodated in the system further increases this challenge. Also, the procedure required for connectors' design and development and their testing in order to determine the reliability before installing in an application is time consuming and labor intensive process. In this work, a systematic approach to the parametric modelling and design optimization of electrical connectors using structural and coupled structural-thermal-electric finite element method (FEM) along with the methodology using data driven statistical process for prognosis of the state of health (SoH) and lifetime of connectors using the data of contact resistance development in short term tests is introduced. In this way, the time required from design conception of electrical connectors to their installation in a system after confirming the reliability is significantly scaled down.

For design optimization, a 13.6 mm silver coated round connector with brass as base material is used as a reference connector and multiple CAD models are generated using parametric modelling method through variation of dimensions of reference connector within prescribed limits. The structural analysis of various models is conducted using structural FEM simulation and contact force and contact area between receptacle and pin are determined. The connector model having maximum contact area and contact force within acceptable limits is identified as structurally optimal and is further analyzed for thermal-electrical performance using coupled structural-thermal-electric FEM simulation. The electrical resistance and joule heating of the optimized connector model is compared with the reference connector. In order to validate the simulation model, the simulated electrical resistance and joule heating in reference connector is compared with experimental results. For confirming the conclusions derived from the proposed approach and it's applicability to different connectors, a smaller connector of 2.5 mm size is analyzed using the similar procedure and the simulation results are compared with experimental results. The tribological performance of connector is investigated by simulating the rough surface deformation using FEM with a view to determine the real contact area for given contacting conditions. The surface roughness is modelled in the form of triangular ribs using core roughness $R_K$ obtained from bearing area curve and the average groove width $R_{SM}$. The simulation results are indirectly verified using measured electrical contact resistance and the correlation between contact resistance, contact force and the effective electrical contact area is established.

In accelerated life testing (ALT) of connectors subjected to thermal cycling, irrespective of their design, a strong correlation between the contact resistance development from initial period and

number of failures in later stages of tests is observed. This correlation is exploited and a statistical procedure utilizing the contact resistance data from initial short term test for prognosis of connector reliability is introduced. Through this method, the data of 10 to 50 days of test can be applied to predict the results up to 2 years with a good precision. In this way, the proposed work introduces an adequately reliable and promising approach to significantly shorten the time required for designing and testing of electrical connectors.

# Kurzfassung

Elektrische Steckverbinder sind wichtige Bestandteile eines Systems, dessen Leistungsfähigkeit direkt abhängig ist von der Fähigkeit der Steckverbinder, über ihre Lebensdauer hinweg die benötigten Signale oder Ströme übertragen zu können. Die Leistungsfähigkeit eines einzelnen Steckverbinders kann im Hinblick auf seine strukturelle, thermische und elektrische Leistung beurteilt werden, welche wiederum miteinander verknüpft sind. Aus diesem Grund ist die Entwicklung eines elektrischen Steckverbinders für einen bestimmten Anwendungsfall eine große Herausforderung, welche durch die Notwendigkeit der Miniaturisierung, um immer mehr Steckverbinder im System unterbringen zu können, nochmal anspruchsvoller wird. Außerdem ist der Prozess der Entwicklung und des Testens, um vor dem Einsatz bereits die Zuverlässigkeit zu bestimmen, zeit- und arbeitsintensiv. In dieser Arbeit wird ein systematischer Ansatz für eine parametrische Modellierung sowie Designoptimierung elektrischer Steckverbinder vorgestellt, welche mittels struktureller sowie gekoppelter struktureller-thermo-elektrischer Finite Elemente Methode (FEM) erfolgt. Weiterhin wird eine datenbasierte, statistische Methode für die Prognose des State of Health (SoH) sowie der Lebensdauer elektrischer Steckverbinder entwickelt. Die Daten dafür beruhen auf der Entwicklung des Kontaktwiderstands aus Kurzzeittests. Auf diese Weise wird die Dauer vom Designentwurf eines Steckverbinders bis zum Einsatz in der späteren Anwendung nach Bestätigung seiner Zuverlässigkeit deutlich verkürzt.

Für die Designoptimierung wird ein silberbeschichteter Rundkontakt mit einem Durchmesser von 13,6 mm und Messing als Basismaterial verwendet. Ausgehend von diesem Modell wird über die parametrische Modellierung eine Vielzahl verschiedener CAD-Modelle erstellt, bei welchen bestimmte Maße innerhalb von festgelegten Grenzwerten variiert werden. Die strukturelle Analyse dieser Modelle erfolgt anschließend mittels FEM-Simulation. Dabei werden die Kontaktkraft sowie die Kontaktfläche zwischen Buchse und Stift bestimmt. Das Modell mit der größten Kontaktfläche und einer noch akzeptablen Kontaktkraft wird als Optimum identifiziert und mittels der gekoppelten strukturellen-thermo-elektrischen FEM-Simulation weiter untersucht. Der elektrische Widerstand sowie die Stromerwärmung des optimierten Steckverbinders wird mit dem Referenzmodell verglichen. Um die Ergebnisse zu validieren, werden diese Daten des Referenzmodells zusätzlich in Laborversuchen experimentell ermittelt und ebenfalls für den Vergleich herangezogen. Für eine Bestätigung der

aus diesem Ansatz abgeleiteten Ergebnisse wird dieses Verfahren auf einen weiteren Steckverbinder mit einem Durchmesser von 2,5 mm angewendet und die über die Simulation erhaltenen Daten ebenfalls mit den Werten aus Laborversuchen abgeglichen. Dies dient außerdem dazu, die Anwendbarkeit des Verfahrens auch auf andere Steckverbinder zu überprüfen. Die tribologischen Eigenschaften der Steckverbinder werden untersucht, indem die Oberflächenrauheit bzw. deren Verformung mittels FEM simuliert wird, um die reale Kontaktfläche unter den gegebenen Bedingungen ermitteln zu können. Die Oberflächenrauheit wird durch dreiecksförmige Rippen modelliert mit einer aus der Abbott-Kurve abgeleiteten Kernrautiefe $R_K$ sowie der mittlere Rillenbreite $R_{SM}$. Die Simulationsergebnisse werden indirekt über den gemessenen elektrischen Kontaktwiderstand verifiziert und eine Korrelation zwischen Kontaktwiderstand, Kontaktkraft sowie der elektrisch wirksamen Kontaktfläche festgestellt.

In beschleunigten Lebensdauertests von elektrischen Steckverbindern werden die Belastungen in Form von Temperaturwechseln ausgesetzt. Dabei wird eine gute Korrelation von der Entwicklung des Kontaktwiderstands in der Anfangsphase der Prüfungen sowie der Anzahl an ausgefallenen Steckverbindern im späteren Verlauf der Prüfungen festgestellt. Auf Basis dieser Korrelation wird eine statistische Methode vorgestellt, welche auf den Widerstandsdaten der Frühphase der Prüfungen beruht und eine Prognose der Zuverlässigkeit von Steckverbindern ermöglicht. Mit Hilfe dieser Methode können die Daten von 10 bis 50 Tagen der Prüfung verwendet werden, um die Ergebnisse bis zu 2 Jahre andauernden Versuchs zu prognostizieren. Diese Arbeit bietet folglich einen zuverlässigen sowie vielversprechenden Ansatz, um die benötigte Dauer für den Entwurf und die Prüfung von elektrischen Steckverbindern erheblich zu verkürzen.

# Table of Contents

# Abbreviation and formula symbols

## Abbreviation and indices

| Abbreviation | Meaning |
|---|---|
| $\mu$ | Mean; location parameter |
| $A$ | Constant |
| a; k | Coefficients of exponential fit |
| $A_f$ | Acceleration factor |
| $A_{f\_N\text{-}L}$ | Acceleration factor based on Norris-Landzberg model |
| $A_{f\,Arrhenius}$ | Acceleration factor based on Arrehnius model |
| $A_{f\,C\_M}$ | Acceleration factor based on Coffin-Manson model |
| Ag | Silver |
| ALT | Accelerated life test |
| Au | Gold |
| $c$ | Standard variate of a distribution |
| $CL$ | Confidence interval |
| CLT | Characteristic life time |
| $c_p$ | standard variate for probability p |
| DoE | Design of experiment |
| EDH | Equivalent device hours |
| $F(p,t)$ | Failure probability |
| $F(t)$ | Cumulative failure probability distribution function |
| $f(t)$ | Instantaneous failure rate in given time period |
| FIT | Failure in time rate |
| $FIT_{Chi\text{-}square}$ | Failure in time rate based on Chi-square distribution |
| $FIT_{Weibull}$ | Failure in time rate based on Weibull distribution |
| $GEV$ | Generalized extreme value distribution |
| $Gr$ | Grashof number |
| $k$ | Shape parameter in generalized extreme value distribution |
| m; n | Coefficients of logarithmic fit |
| MTBF | Mean time between failure |
| MTTF | Mean time to failure |
| $n$ | number of a spots |
| $N$ | number of spring segments |
| N; $N_{spring}$ | Number of spring elements in receptacle |
| $N_{failure}$ | Number of failures |

| Abbreviation | Meaning |
|---|---|
| $N_{field}$ | Number of cycles in field |
| Ni | Nickel |
| $N_{samples}$ | Number of samples |
| $N_{test}$ | Number of cycles in test |
| *Nu* | Nusselt number |
| *P* | failure probability |
| *p* | failure probability |
| *Pr* | Prandtl number |
| *q* | Quotient q |
| *R(t)* | Survivorship function |
| *Ra* | Rayleigh number |
| *Re* | Reynolds number |
| SoH | State of health |
| w.r.t. | With respect to |
| x; y | Coefficients of linear fit |
| $\alpha$; $\beta$ | Scale and shape parameter in Weibull distribution |
| $\sigma$ | Standard deviation; scale parameter |

## Formula symbols

| Symbols | Value or unit | Description |
|---|---|---|
| $(\sigma_c)_{max}$ | Pa | Maximum contact stress |
| $\sqrt{\mu}$ | mm | semi axis of ellipsoid |
| μ | Ω | Mean contact resistance |
| $\mu_d$ | Pa-s | Dynamic viscosity |
| $\mu_{initial}$ | Ω | Mean initial contact resistance |
| A | $mm^{-2}$ | Area; cross sectional area |
| *a* | $m\ s^{-2}$ | Thermal diffusivity |
| $a;a_c$ | mm | Contact spot radius |
| *a;b* | mm | major and minor semi-axes of ellipse |
| $A_{conv}$ | $mm^2$ | Area for convection heat transfer |
| $A_{rad}$ | $mm^2$ | Area for radiation heat transfer |
| $A_{real}$ | $mm^2$ | Real contact area |
| $A_s$ | $mm^2$ | Surface area |
| b° | radians | Width in radians of outer radius of receptacle |
| CLT | hrs; days | Characteristic life time |
| $c_p$ | $J\ kg^{-1}\ K^{-1}$ | Specific heat capacity |
| d | mm | Diameter |

| Symbols | Value or unit | Description |
|---|---|---|
| D1 | mm | Outer diameter of receptacle |
| $dP_l$ | W | Power loss due to joule heating |
| $dQ_{cond}$; $Q_{cond}$ | W | Heat rate through conduction |
| $dQ_{conv+rad}$ | W | Combined heat rate through convection and radiation |
| $dQs$ | W | Heat stored |
| $dT$ | K | Temperature gradient |
| $dx$ | mm | Conductor thickness |
| $E$ | V $m^{-1}$ | Electric field |
| $E$ | Pa | Modulus of elasticity |
| $E_1$; $E_2$ | Pa | Modulus of elasticity of body 1; body 2 |
| $E_a$ | 0.45 eV | Activation energy |
| $EC_{contact}$ | S | Electrical contact conductance |
| $ER_{contact}$ | Ω | Electrical contact resistance |
| $F$ | N | Force; Load |
| $F_a$ | $mm^2$ | Contact area between receptacle segment and pin |
| $F_e$ | N | Contact force |
| $f_{field}$ | Hz | Thermal cycling frequency in field |
| $F_i$ | N | Insertion force |
| $F_{i\_1}$;$F_{i\_2}$ | N | Insertion force in phase 1; phase 2 |
| $F_{i\_total}$ | N | Total insertion force of receptacle |
| $F_k$ | N | Contact force between receptacle segment and pin |
| $F_N$ | N | Normal force |
| $f_{test}$ | Hz | Thermal cycling frequency in test |
| $g$ | 9.81 m $s^{-2}$ | Acceleration due to gravity |
| $H$ | Pa | Hardness |
| I | A | Current |
| J | A $m^{-2}$ | Current density |
| $k$ | N $mm^{-1}$ | Spring stiffness |
| $k_B$ | 8.6173303E-05 ev $K^{-1}$ | Boltzmann constant |
| $L$ | 2.45E-08 $V^2$ $K^{-2}$ | Lorentz constant |
| L | mm | Length; Initial length |
| L1 | mm | Total length of spring element |
| L2 | mm | Length of bended portion of spring element |
| $l_{char}$ | mm | Characteristic length |
| $L_{initial}$ | mm | Initial length |
| $P$ | W | Power |
| $p$ | 1.9 to 2 | Temperature difference coefficient |
| $q$ | 0.33 | Temperature change coefficient |
| $Q_{rad}$ | W | Heat rate emitted due to radiation |
| R | Ω | Electrical resistance |
| R | mm | Radius of conductor; Contact radius |

| Symbols | Value or unit | Description |
|---|---|---|
| $R_a$ | µm | Average roughness |
| $R_P$ | Ω | Bulk resistance of pin |
| $R_R$ | Ω | Bulk resistance of receptacle |
| $R_{connector}$ | Ω | Total electrical resistance of connector |
| $R_{constriction}$ | Ω | Constriction resistance |
| $R_C$ | Ω | Contact resistance |
| $R_{failure}$ | Ω | Failure criteria |
| $R_{film}$ | Ω | Film resistance |
| $R_{initial}$ | Ω | Initial electrical resistance |
| $R_K$ | µm | Core roughness |
| RMS | µm | Root mean square roughness |
| $R_{outer}$ | mm | Outer radius of spring (D1/2) |
| $R_{PK}$ | µm | Reduced peak height |
| $R_{SM}$ | µm | Average groove width |
| $R_{upper\_spread}$ | Ω | Upper spread of contact resistance |
| $R_{VK}$ | µm | Reduced valley depth |
| $R_z$ | µm | Average roughness depth |
| S(p) | Ω | Upper spread of resistance based on failure probability |
| $Sq$ | µm | Root mean square roughness |
| $T$ | °C | Temperature |
| t | hrs; days | Time |
| t1 | mm | Spring thickness |
| $T_1$; $T_2$ | °C | Temperature of body 1; body 2 |
| $t_1$;$t_2$ | µm | Oxide film thickness |
| $T_{air}$ | °C | Temperature of surrounding air |
| $T_{cable\_core}$ | °C | Temperature measured at cable core |
| $TC_{contact}$ | W $m^{-1}$ $K^{-1}$ | Thermal contact conductance |
| $t_{CL}$ | hrs; days | Characteristic life time (CLT) |
| $t_{CL\_ALT}$ | hrs; days | Characteristic life time (CLT) in accelerated life test (ALT) |
| $T_{connector}$ | °C | Connector temperature |
| $T_{contact}$ | °C | Temperature measured near contact zone |
| $T_{crimp}$ | °C | Temperature measured at crimp |
| $t_{failure}$ | hrs; days | Time to failure |
| $t_{field}$ | hrs; days | Time in field |
| $T_{field}$; $T_{max\_field}$ | °C | Temperature in field |
| $t_h$ | hrs | Time in hours |
| $T_m$ | °C | mean temperature of connector and air |
| $T_{max}$ | °C | Maximum temperature |
| $TR_{contact}$ | K $W^{-1}$ | Thermal contact resistance |
| $T_s$ | °C | Surface temperature |

| Symbols | Value or unit | Description |
|---|---|---|
| $t_{test}$ | hrs; days | Time in test |
| $T_{test;}T_{max\_test}$ | °C | Temperature in test |
| $u_i$ | mm | Indentation depth |
| V | V | Voltage |
| $W$ | joules | Work done |
| $x$ | mm | Deflection distance |
| $X_{Si}$ | µm | Individual groove width |
| $\alpha$ | degree; W $m^{-2}$ $K^{-1}$ | Entry angle of spring with blade; combined coefficient of heat transfer due to convection and radiation |
| $\alpha_{base}$ | degree | Angle of revolution for generating base of receptacle |
| $\alpha_{conv}$ | W $m^{-2}$ $K^{-1}$ | Convection coefficient |
| $\alpha_H$ | mm | Holm radius |
| $\alpha_L$ | $K^{-1}$ | Coefficient of thermal expansion |
| $\alpha_R$ | $K^{-1}$ | Coefficient of electrical resistance |
| $\alpha_{spring}$ | degree | Angle of revolution for generating spring segment |
| $\beta_p$ | $K^{-1}$ | Thermal expansion coefficient |
| $\delta$ | kg $m^{-3}$ | Density |
| $\Delta L$ | mm | change in length of conductor |
| $\Delta R$ | Ω | change in the electrical resistance |
| $\Delta T$ | K | Change in temperature |
| $\Delta T_{cable}$ | K | Joule heating in cable |
| $\Delta T_{contact}$ | K | Joule heating near contact zone |
| $\Delta T_{crimp}$ | K | Joule heating in crimp |
| $\Delta T_{field}$ | K | Temperature difference between upper and lower test temperature |
| $\Delta T_{test}$ | K | Temperature difference between upper and lower field temperature |
| $\varepsilon$ | | Emissivity of surface |
| $\varepsilon_1; \varepsilon_2$ | | Emissivity of surface 1; surface 2 |
| $\varepsilon_{12}$ | | Thermal radiation exchange coefficient |
| $\theta$ | hrs; days | Mean time to failure (MTTF) |
| $\lambda$ | W $m^{-1}$ $K^{-1}$ | Thermal conductivity |
| $\lambda$ | $time^{-1}$ | Failure rate |
| $\lambda_1;\lambda_2$ | W $m^{-1}$ $K^{-1}$ | Thermal conductivity of body 1; body 2 |
| $\lambda_{air}$ | W $m^{-1}$ $K^{-1}$ | Thermal conductivity of air |
| $\lambda_{cond}$ | W $m^{-1}$ $K^{-1}$ | Thermal conductivity |
| $\lambda_{h\_Chi\text{-}square}$ | $h^{-1}$ | Failure rate from Chi-square distribution |
| $\lambda_{h\_Weibull}$ | $h^{-1}$ | Failure rate from Weibull distribution |
| $\lambda_h$ | $h^{-1}$ | Failure rate in hours |
| $\nu_1;\nu_2$ | | Poisson ratio of body 1; body 2 |
| $\nu_k$ | $m^2$ s | Kinematic viscosity |
| $\rho$ | Ω mm | Specific resistivity |

| Symbols | Value or unit | Description |
|---|---|---|
| $\rho_1, \rho_2$ | Ω mm | Specific resistivity of body 1, body 2 |
| $\sigma$ | S $m^{-1}$ | Electrical conductivity |
| $\sigma$ | Ω | Standard deviation of contact resistance |
| $\sigma_B$ | $5.67 \cdot 10^{-8}$ W $m^{-2}$ $K^{-4}$ | Stefan-Boltzmann constant |

# 1 Motivation and Thesis Structure

The main motivation of this work is the development of a systematic approach for the comprehensive design and optimization of electrical connectors and the development of a data driven statistical process for state of health and lifetime prognosis of electrical connectors using short term results of accelerated life tests. The integration of the developed approaches to the designing and testing phase of electrical connectors can lead to significant savings in the time and effort required for developing a reliable electrical connector. The design approach has been developed to enable the generation of connector models with optimum combination of structural, tribological, thermal and electrical performances using CAD, FEM and statistical modelling tools. For the scaling down of the total test duration required in accelerated life test of electrical connectors subjected to thermal cycling, a concise and potent statistical process has been developed by correlating the contact resistance data from initial test duration with the future failure probabilities.

## 1.1 Motivation

The electrical connectors are meant for the transmission of electric current or signals and their performance and lifetime directly affects the functioning of the whole system. They find their usage in electrical and electronics applications and are being increasingly utilized in industries, automobiles, consumer electronics and telecommunication fields owing to the continuously increasing automation of processes. The failure of an electrical connector can lead to an either partial or complete failure of the system. Their importance is most often underestimated and they can prove to be weak links in the system [1]. The need of miniaturizing the systems stresses the necessity of reducing the size of the electrical connectors installed in them without compromising the reliability and lifetime of the systems. Therefore, delivering the electrical connectors with maximum performance and reliability with reduced size and cost is a challenge for designers. Moreover the shorter product life cycles demand increased pace of design, development and testing of product, thereby further increasing the challenge.

### 1.1.1 Lifecycle and time to market

Innovation and development in the field of automotive systems has been continuously on the rise in recent years. Moreover, globalization has resulted in the increased competition thereby stressing on the need for faster introduction of products in the market along with pricing constraints. A product goes through different phases during its lifecycle as illustrated in Fig.

1.1 [2, p. 419] [3]. A product's journey begins with the planning phase during which the market research and requirement analyses are carried out and the product is conceptualized. During the product development phase, the product parameters are defined and initial product designs are generated and tested for their performance. Based on the test results, the product can be modified by varying the parameters and tested again for its performance. Once the product design is finalized, the steps are taken for its commercialization during which the manufacturing process is developed, followed by production. The manufactured product is then installed and put into use. Once the product completes its lifetime, it is disposed. The product life can end due to various reasons such as failure or replacement by a better technology.

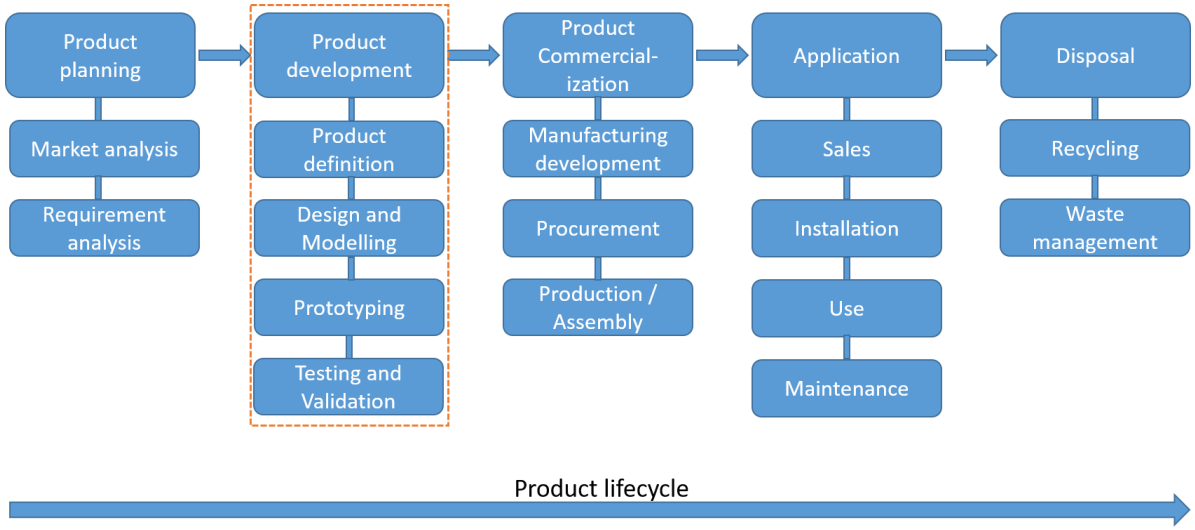


Fig. 1.1: Product lifecycle

Fig. 1.2 illustrates the influence of a product's time to market entry on the profits earned by the organization through the product sales [4, pp. 2, 15]. The market entry of a product is largely dictated by the product development, testing and manufacturing development stages. Also, the profits from the product during these stages are negative considering the planning, development and testing costs incurred by the organization. Once the production facilities are installed, profits grow upwards with the market entry and sale of the product indicated by point 1 in Fig. 1.2. As the technology becomes older and new innovations enter the market, the profits from the product start declining. In order to maximize the profits and utilize the maximum potential of the innovation, it is beneficial to shift the product's market entry point from 1 to 2.

Reduction in the time to entry can be achieved through reduction in the time required for product planning, product development, testing and manufacturing development. Based on the product, the time required for each of these phases could vary significantly. In case of electrical connectors, the time required for product development and testing is considerably longer. Also, as electrical connectors are ideally designed for very long lifetime and higher reliability, the testing time can range from few weeks to multiple years [5]. Thus, product development and

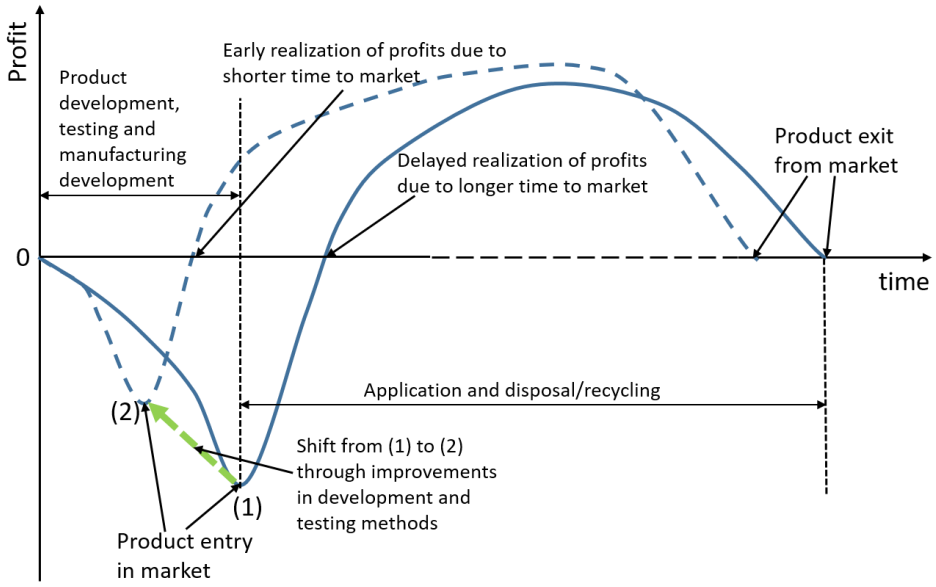


Fig. 1.2: Impact of product entry in market on the organisation's profit

testing costs incurred are significant. Therefore, in the field of electrical connectors, it is vital to find new methods for bringing down the time needed for product development and testing so that the time to market entry can be shortened resulting in increased profits and savings in development cost, time and resources.

### 1.1.2 Complexity of an electrical connector system

Designing an electrical connector is a challenging task since it is expected to meet a number of performance requirements during its operation. These requirements can be broadly classified under structural, tribological, thermal and electrical categories as illustrated in Fig. 1.3.

The performance and reliability of the electrical connectors is directly influenced by the design-technological parameters and the operating parameters [6, p. 249]. The most influential design parameters affecting the performance of electrical connectors are connector geometry, material, contact coatings and topography of contact surfaces. On the other hand, the operational parameters broadly consist of input parameters such as current and voltage and surrounding variables like temperature, humidity, chemical composition of ambient environment, etc. The design and operational parameters directly or indirectly affect the thermal and electrical conductivity between the mating components of an electrical connector and in turn influence its performance and reliability [7] [8] [9]. The design parameters and operational parameters such as current and voltage can be considered as controllable variables whereas ambient conditions are mostly uncontrollable variables in a connector system. The controllable input variables are predetermined based on the system requirements. The design-technological parameters are ideally combined in an optimum way to achieve a reliable electrical connector design fulfilling the intended performance requirements.

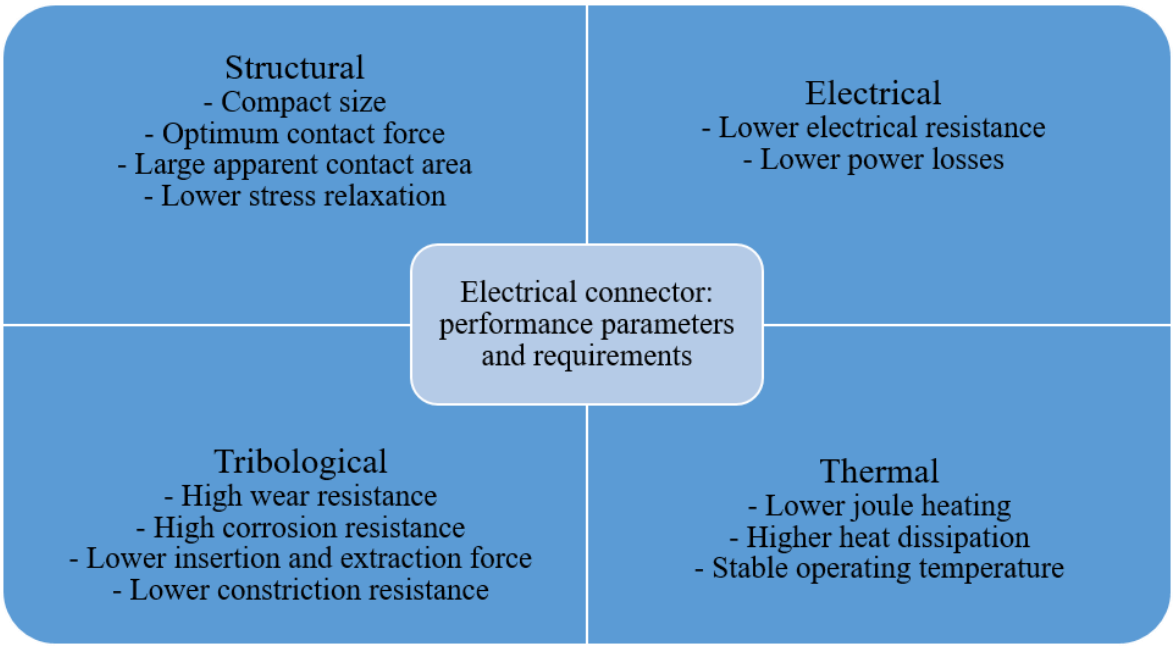


Fig. 1.3: Performance parameters and some of the performance requirements to be fulfilled by an electrical connector

The failures mechanisms in electrical connectors mostly occur in the form of fretting wear, fretting corrosion, wear through of protective coating, oxidation, corrosion, contamination and stress relaxation [10] [11] [12]. These failure mechanisms could either occur individually or in tandem. Apart from stress relaxation, all other failure mechanisms are effective when they occur in the contact zone and are mainly influenced by the coating material.

Also, it is to be noted that an electrical connector undergoes continuous degradation irrespective of the operational and idle state of the system due to variety of degradation mechanisms acting upon it resulting from input loads as well as exposure to environmental variables such as temperature, humidity and chemical compounds present in its vicinity [13] [14]. The degradation mechanisms influence each other due to which the intensity of degradation caused by respective mechanism in the connector fluctuates depending on the given conditions and is highly variable [6, p. 247]. This affects the lifetime of electrical contacts significantly by inducing high degree of randomness in their failure patterns. The direct effect of connector degradation is the increased electrical resistance and joule heating of the connector leading to eventual failure of the connector to perform its function. The degradation occurring at the contact interface between the receptacle and pin or blade is the most significant factor in the reliability of electrical connector and most of the work available in field of electrical connectors is dedicated towards improvement of the contact zone between the mating parts of connectors [9] [10] [15]. For this purpose, the influences of various contact geometries, surface coatings, surface roughness, materials, etc. on the performance of connectors are studied.

### 1.1.3 Electrical connector designing, analysis and optimization

The miniaturization of the connector leads to an increase in the electrical resistance, resulting in further rise in temperature through joule heating. The rise in connector temperature in turn results in the further increase in the electrical resistance. This leads to a cycle of alternate increase of temperature and electrical resistance during operation [6, p. 247]. The higher temperatures in the contact zone between the mating parts of connector lead to the degradation of the surface coating through fretting wear and corrosion caused by the thermal expansion and contraction through thermal cycling depending on the nobility of coating material. The cyclic loading during operations increases this effect [16]. Also, the topology of the contacting surface and the applied coating material have a significant impact on contact resistance thereby directly affecting the quality of connector [17] [18]. The degraded surface results in loss of metallic contact area and causes an increase in contact resistance between mating parts and the temperature of contact zone, thereby accelerating the contact degradation process. From the point of view of lifetime of connector, it is advantageous to maintain the connector temperature as low as possible [11] [19] [20]. The increase in temperature beyond permissible limit can lead to a drastic reduction of the connector lifetime leading to its failure. Thus, the miniaturization of the connector has an opposite effect on the electrical resistance and joule heating. This phenomenon highlights the importance of the need for design optimization of electrical connectors.

In the recent times, the CAD and FEM tools are being successfully applied in design and development of the engineering components and they have been proven to be helpful in speeding up the design and development process with significant reduction in the development cost. Parametric modelling method is applied for the design process of the components having a definite shape and structure. The correlation between the geometrical parameters of the components can be predefined and the respective structural parameter sizes can be varied within allowable limits. Hence through the use of CAD tools enabling the parametric modelling, variety of models of the given component can be generated economically by up scaling or down scaling the geometrical parameters of the reference model. These models can then be further tested using FEM tools for different performance parameters viz. structural, thermal and electrical [21] [22]. Also, the tests can be performed for different materials. The sensitivity analysis can be performed using the results obtained from finite element analysis of different models and the effects of the design variables and their interactions on the respective performance parameter can be evaluated [23] [24]. This can enable in designing a product having an optimal size, thereby reducing the material costs and wastage and simultaneously meeting the intended performance requirements.

The FEM tools enable the multi-physics simulation where direct or indirect coupling between different simulation environments can be established and simulations can be performed in the required sequence based on the corresponding application [22] [25]. The prototype of the

optimized model can be developed and tested in laboratory conditions to verify with the results of the finite element analysis and determine its lifetime and reliability. The identification of the optimal design eliminates the need of prototyping and testing of inefficient designs thereby significantly conserving the resources and effort.

There is considerable amount of literature available on the electrical connectors based on the physical experiments conducted in laboratory as well as field conditions. However, the use of FEM for analysis and optimization of connector designs appears to have gained momentum only in the past couple of decades probably due to the advancements in the computational efficiency and finite element analysis software packages. An extensive review of available researches employing the FEM in the field of electrical connectors has been presented in [26], where a systematic classification of researches based on mechanical field, electrical field, coupled thermal-electric fields and multi-physics analysis involving mechanical, thermal and electrical fields respectively along with consideration of contact zone in some of the researches has been done. The researches have been conducted on the flat as well as round type of connectors. The multi-physics analysis of round pin high power connector composed of three components namely a rigid pin as a male part, a rigid cylindrical female part and a spring sitting on the groove in female part providing contact pressure has been performed in [27] and the effect of current on the gap distance, connector resistance, stress along with the effect of contact resistance variation on the stress and current density of the connector is investigated. In another work, a 2D coupled mechanical-thermal-electric analysis is performed on a 35A automotive flat pin connector and the distribution of equivalent stress, electric potential, and temperature in the connector is obtained [28]. The electrical contact resistance is varied with a view to consider the effect of fretting. The coupled structural-thermal analysis of round connector analyzing the effect of ambient temperature on the receptacle deformation and contact pressure in the contact zone is performed in [29]. The effect of different cable cross-sections and input current on the joule heating and electrical resistance of a flat contact using coupled mechanical-thermal-electric simulation is investigated in [30]. In another study, a parametric optimization and investigation of influence of contact force and connector materials on thermal and electrical performance in cylinder-plane and sphere-plane contact combinations using indirect coupling method is done [31]. Shao et al. performed multi-physics analysis of flat connector under static conditions and vibration [32]. Guan et al. simulated the contact degradation process in a gas-insulated bus plug-in connectors using a coupled electromagnetic-thermal-mechanical FEM model [33].

In a study by Zeng et al., a systematic structural optimization of a micro-D electrical connector having a rigid receptacle and a flexible twisted wire pin is conducted where the parameters of the wire pin are varied with a view to optimize the insertion and extraction force using dynamic analysis [21]. The structural analysis investigating the effect of receptacle length, groove width, shrink range and coefficient of friction on the insertion force in a round connector composed of two components namely pin and socket has been conducted in [24]. In another work, an indirect

structural-thermal-electric coupled simulation is performed on round connector with different size to investigate the effect of different shrink range on the stress, contact resistance and temperature distribution [22]. The influence of the spring length on the contact force, stiffness and stress distribution with respect to the spring deflection has been investigated in [34]. The effect of different materials namely, copper alloys and the radius and thickness of spring on the indentation and insertion force in flat connectors using finite element simulation is investigated in [35].

The comprehensive parametric design procedures considering the wider set of design parameters in optimization of an electrical connector are mainly based on analytical methods [36]. The analytical methods are advantageous from computation and parameter variation point of view. However, they have limitations with regards to the degree of complexity of design and effort in developing precised analytical models. Also, the knowledge of the physics and corresponding mathematical relationships occurring in the system is important for generation of reliable analytical models.

There are relatively larger number of studies applying FEM for analysis of the flat contacts in comparison to the round contacts available to date. The approach used in the structural optimization in the available studies is mainly with a view to optimize the insertion and extraction force in connectors which are significantly a function of coating material, surface roughness and spring thickness. Majority of the available studies generally focus on a selected few parameters for investigating their influence on the connector performance. Also, a comprehensive study considering the complete set of structural parameters on the optimization of round electrical connectors using FEM tools is not available. The contact area and the normal force in the contact zone, which are formed after the contact between the mating parts is established, are vital to the thermal and electrical performance of the connector as they directly influence the tribology and thermal as well as electrical conductivities in the contact zone. Therefore, there exists a scope of designing an electrical connector with a view to obtain a model with an acceptable contact force and larger possible apparent contact area. Once the model with a combination of larger possible contact area and an acceptable contact force is obtained, the performance in the contact zone can be optimized through the proper selection of coating material and surface roughness.

### 1.1.4 Models for determining real contact area

At the microscopic level, the surface roughness of the coating directly affects the real contact area formation and in turn the performance of the contact [37] [38] [39]. The roughness asperities deform under the applied force and form an electrically effective conducting area i.e. real contact area. The real contact area formed under given contact force is larger in relatively smoother surfaces than rough surfaces [40]. In smooth surfaces, the contact area for a contact force can be calculated by Hertz contact theory for standard contact pairs like sphere-sphere,

sphere-plane, cylinder-sphere, cylinder-plane, etc. and the contact performance can be determined [5] [41]. In practical applications, the contact surfaces consist of certain degree of roughness due to which the real contact area formed on contact formation is always smaller than the contact area calculated for perfectly smooth surfaces for the range of contact forces usually used in electrical connectors [38] [42]. Also, the plastic deformation of surface asperities is a significant factor to be considered while determining real contact area in rough surfaces. Hence, for the given contact conditions comprising of the factors such as contact geometry, surface roughness, coating material and substrate material, the estimation of real contact area becomes very important for designing an electrical connector with optimum performance.

There are considerable studies performed which propose the methods to investigate rough surface deformation and determine the real contact area. These methods can be broadly classified into FEM based methods [38] [43] [44] and analytical methods [9] [45] [46]. These studies are conducted for different coating materials, contact geometries and surface topographies. The FEM analyses are used for 2D as well as 3D roughness profiles. Different methods are applied for modelling surface topography for the rough surface deformation analysis. Usually an attempt is to reproduce the surface roughness identical to that of the real surface used for investigation.

The roughness profiles can be generated through statistical methods, self-affine fractal methods or multiscale models [45] [47] [48] [49]. In statistical methods, the surface roughness depends on probability density of asperity heights defined based on the probability distributions like Gaussian, Weibull, etc. whereas the periodicity of the roughness is defined by power spectral density of asperity heights [48] [50]. The self-affined fractal roughness possesses same statistical properties at all surface magnification levels. The fractal rough surfaces are applied in the field of surface deformation analysis in electrical contacts by [49] [51]. The multiscale roughness models have been used in the estimation of real contact area by [45] [52]. The actual surface topography is also modelled in some of the studies to analyze the surface roughness deformation [40] [51]. In order to model the real surface topography, the point cloud data of surface topography is obtained via optical microscopy and using the coordinates, actual topography is modelled. In some of the studies, the shapes of roughness asperities are simplified as sphere, ellipsoid, cone, etc. for the analysis [53] [54]. Majority of the investigations use the roughness parameters like average roughness $R_a$ and root mean square roughness *RMS* as an input for modelling and analysis of roughness profiles. Also, majority of the studies attempt to determine the size and number of contact spots formed between the contacting surfaces. The number and size of contact spots are then used to determine the contact resistance by using the function defined by Greenwood [55]. The number of contact spots formed under given load largely depend on the number and size of asperities which in turn can vary significantly based on the magnification level used during optical microscopy to collect roughness data. It is to be noted that in all the methods of rough surface generation, the magnification level or grid

selection plays an important role in the surface topography modelled. Also the surfaces having different roughness characteristics and asperity shapes can have same average roughness $R_a$.

The surface deformation analysis using analytical methods requires in depth knowledge of the contact mechanics and computation skills to implement the method. In the analysis using 3D FEM and actual surface topography or the topography generated using statistical, fractal or multi-scale model methods, the computation effort required is highly intensive and model is difficult to converge given the extent of deformation occurring at the asperity level. The use of 2D FEM is not always reliable since the details of aperiodic nature of the surface roughness profiles cannot be adequately modelled in 2D. In this way, the analytical methods are relatively difficult to implement, 3D finite element methods are computationally very costly and could face convergence issues and 2D finite element methods are not always adequate for modelling the surface roughness deformation.

Hence, there exists a need of a comparatively easy to implement method for reliable estimation of the real contact area by roughness deformation. Also, an appropriate surface roughness characterization and simplification is required in modelling the roughness profiles similar to those present in the actual surfaces. For this, the roughness parameters other than $R_a$ and *RMS* are needed for modelling the roughness profiles.

It is to be noted that the apparent contact area and contact normal force are a direct result of the connector geometry while the surface coating and roughness parameters influencing the real contact area come into play later on and can be altered independent of the basic connector design. In order to achieve a maximum reliability, the designed connector is expected to have a maximum possible contact area with an optimal contact force. The larger contact area assures larger electrical conductivity and a reduced joule heating [17] [55]. On the other hand, an optimal contact force helps in achieving penetration of oxide and contaminant films to establish conducting metallic contact and sufficient deformation of surface asperities to increase real contact area with smaller surface wear rate [56]. This highlights the possibility for inclusion of the apparent contact area and contact normal force as response parameters in the basic design and optimization phase of the connector so that the influence of the resulting contact force with respect to different surface roughness and coating conditions in the optimized model can be investigated separately in order to further optimize the connector performance from tribology point of view.

### 1.1.5 Test duration for reliability estimation

Apart from designing the connector, performing lifetime tests for determining the performance and reliability under different operating conditions is another important factor in the product lifecycle. The failure in time (FIT) rate is the commonly used measure for the definition of reliability of electronic components [57] [58] [59]. The estimation of the connectors reliability through FIT rate can be done based on different probability distributions such as Chi-square

distribution, Weibull distribution etc. Irrespective of the methods used, the time to failure data of the connectors during operation or in test is required for the FIT rate determination. In case of the Weibull based FIT rate, the characteristic life time (CLT) which is the time needed for 63.2 % failures to occur is required for the calculation of the FIT rate [60] [61]. In such a case, one need not wait for 63.2 % components to fail. Instead, at least 20 % to 30 % failures are allowed to occur and the Weibull distribution is fitted to the time to failure data and CLT is determined.

There are a variety of tests required to be performed on the electrical connectors based on the intended application. The test procedures defined for different components of electrical connector system such as contact, housing, sealing, etc. are given in [62]. During testing, connectors are subjected to different thermal, mechanical, chemical and environmental stresses based on the field of application and their performance is analyzed.

In order to reduce the time needed for the estimation of the reliability of connectors, the stress levels are intensified to accelerate the degradation of the connector system [63] [64, p. 521]. It is generally assumed that the failure mechanisms acting in the contact system subjected to accelerated life tests are similar to those acting during the normal operational life of connectors. However, the duration of the accelerated life tests and failure rates depend on the type of stress and their levels. Also there is a high degree of randomness observed in the failure patterns of electrical connectors [58] [65]. In order to enable a reliable prediction of the FIT rate, adequate number of failures need to occur during the test so that sufficient data is available for fitting the probability distribution to estimate the time required for given component failures. As observed from in-house experiments, the accelerated lifetime tests under vibrational loading usually last from few days to weeks whereas the accelerated lifetime tests for investigating the impact of temperature on connector reliability range from number of weeks to couple of years depending on the connector design. The test duration can be shortened by increasing the acceleration factor i.e. the stress levels. However, the higher acceleration factor can result in the distortion of degradation mechanisms [20]. Therefore, the accelerated life tests are to be conducted using an appropriate acceleration factor, which would reflect the degradation mechanisms in normal operations, till sufficient number of failures occur for reliable estimation of CLT and FIT rate. This creates a need for an alternate method to shorten the test duration required for reliability prediction of electrical connectors.

For this purpose, the prognostic models are proven to be useful for estimation of the remaining useful life or the time required for occurrence of given failures expected to occur in the future. Accurate estimation of upcoming component failures can enable timely preventive measures to prevent the system failure resulting from the connector degradation. Sikorska et al. have discussed a number of prognostic methods and the prerequisites for their applications for the reliability prediction [66]. The different methods in their study are differentiated as knowledge-based models, artificial neural network models, stochastic models and physical models. Of these models, the physical models require a deep understanding of the system physics whereas

the remaining approaches are majorly data dependent. The prognostic methods for determination of state of health or reliability of components have been classified as physical model based, data based or combination of the physical model and data based approaches by [67]. A number of researches on the application of prognostic methods in the remaining useful life and reliability prediction of electronic components are available [68] [69] [70] [71].

In an electrical connector, the contact resistance is the degradation parameter of interest. A connector can be termed as failed after the contact resistance increases beyond a certain limit where the conduction of the required current is no longer possible. In a connector, the contact resistance development is not linear with respect to its operational lifetime [19]. In the case of connectors coated with noble metals, the fretting wear is the important failure mechanism where the increase in contact resistance is smaller till the coating is intact and the failure mostly occurs due to oxidation of the substrate metal [10]. In the non-noble coatings such as tin, the contact resistance can rise to the failure criteria even before the wear through of the coating has occurred since the coating also degrades due to corrosion as well as oxidation [14]. The stress relaxation causing the reduction in the contact force results in the increase in contact resistance and complements the fretting wear and corrosion in degradation process. Apart from, coating materials and wear through of coating, the contact resistance development also depends on the presence of the contaminant films, contact force and stress levels of operating parameters such as input current which affects the joule heating. Given the complexity of the interactions between the failure modes in electrical connectors, the development of reliable physical model defining the relationship between degradation parameter and design and operational parameters is difficult [20].

There are few researches available for determining the remaining useful life and state of health of connectors. Martinez et al. proposed the state of health (SoH) prediction of power connectors using linear fitting model, non-linear fitting model and Markov chain Monte Carlo methods [72]. The linear fitting model applied the history of measured contact resistance data for prediction of degradation whereas the other two methods applied the nonlinear contact resistance development equation proposed by [73], which considered the oxidation as failure mode for predicting the contact resistance and comparing it with the measured value. Sun et al. applied the physical model for vibration and data based particle filtering method for forecasting the contact resistance development in electrical connectors subjected to vibrational accelerated life testing [74]. Ren et al. proposed a model for reliability estimation in accelerated lifetime tests with vibration and current as stress parameters using a modification of Eyring relation and Weibull distribution function [75]. In this way, majority of the approaches use a combination of physical models and statistics.

The data based approach using the historical performance is relatively less complicated and easy to implement. Gómez-Pau et al. developed a method combining the autoregressive models with moving average models to predict the remaining useful life of connectors based on the autoregressive integrated moving average (ARIMA) [65]. The autoregressive models were used

to predict the electrical resistance at given point of time while the moving average models were used to model the error in the prediction. The drawback of data based method is that the collection of adequate amount of data for reliable estimation of lifetime and performance requires considerable resources and longer test time.

The approach using a purely data based statistical procedure using short term test data for failure rate estimation of electrical connectors subjected to accelerated lifetime test under thermal loads needs to be developed since the test duration for accelerated thermal cycling tests are very long. Also, since electrical connectors form a significant subcomponents of the system, the indicators defining SoH of connectors for the application in the management and prognosis of system health via prognosis of degradation of connectors applied in it are to be determined. This could eliminate the need of longer tests and help in early detection of anomalies in the functioning and undertaking timely steps for prevention of system failure through timely replacement of affected sub-components.

## 1.2 Objective of the Thesis

The objective of the study is to introduce a parametric optimization approach for design of an electrical connector having an optimal combination of structural, thermal and electrical performance using FEM as well as a method to significantly reduce the time required for reliability prediction in accelerated lifetime tests (ALT) of electrical connectors subjected to thermal cycling.

As discussed in section 1.1.1, in the current competitive global market, the time to introduction of a new innovation and product to market has a direct bearing on the product lifecycle and profits. The development and testing duration in the field of electrical connectors are, however, considerable. There are numerous studies focusing separately on the design and testing of electrical connectors. Hence there arises the following question:

- Is there a possibility of laying down the framework for a procedure from design and development to testing of an electrical connector, with a view to significantly reduce the time to market?

The performance of an electrical connector, as seen in section 1.1.2, ideally depends on complex interactions between structural, tribological, thermal and electrical parameters. Also, based on the type of application, there are a variety of performance requirements to be fulfilled under each of the structural, tribological, thermal and electrical parameters. Fig. 1.3 illustrates some of the performances requirements of an electrical connector under operation. Considering the large number of parameters influencing the performance of an electrical connector, laying down a general procedure for development which takes into account all the parameters is a tedious task. Hence, there arises the following question:

- Can a practical framework which conveniently integrates the structural, tribological, thermal and electrical performance aspects in the development phase of electrical connectors be laid down?

As discussed in section 1.1.3 and section 1.1.4, there are a number of studies available which investigate the performance parameters and suggest conditions and methods for their improvement and optimization. The studies applying analytical approach for optimization of electrical connector designs require simplification of geometries. In case of connectors with complex geometries, FEM tools can be more suitable for designing and optimization. The majority of studies analyzing connector performance use flat contacts as reference while the studies applying round contacts are comparatively fewer in number. Most of the investigations in the field of structural performance of electrical connectors use only some of the design parameters and mainly focus on the insertion and extraction forces along with the equivalent stress distribution in the connector. The statistical tools can be efficiently applied for investigating the individual and interaction effects of the design parameters and achieving the required performance. The application of the statistics in the design optimization is limited. The

contact area and contact force directly influence the thermal and electrical performance and hence are to be considered together while investigating the structural performance. There are considerable studies investigating the relationship between the electrical contact resistance and the real contact area formed due to the roughness deformation. Instead of the total connector geometry, these studies consider only the standard geometrical combinations of the contact zone such as sphere-sphere, sphere-plane, cylinder-plane, cylinder-cylinder, etc. Therefore, the following questions arise:

- Can the influence of a complete set of design parameters be taken into account while developing a connector model using FEM and statistical tools?
- Can the contact area be incorporated together with the contact force while optimizing the entire connector geometry?
- Can the miniaturization of an electrical connector be achieved through the parametric structural optimization with optimal combination of contact area and contact normal force as a reference criterion?

Further, as seen from the discussion in section 1.1.4, there are certain limitations posed by analytical and FEM based methods proposed for the determination of real contact area in number of studies. The roughness parameter selection has direct influence on the roughness characterization. The surfaces having different topography characteristics could have the same average roughness $R_a$ which is a significant challenge in rough surface modelling. Also, the selection of magnification level and grid size significantly influence the roughness model obtained via statistical modelling methods or CAD modelling using point cloud data. Moreover, the majority of the studies attempt to determine the number of a-spots under given contact force in order to determine the real contact area and in turn the electrical contact resistance. The number of a-spots can vary significantly based on the roughness model used in the analysis thereby resulting in considerable deviations in the estimated electrical contact resistance. The plastic limit and yield strength relationships used in the analytical models may not reflect the actual material behavior. The 2D FEM models are not suitable for aperiodic roughness profiles while the 3D FEM models are computationally expensive and can face convergence issues. Therefore, the following questions arise:

- Can a surface roughness can be efficiently modelled using roughness parameters other than the average roughness $R_a$ in order to determine the real contact area?
- Can the real contact area be determined using a computationally feasible 3D FEM model in order to determine the relationship between the contact normal force, real contact area and the electrical contact resistance for the given contact conditions?

As discussed in section 1.1.5, due to the complex nature of physics of failure occurring in an electrical connector system, the development of physical models for the prognosis of the performance degradation and lifetime is complicated. The majority of available studies focused towards the prognosis of the lifetime of electrical connectors rely on the extrapolation of the

contact resistance development over a period of time in future. Also, a dependable estimation of the connector reliability requires the tests to be conducted till adequate number of failures occur. As electrical connectors are designed to have a very long lifetime, the time to gather the time to failure data even under accelerated lifetime tests could be long. Especially, the time duration needed for reliability estimation of electrical connectors subjected to accelerated thermal cycling tests are considerably longer. The state of health indicators for gauging electrical connectors' performance over time are also needed. Therefore, the following questions arise:

- Can prognoses of the long term performance of an electrical connector be made based on the short term accelerated lifetime test results?
- Can the lifetime of an electrical connector be determined using the short term accelerated lifetime test results?
- Can a set of practical and feasible state of health indicators be defined in order to monitor the performance of electrical connectors?

The answers to the questions in this section pertaining to the parametric design optimization and testing time reduction for reliability estimation are achieved through meeting the following four objectives in this work:

- Investigate the influence of structural parameters on the contact force and contact area of electrical connector using FEM and determine the parameter combination resulting in larger possible contact area with an acceptable contact force.
- Perform coupled structural-thermal-electrical FEM analysis to investigate voltage drop and joule heating in structurally optimized connector model.
- Establish a relatively computationally inexpensive 3D FEM model to determine real contact area in contacts with consideration of surface roughness, topology characteristics, contact force, coating material and substrate material.
- Establish a data driven statistical method based on probability distributions and distribution free method applying test data up to shortly before the occurrence of the first failure to reduce the time required in ALT for estimation of connector reliability.

Through this the structural, thermal, electrical and tribological aspects in the connector modelling as highlighted in Fig. 1.3 are to be included in the design process. Also, through the use of different connector types for reliability prognosis, it is to be shown that the proposed statistical procedure is applicable across different connector types. The parameters of interest based on design and testing optimization of connectors which have been focused upon in this work are shown in Table 1.1. The methodology for meeting the objectives of this work is elaborated in section 1.3.

Table 1.1: Design and testing optimization steps and objectives

| **Optimization step** | **Parameters of interest** | **Objective** |
|---|---|---|
| Parametric CAD modelling | Connector models of predefined sizes based on design of experiments | Reduce time for modelling |
| Structural | Contact area | Maximize |
| | Contact force | Optimize |
| | Size/Volume | Minimize |
| | Stress | Stress within acceptable limits |
| Electrical | Electrical resistance | Minimize |
| | Voltage drop | Minimize |
| Thermal | Joule heating | Minimize |
| Contact area | Real contact area and force relationship for different roughness | Investigate the procedure to determine real contact area in rough surfaces using FEM and simplified 3D roughness model |
| Testing | Time to failure for different failure probabilities and CLT | Eliminate need of lengthy tests by use of short term test data to prognose long term performance |

## 1.3 Methodology

### 1.3.1 Parametric optimization

In this study, a round connector made of brass with silver coating is used as a reference connector (Fig. 1.4). The receptacle has 8 spring elements and the pin diameter is 13.6 mm.

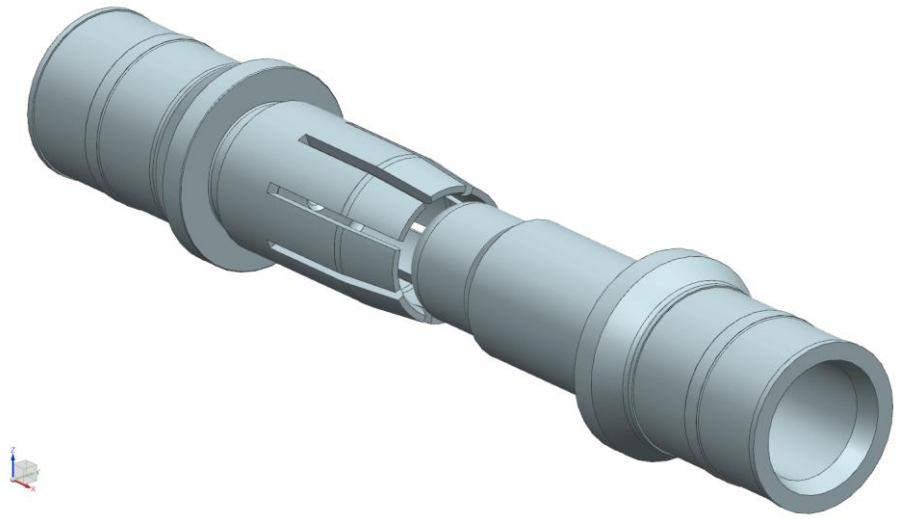

Fig. 1.4: Reference connector model

The optimization process of the reference connector design is carried out through variation of receptacle design while the pin design is unchanged. In this way, the influence of different structural parameters are studied with respect to constant spring deflection. Multiple CAD models of receptacle are generated using parametric modelling method by varying the dimensions of the reference connector within prescribed limits using design of experiment (DoE). The flexible portion of the receptacle is vital from the design point of view as it directly controls the contact force and contact area. Also, the maximum stresses occur at the base of spring [22] [34]. The parameters defining the receptacle are shown in Fig. 1.5. *R1* is the outer radius of the rear portion of the spring element, *t1* is the thickness of the spring element, *L1* is the total length of the spring, *L2* is the length of the bended portion of the spring, *t2* is the shell nosing and *R2* is the contact radius. Also the number of spring elements, *N* are considered as one of the parameters. The design of experiment methods, such as two level full factorial and Taguchi L8, are applied for obtaining various combinations of connector dimensions and the respective CAD models are generated parametrically in CAD tool. Since, the connector under study is a round connector, the advantage of symmetry is taken and the analysis is performed using single spring element of receptacle.

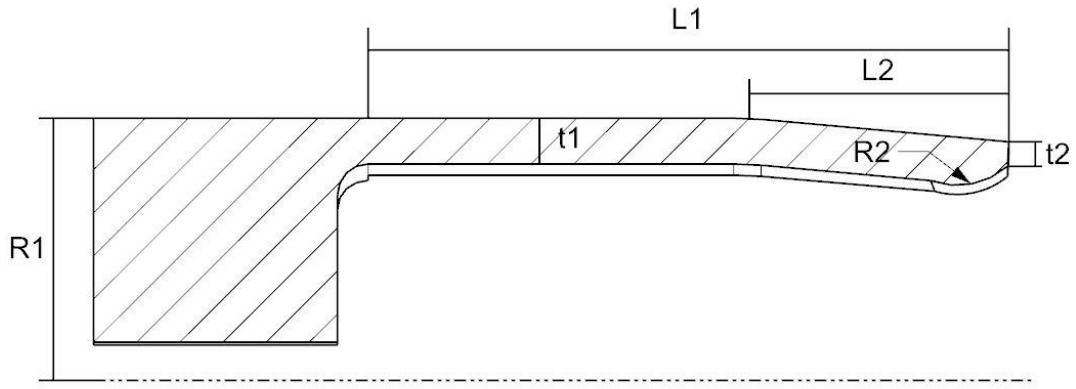


Fig. 1.5: Structural parameters of receptacle spring element

After parametric modelling using CAD tool, structural FEM simulation is performed on the connector models using ANSYS 2019R3 software. From structural point of view, an ideal connector is expected to have a larger contact area and a medium contact force so that the contact resistance remains minimum and wear rate lower. The normal contact force and contact area in the receptacle resulting from insertion of pin are simulated. The correlation between design parameters and the contact force and contact area is investigated. The response surface plots showing the interaction effects of the parameters on contact force and contact area are generated using stepwise regression in MATLAB. The most influential parameters are identified based on the variations of individual parameters in the initial analysis. The further analysis is performed by constructing new models using DoE based on the results of initial analysis by varying the influential parameters. The designs having larger possible contact area along with the contact force and equivalent stress within acceptable limits are categorized as structurally optimal connectors and are selected for investigation of thermal and electrical performance.

In the next step, a coupling is established between structural and thermal-electric environments in ANSYS 2019R3 workbench. Here, the influence of operating conditions such as input current, voltage, temperature and ambient conditions on the thermal and electrical performance of the reference and optimized connector models is analyzed. The results of the FEM simulation of reference connector are compared with the experimental results in order to confirm the validity of the proposed approach. The volumes of the reference connector and optimized connector are compared for purpose of miniaturization. The process of parametric optimization of electrical connector using parametric modelling and coupled structural-thermal-electrical analysis is highlighted in Fig. 1.6. In this way, a comprehensive design optimization procedure through the use of CAD, FEM and statistics tools is introduced.

In order to confirm the applicability of the approach to connectors of other sizes, the procedure is repeated for a relatively small reference connector with pin diameter of 2.5 mm. For the 2.5 mm connector also, the different connector models are generated through three level parameter combinations obtained by Taguchi L9 design of experiment and structural simulations are performed on them. In this way, the effect of the design of experiment and parameter level selection on the optimization process is also understood by comparing results with 13.6 mm connector. The structurally optimal design is chosen for thermal-electric performance evaluation. The results of simulation of reference connector are compared with the experimental results.

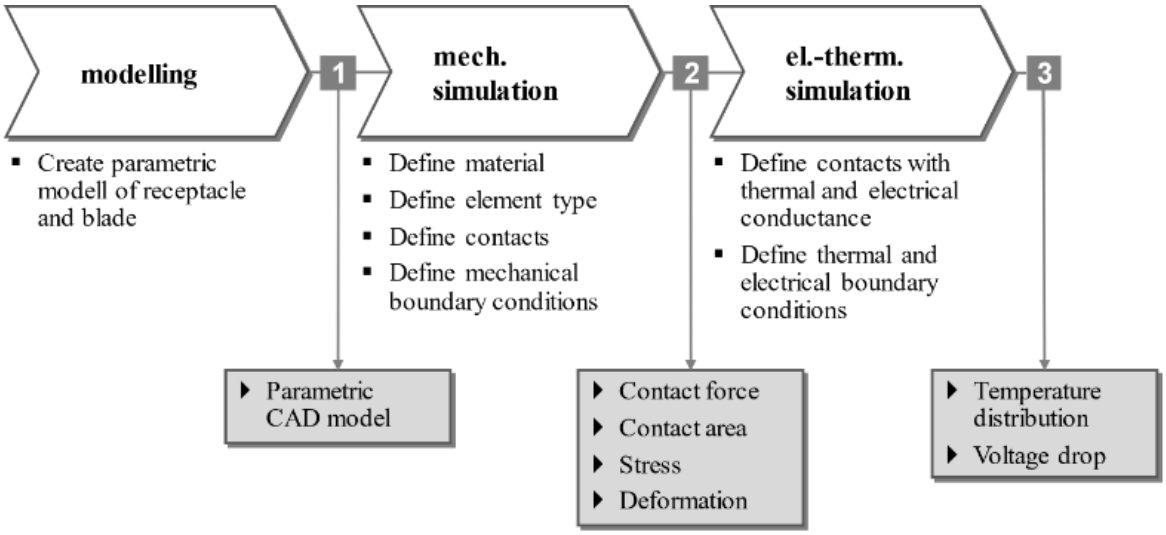


Fig. 1.6: Design optimization procedure using coupled FEM analysis

### 1.3.2 Real contact area determination

The surface roughness plays an important role in the performance and reliability of the connector and the degradation of the contact zone is the main reason for connector failure [37] [76]. The real contact area formed due to surface asperities deformation directly influences the thermal and electrical conductivity. The surface coating is done on the base material of the connector and can be varied as per requirements once the basic connector design giving maximum apparent contact area and optimum contact force is obtained. Therefore, a separate study is conducted in order to investigate the tribological performance of the connector from the real contact area perspective. For this purpose, a sphere–plane contact geometry combination as shown in Fig. 1.7 is used. The contact material used is bronze with galvanic coated gold. Gold is selected as a coating material due to its inertness so that the real contact area obtained can be considered equal to the electrically effective area. This is important for the validation of the simulation and experimental results. The sphere and flat surfaces with different roughness are generated and are broadly categorized into polished and rough surfaces. The contact resistance behavior against contact force for rough and polished surfaces is obtained

through experiments. The electrically effective contact area i.e. real contact area resulting from the surface roughness deformation under different contact forces is determined using 3D FEM simulation.

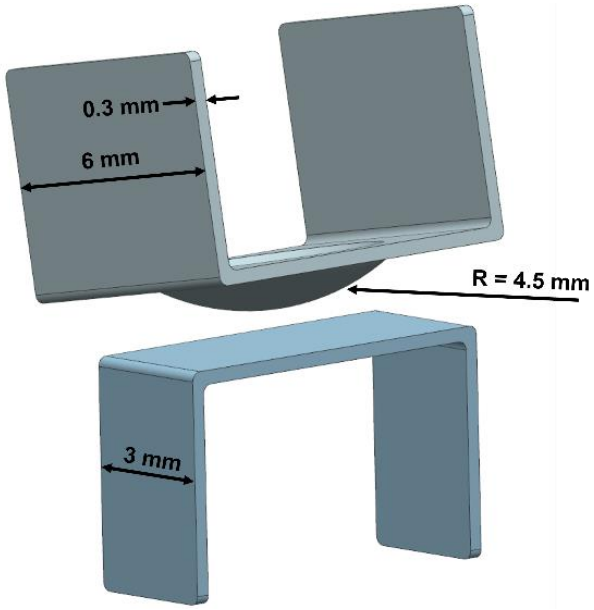


Fig. 1.7: Sphere-plane contact geometry model

The FEM simulation model and surface roughness profile simplification used in this study is based on the simulation method used by Yuan et al. in [18] to estimate the fretting wear in electrical contacts with silver coating. The surface roughness profiles are simplified and modelled in the form of longitudinal triangular rib shaped structure with height equal to the core roughness $R_K$ obtained from bearing area curve and width equal to the average groove width $R_{SM}$. The core roughness $R_K$ and average groove width $R_{SM}$ are measured from the actual polished and rough samples using confocal microscope. The use of bearing area curve helps in appropriate characterization of topography.

The contact area obtained from deformation of rough surface in simulation is equated to the circular area and the equivalent contact radius of the real contact area is calculated. Using the equivalent contact radius, the contact resistance is calculated using the Holm's equation for constriction resistance for circular shaped constriction [9]. The calculated contact resistance is then compared with the measured contact resistance at given force for the validation of the proposed method. In this way a computationally less costly and accurate method for determination of real contact area for given contacting conditions is introduced.

### 1.3.3 State of health and reliability prognosis

In order to investigate the prognosis approach using short term test results for prediction of CLT and definition of SoH indicators of electrical connectors subjected to the accelerated thermal cycling tests, the test data of electrical connectors of different designs and materials is utilized.

A considerable amount of test data of the different types of connectors subjected to thermal cycling in the ALT is available in house which has been accumulated over number of years of test duration. The statistical analysis is performed using this data.

The distribution fitting is performed on the contact resistance data at different test periods. The exploratory data analysis results show a sudden surge in the average and standard deviation of the contact resistance shortly before the occurrence of initial failure. This phenomenon is exploited in order to establish a relationship between the contact resistance development at the time of initial failure and the connector failures in later stages of the test. The respective scores of distribution corresponding to given failure probabilities are used to relate the contact resistance development and failure probabilities. For e.g., in Fig. 1.8, the c score of 0.84 corresponds to failure probability of 20 % considering the standard normal distribution of resistance data. Also, the percentiles of the contact resistance data are directly correlated to the corresponding failure probability as seen in shaded region under the curve. For e.g., the electrical resistance values between $80^{th}$ percentile and $100^{th}$ percentile under distribution curve correspond to 20 % of the failed connectors. Such a correlation between percentiles of electrical contact resistance and the corresponding failure probabilities forms the basis of this investigation. In addition to the method using probability distribution, a distribution free method applying similar procedure as that of distribution based method and using percentiles of actual resistance data instead of the *c*-scores of distribution is also investigated.

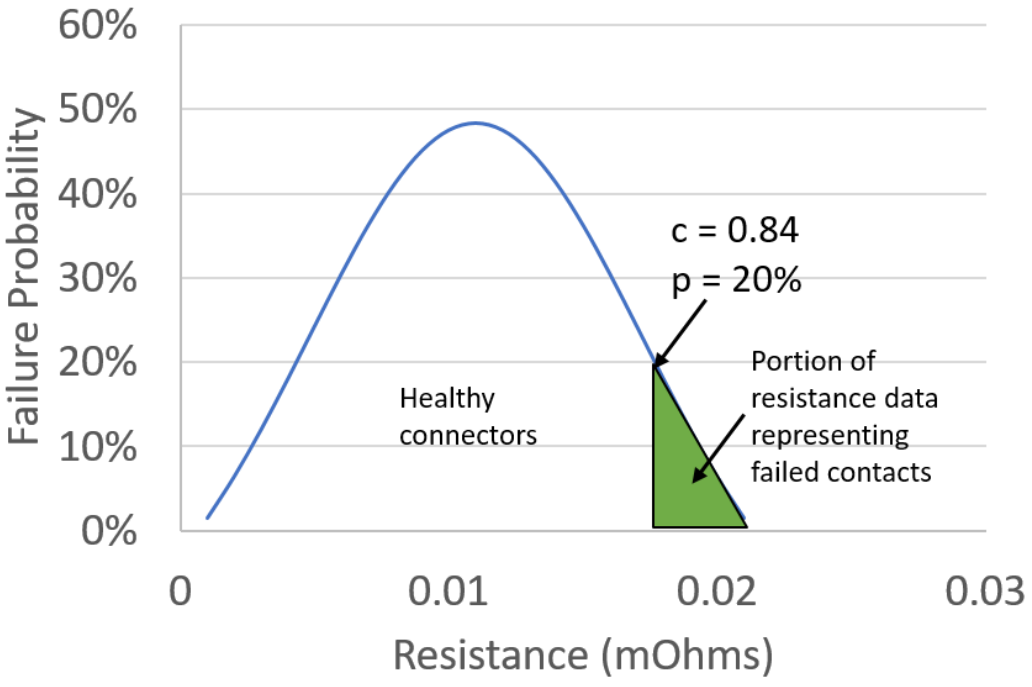


Fig. 1.8: Correlation between electrical resistance and failure probability

The CLT and the FIT rate derived through the proposed statistical procedure are compared with the measured test results. Through the method developed, CLT, FIT rate and SoH of connectors in the later stages of the ALT can be predicted by using the data of electrical resistance development recorded in the early stages of test. Thus, the time required for estimating the connector reliability is significantly reduced. Also, a sensitivity analysis is performed to analyze the effect of the selection of data of different test durations on the prognosis.

## 1.4 Thesis Structure

First, engineering fundamentals from the literature with the focus on the solution to scientific issues and objectives with respect to the design, contact physics, testing and reliability of electrical connectors in this work have been presented in chapter 2. The mathematical and numerical models defining the performance, functioning and different physical phenomenon in an electrical connector system along with the procedure of testing and reliability determination are presented. The contact resistance, joule heating, heat transfer, role of contact force and the degradation mechanisms in electrical connectors are discussed and the generally used models for determining acceleration factor in laboratory tests and the lifetime based on various distributions are given.

The optimization of an electrical connector design in this work is to be achieved through the application of CAD, FEM and statistical modelling tools. The proposed procedure of structural, thermal and electrical optimization of connectors is presented in chapter 3. Also, the experimental test procedures using the reference connector design for the validation of FEM models used in this study is given. The structural, thermal, electrical performance results from the FEM simulation are compared with the experimental results. The results of the influence of the design parameters on contact area and contact force as derived from the statistical modelling of FEM results are presented. The performance of the optimized connector model is compared with the reference connector model and the degree of miniaturization achieved is discussed.

The contact area aspect of an electrical connector in this work is investigated with respect to the real contact area formation resulting from the rough surface deformation. Chapter 4 discusses the procedure and results of the rough surface modelling and roughness deformation simulation using FEM in order to determine the real contact area and electrical contact resistance for given contacting conditions.

The long term performance and reliability prognosis of electrical connectors in this work is done through the application of short term test data. In chapter 5, the data driven statistical method of determining the CLT using short term test data is presented. For purpose of validating the proposed method, the results of the prognosed CLTs are compared with the measured values. Also, the results of influence of state of health indicators on the CLT prognosis are discussed.

Chapter 6 presents conclusions derived from the study and the outlook.

# 2 Theoretical fundamentals of electrical connectors and reliability

## 2.1 Connector System

The electrical connectors are used to facilitate convenient installation, assembly and maintenance of electrical and electronics systems. They provide connections between the components of the system for transmitting electrical current and signals as well as connect the systems to external source of power supply and signal. The number and types of electrical connectors used depend on the system complexity, functional requirements and the layout of the wiring harness. The choice of the connector is decided based on the level of current and voltage to be transmitted and the field of application. Also, the cost is the determining factor in connector selection. The basic electrical contact system along with the electrical resistances formed by different parts of the system is shown in Fig. 2.1. It consists of a contact made of mating parts namely male part i.e. pin and a female part i.e. receptacle, which are connected to the cables. There are contacts occurring at three different locations for a given connector. One separable contact occurs at the contacting terminals while the other two contacts are fixed type where cables are fixed to the connector terminals either through welding, soldering or crimping. The pin and receptacle parts are generally enclosed in an insulated casing which provides protection to metallic parts and enables the mating by providing proper alignment and limits the relative motion between them. The male and female parts conduct current and signal through the contact zone when the contact is closed. An electrical connector can consist of one or more electrical contacts depending on the design and application.

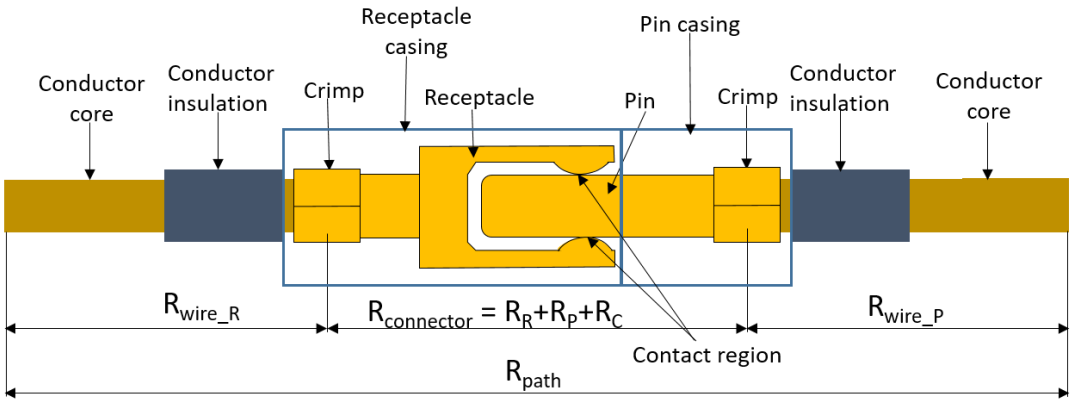


Fig. 2.1: Electrical connector system and electrical resistances [12]

The different parts of the electrical connector and cable system contribute to the electrical resistance as shown in Fig. 2.1. The path resistance $R_{path}$ is the total resistance in the system. It is the sum of the electrical resistance resulting from:

- The bulk resistance of wires on the receptacle $R_{wire\_R}$ and pin $R_{wire\_P}$ sides. These also include the resistances formed by the combination of contact resistance between wire and crimp section and the bulk resistance of wire and crimp on the respective sides.
- The connector resistance $R_{connector}$

In this work, the focus is on the optimization of connector through reduction of $R_{connector}$ which further consists of bulk resistance of receptacle $R_R$ and pin $R_P$ and the contact resistance $R_C$ formed in the contact zone between receptacle and pin. It is given as:

$$R_{connector} = R_R + R_P + R_C \tag{2.1}$$

The connections in a system can be fixed or flexible i.e. separable. The electrical contacts are classified based on their functions into closed contact points, plug-in contacts, sliding contacts and switching contacts [77, p. 389]. The closed contact points are established for permanent contact through different methods such as wire-wire twisting, insulation displacement connection, soldering, welding or crimping the conductors. In case of wire-wire twisting contacts, the required contact force is applied using screw or a spring in an insulated housing. The plug-in contacts conduct current when closed through contact between mating components and are de-energized when open. The sliding contacts are used for conducting current between the components sliding against each other. The switching contacts open or close when the current passes through them such as in the case of solenoid equipment.

Slade classifies the flexible connectors as simple terminal-terminal, rack-panel, plug-receptacle; edge-on and compliant pin [6, p. 378]. The terminal-terminal types have simple design and are used within appliance or system housing. The rack-panel type of connectors are used when one part of connector is installed on the removable part of appliance like a rack and another part denoted as header is installed on the fixed part like panel of the appliance. The plug and receptacle contacts are most widely used type of contact due to the ease of installation in systems with large number of functions such as harnesses in automotive applications. The plug and receptacle could possess either flat or round geometry where the receptacle could be slotted into number of flexible segments or might be a rigid. They might have one or multiple contact points based on the number of spring elements formed by the contact between spring like segments of the receptacle. In some of the designs, the contact force is created by placing a separate spring in the grooves of rigid receptacle. The edge–on type of connectors are used in board-to-board or wire-to-board connections where one of the connector terminals is etched on the printed circuit board with metal and the other terminal consisting of spring like structures is connected to the cable. The compliant pin connectors consists of spring of higher stiffness and is generally press fitted in the printed circuit boards of electronic components and is seen

as an alternative to soldering joints. It has been observed that the designs of plug and receptacle contacts in majority of designs have symmetrical pattern.

The selection of connector material is dependent on the material properties such as electrical conductivity, thermal conductivity, mechanical strength, softening temperature, thermal expansion, machinability and costs to name a few. The connector is expected to transmit current and signal without distortion while retaining its stiffness and shape over larger temperature range and designed lifetime. Copper is a better choice for connector material in majority of the applications due to better combination of conductivity, resistance to thermal expansion, safety, and cost [78]. In order to increase the creep resistance for constructing connectors with longer life and reliability, copper is alloyed with tin, zinc, beryllium, cadmium, zirconium etc. to improve the mechanical strength [6, p. 241]. The brass and bronze have a good compromise between mechanical properties and electrical properties in comparison to pure copper and hence are widely used as connector material [77, p. 289]. There can be other materials such as aluminum, gold, silver and steel used for connector depending on the operating conditions. The material properties of commonly used metals in the electrical applications are highlighted in [79, p. 32].

The base materials used in electrical connectors are mostly non-noble and hence prone to oxidation and corrosion which leads to contact degradation. In order to prevent the contact from degradation and prolong its lifetime, the single or multi-layered coating of other materials is provided on the base material of the contact. An ideal coating material is expected to resist wear and corrosion and have good thermal and electrical conductivity through formation of larger real contact area and air tight contact zone in order to prevent the compounds in the ambient atmosphere from entering the contact zone. The coatings materials can be broadly classified into noble and non-noble based on their resistance to oxidation.

The noble metals such as silver, platinum and gold are resistant to oxidation and the failure in connectors coated with such metals occurs after the surface coating is completely worn through. Gold has a lower hardness and prone to wear. In order to increase its hardness, gold is alloyed with elements such as cobalt, nickel or iron thereby improving its wear resistance [80]. It is widely used in the low current and low force applications. Silver is comparatively cheaper than gold and has very good electrical and thermal conductivity due to which it is widely used in the electronic applications [77, p. 205]. It is suitable for applications involving higher mating cycles. It is resistant to oxidation but has tendency to form tarnish films if exposed to environment consisting of sulphur and chlorine and is prone to adhesion which leads to loss of coating material. Platinum is resistant to oxidation and tarnishing and is suitable for low current applications with high reliability [6, p. 245].

Tin is the commonly used non-noble coating material due to low price and its tendency to oxidize and form a stable and protective hard and brittle layer of oxide on the surface which prevents further corrosion. The tin oxide layer is unaffected by the ambient environment and is

harder than the underlying softer and ductile tin coating and is easily broken with application of adequate amount of force thereby enabling the metal to metal contact between conducting surfaces [6, p. 152] [81]. However tin coatings are not durable and prone to degradation through fretting corrosion and have tendency of whisker formation [82]. Nickel is another commonly used non-noble metal in electrical contact coatings. However, nickel forms a thin protective oxide coating in dry conditions while in moist conditions the film thickness grows rapidly thereby increasing the electrical resistance. Since nickel has good hardness, it is used as an under layer below top coating and helps in improving the wear resistance and acts as a diffusion barrier as it is resistant to formation of intermetallic phases [80]. The contacts with noble coatings have longer life than the contacts with non-noble coatings [83] [84].

The coating material of the mating surfaces in a connector can be same or different. Pairing with same materials is generally preferable with respect to the minimizing the galvanic corrosion [85, p. 120]. Thus the difference in the surface potential of two contacting materials should be as low as possible. Silver-silver and gold-gold pair give stable contact resistance whereas tin-tin pair results in less stable contact resistance [6, p. 452]. However, certain precautions should be taken when selecting the dissimilar pairing materials together. A thick gold and palladium pair results in transfer of gold to palladium surface due to difference in material hardness and forms a gold –gold contact pair and hence stable contact resistance [86]. In a gold and tin contact pair, tin is transferred to gold surface leading to a tin-tin contact on a hard surface. The resulting fretting corrosion of tin and different mechanics of oxide film fracture leads to unstable resistance [87]. Pairing tin with silver results in increased contact life as compared to contact with tin-tin, tin-gold and tin-palladium pairing [88].

The electrical contacts are manufactured mainly through machining the pins in CNC or through stamping the metal strips. In automated stamping process, the thin metal strips of base material in the form of coil are fed in a stamping press at one end. The sheet passes through numerous progressive dies which shear and form the metal to generate an accurate shape with required mechanical properties. The coating of the base material is done through various processes such as electroplating, electro-less plating, hot dipping, cladding, reflowing, physical vapor deposition, etc. [89]. The cladding and electroplating coating processes are most widely used. In electroplating, the metal strip acts as cathode and is dipped in the electrolyte while the coating metal acts as anode. With the supply of electric current, the coating formation starts with the deposition of the coating metal on the strip surface. In electro-less plating, the coating metal is in the form of ions in the solution which gets deposited on the base metal strip by catalysis. In hot dipping, the metal strip is passed through the molten bath of the coating metal where the metal adheres and solidifies on the surface of the strip. In cladding process, the coating metal strip and the base metal strips are rolled and sintered together thereby creating a metallurgical bond between them. In reflowing, the solder is laid on the base metal and melted causing it to adhere to the base metal surface after solidification. It is used to remove residual stresses in the coating for eliminating the formation of whiskers. In physical vapor deposition, the coating

metal is evaporated by electrical arcing or by sputtering in a low pressure atmosphere causing the vapors to condense on the base metal and forming a coating. In some of the applications, the multilayer coatings and coatings containing nanoparticles are also used [90].

## 2.2 Electrical Resistance

As seen in equation (2.1), the electrical resistance of a connector system comprises of the bulk resistances of the receptacle and pin and the contact resistance formed between receptacle and pin. The bulk electrical resistance depends on the electrical resistivity of the base material, geometry of mating components whereas the contact resistance is influenced mainly by the contact zone properties which is in turn affected by the multiple factors such as surface coating material, roughness, contact force, surface finish and presence of contaminants to name a few [6, p. 251].

The electrical resistance $R$ in terms of operating parameters namely voltage $V$ and current $I$ in a conductor is calculated as:

$$R = \frac{V}{I} \tag{2.2}$$

In terms of material properties and geometry, the electrical resistance $R$ in a conductor of uniform cross section can be defined with the help of electrical resistivity $\rho$ and geometric dimensions length $L$ and cross sectional area $A$ of the conductor as:

$$R = \frac{\rho \cdot L}{A} \tag{2.3}$$

The geometry of the conductor influences the current density and hence the current flow developed due to the electric field [6, p. 312] [91]. The conductor of a given material with smaller cross sectional area will have larger resistance to flow of current. The electrical resistivity $\rho$ is an intrinsic property of material and is inverse of the electrical conductivity $\sigma$. An ideal electrical contact is expected to possess high electrical conductivity.

$$\rho = \frac{1}{\sigma} \tag{2.4}$$

According to Joule's law, when an electric current $I$ flows through a conductor with electrical resistance $R$, conversion of certain amount of electrical energy to heat takes place due to resistance to flow of current. The amount of work done $W$ i.e. electrical energy transformed in time $t$ in the form of heat is given as:

$$W = I^2 \cdot R \cdot t = V \cdot I \cdot t \tag{2.5}$$

The unit of $W$ is joules. The power loss $P$ in a conductor in terms of joules per second can therefore be written as:

$$P = I^2 \cdot R = V \cdot I \tag{2.6}$$

The conversion of the electrical energy into heat results in the temperature rise of the contact. The small sized electrical contact conducting a given electrical current will have higher heat generation in comparison to large sized contact of same material due to the difference in the electrical resistance resulting from the geometry of contact. Thus the temperature and electrical resistance are positively correlated. The increase in the temperature of contact causes the expansion of the contact material. The extent of expansion of contact is governed by the temperature dependent coefficient of thermal expansion $\alpha_L$. The relationship between thermal expansion and temperature in linear conductors is given as [6, p. 238]:

$$\alpha_L \cdot L_{initial} = \frac{\Delta L}{\Delta T} \tag{2.7}$$

where, $L_{initial}$ is the initial length of conductor, $\Delta L$ is the change in length of conductor due to change in temperature $\Delta T$.

With the fluctuations in the ambient conditions and load on connector, the temperature of connector also fluctuates resulting in the expansion and contraction of the material. This causes the fretting wear and corrosion in electrical connectors which degrades the contact zone and increases the electrical resistance resulting in the increase in joule heating. The relationship between the temperature change and electrical resistance is governed by coefficient of electrical resistance $\alpha_R$ given as [6, p. 238]:

$$\alpha_R \cdot R_{initial} = \frac{\Delta R}{\Delta T} \tag{2.8}$$

where, $R_{initial}$ is the initial electrical resistance of conductor, $\Delta R$ is the change in the electrical resistance of conductor due to change in temperature $\Delta T$.

The coefficient of electrical resistance and coefficient of thermal expansion are positive for the metals and alloys [92] [93]. Due to degradation mechanisms acting in the connector system, the temperature increase and resistance increase go hand in hand during the operation and the thermal conductivity decreases with the increasing electrical resistivity [9] [94]. This causes the temperature of the connector to increase beyond acceptable range leading to eventual failure.

The contact resistance has inverse relationship to the contact area. In an electrical connector, the contact surface is not smooth and consists of certain degrees of roughness and surface asperities. The conductive metallic contact is formed through the contact interaction between the surface asperities. The volume of the material available for conduction is reduced due to the asperities which increases the electrical resistance at the contact interface. This is due to the concentration and bundling of current lines as they approach the contact junction formed by the asperities causing the rise in the current density at the contact interface [6, p. 4]. When the two

surfaces contact under certain contact force, the asperities on the surface deform due to friction and compression forming the conductive contact spots at different locations within a contact zone called as a-spots as shown in Fig. 2.2. The asperity deformation also occurs during the insertion and extraction process.

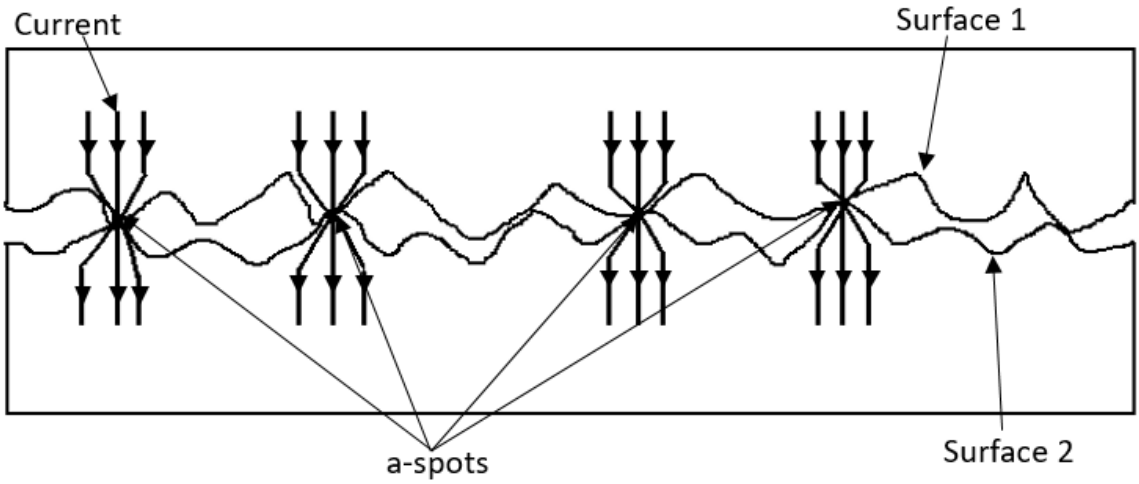


Fig. 2.2: Current flow across rough surface asperities

The real contact area in the clean metallic surfaces is the sum of the areas of the contact spots which is generally smaller than the apparent contact area resulting from the contact of perfectly smooth surfaces. With the increasing force, the smaller asperities also form new contact spots thereby increasing the number and size of a-spots. The real contact area is influenced by the shape of the asperities, asperity distribution, gap between asperities, mechanical strength and hardness of the material [95]. When the asperity is approximated to have circular cross section, the real contact area increases with increase in radius of curvature and decreases with increasing hardness and modulus of elasticity [96, p. 38]. The effect of the shape and dimensions of the contact spots and contact force on the electrical resistance has been discussed in [9]. It is found that the constriction resistance is largely influenced by the shape of constriction. Also, the contact spots are greatly affected by the current flowing through them.

When the larger current flows through the asperities, the localized temperature in the contact zone rises leading to the softening of the metal. This increases the size of a-spots. Kharin et al. related the ratio of material hardness above softening temperatures to the ratio of change in radius of a-spots [97]. It was found that the radius of a-spots increases by 40% for copper and 65% for silver for the hardness ratio at 500 °C to 200 °C. The potential difference across the contact needed for the melting of the metal is termed as melting voltage. In cases where the voltage drop across the asperities exceeds the melting voltage, hardness of the material drops significantly and the asperities melt and are unable to bear the mechanical load. The load gets transferred to the adjoining smaller asperities [98]. The melted material at the contact interface could fuse and after solidification form welded joints. However, during the fretting motion,

these joints can fracture forming new load bearing areas and contact spots. In this way the contact spots formation and destruction is a dynamic process.

The electrical resistance at the contact spots comprises of the resistance due to the metallic contact between contact spots termed as constriction resistance $R_{constriction}$ and the resistance due to the presence of thin insulating layers of oxides or other corrosion products formed on the contact surface depending on the nobility of the coating material termed as film resistance $R_{film}$. The contaminant films of dust or polymer compounds can also be found on the contact surface based on the coating material and field of use. For example, tin and copper surfaces form the protective thin layers of oxides on the metal surface whereas palladium surfaces could get contaminated by the polymers from the connector casings forming the frictional polymers. These films of oxides and contaminants are highly resistive and add to the electrical resistance occurring at the contact zone by reducing the real contact area formed by asperity deformation at $a$-spots. The contact force plays an important role in piercing the insulating films and establishing the metallic conductive contact. With the piercing of the oxide film, the metal to metal contact is established and the electrical resistance at the contact interface drops significantly [99]. The $R_C$ in equation (2.1) can be written as:

$$R_C = R_{constriction} + R_{film} \tag{2.9}$$

The variations in the bulk resistance for the given geometry and input current are more predictable as there are universal equations defining the relationships between current, dimensions and material resistivity available as seen earlier in equation (2.3). Also, for the given current load, the geometry of the connector can be appropriately designed through investigation of the current density distribution and joule heating by FEM [100]. However, the contact resistance development at the contact interface is more complex process as it is influenced by large number of design and operational parameters and interactions [84]. The extent of degradation in contact resistance is different at different stages of connector life caused by the wear mechanisms acting at the contact interface. Due to complex interactions between failure modes, design and operational parameters which are strongly influenced by time, the equations defining the contact resistance development with these parameters are difficult to generate [66] [101]. However, there are some time dependent models applied for contact resistance development prediction with respect to specific degradation mechanisms [69] [73] [74]. The connector is said to be failed when its contact resistance increases beyond acceptable limit. Since, in an electrical connector, the bulk resistance is precisely predictable and is less fluctuating under a given current load, the significant part of the increase in the resistance is due to increase in the contact resistance over the period of time leading to eventual failure. Therefore, the development of electrical resistance and degradation mechanisms at contact interface of mating parts of connector are of high significance in the development of connector.

The magnification in the contact zone allows the further classification of the contact zone due to presence of the surface roughness asperities and the insulating film layers in the contact zone [102, p. 7]. The contact zone is considered to be consisting of following areas as shown in Fig. 2.3.

- Apparent contact area ($A_A$): It corresponds to the geometrical contact area formed between perfectly smooth surfaces.
- Load bearing area ($A_L$): It corresponds to the sum of the areas formed due to the deformation of the asperities within the apparent contact zone.
- Contaminant film area ($A_C$): It corresponds to the area covered by the oxide and contaminant films within the load bearing area. Depending on the thickness of these films, they can form quasi-metallic contact spots with very small thickness allowing the electrons to jump across through tunneling effect or a highly resistive layer for films with higher thicknesses.
- Effective conducting area ($A_E$): It corresponds to the metal-metal contact in the load bearing contact zone through which actual electrical conductance takes place and is usually referred as *a-spot*.

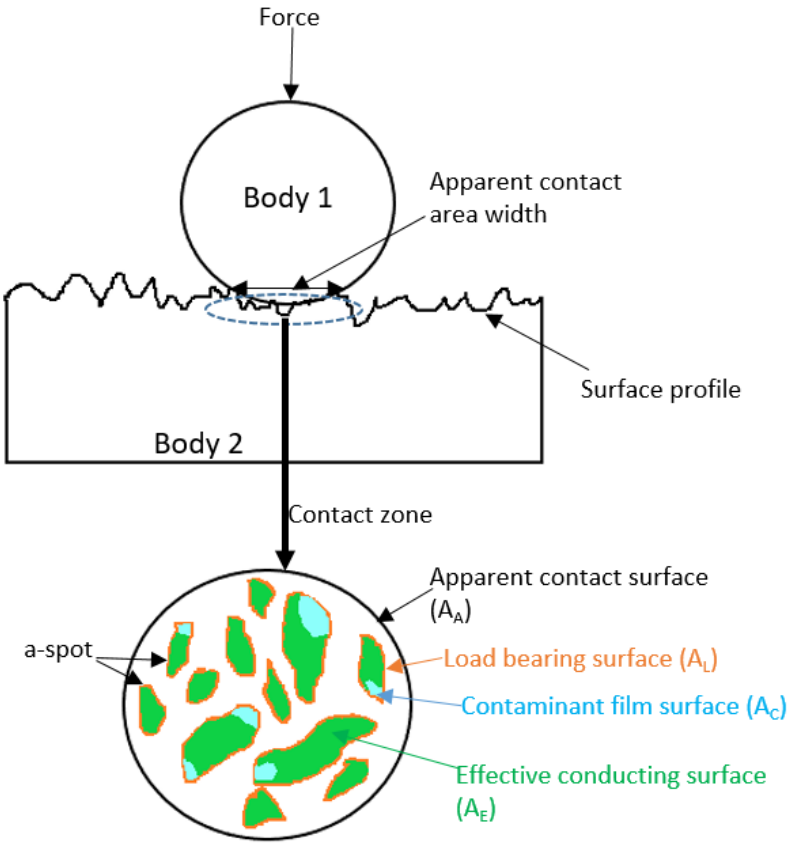


Fig. 2.3: Contact zone classification

### 2.2.1 Electrical contact resistance

In a contact with perfectly smooth and clean surface, the apparent contact area, load bearing area and effective conducting area will be equal. In the rough surfaces, the effective conducting area is the smaller than the load bearing area due to presence of surface asperities as seen in Fig. 2.3. The presence of the contaminant films further reduces the conducting area. Due to the continuously changing contact conditions at the contact interface, the load bearing area, contaminant film area and effective contact area undergo continuous changes. The contact with larger apparent contact area will have sufficient number of a-spots for the reliable conduction of electric current and bearing the load in spite of contact deterioration over the period of time [96, p. 293].

There are different studies available investigating the effect of shape of constriction on contact resistance [102, p. 16] [103] [104]. According to Holm, the equipotential lines formed inside the contact near the contact spot of radius $a$ are in the form of the semi-ellipsoids with $\sqrt{\mu}$ as the semi-axis, Fig. 2.4 (b) [102, p. 16]. In such a case, the constriction resistance as a function of $\sqrt{\mu}$ and contact radius $a$ of circular constriction is given as:

$$R_{constriction} = \frac{\rho}{2\pi a} \cdot arctan\sqrt{\frac{\mu}{a}} \tag{2.10}$$

At sufficient distance away from the contact surface with larger $\mu$ values, the constriction resistance for one side of the contact is given as [102, p. 16]:

$$R_{constriction\_1} = \frac{\rho}{4a} \tag{2.11}$$

Considering both the contact partners having same electrical resistivity, the total constriction resistance $R_{constriction}$ is twice the $R_{constriction\_1}$ and is given as [102, p. 16]:

$$R_{constriction} = \frac{\rho}{2a} \tag{2.12}$$

Thus the constriction resistance in contact between similar metals for given roughness can be calculated once the diameter of the constriction $2a$ is determined. This forms the basis of validation of the results of tribological aspect of optimization of contact for given contacting conditions in this work. Fig. 2.4 (a) illustrates the current flow through a circular a-spot.

As seen in Fig. 2.2, the mating surfaces contact at multiple a-spots within the contact zone based on the dimensions and distribution of the surface asperities. In a contact with uniformly distributed a-spots, the resistance decreases with increasing number of a-spots and becomes

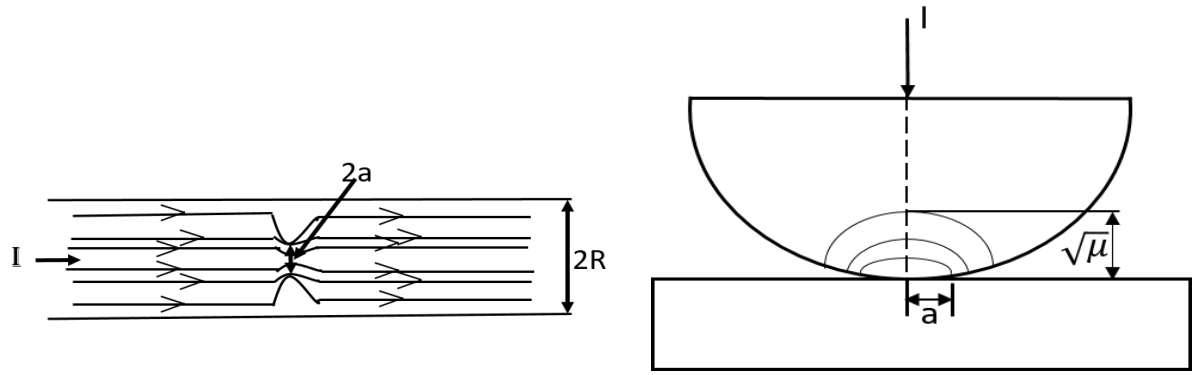


Fig. 2.4: (a) Current flow through circular constriction (left) and (b) equipotential surface near constriction (right) [36] [102]

almost constant after a certain value of a-spot numbers is reached [55]. The equivalent radius of the real contact area $A_{real}$ formed through multiple contact spots can be calculated as:

$$a = \sqrt{\frac{A_{real}}{\pi}} \tag{2.13}$$

For the ease of application, the a-spots are assumed to be of circular shape. However, there are equations available for the a-spots of shapes other than circular such as elliptical, rectangular, square and ring shaped [6, p. 8] [103] [104]. The square or rectangular shaped constrictions occur in the surfaces having pyramidal knurls whereas ring shaped constrictions occur on the cladded layer on the knurled surface [6, p. 11].

For two dissimilar materials with resistivity $\rho_1$ and $\rho_2$ respectively in contact, the constriction resistance is given as [6, p. 6]:

$$R_{constriction} = \frac{\rho_1 + \rho_2}{4a} \tag{2.14}$$

Greenwood et al. showed that the surface asperities deform plastically and the load bearing contact area which is also the real contact area in the case of absence of alien films in contact zone, can be given by the relationship with load carried $F$ and the hardness $H$ of the softer material of the contacting pair as [42]:

$$A_{real} = \frac{F}{H} \tag{2.15}$$

The Holm's radius $\alpha_H$ is given as:

$$\alpha_H = \sqrt{\frac{F}{\pi H}} \tag{2.16}$$

Therefore, the equation (2.12) for constriction resistance can be written as:

$$R_{constriction} = \frac{\rho}{2 \cdot \left(\frac{F}{\pi H}\right)^{0.5}} \tag{2.17}$$

This equation for constriction resistance is independent of the actual dimensions of the a-spots in the contact zone and the contact resistance for a clean surface can be easily determined with the knowledge of the electrical resistivity, applied contact force and the material hardness. This equation has been validated by number of works [105] [106]. However, since the influence of the plastic deformation of the surface asperities of the contact is not adequately considered by equation (2.15), it can be ideally applied for the qualitative analysis rather than the accurate determination of the constriction resistance.

Slade classifies the insulating films formed on the contact surfaces based on chemical composition and film thickness [6, p. 102]. Based on the chemical composition, the films are classified into three categories as pre-tarnish films, tarnish films and alien films. The tarnish films are formed by the reaction of atmospheric contents with the contact metal whereas the alien films could be a result of deposition of lubricant, water or other contaminants on the contact surface. They can be continuous or in the form of islands on the contact surface. Based on the thickness, the films are classified as microfilms which are few atoms thick and passivating films which stop growing or grow very slowly after certain thickness. Examples are oxide films of tin and nickel [107] [6, p. 51]. The films after reaching certain thickness have a strong influence on the electrical conductivity and also the extent of the influence strongly depends on the substrate metal [108]. The electrical resistance due to metal oxide films of electrical resistivity $\rho_1$ and $\rho_2$ and thicknesses *t1* and *t2* respectively formed on the contacting surface area *A* is given as [6, p. 55]:

$$R_{film} = \frac{\rho_1 t_1 + \rho_2 t_2}{A} \tag{2.18}$$

In this work, the coating materials of the reference contacts applied for design optimization and influence of surface roughness on real contact area are noble in nature. Due to this, the contact zone is assumed to be perfectly clean and oxide free and hence the film resistance $R_{film}$ is not considered in the analyses.

The magnitude of the surface roughness has a direct influence on the real contact area and hence the contact resistance. The real contact area in smoother surfaces is larger than the rough surfaces [38] [40]. Also with the increasing contact force, the surface asperities in rough

surfaces deform strongly as compared to the smoother surfaces and the real contact area in rough surfaces moves closer to the real contact area in smoother surfaces [109]. As the force increases, the surfaces move closer to each other forming more contact spots [44]. Hence, with the increasing force, the contact resistance in rough surfaces approaches closer to the contact resistance in smoother surfaces [47].

## 2.3 Contact heating

The electrical and thermal conductivities of material are temperature dependent properties. The validity of the Holm's equation for constriction resistance holds true for the current flow with lower densities passing through the a-spots. At the higher current densities, the joule heat generation in the a-spots is considerably large and causes the thermal gradient normal to a-spot surface. Also the equilibrium temperature within the contact spot reaches within a very short time [6, p. 57]. The heat dissipation within the contact interface takes place by conduction. Based on the thermal-electrical analogy, the voltage and current flowing through a conductor are analogous to the temperature and the heat flow rate respectively [110]. This causes the heat current to follow the same path as that of the electric current in materials with isotropic properties. In such a situation, the isothermal surface and equipotential surface are the same. This results in the interactive relationship between the voltage and temperature in the contact zone [6, p. 63]. The equations defining the voltage temperature relationship based on the thermal conductivity and electrical resistivity of a material are given in [111]. In case of the two dissimilar materials 1 and 2 contacting each other, the voltage drop $V$ at the contact interface with $T_1$ and $T_2$ being the bulk temperatures of the respective materials measured away from the contact interface and the maximum temperature as $T_{max}$ is given as:

$$V = \left(2\int_{T_1}^{T_{max}} \lambda_1 \rho_1 dT\right)^{0.5} + \left(2\int_{T_2}^{T_{max}} \lambda_2 \rho_2 dT\right)^{0.5} \tag{2.19}$$

with $\lambda$ and $\rho$ being the thermal conductivity and electrical resistivity for respective materials. For the contacts with same materials, the voltage temperature relationship is given as:

$$V = 2\left(2\int_{T_1}^{T_{max}} \lambda \rho dT\right)^{0.5} \tag{2.20}$$

In the cases where the electrical resistivity and thermal conductivity are nearly constant with respect to the temperature, relationship between the voltage and temperature for monometallic contacting surfaces is given as [6, p. 59]:

$$T_{max} - T_1 = \frac{V^2}{8\lambda\rho} \tag{2.21}$$

Since the maximum temperature occurs in the a-spot or adjacent to it, the term $T_{max} - T_1$ represents the temperature difference in the contact interface and the bulk temperature. This temperature difference is termed as contact super temperature and for reliable connectors it should not exceed more than 1 °C to 3 °C [9]. The voltage drops at the contact interface beyond a certain limit resulting in the larger contact super temperatures which cause the softening of

asperities through reduction of hardness and melting of the contact spots are termed as the softening voltage and melting voltage respectively. The voltage drop at the contact interface in excess of 0.1 V is generally significant for softening or melting of the contact and also the melting voltages are generally two to four times larger in magnitude than the softening voltages for most of the materials [6, p. 61]. The softening and melting of the contact spots can be interpreted from the abrupt changes in the measured contact resistance as it results in the sudden changes in the real contact area and hence contact resistance [98] [112]. Also the softening and melting voltages area greatly influenced by the size of contact spots [113]. The reduction in the contact force overtime can also lead to the increase in contact zone temperature through increased constriction resistance [114] [115]. The softening and melting voltages for copper are 0.12 V and 0.43 V respectively.

Alternatively, the contact super temperature can be determined through application of the Wiedemann-Franz law which relates the thermal conductivity, electrical resistivity and absolute temperature through following equation [102, p. 69]:

$$\lambda\rho = LT \tag{2.22}$$

where $L$ is the Lorentz constant with a value of 2.45E-08 $V^2$ $K^{-2}$

Since $L$ is a constant, for the given absolute temperature for different metals following Wiedemann-Franz law, the product of thermal conductivity and electrical resistivity are equal [102, p. 70]. The voltage and contact super temperature relationship independent of the thermal conductivity and electrical resistivity is given as [9]:

$$V^2 = 4L(T_{max}^2 - T_1^2) \tag{2.23}$$

The contact super temperatures values derived using equation (2.21) and equation (2.23) show good agreement with each other [9].

## 2.4 Contact deformation

The contact area between the two isotropic elastic bodies with smooth surfaces in frictionless contact can be calculated using Hertz contact theory. In electrical connectors, various contact geometry combinations in the form of sphere-sphere, sphere-flat, cylinder-cylinder or cylinder-flat are observed. The point contact is obtained in case of sphere-sphere and sphere-flat contact whereas in case of cylinder-cylinder contact with parallel axes the contact is in the form of line. The crossed cylindrical contact combination results in the elliptical shaped contact zone. In the cylinders with perpendicular axes, the contact zone is almost circular and such a contact can be modelled as sphere-plane contact [116] [117].

According to Hertz theory, the contact area is created through elastic deformation of the mating surfaces even with the application of very small force. The stresses in the contact zone are very high and are called Hertz contact stresses. The Hertz theory also states that the two elastic bodies in contact can be modelled as a contact between an equivalent ellipsoid and a rigid flat [118] [119, p. 6]. For the deformation of the contacting surfaces within the elastic limits, the Hertz contact theory can be used to derive the critical load values, width of contact, indentation depth and contact pressure distribution within the contacting bodies at the contact zone.

In case of sphere-flat contact combination, the radius of the circular contact zone *a* formed due to elastic deformation of two dissimilar materials is given as [102, p. 368] [120] [121]:

$$a = \left(\frac{3RF}{2E}\right)^{1/3} \tag{2.24}$$

where, *F* is the applied load, *R* is the radius of the sphere and *E* is combined elasticity modulus of the contacting bodies in sphere-flat combination given by:

$$\frac{1}{E} = \frac{1}{2}\left(\frac{1-\nu_1^2}{E_1} + \frac{1-\nu_2^2}{E_2}\right) \tag{2.25}$$

where, $\nu_1$ and $\nu_2$ are Poisson ratios and $E_1$ and $E_2$ are elasticity moduli of the respective bodies. The indentation depth $u_i$ is given as [120]:

$$u_i = \left(\frac{2F^2}{E^2R}\right)^{1/3} \tag{2.26}$$

The resulting maximum contact stress $(\sigma_c)_{max}$ is given as [120]:

$$(\sigma_c)_{max} = \frac{3}{2}\frac{F}{\pi a^2} \tag{2.27}$$

The Hertz radius *a* can be applied for approximation of contact resistance for the clean and smooth contacts. According to Ossart et al., for the lower forces with the deformation within

elastic limits, the contact area obtained by Hertz model is in good confirmation with simulated contact area and with the increasing load, the simulated contact area deviates from the area obtained by Hertz model [122]. Also the materials with higher yield strength in comparison to lower yield strength have actual contact area closer to that calculated by Hertz model at higher loads. At lower loads, the contact area is hardly influenced by the yield strength. Also, the contact area under the given force is strongly affected by coating thickness [122] [123]. Thus for the contact area determination in case of coated surfaces and high load conditions, the effect of underlying material should be taken into consideration. Fig. 2.5 and Fig. 2.6 highlight the stress distribution in sphere-flat contact geometry with and without coatings respectively. In case of contact without coating, it can be seen that the maximum stress occurs at certain depth from the contact surface. In the case of contact with multilayer coatings, the maximum stress occurs in the base material copper at the interface with nickel. This could lead to the delamination wear in contact. The surfaces with smaller roughness deformed using considerably higher loads result in the contact area closer to that calculated using Hertz model [77, p. 12]. For solving the elastic contact problems with rough surfaces the methods such as Greenwood & Williamson theory, Persson scaling theory, theory of Bush, Gibson & Thomas and Boundary element method are available [41] [50].

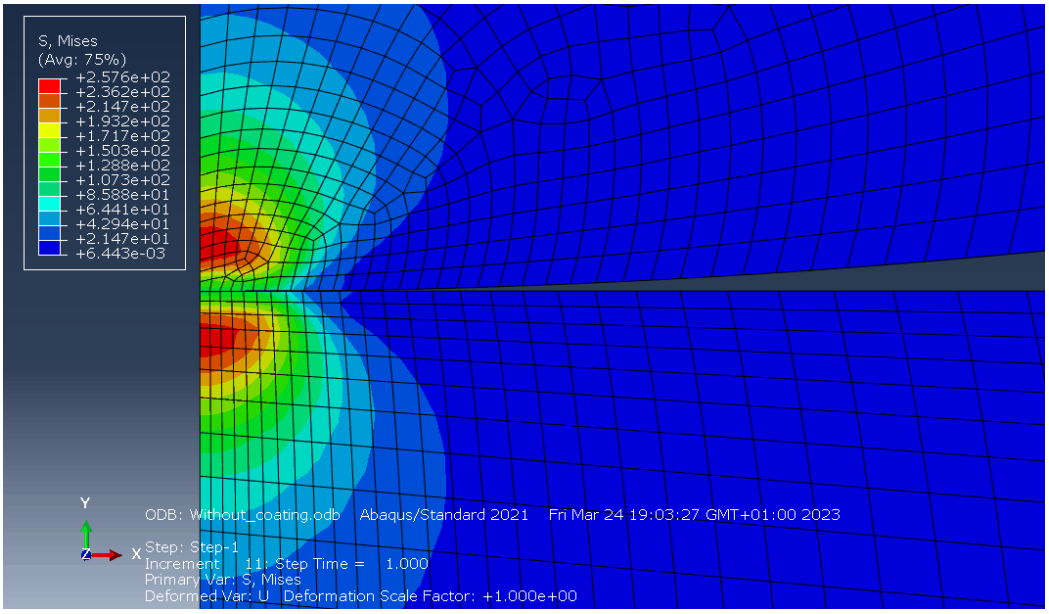


Fig. 2.5: Stress distribution in sphere-flat copper contact

In case of plastically deformed surface having large number of contact spots and sufficiently larger force, the contact area is derived using the force and hardness relationship as given in equation (2.15). The hardness H is measured from Vickers hardness. In the majority of the cases, the hardness is approximately thrice the compressive yield stress of material [17] [41]. The deformation in metallic contacts is usually a combination of elastic and plastic deformations. The different approaches for solving the elastic-plastic contact problems have been mentioned in [124]. The electrical connectors are generally coated with the protective

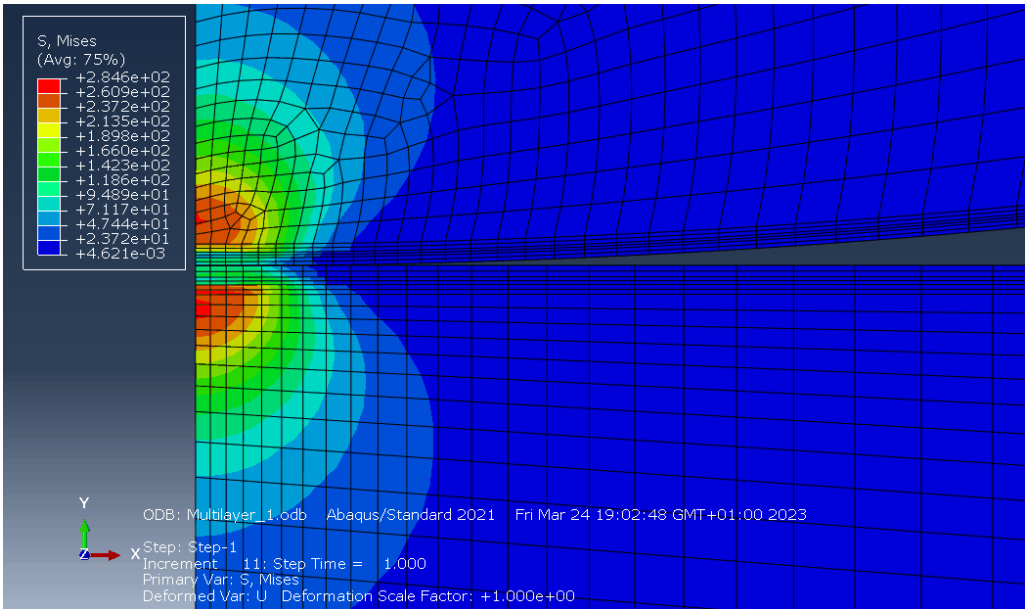


Fig. 2.6: Stress distribution in sphere-flat contact with multilayer coating (Ag-Ni-Cu)

coating which undergo plastic deformation. The analytical approaches for 3D rough contact in multi-layered surfaces has been investigated by [125] [126]. Similarly, the analytical approach to solve the contact problem in 2D rough surface is presented in [127] [128]. In the recent period, the due to better efficiency FEM tools have been widely and effectively employed for the simulation of rough surface deformation [129] [115] [118]. The real contact area in the case of elastic-plastic deformation of a surface is larger than that of the pure elastic deformation resulting in relatively smaller contact resistance [130]. Also, the contact resistance calculated with pure elastic deformation agrees well with the measured values at smaller loads whereas at higher loads the contact resistance values calculated with elastic-plastic deformation show better agreement with the measured values indicating the plastic deformation at higher loads [36, p. 57]. The hardness of the coating and the coating thickness also affect the contact area obtained under a given load. The larger contact areas are obtained for softer tin coating than with harder tin coating and also the thicker silver coating result in larger contact areas [17].

The application of the increasing contact force has the following main effects on the deformation and in turn on the contact resistance of the rough surface of a contact [6, p. 15]:

- To increase the number of load bearing asperities.
- Causing the flattening of the asperities thereby increasing the contact radius formed by the asperities and hence reducing the constriction resistance.
- Causing the strain hardening of the deforming asperities so that the flattening effect and increase in number of contacting asperities reduces even though with increase in the contact force beyond certain limit.

Fig. 2.7 illustrates the effect of plastic deformation of the surface with the help of contact resistance and force relationship. During loading cycle, the contact resistance decreases steeply during initial application of load as more contact spots are formed during initial contact

displacement and after a certain load it tends to stabilize. During the unloading cycle, the contact resistance increases at comparatively slower rate with decreasing force which is due to the plastic deformation of the asperities. Also at lower contact forces, the lower contact resistance is observed in comparison to the loading cycle indicating plastic deformation in the contact zone.

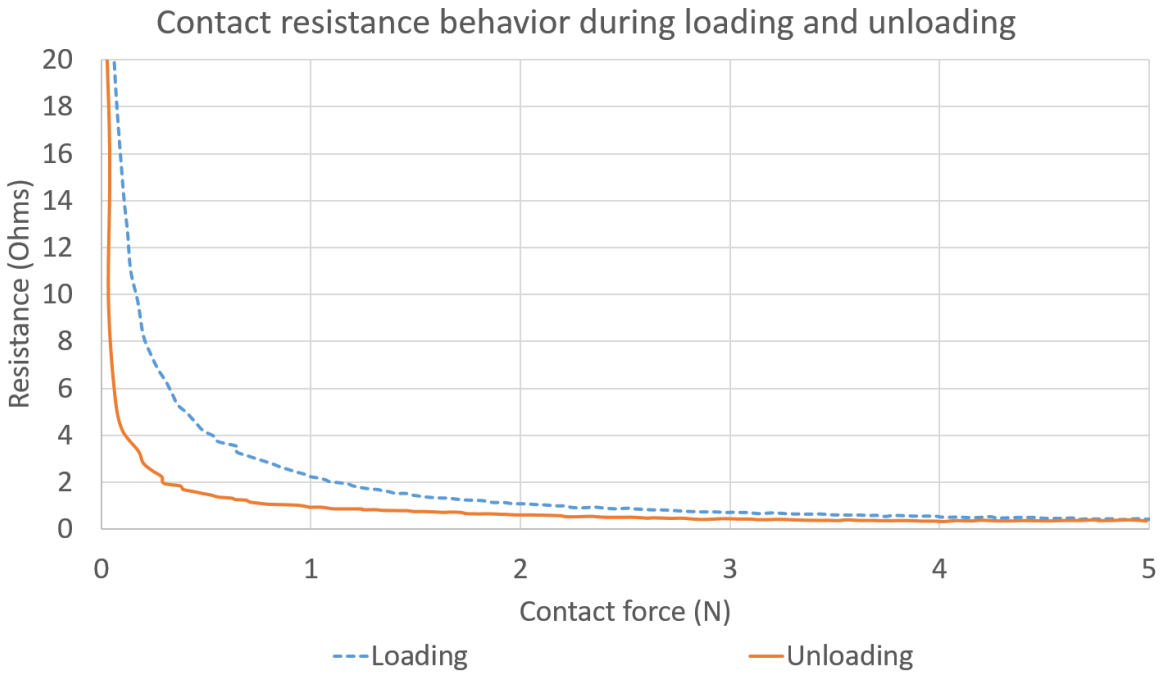


Fig. 2.7: Effect of loading and unloading force on the contact resistance

### 2.4.1 Contact force

The lower contact force results in higher contact resistance. For the optimization of the connector, it is important to achieve lower contact resistance with smaller contact dimension which in turn cause lower contact forces. One method to influence the contact resistance is through the appropriate surface roughness while the other method could be use of noble coating material such as gold and silver which have good metallic contacts even at smaller loads due to absence of oxide films. The surface roughness and asperity distribution have direct bearing on the contact deformation and contact resistance of the connector [131] [132]. The relatively smoother surfaces result in smaller fluctuations in the contact resistance at given load and also elastic deformation is more dominant in comparison to rougher surface. The slope of the contact resistance at lower contact forces becomes steeper with increasing roughness. The surfaces with higher asperities show more deformation at the given load in comparison to the relatively smaller asperities. At higher loads, when the asperities have undergone complete deformation, the deviation in the ratio of real contact area to nominal contact area with respect to asperity

deformation decreases. Also the smoother surfaces have higher contact stiffness under elastic-plastic deformation [131].

The contact force becomes more vital in the connectors coated with non-noble materials such as tin which undergo oxidization. The oxide films greatly influence the contact resistance. A sufficiently larger contact force is required to pierce through the oxide film and establish the metal to metal conducting contact. The oxide film thickness increases rapidly and linearly up to 5 nm in the initial few hours of exposure to the environment after which the growth rate reduces and saturates around 15 nm [133]. Also the amount of the force required to pierce the oxide film depends on the film thickness. The good contact is achieved at the force above 4 N in tin coatings [134]. In case of the clean gold contact surfaces, a good contact enabling the stable contact resistance is obtained with very small contact force between 0.2 N and 0.5 N [135].

The contact force in an electrical contact is generated by the normal force exerted by the deflection of the spring like flexible portion of the receptacle on the. pin or blade. The contact force $F_e$ can be calculated by the Hooke's law according to which, the force resulting from the deflection of the spring is directly proportional to the deflected distance $x$.

$$F_e = k \cdot x \tag{2.28}$$

where $k$ is the spring constant or spring stiffness. Thus, the contact force increases linearly with increasing deflection and its magnitude is influenced by the spring stiffness. The spring stiffness depends on the number of factors such as geometrical dimensions of the spring element and the material properties. The spring stiffness can be experimentally determined from the slope of the force and displacement relationship as highlighted in Fig. 2.8.

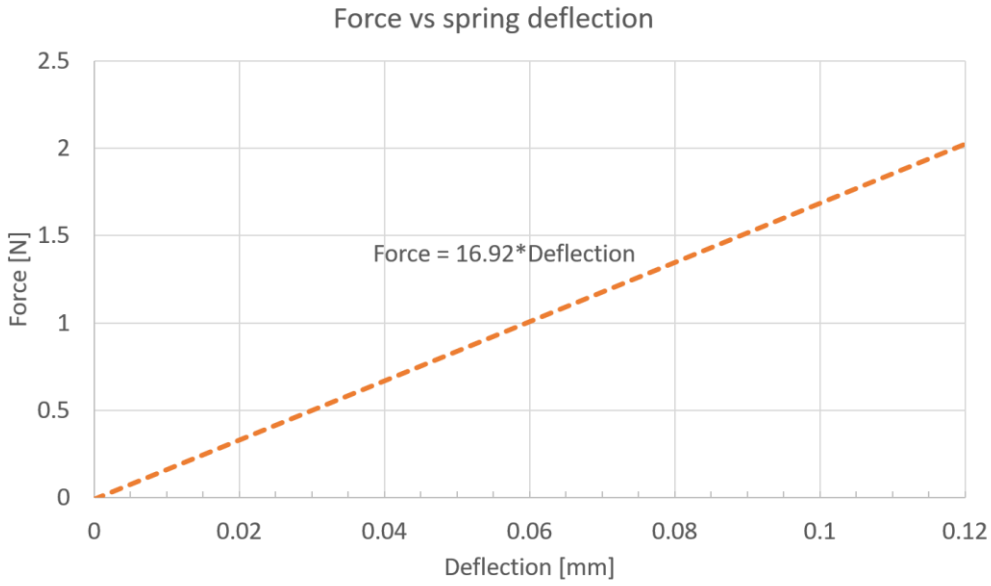


Fig. 2.8: Force and spring displacement relationship

For the given material and deflection, the bigger spring will have larger contact force as compared to the springs with smaller dimensions [136]. At higher temperatures, the spring stiffness decreases thereby decreasing the contact force. Under the influence of the thermal expansion and vibration, the mating parts of connectors can move relative to each other thereby affecting the contact resistance. The higher contact force in combination with higher friction and larger contact area can limit the relative motion of the mating parts. The insertion and extraction forces are also vital for the connector reliability. The contact resistance is found to be increasing with repeated insertions [130] [137]. Also the temperature influences the insertion and extraction forces. The decline in the insertion and extraction forces is higher at higher temperatures [137].

Over a period of time, the plastic deformation of the connector spring occurs due to stress relaxation phenomenon leading in the reduction in insertion, extraction and contact forces respectively. A lower extraction force can result in the contact pull out during the operation. The amplitude of the relative motion between the mating parts under the influence of vibration and thermal expansion can also increase due to reduced forces which in turn affect the fretting corrosion and wear behavior of the contact. On the other hand, larger insertion force could enhance wear of the contact zone. Therefore there is need to optimize the insertion force and extraction force relationship. The insertion force is mainly influenced by the friction coefficient and the geometry of pin tip and spring entrance [8]. As seen in Fig. 2.9, the insertion force occurs in two phases, first at the entrance which is geometry and friction coefficient dependent during which the insertion force rises to maximum value after reaching a certain insertion depth based on the tip of the pin or blade. The second phase occurs after the contact spot crosses the tip of blade during which the constant insertion force occurs which depends on the coefficient of friction. Also, the maximum deflection limit of the contact is reached and a stable contact force is established after crossing the tip.

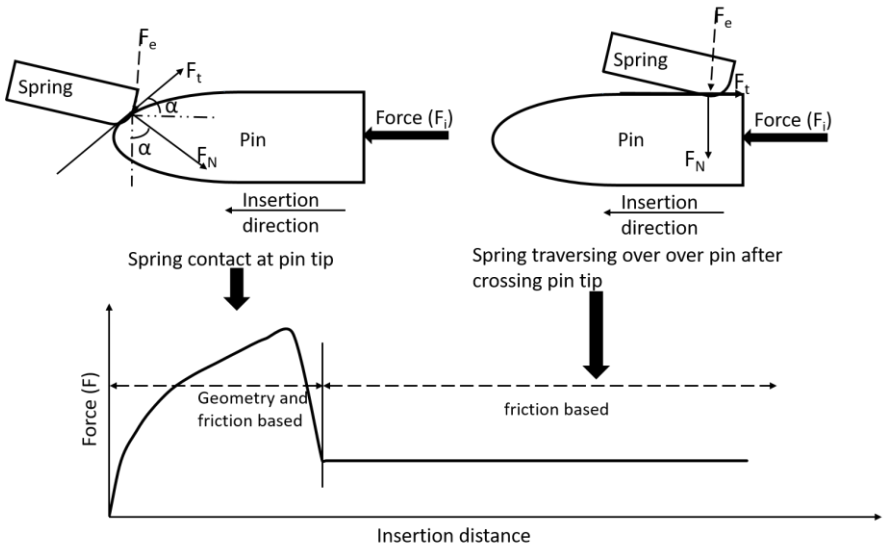


Fig. 2.9: Force and insertion distance relationship with respect to contact geometry [136] [138]

The tip of the pin is generally pointed as compared to the rear cylindrical portion to assist in the mating. As the pin contacts the receptacle, the front portion of the receptacle spring forms an entry angle $\alpha$ with the axis of the pin. At this time, the contact normal force $F_N$ is perpendicular to the contact zone and inclined to the axis of pin. As the pin slides further into the receptacle, the contact zone is established on the cylindrical portion where the contact normal force $F_N$ is perpendicular to the pin axis and insertion force is stable. The insertion force during the first phase of insertion for single contact point is given as [85, p. 68] [138]:

$$F_{i\_1} = F_e \frac{\mu \cdot \cos\alpha + \sin\alpha}{\cos\alpha - \mu \cdot \sin\alpha} \tag{2.29}$$

For the receptacle with $N$ number of spring elements, the total insertion force is given as:

$$F_{i\_total} = N \cdot F_i \tag{2.30}$$

The relationship between the insertion force $F_i$ and the contact force $F_e$ exerted by spring in the second phase of insertion governed by the coefficient of friction $\mu$ given as [139]:

$$F_{i\_2} = \mu \cdot F_e \tag{2.31}$$

For a constant $\mu$ = 0.4 and entry angle $\alpha$ = 15°, the maximum insertion force occurring in first insertion phase is approximately 87% higher than insertion force in phase two [85, p. 68]. Also for the given $\mu$ = 0.4, change in the entry angle $\alpha$ from 15° to 30° increases the insertion force by approximately 1.5 times. The entry angle $\alpha$ can be influenced by the selection of the appropriate geometry of pin tip. Hong-Yang [140] and Queffelec et al. [141] have investigated the effect of the contact geometries on the insertion force. Their investigations show that the geometry of the pin tip has high influence on the peak insertion forces. The circular or arc shaped tip of pin is most effective from geometry point of view for reduction of insertion force and the radius of the tip of the pin should be at least 2.3 times the maximum deflection of spring [140]. The best results are obtained when the radius of pin tip is greater than 10 times the maximum deflection of spring. The conical or pointed shaped pin tips need longer length of tip in order to guide the pin in such a way that the insertion force is gradually increased and the maximum insertion force is reduced. However, from the miniaturization point of view, the increase in the length of pin is not desirable. The insertion force can also be reduced through reduction of coefficient of friction $\mu$ by selecting the appropriate coating metal combination, smoother surfaces and use of lubricants.

## 2.5 Heat transfer in electrical connectors

The heat generation in an electrical connector and cable during operation is mainly caused by the joule heating which is direct result of the electrical resistivity of conducting material and conductor geometry. Apart from joule heating, a certain amount of the connector heating can be also caused due to the incident sun rays and ambient temperature. The heat transfer in an electrical connector system is through the thermal conduction along the connector cable assembly and the heat exchange between the connector surface and the surroundings through means of convection and radiation. For a highly conducting material like copper and its alloys, thermal conduction contributes the major part of the heat transfer occurring in the connector cable assembly in comparison to convection and radiation [142]. Also, the intensity of heat transfer in electrical conductors due to convection is larger than that of radiation [36, p. 80]. From the point of view of optimizing the thermal performance of the connector, the heat transfer through all possible modes should be taken into account.

The heat transfer calculations in the connector system are based on the principle of energy conservation so that there exists a balance between energy entering and leaving the system [142, p. 14] [143, p. 92]. In order to highlight the heat transfer in the connector system a control volume in the form of a rectangular prism with cross sectional area *A* and length *dx* is considered as shown in Fig. 2.10 [36, p. 72] [143, p. 92].

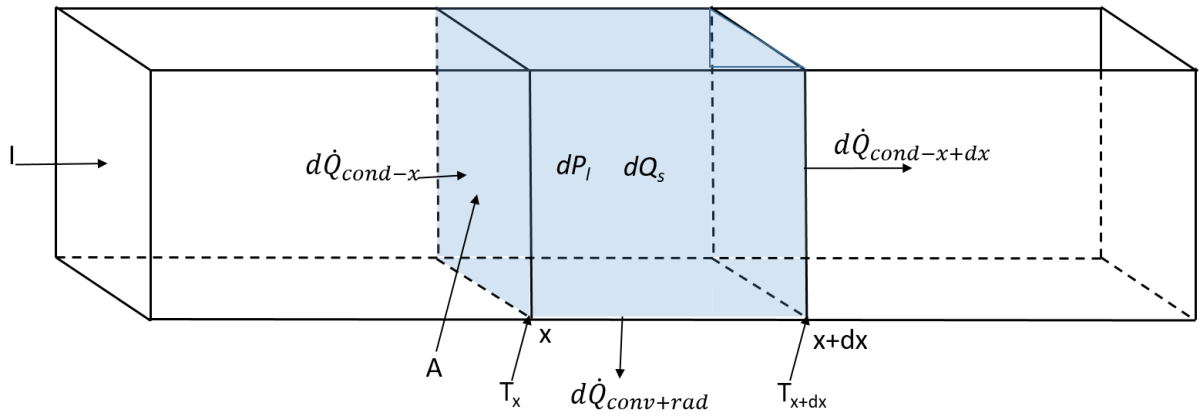


Fig. 2.10: Heat balance in a control volume in an electrical connector [36] [143]

In the control volume, the power loss $dP_l$ due to joule heating takes place and heat $d\dot{Q}_s$ is stored. By the axial heat flow through conduction, the heat rate $d\dot{Q}_{cond-x}$ enters the control volume at distance *x* and the heat rate $d\dot{Q}_{cond-x+dx}$ leaves the control volume at distance *x+dx*. From the surface boundaries of the control volume, the heat rate $d\dot{Q}_{conv+rad}$ is dissipated to the surrounding through convection and radiation. According to the principle of energy conservation in the control volume of electrical connector is given as [36, p. 72] [143, p. 92]:

$$dP_l - d\dot{Q}_s + d\dot{Q}_{cond-x} - d\dot{Q}_{cond-x+dx} - d\dot{Q}_{conv+rad} = 0 \tag{2.32}$$

where,

$$dP_l = \frac{I^2 \cdot \rho}{A} dx \tag{2.33}$$

where, $\rho$ is the specific resistivity ($\Omega \cdot m$)

$$d\dot{Q}_s = Ac_p \delta \frac{\partial T}{\partial t} dx \tag{2.34}$$

where, $c_p$ is the specific heat capacity ($J \cdot kg^{-1} \cdot K^{-1}$), $\delta$ is the material density ($kg \cdot m^{-3}$), $T$ is the temperature at position $x$ and time $t$ (K)

$$d\dot{Q}_{cond-x} = -\lambda_{cond} A \frac{\partial T}{\partial x} \tag{2.35}$$

where, $\lambda_{cond}$ is the thermal conductivity ($W \cdot m^{-1} \cdot K^{-1}$)

$$d\dot{Q}_{cond-x+dx} = -\lambda_{cond} A \frac{\partial T}{\partial x}\left(T + \frac{\partial T}{\partial x} dx\right) \tag{2.36}$$

$$d\dot{Q}_{conv+rad} = \alpha A_s (T - T_{air}) dx \tag{2.37}$$

where $A_s$ is the surface area and $\alpha$ is the effective coefficient of heat transfer due to convection and radiation.

During the thermal-electric simulation using FEM tools, for a given connector design, the thermal conductivity of the material, convection and radiation coefficients have to be defined. The thermal conductivity is the universal material property. The convection and radiation coefficients are variable and influenced by the temperature difference between the conductor and ambient temperature as well as by the geometry and surface characteristics of the conductor. Moreover, the type of convection, i.e. free or forced, significantly influences the heat transfer from the conductor. In this work, the simulations are performed considering the steady state thermal conduction and heat transfer through free convection and laminar flow of the air at connector boundary. The reason for considering the free convection is that since the contacts are generally contained inside the connector casing, the velocity of the surrounding fluid medium in the contacts proximity can be assumed to very small.

### 2.5.1 Thermal conductivity

The heat conduction through the connector takes place as a result of the temperature gradient present along the direction of heat flow. Based on the Fourier law, the heat rate due to the

conduction $\dot{Q}_{cond}$ through the conductor along the direction *x* with cross section area *A* and thermal conductivity $\lambda_{cond}$ is calculated as [144]:

$$\dot{Q}_{cond} = -\lambda_{cond} A \frac{dT}{dx} \tag{2.38}$$

where, *dT* is the temperature gradient along the conductor thickness *dx*. In an electrical connector, the temperature gradient occurring along the connector is a direct result of the joule heating which is inturn further influenced by the variations in the cross section area along the path of the current.

### 2.5.2 Convection coefficient:

The heat flow rate from the connector surface i.e. source to the surrounding medium air i.e. sink, through convection can be calculated using the heat rate equation derived using Newton's law of cooling as [143, p. 82]:

$$\dot{Q}_{conv} = \alpha_{conv} \cdot A_{conv} \cdot (T_{connector} - T_{air}) \tag{2.39}$$

where $\alpha_{conv}$ is the convection heat transfer coefficient, $A_{conv}$ is the effective surface area of the connector through which convective heat transfer occurs, $T_{connector}$ and $T_{air}$ are the connector surface and air temperatures respectively. In order to calculate heat flow rate through convection, the convection coefficient $\alpha_{conv}$ is to be determined. The convection coefficient is determined empirically through the use of dimensionless numbers which are obtained by solving the set of partial differential equations based on the balance equations considering that the variations in heat transfer for various geometries and mediums are attributed to a set of characteristic numbers [144, p. 78]. These dimensionless numbers are as follows:

- Reynolds number (*Re*)
- Prandtl number (*Pr*)
- Nusselt number (*Nu*)
- Grashof number (*Gr*)
- Rayleigh number (*Ra*)

The $\alpha_{conv}$ can be determined using Nusselt number as [144, p. 82], [143, p. 82]:

$$\alpha_{conv} = Nu \cdot \frac{\lambda_{air}}{l_{char}} \tag{2.40}$$

where $l_{char}$ is the characteristic length based on the geometry and $\lambda_{air}$ is the thermal conductivity of air. For horizontal cylinder with diameter *d*, $l_{char}$ is calculated as [144, p. 129]:

$$l_{char} = \frac{\pi \cdot d}{2} \tag{2.41}$$

The Nusselt number *Nu* is calculated differently for free and forced convection. The *Re*, *Pr* and *Nu* are applied for determining $\alpha_{conv}$ in forced convection while *Nu*, *Gr* and *Ra* are applied for determining the $\alpha_{conv}$ in free convection [143, p. 82]. The Nusselt number for free convection is given by [143, p. 82]:

$$Nu = c_1 \cdot (Gr \cdot Pr)^{n_1} \tag{2.42}$$

The values of $c_1$ and $n_1$ for different geometries and installation conditions can be found in [143, p. 84]. For the horizontally mounted cylindrical connector which is the case in this work, the values of $c_1$ and $n_1$ are 0.54 and 0.25 respectively. Alternatively, the *Nu* for horizontal cylinder can be calculated through following empirical correlation [144, p. 129]:

$$Nu = \ [0.752 + 0.387 \cdot Ra^{\frac{1}{6}} \cdot f_3(\mathrm{Pr})]^2 \tag{2.43}$$

$$f_3(Pr) = \left(1 + 0.721 \cdot Pr^{-\frac{9}{16}}\right)^{-\frac{8}{27}} \tag{2.44}$$

$$Ra = Gr \cdot Pr \tag{2.45}$$

The Prandtl number *Pr* is calculated as [143, p. 82] [144, p. 82]:

$$Pr = \frac{\nu_k}{a} = \frac{\mu_d \cdot c_p}{\lambda_{air}} \tag{2.46}$$

where, $\nu_k$ is the kinematic viscosity, $a$ is the thermal diffusivity of air, $\mu_d$ is the dynamic viscosity of air, $c_p$ is the specific heat capacity of air and $\lambda_{air}$ is the thermal conductivity of air.

The Grashof number *Gr* is calculated by [143, p. 82] [144, p. 119]:

$$Gr = \frac{g \cdot l_{char}^3 \cdot \beta_p (T_{connector} - T_{air})}{\nu_k^2} \tag{2.47}$$

where, $g$ is the acceleration due to gravity and $\beta_p$ is the thermal expansion coefficient of air calculated as:.

$$\beta_p = \frac{1}{T_m} \tag{2.48}$$

where, $T_m$ is the mean of connector surface temperature and ambient fluid temperature given as:

$$T_m = \frac{(T_{connector} + T_{air})}{2} \tag{2.49}$$

The values of physical constants of air at different temperatures used for the determination of Nusselt number *Nu* are given in [143, p. 88].

### 2.5.3 Thermal radiation

The thermal radiation causes the heat transfer between the connector surface and the surrounding environment through the means of electromagnetic waves. The thermal radiation contrary to the convection does not necessarily need the material or fluid medium for heat transfer and can occur from a hot body placed in the vacuum also. In fact, in the vacuum, the heat transfer to the surrounding takes places solely due to thermal radiation. It occurs from the solids, liquids as well as gases with its intensity increasing with the temperature [144, p. 189]. Thermal radiation is significantly influenced by surface characteristics since it directly affects the reflectivity, absorptivity and transmissivity of the incident radiation on surface of the body. Apart from these, emissivity is also an important characteristic of a surface which signifies the intensity at which the radiation occurs from the surface at a given temperature. It is to be noted that in thermal simulation, in order to account for heat transfer component due to thermal radiation, the emissivity of the surface is the quantity to be defined as an input. Also based on the properties of reflection, absorption and transmission, the bodies are classified as black, white, gray, colored and reflective [144, p. 190].

A black body can emit the radiations at highest intensity at a given temperature as well as absorb the complete incident radiation in comparison to other bodies and has the emissivity of 1. In case of black body, according to Stefan-Boltzmann law, the maximum heat flux emitted from the given surface with temperature $T_s$ is given as [145, p. 22]:

$$\dot{Q}_{rad} = \sigma_B \cdot A_{rad} \cdot T_s^4 \tag{2.50}$$

where $\sigma_B$ = 5.67·10$^{-8}$ W/m$^2$-K$^4$, is the Stefan-Boltzmann constant and $A_{rad}$ is the effective surface area from which radiation occurs. At a given temperature, the real surfaces have the heat flux emission lower than the black body and the heat flux emitted through such surfaces is given as [145, p. 22]:

$$\dot{Q}_{rad} = \varepsilon \cdot \sigma_B \cdot A_{rad} \cdot T_s^4 \tag{2.51}$$

where $\varepsilon$ is the emissivity of the surface. In case of the two surfaces with temperatures $T_1$ and $T_2$, and emissivity $\varepsilon_1$ and $\varepsilon_2$ where surface 1 is surrounded by surface 2 which is also the case for electrical contact placed inside the casing, the heat exchange rate due to radiation is given as [143, p. 81] [145, p. 32]:

$$\dot{Q}_{rad} = \varepsilon_{12} \cdot \sigma_B \cdot A_{rad} \cdot (T_1^4 - T_2^4) \tag{2.52}$$

where, $\varepsilon_{12}$ is the thermal radiation exchange coefficient and is calculated as [143, p. 81] [144, p. 196]:

$$\varepsilon_{12} = \frac{1}{\frac{1}{\varepsilon_1} + \frac{A_{rad\_1}}{A_{rad\_2}}(\frac{1}{\varepsilon_2} - 1)} \tag{2.53}$$

For the cases where, the area of the hot surface $A_{rad\_1}$ is very small in comparison to the area of the relatively cold surface area $A_{rad\_2}$, the thermal radiation exchange coefficient $\varepsilon_{12}$ is approximately equal to the emissivity of the hot surface $\varepsilon_1$. In this work, as the connector is surrounded by the air, the heat transfer rate due to radiation from the surface can be given as [142, p. 30]:

$$\dot{Q}_{rad} = \varepsilon_1 \cdot \sigma_B \cdot A_{rad} \cdot (T^4_{connector} - T^4_{air}) \tag{2.54}$$

### 2.5.4 Combined heat transfer coefficient

When the heat transfer through radiation and convection occurs through the same surface area, the combined heat transfer rate is given as [145, p. 32]:

$$\dot{Q} = \dot{Q}_{conv} + \dot{Q}_{rad} = (\alpha_{conv} + \alpha_{rad}) \cdot (T^4_{connector} - T^4_{air}) \tag{2.55}$$

Where $\alpha_{rad}$ is the heat transfer coefficient due to radiation and is given as:

$$\alpha_{rad} = \varepsilon_1 \cdot \sigma_B \cdot (T_{connector} + T_{air}) \cdot (T^2_{connector} + T^2_{air}) \tag{2.56}$$

## 2.6 Degradation and failure mechanisms

The electrical connector assembly is subjected to operational and environmental loads throughout its lifetime. It undergoes degradation during insertion, extraction and assembled state irrespective of being under operation or not. The degradation is mainly due to the stress relaxation and the relative motion occurring at the contact interface while the gases in atmosphere aggravate the degradation [11] [76]. Also, the failure modes and in turn the connector life are greatly influenced by the coating material. In house analyses of the electrical connectors in long term field vehicles show that the failure of a connector mainly occurs due to following failure mechanisms occurring in the contact zone [12] [76]:

- Fretting corrosion
- Fretting wear
- Oxidation
- Corrosion
- Contamination
- Relaxation

These failure mechanisms can occur either individually or simultaneously. Of these failure mechanisms, the fretting wear and fretting corrosion are observed to cause the majority of failures. The studies by other researchers also suggest fretting wear and fretting corrosion resulting from the fretting motion as main causes of contact failure [10] [146].

The wear occurs as a result of the relative motion between mating parts of connectors in the contact zone. There are four main causes of relative motion in electrical connectors as follows [8]:

- Insertion and extraction process
- Insufficient stiffness of the spring elements
- Thermal relaxation
- Vibrations

Amongst these, the relative displacement resulting from insertion and extraction is of large magnitudes. The remaining three factors result in the relative micro-motions of the contact zone. During insertion and extraction, the mating parts experience peak forces along with large relative displacement affecting the surface coating as well as the stiffness of the spring element resulting in bending and misalignment. The misalignments in a contact system can cause asymmetric contact forces in the connector system thereby impacting the contact resistance [147]. Also, over the large number of insertion and extraction cycles and contacts in continuously assembled state, the stress relaxation of the spring elements sets in over a period of time causing the reduction in contact forces [138]. In stress relaxation, the deformation of the spring elements remains same and the elastic stress decreases over time causing the decrease

in the contact force. The decrease in the contact force reduces the real contact area and hence conduction across the contact interface. The stress relaxation occurring at higher operating temperatures results in further decrease in the force and increase in the contact resistance [96, p. 242] [137]. Fig. 2.11 compares the contact opening dimensions in the new contact before mating, after first mating and after exposure to 3000 h of thermal cycling test. After the first mating the contact opening increases by 14 µm. After exposure to 3000 h of thermal cycling where the contact is in continuously mated condition, the contact opening dimension increases by 362 µm.

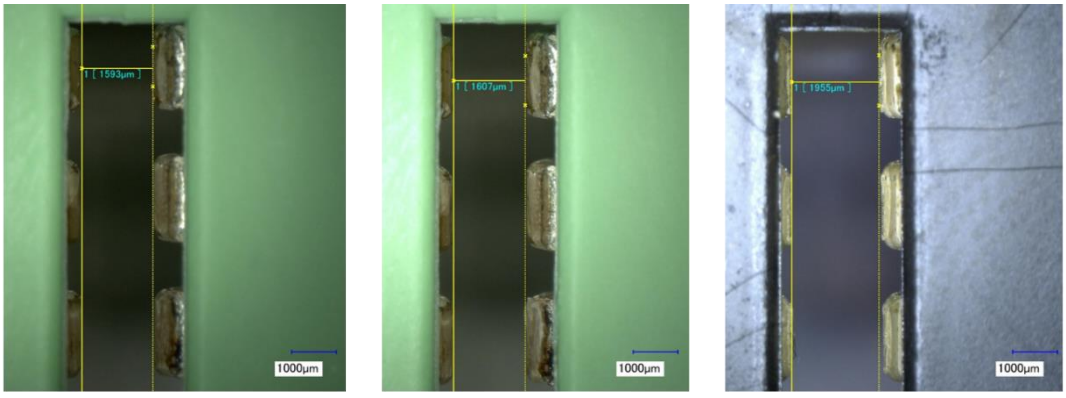


Fig. 2.11: Changes in contact opening dimensions due to mating and thermal stresses

The influence of stress relaxation on connector performance is illustrated in Fig. 2.12 where the contact resistance curve moves upwards from point 1 to point 2 due to reduction in contact force caused by stress relaxation. The further upward shift in the resistance is caused by the degradation due to different failure mechanisms such as fretting wear, corrosion, etc. occurring in the contact zone which is accelerated due to the reduction in contact force due to stress relaxation. The design of the connector receptacle should be such that the bending stresses are maintained below the yield strength in order to minimize the stress relaxation effects on reliability.

When the system is operating, the current flows through the connector thereby inducing the joule heating in the mating partners as well as at their contact interface. The joule heating at the contact interface induces the degradation of the contact zone through different mechanisms such as fretting wear, corrosion, creep, contact spot welding, migration of coating material from one partner to other, formation of intermetallic compounds etc. [85, p. 103]. In the situations where the connector is idle with no current flowing through it and in assembled state, the fluctuations in the ambient temperature cause the expansion and contraction of the mating parts causing micro motions between them. When the electrical contact is held in position by use of plastic casing, the viscous behavior of the plastic can result in the change in strain over a period of time leading to the reduction in retention force and relative displacement in the contact zone.

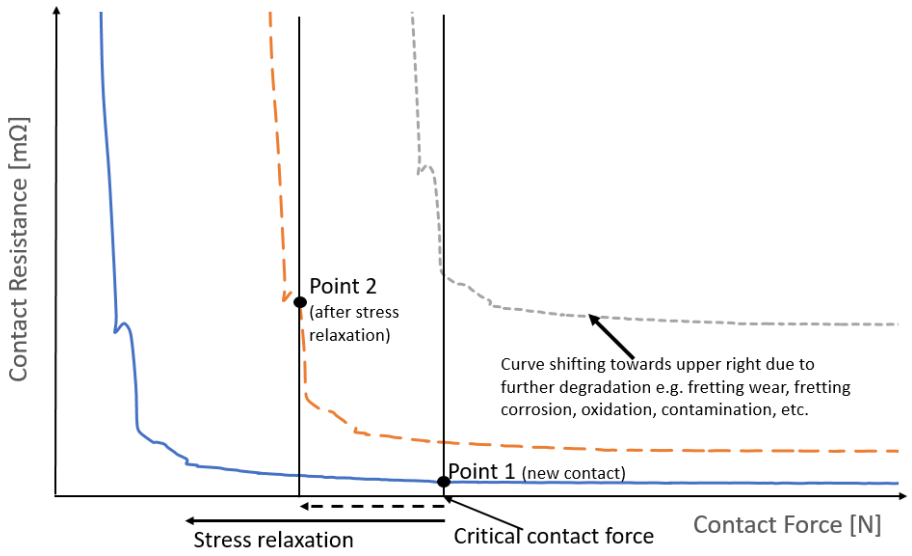


Fig. 2.12: Influence of stress relaxation on contact resistance [58]

The end effect of the various failure modes such as stress relaxation, creep, vibration and thermal cycling mainly results in the micro-motions causing the wear at the contact interface. These micro-motions expose the metal surface to the ambient conditions which damage the surface through chemical reactions.

Since the degradation of the contact zone progresses with fretting motion and chemical reactions in the contact zone, these phenomena are briefly discussed below.

### 2.6.1 Fretting

The mechanism of the contact zone degradation is greatly influenced by the nobility of the coating material used [84]. These relative motions at the contact interface lead to rupture of the existing contact spots and forming new contact spots. Also, the ruptured parts form third bodies and participate in the wear process as long as they are locked within the contact zone. In noble coatings, fretting wear occurs in the beginning while the fretting corrosion occurs after the wear off of the coating. Also the third bodies formed during initial phase of fretting wear consist of noble metal itself which do not influence the contact resistance significantly. However, with coating wear off, the underlying non-noble metal is exposed to the surrounding causing the oxidation and reduction of noble metal content in third bodies thereby leading to eventual failure [117] [148]. In non-noble coatings, the intact contact zone as well as the ruptured contact spots also oxidize and the presence of the gases and contaminants in the ambient atmosphere cause increase in the degradation rate [14]. Thus, the fretting wear and fretting corrosion in non-noble coatings take place from the initial phase and the contact failure can occur due to complete oxidation of protective coating itself. The lifetime of the contacts with non-noble coatings under fretting is shorter than that of the contacts with noble coating as illustrated in Fig. 2.13.

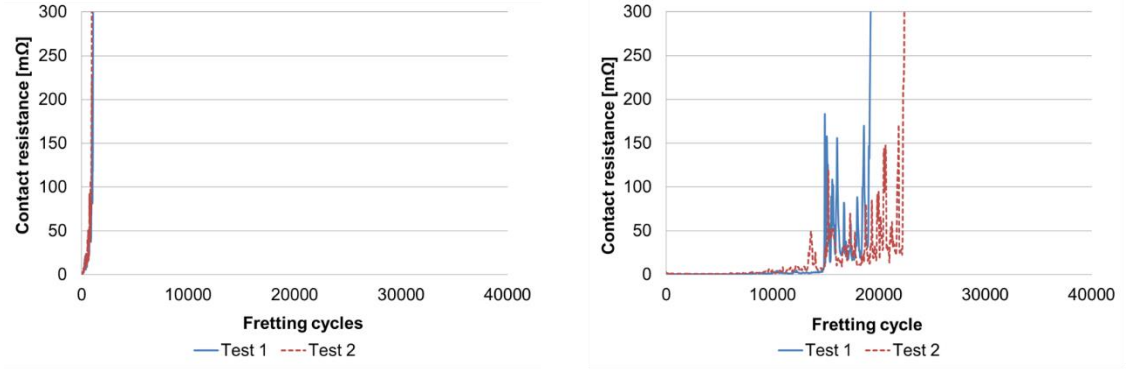


Sn-Sn contact pairs

Ag-Ag contact pairs

Fig. 2.13: Lifetime under fretting in tin and silver contacts [214]

During the micro-motions, the contact goes through partial slip or gross slip regimes depending on the relative displacement magnitude [149] [150]. The displacement magnitude in turn is affected by the external tangential forces and coefficient of friction. When the relative displacement is large, the gross slip occurs thereby exposing the larger portion of contact zone to the gaseous compounds present in the surrounding atmosphere. This results in the larger wear and corrosion and could lead to early failure of the connector depending on the coating material. On the other hand, when the magnitude of micro-motions is small, the partial slip occurs in which the middle portion of the contact zone is sticking and the slip occurs in the annular portion of the contact thereby exposing very small contact zone to surrounding. In such a situation the contact resistance remains low for longer periods due to the metal to metal contact formed at the inner potion of the contact zone resulting in extended connector lifetimes.

Fouvry et al. showed that the gross slip for tin and silver coatings occurs at the displacement above 4 µm whereas for the gold coating at displacement greater than 5 µm [117]. A considerable reduction in degradation in the connectors with silver and gold coatings was observed with smaller displacements. However, this may not be applicable to oxide forming coatings such as tin which require the oxide particles formed to be dispersed from the contact zone. At smaller displacements, the oxide debris gets trapped in the contact zone leading to the early failure. Park et al. showed that in the tin coatings under displacement close to partial slip regime, the wear through of coating did not occur and the failure was due to accumulation of tin oxide debris in the contact zone whereas the lifetime was increased while operating under gross slip regime as it allowed the removal of oxide debris from contact zone [151]. Also the failure in the tin coated contacts with smaller fretting amplitude is relatively sudden occurring within few fretting cycles after the initial observation of the surge in the contact resistance as compared to larger fretting amplitudes where more number of cycles are required to reach failure limit [152]. However, under the gross slip, the wear through of the coating was observed. The fretting amplitude also has a great influence on the stability of the contact resistance. The lower contact forces under higher fretting amplitudes result in the gross slip regimes and also

the fluctuations in the contact resistance tend to increase with the increase in the fretting amplitude in the contacts with noble as well as non-noble coatings [13] [152].

Therefore, for the given coating material, selection of the contact force which influences the friction coefficient thereby affecting the fretting amplitude and reliability, becomes critical in connector design. Other methods to reduce the effect of fretting wear on contact reliability are achieved through modifications in the coating such as use of nickel as intermediate layer, incorporation of nanoparticles or use of lubricants [10] [15].

### 2.6.2 Chemical reactions

The connector materials undergo electrochemical reactions in the presence of the oxygen and other compounds present in the ambient atmosphere. These chemical reactions lead to the corrosion of the contact surface. The base metal and the coating metal act like anode and cathode and the compounds or gases such as water molecules or other contaminants in the ambient atmosphere act like electrolyte. This causes the oxidation and reduction chemical reactions on the anode and cathode surface thereby causing the degradation of the contact material through oxidation corrosion or corrosion by other gases. The oxidation and hence the degradation rate is directly influenced by the amount of the oxygen present in the surrounding [14] [153]. The contact resistance decreases and lifetime of the tin plated connector shows great improvement when the contact zone is starved of oxygen.

In the silver coated contacts, the silver reacts with the chlorine or sulphur containing compounds to produce tarnish films. In case of the plating of noble metal such as gold, the pore corrosion or creep corrosion can occur. In the pore corrosion, the underlying non-noble metal exposed to the atmosphere through the pockets present in the thin protective coatings undergoes chemical reactions forming the localized corroded pockets in the contact zone [11] [6, p. 120]. Creep corrosion occurs in presence of reactive under layer like copper in contact with gold. In creep corrosion, the underlying non-noble metal migrates out to the surface of the protective noble coating under the influence of corrosive compounds such as sulphides and moisture forming the insulating film [11] [85, p. 122].

## 2.7 Connector testing and reliability estimation

The procedures for testing and qualification of automotive connectors for the German car manufacturers are stated in TLF 0214 standards [62]. This document describes test procedures, accelerated stress levels and failure criteria for different types of stresses which occur during operation. Also, the test procedures for different parts of an electrical connector such as mating parts, casing and crimp are mentioned in TLF 0214 standards.

The ISO 26262 standards for functional safety of automobiles define the safety requirements of the automotive components using automotive safety integrity levels (ASIL) [154]. Based on the integrity requirements, the automotive components are classified into four main categories as ASIL A, ASIL B, ASIL C and ASIL D. The components having the lowest potential hazards on failure are classified as ASIL A while those having highest potential hazard are classified into the ASIL D category. The components belonging to the ASIL D category are required to have a maximum FIT rate of 10 [155]. The failure rate values of various components are found in norms such as MIL-HDBK-217F and SN 29500-1 [156] [157]. As electrical connectors constitute one of the subcomponents of the given system, they are expected to have a FIT rate equal to 1 or smaller, so that the required reliability of the complete component which is in turn dependent on the reliabilities of subcomponents can be achieved [154]. The various standards for determining the reliability of electrical connectors are mentioned in [158] [159] [160]. The failure rate of the components is usually calculated as the product of the base failure rate and the various ‘pi’ factors corresponding to operational stress levels, environmental stress levels, quality, configuration, etc. [156] [158] [159]. The MIL-HDBK-217F defines the models for calculating the base failure rate which are based on the insert materials and connector as well as ambient temperatures. Also the ‘pi’ factors belonging to mating cycles, number of contacts and environmental factor are considered [156]. The ‘pi’ factors are based on unspecified experimental data and field data. Such methods can be used for the qualitative comparison of the reliabilities of identical components. However, there are considerable deviations observed in the failure rates estimated for the same component using different methods [158] [159]. Due to this, the results could be misleading. Also, the data for new component and material types are not available [155].

### 2.7.1 Lifetime determination

The reliability prediction requires the lifetime data of the connectors which could be time consuming and not practical to acquire under norming operating conditions. To overcome this problem, the stress levels in the connectors during testing are increased to accelerate the degradation rate of the connector and reduce the test duration required to achieve the required

contact failures [63] [161]. Such tests with increased stress levels are termed as accelerated life tests. The accelerated life tests can serve different purposes such as:

- Identify design failures and manufacturing defects
- Investigate the effect of variables such as design, materials, operating conditions etc. on the reliability
- Estimate the mean time to failure, degradation rate, failure rate, reliability, etc. in order determine warranty of the component
- Burn-in of the components to eliminate early failures which are generally caused due to manufacturing defects

There are different classifications of the accelerated life test methods defined by different sources. According to Nelson, the accelerated tests are distinguished as high usage rate testing and overstress testing [64, p. 15]. In high usage rate test method the components are operated at faster operation rates by reducing the idle time. Under overstress testing method, the stresses acting on the component are accelerated to a higher level as compared to the stress in the normal operation. Collins et al. classify the accelerated test methods as accelerated life testing (ALT) and highly accelerated life testing (HALT) with the purpose of ALT being determination of the life of the component and that of HALT being to enforce the failures for identification and correction of the faults in design [162]. The stresses in the accelerated tests could be applied in constant, cyclic, random, stepwise or progressive patterns over the test duration. The higher stress levels result in higher degradation rates and shortened lifetimes as compared to lower stress levels [63] [163]. Fig. 2.14 illustrates the relationship between the components lifetime and failure rate with stress levels in ALT. As the stress level increases, the time to reach the given failure percentage decreases.

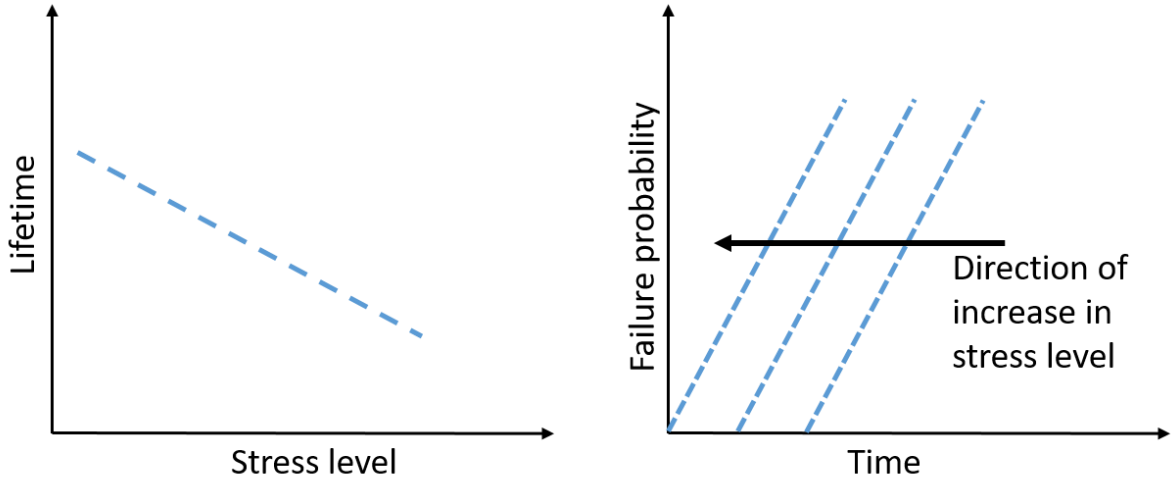


Fig. 2.14: Lifetime and failure probability relationship with stress level [64, p. 20]

In the testing of electrical connectors, the higher cycling rates, temperature, current and environmental loads such as contaminants and humidity are applied at stress levels higher than

those occurring during normal operation [58] [164] [165]. The main aim of ALT is to obtain data in shorter time so as to get required information about the connector performance and reliability when operated under normal field conditions through the application of appropriate modelling of the gathered data and acceleration factor. The ALT reduces the time and effort in estimating the reliability. As discussed in section 2.6.1, the fretting motion resulting from vibration and thermal expansion is the main cause of failures in the connectors. From the observations from in-house tests, the ALT under vibrations yields faster failures and the test duration could range from few days to number of weeks. However, the ALT under thermal stresses can extend from several weeks to number of years.

The ALT can be conducted with a view to obtain the data about life of the component or the data about the performance of the component. The performance data reflects the degradation in the intended performance of the component over the period of time. The data gathered for performance degradation can be analyzed before the component failure occurs and the degradation trajectories obtained can be extrapolated till the failure criteria defined by the performance parameters using proper model so that the time to failure can be estimated [72] [101] [161]. This helps in reducing the time required for predicting the results of the ALT. However, finding the right model for extrapolating the results remains a challenging task. Also, the degradation through multiple failure modes complicates the estimation process. Each failure mode degrading the performance could require a separate model. In an electrical connector, the degradation is caused by complicated interactions of failure modes acting, thereby causing the randomness in the performance degradation which makes the reliability modelling difficult [20].

In order to gather the failure data, the ALT are conducted in such a way that either partial or complete failure of the component population occurs [61, p. 34] [64, p. 13]. Based on the test duration, failures, modes of failures, etc. the data collected from the ALT can be classified as complete test data, time censored data, failure censored data and multiply censored data [64, p. 13]. When the time to failure of all the components in the test is known, it is classified as complete test data. The complete test data would give the exact time to failures of each component tested. In the case of connectors having low reliability, the test duration required to collect the time to failure data of all the connectors in test is relatively shorter as compared to connectors with medium or high reliability. In case of connectors with medium to high reliability the time to failure data collection of all the connectors in test is not practical since the test duration required would stretch very long. In such cases the connectors are tested till a certain number of failures occur or till a certain test duration is completed. The partial failure data implies that time to failure of only some of the tested components is available at the end of the test. The data collected from the test where a predetermined number of failures occur till the end of test time is termed as singly failure censored and the time to failures in such data is random. On the other hand, the test data collected when the test duration is predefined is known as singly time censored. In singly time censored data there is a possibility of no failures

occurring during the test when the component reliability is very high. In above mentioned data types, all the components are subjected to test at the same start time. In the tests where the components have different start times, the data collected from such tests is classified as multiply censored which is further classified as multiply time censored and multiply failure censored similar to the singly censored data type.

In the case of electrical connectors under investigation in this work, all the connectors belonging to a given type are subjected to test at the same starting time and hence the multiply failure censored data type does not apply in this study. From the ALT conducted in the laboratory, it has been observed that the failure data could be either complete data or partial data depending on the reliability. Also, some connectors having very high reliability do not fail during the ALT. The failure criteria of the component needs to be well known before commencement of the test. The failure of the component could be sudden i.e. catastrophic failure due to breakage of component or a gradual failure which results overtime from the degradation. The test results of the electrical connectors in-house indicate that the connector failure is mostly gradual as a result of the degradation of the contact zone. In case of electrical connectors, the contact resistance is the most commonly used failure criterion since it directly affects the current conducting capacity of the connector [9] [20]. The failure criteria can thus be predefined and depending on the intended application the connector can be termed as failed after a certain contact resistance limit is reached. The life of the component during the test can be measured in terms of number of cycles required for failure or in terms of time to failure.

### 2.7.2 Acceleration factor

The lifetime obtained from accelerated life tests is correlated to the lifetime of the component under normal operating conditions using the acceleration factor $A_f$ which is a measure of degree of down scaling of time to degradation gained by operating the components at higher stresses. The relationship between the lifetime during normal operation $t_{field}$ and the lifetime obtained during accelerated test $t_{test}$ using the acceleration factor $A_f$ is given as [163] [166]:

$$t_{field} = A_f \cdot t_{test} \tag{2.57}$$

The lifetime of the components at different stress levels are different [58] [165]. The acceleration factor should be chosen in such a way that the failure modes during the test replicate the failure modes in field operations. Use of higher acceleration factor could introduce different failure modes in the test which probably might not occur during actual operation [163]. There are various models used for determining the acceleration factor in tests with thermal stresses such as Arrhenius model, Coffin-Manson model and Norris-Landzberg model to name a few [163] [166] [167] [168].

2.7.2.1 Arrhenius model

The Arrhenius relationship is widely used to describe the degradation rate as a function of the temperature. The time to failure $t_{failure}$ based on the Arrhenius life relationship is given as [64, p. 76]:

$$t_{failure} = A \cdot e^{(\frac{E_a}{k_B \cdot T})} \tag{2.58}$$

where, $T$ is the temperature, $E_a$ is the activation energy equal to 0.45 eV, $k_B$ is the Boltzmann constant and $A$ is the constant depending on test conditions and failure mode. When modelling the constant failure rate, it is assumed that the component life follows the exponential distribution. Therefore, from equations (2.71) and (2.58), the failure rate can be related to the degradation rate as [168]:

$$t_{failure} = \frac{1}{\lambda} \propto e^{(\frac{E_a}{k_B \cdot T})} \tag{2.59}$$

The acceleration factor using Arrhenius life relationship is obtained by the ratio of time to failure at field temperature to time to failure at test temperature as [64, p. 77] [163]:

$$A_{f\,Arrhenius} = e^{\frac{E_a}{k_B}(\frac{1}{T_{field}} - \frac{1}{T_{test}})} \tag{2.60}$$

where $T_{field}$ and $T_{test}$ are the temperatures in field and test conditions respectively. The field temperature, test temperatures and Boltzmann constant are known quantities and only the activation energy is the quantity to be determined for application of Arrhenius model.

2.7.2.2 Coffin-Manson model

The Coffin-Manson model is used to model the tests with thermal cycling and the relation between the cycles to failure $N_{failure}$ and the difference between two temperature stress levels $\Delta T$ is given as [163] [169]:

$$N_{failure} = C \cdot \Delta T^{-m} \tag{2.61}$$

where $C$ and $m$ are constants. The acceleration factor between the stress levels in test and in the field conditions can therefore be related as [58] [169]:

$$A_{f\,C-M} = \frac{t_{field}}{t_{test}} = \frac{N_{field}}{N_{test}} = (\frac{\Delta T_{test}}{\Delta T_{field}})^p \tag{2.62}$$

where, $N_{test}$ and $N_{field}$, are the number of cycles in test and field conditions respectively while $\Delta T_{test}$ and $\Delta T_{field}$ are the difference in the upper and lower temperature stress levels in test and field conditions respectively. The exponent $p$ is the damage coefficient due to the difference in

the stress levels. The acceleration factor is linear and is used to extrapolate the lifetime under field conditions. According to Fan et al., Coffin-Mason model requires results under multiple test conditions and lacks the clarity about the effects of temperature ramp up and dwell period at a given stress level on the acceleration factor [170].

2.7.2.3 Norris-Landzberg model

The Norris-Landzberg model (*N-L*) combines the Arrhenius model and Coffin-Mason model thereby including the effects of the temperature levels and thermal cycling frequency which results in better prediction in cases where the lifetime is significantly influenced by higher temperatures and temperature changes [58] [169] [163] [171]. The Norris-Landzberg acceleration factor $A_{f\_N\text{-}L}$ is given as:

$$A_{f\_N-L} = \frac{N_{field}}{N_{test}} = \left(\frac{\Delta T_{test}}{\Delta T_{field}}\right)^{p} \left(\frac{f_{field}}{f_{test}}\right)^{q} e^{\left(\frac{E_a}{k_B}\left[\frac{1}{T_{\max\_field}} - \frac{1}{T_{max\_test}}\right]\right)} \tag{2.63}$$

where $f_{field}$ and $f_{test}$ are the thermal cycling frequencies in field and test, $T_{max\_field}$ and $T_{max\_test}$ are the maximum temperature in field and test respectively. $q$ is the damage coefficient due to the thermal cycling frequency. The values of coefficient $q$ equal to 1/3 and coefficient $p$ equal to 1.9 and 2 are mentioned in different studies [163] [169] [171]. The acceleration factor in this study are calculated using Norris-Landzberg model with values of $p$ and $q$ being equal to 2 and 0.33 respectively.

### 2.7.3 Failure rate

The failure rate of the component is the given by the number of failure occurrences over a given period of time. It is used as a measure of the component reliability and is generally expressed in terms of failures per million hours of operation [172]. The failure rate expressed in terms of number of failure occurrences per billion hours of operation is known as the failure in time (FIT) rate of the component [59] [173] and can be written as:

$$FIT = \lambda_h \cdot 10^9 hours \tag{2.64}$$

where $\lambda_h$ is the failure rate in failures per hour.

In the ALT, the failure rate in hours is calculated from the ratio of number of failures to the equivalent device hours (EDH) [174] as:

$$\lambda_h = \frac{N_{failure}}{EDH} = \frac{N_{failure}}{N_{samples} \cdot t_h \cdot A_f} \tag{2.65}$$

where, $N_{failure}$ are the number of failures occurred during test, $N_{samples}$ are the total number of samples tested, $t_h$ is the test duration per test sample in hours and $A_f$ is the acceleration factor based on stress level applied during test

The test duration could be pre-defined or else the test could be ended after a certain number of components fail while testing. In order to achieve a reliable estimation of the FIT rate of the component at a given stress level, sufficient failure data is to be collected during the test. For this purpose, the tests are allowed to run till at least 30% to 50% components fail so that their failure data can be recorded. Using the failure data, failure probabilities against failure time are modelled using suitable distribution. This allows the prognosis of the failure time of the higher failure probabilities and thereby allowing early stoppage of the test in turn saving time and effort.

During the operational lifetime, the failure rate of the component follows a bathtub shaped pattern as shown in Fig. 2.15 [59] [175]. The initial failure rates are expected to arise as a result of the extrinsic factors such as manufacturing defects. After exposure to accelerated loads, the components with manufacturing defects undergo quick initial failures after which the failure rate stabilizes. The failure rate therefore shows a steep decrease in the starting phase of the test and becomes constant during the second phase. This initial period is termed as burn-in or infant mortality phase. In case the component design is faulty, most of the components under test could fail in the initial phase of the accelerated test [176]. After the initial failures are precipitated, the failure rates enter second phase known as normal life during which the failures are random and failure rate is approximately constant. This is the useful life of the component and the failure rate during this phase is the basis of reliability estimation [177]. Towards the

end of the lifetime, the failures occur due to wear out during which the failure rate increases continuously.

The vertical axis in the bathtub curve is the instantaneous failure rate *λ(t)* which is also termed as hazard rate. It is defined as the ratio of the number of failed components in the given time period during the test to the number of the healthy or surviving components in that period of time [64, p. 57] [175]:

$$\lambda(t) = \frac{f(t)}{R(t)} = \frac{f(t)}{1 - F(t)} \tag{2.66}$$

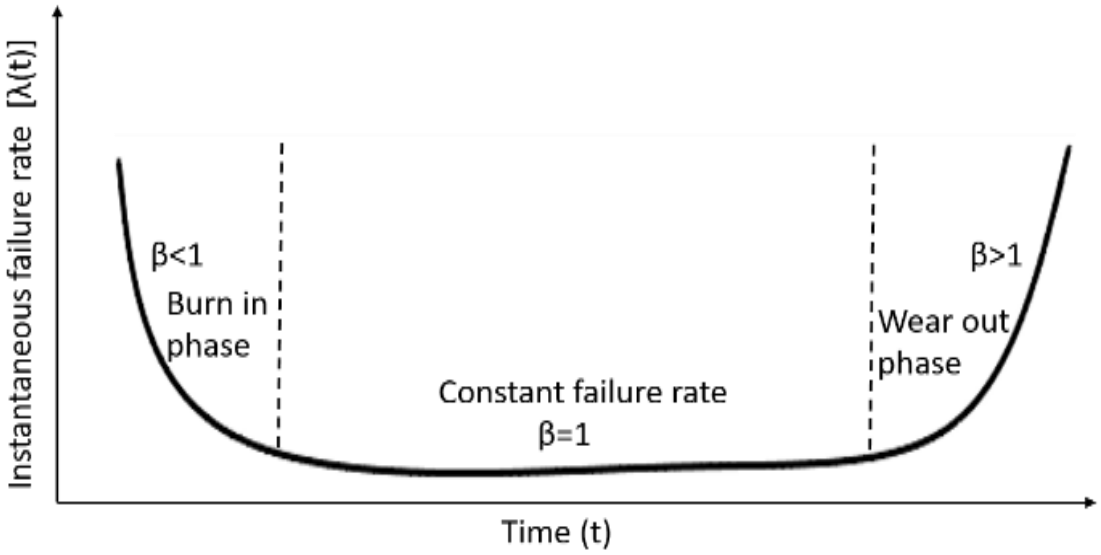


Fig. 2.15: Bathtub curve representing failure rate pattern [59] [175]

The terms *f(t)*, *F(t)* and *R(t)* can be understood from the graph of failure probability density function against time in Fig. 2.16. *F(t)* is the failed population fraction till given time *t*. *f(t)* is the probability density function and is given as first order derivative of *F(t)* with respect to time *t* [64, p. 55]:

$$f(t) = \frac{dF(t)}{dt} \tag{2.67}$$

The *F(t)* is the cumulative failure probability distribution function and is calculated by integrating the failure probability density function from beginning of the test till given time *t* as [64, p. 55]:

$$F(t) = \int_{-\infty}^{t} f(y)\, dy \tag{2.68}$$

*R(t)* is the survivorship function or healthy population fraction till given time t and is given as [64, p. 54] [175]:

$$R(t) = 1 - F(t) \tag{2.69}$$

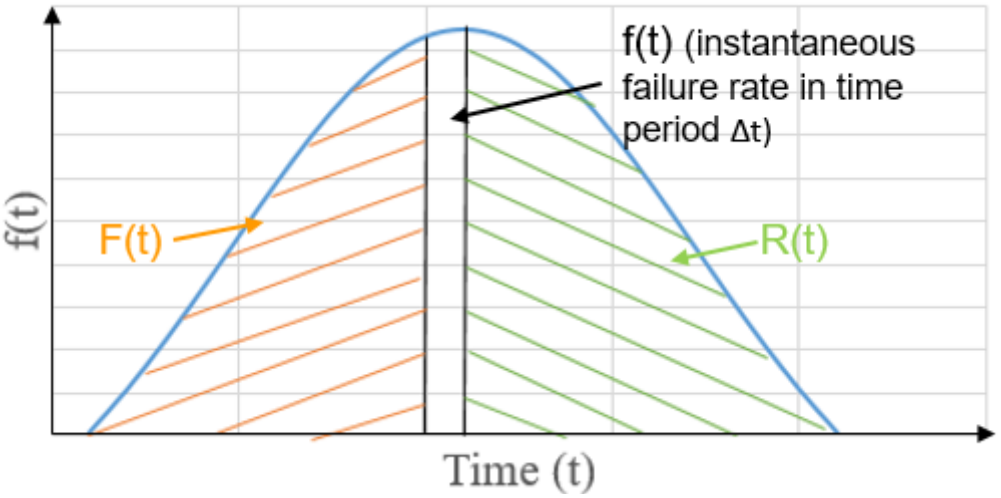


Fig. 2.16: Reliability function parameters according to probability density [175]

The parametric distributions are applied to model the failure rate data and *f(t)*, *F(t)* and *R(t)* are obtained from the respective lifetime distributions. The cumulative distribution function gives the number of the components expected to fail before the given time. In reliability analysis of the electronic components, the exponential cumulative distribution function and the Weibull cumulative distribution function are most commonly used [61] [162]. The Chi-square distribution is also applicable in the cases where failure rate follows exponential distribution [58] [178]. The exponential function is ideal for modelling constant failure rates whereas the Weibull distribution is more versatile and ideal for degradation resulting from wear as it can easily model the increasing and decreasing failure rates along with constant failure rates [64, p. 63] [179]. Also, the exponential distribution and Chi-square distribution are defined using single parameter while the Weibull distribution can be defined using either two or three parameters. In this study, the Weibull distribution defined using two parameters namely scale and shape, are used for modelling the time to failures.

#### 2.7.3.1 FIT rate with Exponential distribution

According to the exponential cumulative distribution function, the fraction of the total number of components expected to fail by the time *t* is given as [64, p. 53]:

$$F(t) = 1 - e^{-t/\theta} \tag{2.70}$$

where, $\theta$ is the mean time to failure (MTTF) or mean time between failures (MTBF) and is greater than 0. The failure rate $\lambda$ is the reciprocal of the MTTF or MTBF and is given as [64, p. 53]:

$$\lambda = 1/\theta \tag{2.71}$$

Therefore, for constant failure rates, *F(t)* can be written in terms of failure rate $\lambda$ as:

$$F(t) = 1 - e^{-\lambda \cdot t} \tag{2.72}$$

2.7.3.2 FIT rate with Weibull distribution

The cumulative distribution function based on two parameter Weibull distribution showing the fraction of the total number of components expected to fail by given time *t* is given as [64, p. 63]:

$$F(t) = 1 - e^{-(t/\alpha)^{\beta}} \tag{2.73}$$

where $\alpha$ and $\beta$ are the respective scale and shape parameters of the fitted Weibull distribution to failure data. The scale parameter $\alpha$ represents the duration and $\alpha$ corresponding to the 63.2 percentile of total population failure is called the characteristic lifetime (CLT). The shape parameter $\beta$ is a unitless quantity representing the slope of the distribution. The early life, constant failure rate and wear out phases of the bathtub curve shown in Fig. 2.15 can be correlated to the Weibull distribution using the shape parameter values. $\beta < 1$ describes the early life period, $\beta = 1$ describes the constant failure rate and $\beta > 1$ describes the wear out phase of the bathtub curve [64, p. 65] [180]. The Weibull cumulative distribution functions irrespective of the shape parameter values intersect at the time corresponding to 63.2 % of the failure probability. Therefore, the time corresponding to 63.2 % of the component failures is called as characteristic lifetime (CLT) and is applied for failure rate prediction in reliability analysis [181].

The failure rate $\lambda(t)$ based on the Weibull distribution is given as:

$$\lambda(t) = \frac{\beta}{\alpha}\left(\frac{t}{\alpha}\right)^{\beta-1} \tag{2.74}$$

with $\alpha$ equal to characteristic life time. At constant failure rate with $\beta = 1$, the Weibull failure rate becomes equivalent to the failure rate obtained from exponential distribution function in equation (2.71). Also, from the reliability point of view, it is essential to determine the failure rate when the failures occur randomly which is represented by $\beta = 1$ in the bathtub curve in Fig. 2.15. Therefore for $\beta = 1$, the failure rate in hours using the Weibull distribution, $\lambda_{h\_Weibull}$, can be written as:

$$\lambda_{h\_Weibull} = 1/t_{CL} \tag{2.75}$$

with, $t_{CL}$ being the characteristic life time of the component.

In the laboratory test, since the components are stressed at higher load levels, the acceleration factor is multiplied to the measured CLT in test $t_{CL\_ALT}$ and the FIT rate based on the Weibull distribution using equation (2.64) is calculated as:

$$FIT_{Weibull} = \frac{10^9 hours}{A_f \cdot t_{CL\_ALT}} = \frac{10^9 hours}{t_{CL\_field}} \tag{2.76}$$

Therefore, for the determination of FIT rate of a component based on Weibull, time to failure for 63.2% of components and acceleration factor $A_f$ are required. For a given load level under test and field conditions, $A_f$ is known. The methods to determine acceleration factor are discussed in section 2.7.2. Thereby, through estimation of CLT, the FIT rate and hence reliability of the component can be determined. Hence, this work focusses on the statistical methods for the prognosis of the CLT of component in order to determine the FIT rate of electrical connectors based on the Weibull distribution.

2.7.3.3 FIT rate with Chi-square distribution

By exploiting the relationship between the gamma, exponential and Chi-square distributions, the Chi-square distribution is used to determine the reliability of the tested components in the cases where the failure rate follows the exponential distribution [178]. The failure rate using probability function of Chi-square distribution with confidence level *CL* and degree of freedom equal to $(2 \cdot N_{failure} + 2)$ is given as [58] [174]:

$$\lambda_{h\_Chi-square} = \frac{\chi^2(CL, 2 \cdot N_{failure} + 2)}{2 \cdot N_{samples} \cdot t_h} \tag{2.77}$$

Thus for calculating the failure rate using the Chi-square distribution through equation (2.65), the numerator term $N_{failure}$ is replaced by $\frac{\chi^2(CL, 2 \cdot N_{failure} + 2)}{2}$ which is the probability function of Chi-square distribution [174] [178]. The value of $\chi^2(CL, 2 \cdot N_{failure} + 2)$ is obtained from the Chi-square distribution table [182, p. 550]. The CLT is predicted using a confidence interval of 90 % or 95 % [60]. It is to be noted that the failure rates have been calculated using a confidence interval of 90% in this study.

From equation (2.64) and (2.77), the FIT rate using Chi-square distribution in laboratory test conditions by including the acceleration factor $A_f$ is calculated as:

$$FIT_{Chi-square} = \frac{\chi^2\left(CL, 2 \cdot N_{failure} + 2\right) \cdot 10^9(hours)}{2 \cdot N_{samples} \cdot t_h \cdot A_f} \quad (2.78)$$

The advantage of using Chi-square distribution is that it enables the estimation of the reliability where no failure or very small number of failures occur which cannot be modelled using the Weibull distribution. In this study, for the connectors with no failures, the FIT rate calculated using the Chi-square distribution is substituted in equation $FIT_{Weibull}$ and the characteristic life time for 63.2% failure rate is determined using equation (2.76) for comparison of the CLT obtained using the proposed method.

### 2.7.4 Probability distributions

In this work, normal and generalized extreme value (GEV) distributions are used for fitting the distribution to contact resistance data measured during the ALT and for prognosis of lifetime.

#### 2.7.4.1 Normal Distribution

The normal distribution is a bell shaped symmetric distribution. The probability density function for normal distribution is given by [182, p. 34]:

$$y = f(x|\mu, \sigma) = \frac{1}{\sigma\sqrt{2\pi}} e^{\frac{-(x-\mu)^2}{2\sigma^2}} \tag{2.79}$$

where $\mu$ is the mean and $\sigma$ is the standard deviation of the population sample. Also $\mu$ is the location parameter whereas $\sigma$ is the scale parameter for normal distribution.

The normal distribution with $\mu$ = 0 and $\sigma$ = 1 is known as Standard Normal Distribution. The areas under the probability density function curve for a given probability can be obtained using the quantity known as the standard normal percentile, standard normal variate or a standard score. In this work, the standard score is represented by '*c*'. The standard score *c* rescales the μ and σ of a given population to 0 and 1 respectively and for a given measurement *X* in a population it is calculated by [182, p. 35]:

$$c = \frac{X - \mu}{\sigma} \tag{2.80}$$

Conversely, the value of the measurement *X* for a given probability *p* can be calculated when value of *c* for corresponding probability is known:

$$X_p = \mu + c_p\sigma \tag{2.81}$$

For *c* = 1, 68.3% of the observations in the measurement will lie within distance of $\mu \pm \sigma$. Similarly for *c*= 2 and 3, 95.4% and 99.7% of the observations will lie in the interval of $\mu \pm 2\sigma$ and $\mu \pm 3\sigma$ respectively [183, p. 134]. For the given probability, the *c* score values can be derived using the inverse of the probability distribution. In this study, the c score value of 2 is used for exploratory data analysis and those corresponding to 2 %, 10 %, 20 %, 40 % and 45 % failure probabilities have been used for reliability prognosis

#### 2.7.4.2 Generalized Extreme Value (GEV) Distribution

The probability density function for the generalized extreme value distribution is given as [184] [185]:

$$y = f(x|k,\mu,\sigma) = \left(\frac{1}{\sigma}\right) exp\left(-\left(1+k\frac{(x-\mu)}{\sigma}\right)^{-\frac{1}{k}}\right)(1+k\frac{(x-\mu)}{\sigma})^{-1-\frac{1}{k}} \quad (2.82)$$

where $\mu$ is the location parameter, $\sigma$ is the scale parameter and $k$ is the shape parameter. For $k = 0$, the probability density function is given as:

$$y = f(x|0,\mu,\sigma) = \left(\frac{1}{\sigma}\right) exp\left(-exp\left(-\frac{(x-\mu)}{\sigma}\right)-\frac{(x-\mu)}{\sigma}\right) \quad (2.83)$$

The generalized extreme value distribution can model the largest as well as the smallest values in the set of measurements and it combines three types of distributions which are also referred as Type 1, 2 and 3 extreme value distributions respectively. It allows to choose the most appropriate distribution based on the data [186]. The type 1 distribution has an exponential decreasing tail, type 2 distribution has polynomial decreasing tail while type 3 distribution has a finite tail [185]. The type 1 corresponds to the Gumbel distribution where shape factor is equal to zero, and type 3 corresponds to the Weibull distribution with negative value of shape factor. The type 2 distribution also known as the Frechet distribution is obtained by taking the reciprocal of values from the standard Weibull distribution. It has a positive value of the shape factor [186]. The type 1 distribution i.e. Gumbel is the mirror image of the distribution calculated by the function of extreme value distribution while type 2 i.e. Frechet distribution is equivalent to the reciprocal of the standard Weibull distribution [185].

Similar to the standard normal distribution, for a standard extreme value distribution with location parameter $\mu = 0$ and scale parameter $\sigma = 1$, the value of the measurement $X$ for a given probability p is calculated by [64, p. 66]:

$$X_p = \mu + c_p\sigma \quad (2.84)$$

Here, $c_p$ is the standard extreme value percentile or standard extreme value score and is calculated as:

$$c_p = \ln[-\ln(1-p)] \quad (2.85)$$

Similar to the standard extreme value distribution, the score $c$ for the given probability can be derived for other distribution types with known parameters through the inverse of the respective probability distribution.

# 3 Parametric optimization

Some parts of this chapter have been published in the paper “Parametric optimization of connectors by means of coupled simulation” [187] in the proceedings of ‘8. Symposium Connectors – Elektrische und optische Verbindungstechnik, Lemgo, Germany, 2021’.

## 3.1 Procedure of structural, thermal and electrical performance optimization

### 3.1.1 Connector samples and materials

For the parametric optimization of connectors, two round connectors, namely, a larger 13.6 mm connector and a smaller 2.5 mm connector are used as a reference connector in this work. The model images of both the reference connectors are illustrated in Fig. 3.1.

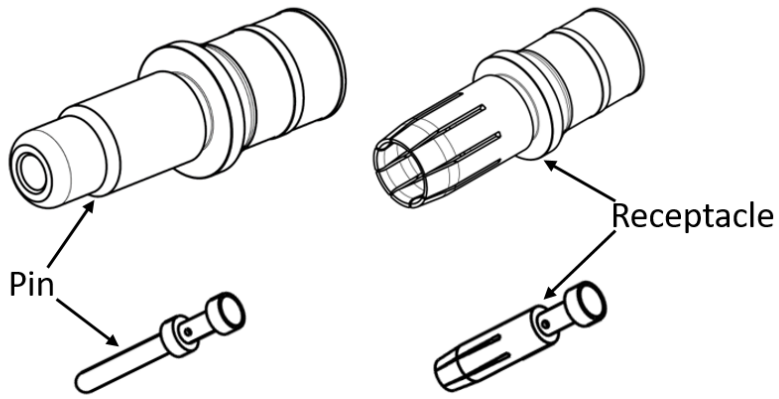


Fig. 3.1: Reference large (13.6 mm) and small (2.5 mm) round connector models

The base material of the connectors is brass (CuZn36Pb3) with silver coating. The coating thickness in 2.5 mm and 13.6 mm connectors is 5 µm and 9 µm respectively. The spring segments of the receptacle are cylindrical in shape at the rear and taper towards the tip and on contact with cylindrical pin form the cylinder on cylinder contact with axes perpendicular to each other. The material properties of brass and silver are given in Table 3.1 [188] [189]. For joule heating experiments, 1 m long copper cables with 95 mm² cross section with multiple strands and 2 mm thick PVC insulation are crimped to the receptacle and pin of the 13.6 mm

connector. Similarly, 2.5 mm² copper cable with multiple strands and 1 mm thick PVC insulation is crimped to receptacle and pin of 2.5 mm connector.

Table 3.1: Material properties of brass and silver [188, 189].

| **Material Property:** | **Brass** | **Silver** |
|---|---|---|
| Young's modulus (GPa) | 102 | 71 |
| Yield strength (MPa) | 350 | 239 |
| Poisson's ratio | 0.34 | 0.39 |
| Density (kg/m³) | 8450 | 10500 |
| Resistivity (Ωm) | 6.50E-08 | 1.74E-08 |
| Thermal conductivity (W/m/K) | 116 | 419 |
| Coefficient of thermal expansion (1/°C) | 2.02E-05 | 1.97E-05 |

### 3.1.2 Parameter selection and DoE

The round connector used in this work consists of receptacle i.e. female component and a round pin i.e. male component. The 2.5 mm connector receptacle has 6 spring segments whereas 13.6 mm connector receptacle has 8 spring segments. The pin size is kept constant for the optimization purpose. The dimensions of the front portion of the receptacle containing the spring segments are varied to optimize the connector performance since for a fixed pin dimension, an effective connector design can solely be achieved by modifying spring dimensions as it directly dictates the contact force and contact zone which are defining output parameters for connectors performance [24] [34] [136]. The crimp portion of the receptacle is unchanged. The larger connector is investigated initially and the required changes are made in the parameter selection, parameter values and design of experiments accordingly with a view to achieve the optimization objectives. The optimization of the smaller connector is performed after the optimization of the larger connector and the results of the two connectors are compared for the validation of the conclusions derived from the optimization process. The applicability of different design of experiments such as single parameter variation, two level full factorial design, Taguchi design with two parameter level and three parameter level respectively for the optimization is also tested.

The design parameters required for defining the spring segment of receptacle and their values for 13.6 mm connector are shown in Fig. 3.2 and Table 3.2. Each parameter is allocated lower and upper bounds which are defined with respect to the dimensions of the reference connector. In the first step, single parameter investigation is performed where influence of only individual design parameter is studied [190, p. 49]. To study the individual effect of the given parameter on the contact force, contact area and equivalent stress distribution in the receptacle, different receptacle models are created by varying the respective parameter between upper and lower limits with the given step size. The other parameters are kept same as that of the reference connector. For e.g., to investigate the effect of outer diameter *D1,* five receptacle models are generated with *D1* ranging from 16 mm to 20 mm with the step size of 1 mm. For these five

models, the dimensions of remaining parameters are same as that of reference model. By performing structural simulations on the models with individual parameter variation, the correlation between the individual design parameter and the performance parameters viz. contact area, contact force and maximum equivalent stress is investigated.

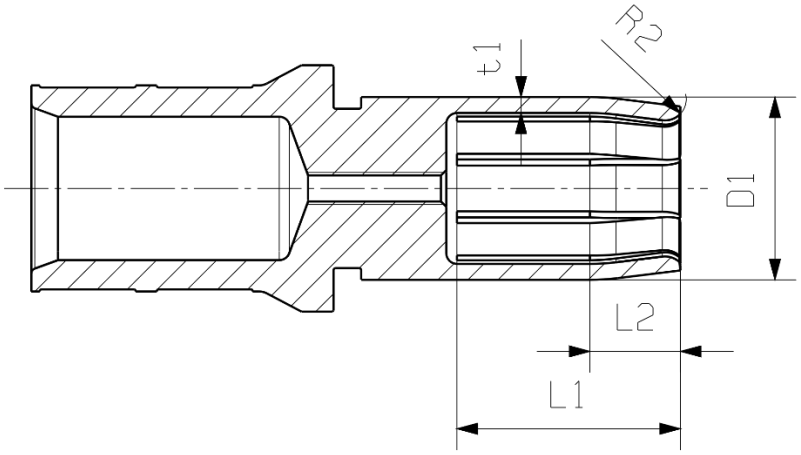


Fig. 3.2: Design parameters defining the spring segment of receptacle

Table 3.2: 13.6 mm connector: Design parameters and range of variation for parametric modelling

| **Parameter** | **Min.** | **Max.** | **Reference** | **Step size** |
|---|---|---|---|---|
| Outer diameter (*D1*) | 16 mm | 20 mm | 17.2 mm | 1 mm |
| Total length of spring element (*L1*) | 17 mm | 25 mm | 21 mm | 2 mm |
| Length of bended portion of spring element (*L2*) | 6 mm | 16 mm | 8.5 mm | 2.5 mm |
| Number of spring elements (*N*) | 6 | 10 | 8 | 2 |
| Contact radius (*R*) | 1 mm | 5 mm | 2 mm | 1 mm |
| Thickness of spring element (*t1*) | 1 mm | 2 mm | 1.5 mm | 0.25 mm |

In order to investigate the interaction effects of the design parameters, multiple receptacle designs are generated based on the two level full factorial design of experiment (DoE) where the upper and lower limits of individual parameter are selected as two levels. For n design parameters, a two level full factorial DoE results in $2^n$ different receptacle designs [190, p. 128]. Since, there are a total of 6 design parameters under consideration, it would result in $2^6 = 64$ designs which could be time and labor intensive to analyze. In order to reduce the effort, the four most influential parameters are selected based on the results of single parameter analysis from first step. This results in $2^4 = 16$ designs.

Using the structural FEM simulation results of the models from two level full factorial experiment, multiple regression analysis is performed with help of model based calibration toolbox (MBC) in MATLAB [191]. This enables the investigation of individual and interaction effects of the parameters variations on the contact force and contact area through multiple regression analysis and surface response plots. Thus the conclusions from the first step where individual parameters are varied can also be validated.

The multiple regression equation defines a surface which best fits the set of data points existing in a multidimensional space. The multiple regression model results in an equation of the form:

$$Y = a + b_1 \cdot X_1 + b_2 \cdot X_2 + b_3 \cdot X_3 + \cdots + b_k \cdot X_k \quad (3.1)$$

where $Y$ is an output variable, $a$ is the regression constant, $X_i$ are the individual input variables or parameter interactions and $b_i$ are their respective regression coefficients [182, p. 382]. The greater the absolute value of regression coefficient, higher is the influence of the corresponding individual parameter or interaction effect of parameters. The stepwise regression method is used for filtering out insignificant parameters and interactions with a view to simplify the statistical model [182, p. 413].

When the contact force is outside the acceptable limits, the upper and lower levels of the parameters at times need to be adjusted to achieve the optimum contact force. Also, other parameters apart from the top four influential ones could be required to be considered for optimizing the connectors further as their interaction with other parameters could have significant influence on output parameters. In such cases, the statistical models of the contact area and contact force obtained via stepwise regression are analyzed and the comparatively redundant parameter is replaced by new parameter. Thereby, a new set of receptacle designs is created based on the parameters combinations obtained using Taguchi DoE in Minitab software as it facilitates significant reduction in computation cost [190, p. 199]. For this purpose, an alternate two level experiment based on Taguchi L8 design of experiment is used, where the total number of models for four factors are restricted to 8 instead of 16 as in the case of two level full factorial DoE. Table 3.3 highlights the number of models required for analysis based on the number of factors and their levels which are obtained using Taguchi DoE and full factorial DoE.

Table 3.3: Comparison of number of models required according to Taguchi DoE and full factorial DoE [190, p. 199]

| **Factors** | **Levels** | **Number of models** | |
|---|---|---|---|
| | | **Taguchi** | **Full factorial** |
| 7 | 2 | 8 | 128 |
| 4 | 3 | 9 | 81 |
| 13 | 3 | 27 | 1,594,323 |

Once, the detailed analysis of 13.6 mm connector is completed, the parametric optimization of 2.5 mm connector is performed with the consideration of the four most influential parameters based on the conclusions from optimization of the larger connector, with the only difference being in the levels used for DoE. Three levels of parameters consisting of the 2.5 mm reference connector values as middle values along with lower and upper limits of the parameters are used as seen in Table 3.4. A total of 9 connector models with four factors and three levels are generated using Taguchi L9 DoE as seen in Table 3.3. The impact of the respective design

parameters in 13.6 mm and 2.5 mm are compared. It is to be noted that based on the results of the larger connector, the contact radius *R* and number of spring segments *N* are kept same as the reference connector. The number of spring elements *N* is 6 and contact radius *R* is 1 mm.

Table 3.4: 2.5 mm connector: Design parameters and range of variation for parametric modelling

| **Parameter** | **Min.** | **Reference (middle)** | **Max.** |
|---|---|---|---|
| Outer diameter (*D1*) | 4 mm | 4.5 mm | 5 mm |
| Total length of spring element (*L1*) | 9.2 mm | 10.2 mm | 11.2 mm |
| Length of bended portion of spring element (*L2*) | 3 mm | 3.6 mm | 4.2 mm |
| Thickness of spring element (*t1*) | 0.7 mm | 0.75 mm | 0.8 mm |

### 3.1.3 Model generation with parametric CAD modelling

The 3D CAD models of the reference connectors and the connector designs for parametric optimization are constructed using Siemens NX 12 software. As the connector is a round connector and receptacle consists of multiple spring segments with each segment having exactly same dimensions, the symmetry of the connector is exploited and the CAD models of single spring segment are firstly generated as shown in Fig. 3.3. The circular pattern command is then used based on the number of spring segments and the complete connector model is obtained.

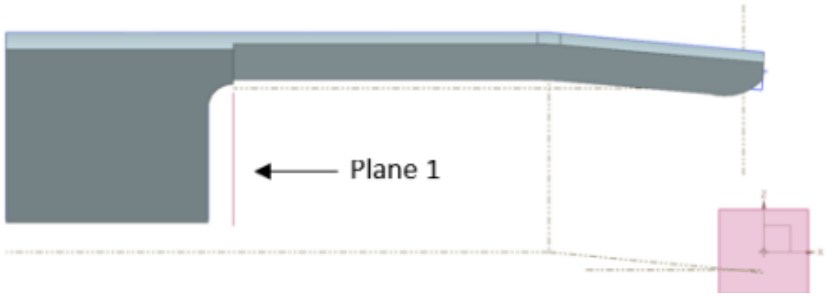


Fig. 3.3: CAD model of single spring segment modelled using parametric CAD modelling

The receptacle segment model is constructed in two steps. In the first step, the spring segment of the receptacle without the cylindrical contact point is generated by revolving the 2D sketch around the reference *Plane 1* highlighted in in figure Fig. 3.3.

The angle of the revolution defines the width of the spring segment. It is derived from the number of spring segments $N_{spring}$ and the width between two successive spring segments i.e. groove width *b* which is held constant for all the models in this study. The groove width in 13.6 mm connector is 1.2 mm and in 2.5 mm connector is 0.5 mm. The condition of revolving the 2D sketch is such that the 2D sketch is revolved equally on both sides of the reference *Plane 1* which cuts the spring segment into two equal parts along the axis of the cylinder. For

the parametric CAD modelling, two angles namely $\alpha_{base}$ and $\alpha_{spring}$ are required to be given as an input in the Siemens NX 12 software. They are calculated as follows:

$$\alpha_{base} = \frac{1}{2} \cdot \left( \frac{360\,°}{N_{spring}} \right) \tag{3.2}$$

Where $\alpha_{base}$ is the angle of revolution on each side of reference plane for generation of the spring segment base which is wider than the spring segment. The wider base of the spring segment is considered during structural FEM analysis as the higher equivalent stresses are expected to occur at the base of the spring segment. If a connector has 8 spring segments, then angle of revolution on each sides of the reference *Plane 1* to generate base of spring segment would be 22.5°. The angle of revolution for spring segment is calculated as:

$$\alpha_{spring} = \frac{1}{2} \cdot \left( \frac{360\,°}{N_{spring}} \right) - \frac{1}{2} \cdot b^{\circ} \tag{3.3}$$

where $\alpha_{spring}$ is the angle of revolution from reference plane for generation of spring segment and $b°$ is the width in radians for a given outer radius of receptacle. It is calculated as:

$$b^{\circ} = \frac{1}{2} \cdot \frac{b}{2 \cdot \pi \cdot R_{outer}} \cdot 360 \tag{3.4}$$

The reference connector with 8 spring segments and groove width of 1.2 mm in this study will have the angle of revolution of 18.5° on each side of the reference plane to generate the spring segment.

In the second step, a cylindrical section with radius equal to the given contact radius is added to the spring segment at its tip by merge operation. The cylindrical section is merged in such a way that the spring tip thickness as well as the spring deflection remains constant for all the models. Then using the trim operation, the portion between the spring tip and cylindrical body is deleted as highlighted in Fig. 3.4.

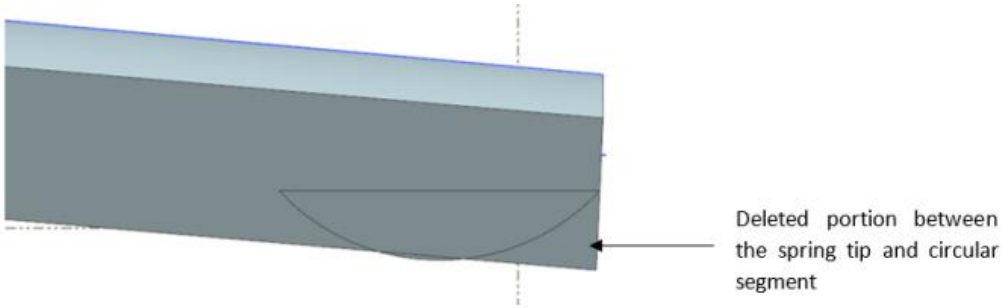


Fig. 3.4: Spring tip construction by merging cylindrical part

Once the single element of spring segment and spring base are generated, complete connector receptacle with a total of given spring segments can be generated by applying circular pattern.

In order to accelerate the generation of different connector designs in Siemens NX 12 software, the process is automated using parametric CAD modelling. This avoids the need to manually edit or create 2D sketch for given connector design. By entering the values of the individual design parameters of receptacle, the 3D model can be created as well as edited as per requirement.

### 3.1.4 Experiments

3.1.4.1 Contact force measurement

The contact force is determined using a contacting test machine developed in-house for the testing of electrical connectors as shown in Fig. 3.5. This machine can also measure the contact resistance and contact force relationship in a connector. The setup consists of a lower fixed clamp on which the receptacle is mounted and an upper movable clamp fixed to the stepper motor having displacement along vertical axis. The measurement system is controlled via LabVIEW program which allows the input of necessary parameters for the operation of stepper motor. For contact force measurement, a probe with spherical tip is clamped to the movable upper clamp and is displaced downwards to cause the given spring deflection.

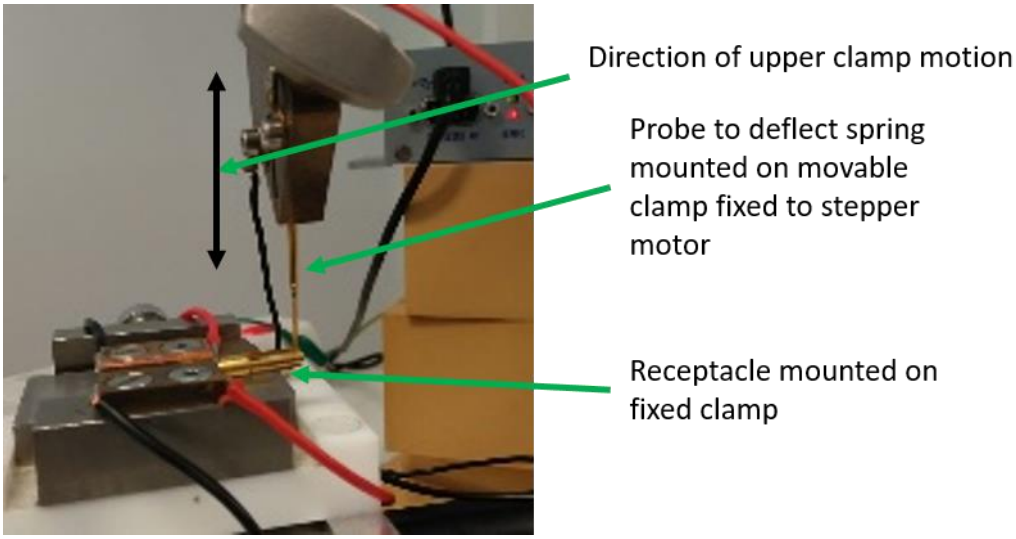


Fig. 3.5: Contact force measurement setup

The receptacle needs to be prepared before testing by cutting some of the spring segments of the receptacle in order to provide space for the contact of the probe with the inner surface of the spring segment of receptacle so that the actual displacement of the spring when contacted with pin can be replicated. After proper alignment of probe and the spring segment of the receptacle, the probe is pushed downwards to provide displacement to the spring segment. It is to be noted that the vertical traversing distance of the probe is same as the displacement in the reference connector. The 13.6 mm connector receptacle has a spring displacement of 0.40 mm when the contact pin is inserted in it while 2.5 mm connector receptacle has a displacement of

0.055 mm. The spring force i.e. contact force for the given spring deflection is obtained as an output in the LabVIEW program.

3.1.4.2 Contact area measurement

The contact area measurement in laboratory is difficult as the insertion of pin into the receptacle creates the wear scars on both receptacle and pin surfaces. However, a coarse method using optical measurement is introduced to roughly estimate the contact area. In order to determine the contact surface of the electrical contact, it must first be contacted with the contact pin. The receptacle and pin are silver coated and the wear scars created on silver surface cannot be clearly distinguished under the optical microscope. Also the silver contacting surfaces have the tendency of cold welding due to bonding between the atoms in the contact zone. During relative displacement between contact surfaces, these cold welds are broken and the material transfer between surfaces occurs [192] [193]. Therefore, when unmated, the optical measurements can result in huge deviation from actual contact area. In order to avoid this phenomenon, the tip of the spring segment where the contact zone is expected to occur, is coated with a thin layer of gold with thickness of approximately 0.1 µm using electroplating coating method. This thin layer is easily removed after one insertion cycle and the major and minor axes dimensions of wear zone are optically measured using the color contrast in Keyence optical microscope as shown in Fig. 3.6. Also, as the cylindrical tip of the spring segment contacts the cylindrical pin, the contact zone is elliptical in shape. The contact area is calculated using the following equation:

$$Contact\ Area = \pi \cdot \frac{Major\ axis}{2} \cdot \frac{Minor\ axis}{2} \tag{3.5}$$

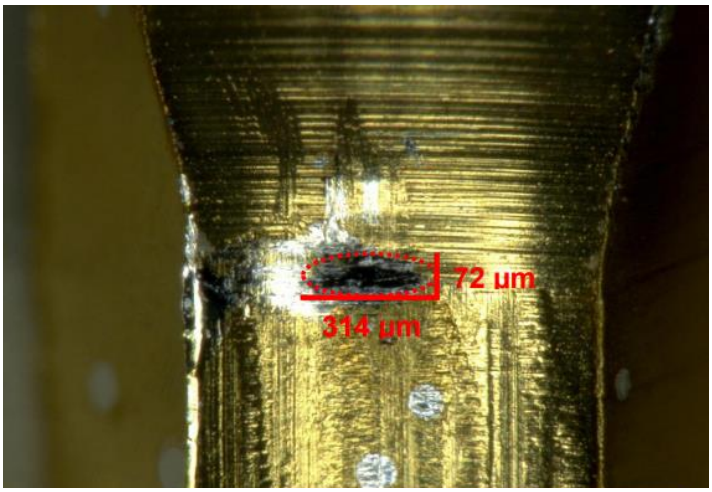


Fig. 3.6: Wear scars on gold coated contact for contact area measurement

3.1.4.3 Contact resistance measurement

The contact resistance of the connectors is measured using Kelvin or four-wire method using Keithley 2182A voltmeter. The schematic representation of four-wire electrical resistance measurement method is illustrated in Fig. 3.7. The current is passed through the connector in closed condition and the voltage drop across connector is measured using voltmeter. Thus, with the known input current i.e. 100 mA in this work and the measured voltage drop across the connector, the electrical resistance is calculated using Ohm's law as given in equation (2.2).

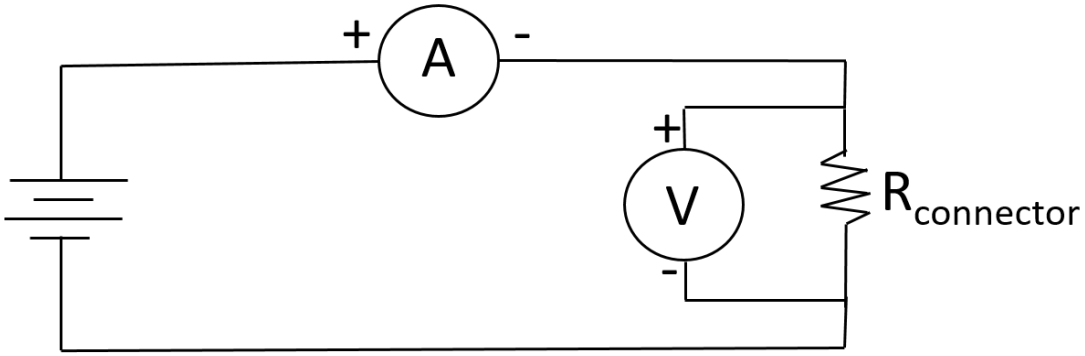


Fig. 3.7: Schematic of four wire contact resistance measurement method

3.1.4.4 Connector heating

The experiment to measure the temperature rise in connector against the given current load is carried out in two steps. K-type thermocouples are used for sensing the temperatures of cable and connector. Keithley 2700 is used for acquisition of temperature from thermocouples. The current load is provided at the cable ends using Delta Elektronika SM18-220 DC power supply. Firstly, the joule heating i.e. rise of temperature in cable with respect to current load without connector is measured. The setup for conducting cable joule heating experiment is illustrated in Fig. 3.8. The thermocouples are inserted under the insulation to measure cable temperature. The cable is mounted with the help of a support made of insulating material in such a manner that it is suspended in free air. The entire setup is placed on the top of a wooden plate base at a height of 150 mm inside transparent polycarbonate box so that the air in the proximity of cable surface remains stable and the heat transfer from the surface occurs via free convection and radiation. The wooden base has higher absorptivity and prevents the reflection back to the connector surface. The temperature from the thermocouple placed on the cable core surface at the center of cable length ($T_{cable\_core}$) is recorded since the connector receptacle and pin sides would be attached to the cables of equal lengths while conducting the joule heating measurements with cable-connector assembly. For the 95 mm² cable used for 13.6 mm connector, the joule heating i.e. the temperature rise is measured for the current loads of 25 A, 50 A, 75 A and 100 A. Whereas for the 2.5 mm² cable used for 2.5 mm connector, the current

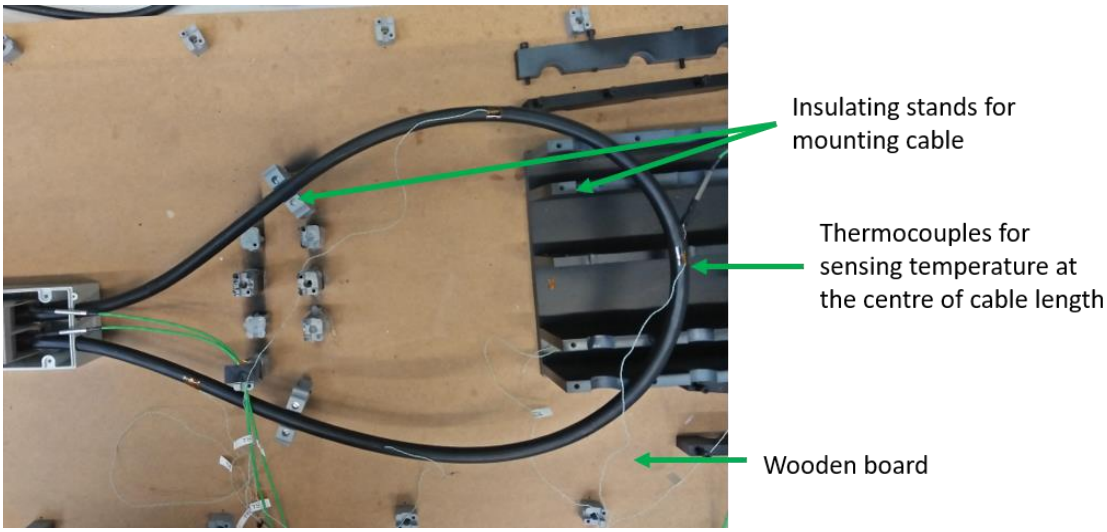


Fig. 3.8: Cable joule heating measurement setup

loads of 5 A, 10 A, 15 A, 20 A, 25 A and 30 A are applied. It is to be noted that, the same set of current loads are used for joule heating with cable-connector assembly.

In the next step, the joule heating measurements are performed on the cable-connector assembly. The setup for cable-connector joule heating experiment is similar to the setup of cable joule heating highlighted in Fig. 3.8 with the difference being the addition of connector at the center of the cable length. Here the connector is blank i.e. without casing. The connector portion stays completely exposed to the surrounding. The temperatures are measured at different locations along the connector as shown in Fig. 3.9. The temperatures are measured on the inner surface of the crimps of receptacle and pin sides, surface on the middle portion of receptacle and pin and on the outer receptacle surface closest to the contact zone between the receptacle spring and pin. This temperature is considered to be temperature of the contact zone ($T_{contact}$) and used for comparison with simulation results since direct temperature measurement at the contact interface of receptacle and pin was not possible. For both 2.5 mm and 13.6 mm connectors, 1 m long cables of 2.5 mm² and 95 mm² cross-sections respectively are crimped to receptacle and pin.

In a connector-cable assembly, there exists an exponential temperature gradient along the length of the assembly with highest temperature occurring at the contact and after a certain distance from the contact the temperature along the cable becomes almost stable [36, p. 92] [143, p. 118]. The joule heating at the cable connector contact interface where the cable is connected also increases the connector temperature. In order to account for the temperature gradient effect so that the cable temperature does not influence the connector heating, a certain minimum length of the cable to be employed in joule heating experiments exists. The minimum length is defined using a thermal location constant which is the distance at which the temperature reduces by 36.8 %. The minimum cable length is taken to be five times the thermal location factor [194]. The minimum cable length in this work is selected based on the thermal location constant and

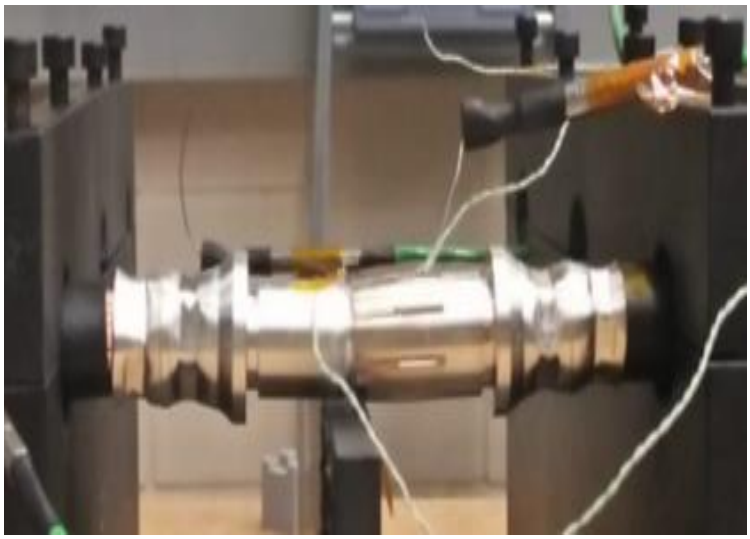

Fig. 3.9: Connector joule heating measurement setup

cable size relationship given in [194]. 1 m long cables are used for 2.5 mm² and 95 mm² cables in this work. The contribution to the temperature rise due to the cable $\Delta T_{cable}$, contact between crimp and cable $\Delta T_{crimp}$, and joule heating near contact zone of connector $\Delta T_{connector}$ is estimated by:

$$\Delta T_{cable} = T_{cable\ core} - T_{air} \tag{3.6}$$

$$\Delta T_{crimp} = (T_{crimp} - T_{cable\ core}) - T_{air} \tag{3.7}$$

$$\Delta T_{contact} = T_{contact} - T_{air} \tag{3.8}$$

where, $T_{crimp}$ is temperature at the crimp and cable interface and $T_{air}$ is the ambient temperature.

### 3.1.5 FEM modelling

3.1.5.1 Structural FEM simulation

The structural simulations are performed with Ansys 2019 R3 Static Structural analysis software. In order to exploit the axis-symmetry of the geometrical structure, 1/8$^{th}$ portion of 13.6 mm connector and 1/6$^{th}$ portion of 2.5 mm connector is simulated i.e only one spring segment in both the connectors is considered for the simulation as the contact area and contact force is identical for all the spring segments in the given connector. For structural simulations, the crimp portion of the pin and the receptacle where the cable is attached to the connector are redundant. Hence, to reduce the computational effort, only the front portion of the receptacle segment and front portion of pin which contacts the receptacle are simulated as shown in Fig. 3.10. The receptacle is fixed on the sides and bottom, shown in blue colored surface. The spring portion is unconstrained.

As the pin is stiffer as compared to the receptacle spring portion, the behavior of pin and receptacle are set as rigid and flexible respectively. By treating the pin as a rigid body, only the surface meshing is required for the contacting surface on pin. This also reduces the computational effort by reducing the number of mesh elements in the model, thereby reducing the total time needed for identification of the optimum connector design amongst the available models.

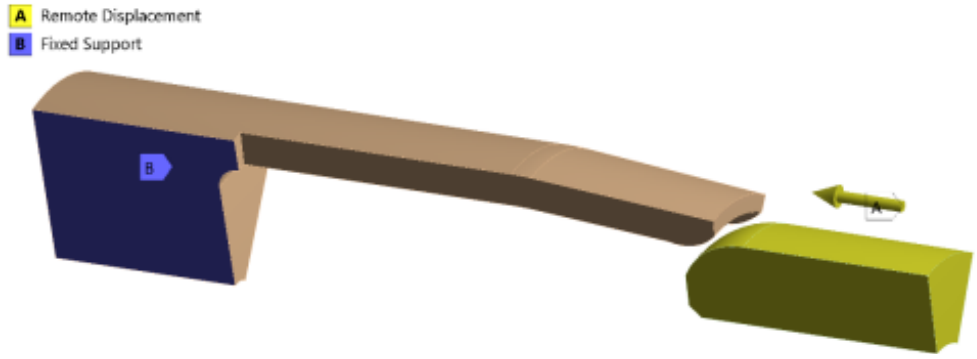


Fig. 3.10: Structural simulation model and boundary conditions

The pin is inserted in the receptacle with a remote displacement of 5 mm and 2.5 mm for 13.6 mm and 2.5 mm connectors respectively along the insertion axis. The receptacle spring segments in 13.6 mm and 2.5 mm connectors have a vertical displacement of 0.4 mm and 0.055 mm respectively due to the insertion of respective pins. The normal contact force is obtained by the vertical component i.e. Z component of force exerted by the spring on the pin. Solid187 element is used to mesh the receptacle as it has a complex structure. Solid 187 element is a 10-node, higher order 3-D element having a quadratic displacement behavior and is suitable for modelling with irregular meshes which is ideal for complicated receptacle design in this work [195]. The rigid surface is defined as a target surface and the flexible surface as contact surface. The pin and receptacle surfaces have a frictional contact between them with coefficient of friction equal to 1. This value is selected for the silver-silver contact [192]. The contacting surfaces are meshed with 8 node polygon Conta174 and 6 node triangle Targe170 elements [27] [196] [197]. Conta174 is used for receptacle i.e. deforming body and Targe170 for rigid pin surface.

The highest stress in the receptacle segments occurs at the base of the spring segment causing the stress relaxation [24] [34]. For a reliable connector the maximum stress should be lower than the yield stress. Therefore, the fine analysis of stress distribution at base of the spring segment is required. Also, in the contact zone, the contact area needs to be determined reliably. For this reason the finer mesh elements are used at the base and in the contact zone highlighted in green color in Fig. 3.11. It is to be noted that the contact area and the contact force are obtained as an output in the structural simulation. Additional experiments are performed in order to verify the contact area results obtained from simulation (Appendix 8).

Fig. 3.11: Regions requiring fine meshing in receptacle (green coloured)

The 13.6 mm connector is a considerably larger connector and with the licensed computation capacity of Ansys 2019 R3 software in the laboratory, the use of very fine mesh size was not feasible from computational point of view. Also the mesh convergence analysis was not feasible for such a large connector. Therefore, it was decided to use a relatively intermediate mesh elements sizes for the study of larger connector. The global element size of 200 µm and element size of 50 µm in the contact zone and at the base have been used for comparative analysis of all the receptacle models of 13.6 mm connector. The selection of such a medium sized mesh for the larger connector is done with a view to reduce the computation time and effort. Also, the application of same mesh element sizes in all the designs will not influence the choice of the best connector design.

On the other hand, the 2.5 mm connector is considerably smaller in comparison to 13.6 mm connector enabling the efficient execution of mesh convergence analysis with respect to contact area and contact force which form the basis of selection of optimum connector design in this study. Based on the results of the mesh convergence analysis as shown in Table 3.5, the global element size of 50 µm and element size of 10 µm in the contact zone and at the base of the spring segment corresponding to trial 6 are applied for all the receptacle designs of 2.5 mm connector. The maximum variation of 0.04 N i.e. 3.4 % in contact force is recorded between the coarse and fine mesh sizes. Thus it can be seen that the mesh size has very small influence on the contact force results. On the other hand, the contact area calculated with fine mesh varies by 36 % with respect to the coarse mesh. The contact area convergence is obtained with the mesh size of 0.01 mm in contact zone shown by trial 6.

Table 3.5: Mesh convergence analysis of 2.5 mm connector

| **Trial nr.** | **Global element size (mm)** | **Element size in contact zone (mm)** | **Contact area ($mm^2$)** | **Contact force (N)** |
|---|---|---|---|---|
| 1 | 0.10 | 0.030 | 0.0050 | 1.180 |
| 2 | 0.10 | 0.020 | 0.0040 | 1.170 |
| 3 | 0.10 | 0.010 | 0.0045 | 1.167 |
| 4 | 0.05 | 0.030 | 0.0044 | 1.159 |
| 5 | 0.05 | 0.020 | 0.0037 | 1.147 |
| 6 | 0.05 | 0.010 | 0.0032 | 1.143 |
| 7 | 0.05 | 0.005 | 0.0032 | 1.142 |

3.1.5.2 Coupled Structural-thermal-electric FEM simulation

After the structural FEM simulations of the receptacle designs obtained from design of experiments, the design having a combination of an optimum contact force and largest possible contact area is selected for the thermal-electric analysis using Ansys 2019 R3 software. The thermal-electric performance of the reference connector is compared with the thermal-electric performance of structurally optimized design. The temperature rise and electrical resistance in contact zone are chosen as the parameters to validate the connector performance.

In order to perform coupled thermal-electric simulation, the load transfer coupled physics analysis method is applied where the receptacle and pin parts of the connector are firstly contacted through insertion similar to the process discussed in the structural FEM simulation in section 3.1.5.1 and then the static structural simulation environment with deformed model is coupled to thermal-electric simulation environment in the Ansys 2019 R3 software as shown in Fig. 3.12. The material data from the static structural is linked to the material data in the thermal-electric environment. The solution module in the static structural which contains the results of the deformed model is linked to the model module in the thermal-electric environment.

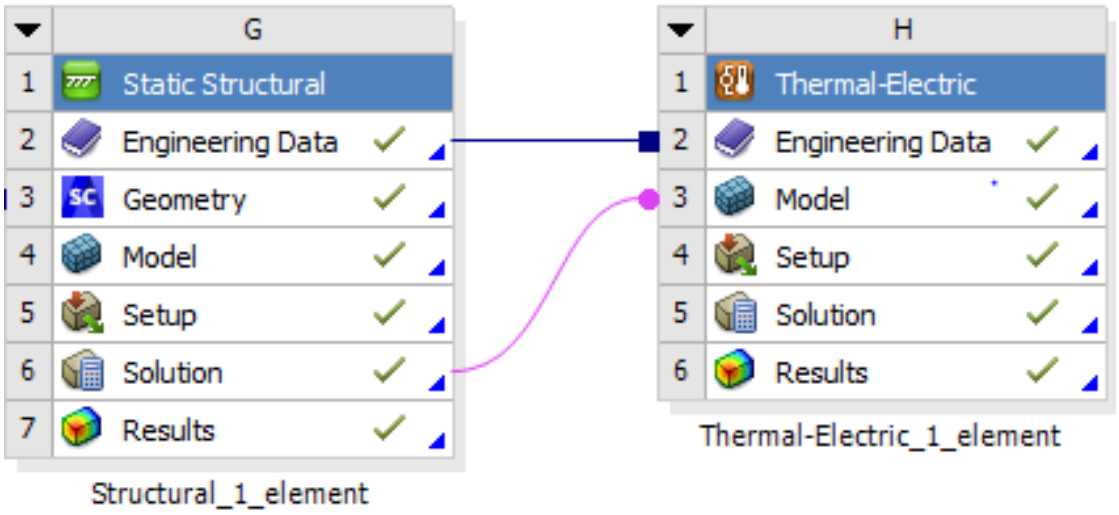


Fig. 3.12: Coupling between Static Structural and Thermal-Electric simulation environments in Ansys 2019 R3

The model considered for the static structural simulation in coupled analysis is different from that used in the structural simulation. Here the crimp portion of the pin and receptacle are considered as electrical resistance and joule heating are influenced by entire connector geometry as shown in Fig. 3.13. Also, 3D Solid227 element which is 10 node tetrahedral element suitable for coupled structural-thermal-electric simulation is used for meshing the model instead of 3D Solid187 tetrahedral elements which are suitable for structural simulation [198]. The structural simulation results obtained with Solid187 and Solid227 are similar [199]. The contacting surfaces are meshed with 8 node polygon Conta174 and 6 node triangle

Targe170 elements which are applicable to the structural as well as coupled field analysis [196] [27]. Variable element sizes are used in different regions of the connector. The element sizes in the contact zone and at the base of the spring segment are finer as compared to other regions and of same size as that in the structural simulation in section 3.1.5.1. The influence of the element size on the temperature distribution results is also very small due to which coarse mesh in the remaining portions of the connector is acceptable [200].

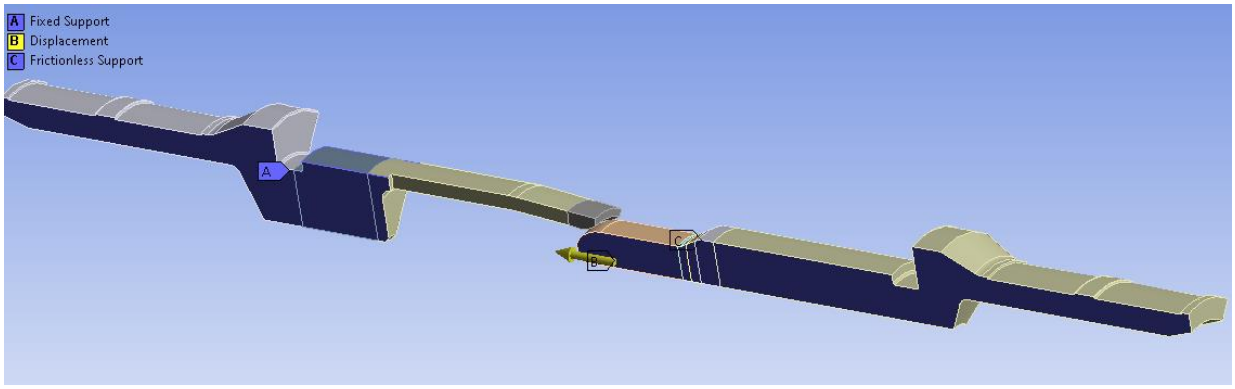


Fig. 3.13: Structural simulation model with crimp section of receptacle and pin used for coupled simulation

Similar to the structural simulation, the symmetry is exploited and the simulations are performed on single spring segment of receptacle. In the static structural step, fixed support is provided to the receptacle on the sides of the crimp and middle cylindrical portion and only spring segment is allowed to be deflected on insertion with pin as shown in Fig. 3.13. The pin is defined as a rigid body and allowed to translate along the insertion axis only using frictionless support and a remote displacement of 5 mm for 13.6 mm connector and 2.5 mm for 2.5 mm connector is given for simulating insertion process.

The boundary conditions for coupled structural-thermal-electric simulation used in 13.6 mm reference connector are shown in Fig. 3.14. In the thermal-electric environment, the convection coefficient with respect to the surface geometry, emissivity, input current, voltage and ambient temperature are required to be defined as boundary conditions. The heat convection coefficients values are calculated with respect to free convection as discussed in section 2.5, using ambient temperature of 20 °C while the surface temperature value used for 13.6 mm connector is 30 °C and for 2.5 mm connector is 70 °C. The surface temperatures for convection coefficient are selected based on the connector heating experiment. The 2.5 mm connector is small and maximum temperature during the test reached around 70 °C. However, in case of 13.6 mm connector, the maximum surface temperature during connector heating test was around 30 °C. This was due to the limited capacity of equipment in the laboratory for suppling current. The maximum current input possible was 100 A which is relatively smaller for 13.6 mm connector. In order to replicate the actual test conditions, the measured ambient and surface temperatures were used. The emissivity value of 0.02 corresponding to polished silver surface is used as an input for radiation [201]. It is to be noted that during connector heating experiment, owing to

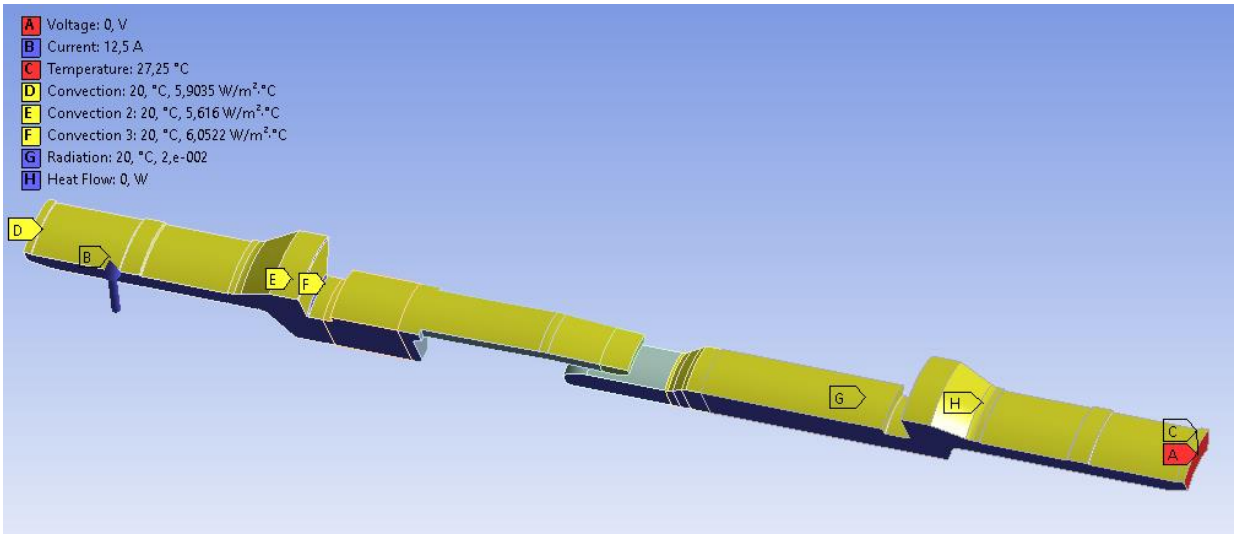


Fig. 3.14: Coupled simulation model and boundary conditions in thermal-electric simulation environment

larger surface area available, the thermocouples could be fixed on the 13.6 mm connector surface using small patches of polypropylene tape thereby leaving the majority of the silver surface exposed to surrounding due to which the emissivity value of silver is used (Fig. 3.9). On the other hand, due to the smaller surface area of 2.5 mm connector, the polypropylene tape was required to be wrapped around complete surface of the connector in order to keep thermocouples in place. Due to this, simulations are performed for 2.5 mm connector with the emissivity value of 0.97 for propylene to replicate actual test conditions [201]. The constants for free convection in cylindrical surface and values of the thermal properties of air required for calculation of convection coefficient as discussed in section 2.5 are given in [143, pp. 81-88]. The values of the convection coefficient for the reference connectors are given in Appendix 2.

The current input is defined on the inner surface of the crimp on the receptacle side shown by point B in Fig. 3.14. Due to the symmetry considered for simulation, the current input defined in boundary conditions is equal to the actual current used in experiment divided by the number of receptacles. This is based on the assumption that the current flows across the parallel circuit while flowing through the spring segments of receptacle. Based on the thermal-electrical analogy, the voltage drop is analogous to the temperature rise in the model. Voltage drop across one symmetrical portion of connector is equal to the voltage drop across complete connector considering the parallel circuit. Also, the temperature distribution in one symmetrical segment is equal to the temperature distribution in complete connector. Additional coupled structural-thermal-electric simulation with quarter model i.e. two spring segments is performed to validate the assumptions based on thermal-electrical analogy. In order to obtain the voltage drop for determining the electrical resistance of connector, a voltage of 0 V is defined on the vertical surface at the end of the crimp on pin side shown by label A.

The temperature boundary conditions are defined on the vertical surfaces at the end of receptacle and pin highlighted by label C. The major proportion of the temperature rise in an electrical connector is due to the joule heating in cable [28]. In addition to the joule heating contribution by cable, the joule heating in the crimp and cable contact surface also contributes to the temperature rise in connector. The consideration of cable in the simulation is not computationally feasible given the large number of copper strands in the cable and the complexity of interactions at crimps. Defining the contact interactions and thermal and electrical contact conductance for such a large number of contacts is not practical with the available computation capacity. Moreover, simulating the interaction at contact surfaces between cable and crimp along with the contact between receptacle and pin in a single simulation is also presently computationally not feasible. As this work focuses on optimization of the connector by improving the contact area and contact force between the mating parts, the effect of the cable is considered by separate joule heating experiment performed on the cable without connector as discussed in section 3.1.4.4. The temperature measured by the thermocouples placed under the crimp near the contact interface of crimp portion and copper strands $T_{crimp}$ is used as an input for temperature boundary condition. The symmetric surfaces of the connector are defined as perfectly insulated so that the heat dissipation occurs only from outer cylindrical surfaces of the receptacle and pin parts of connector.

The thermal contact conductance and electrical contact conductance between the mating surfaces of receptacle and pin are required to be defined as an input in simulation. For this purpose, the electrical contact conductance and pressure relationship for silver coated surface derived from internal study in laboratory is used (Appendix 3). The pressure is calculated from the contact force and contact area obtained from structural simulation.

The thermal contact conductance $(TC_{contact})$ is calculated using the relationship between electrical contact resistance ($ER_{contact}$) and thermal contact resistance ($TR_{contact}$) given as [28] [202, p. 83]:

$$TR_{contact} = \frac{ER_{contact}}{\lambda \cdot \rho} \tag{3.9}$$

Where, $\lambda$ is the thermal conductivity and $\rho$ is the resistivity. The electrical contact resistance is the inverse of electrical contact conductance given as:

$$ER_{contact} = \frac{1}{EC_{contact}} \tag{3.10}$$

The thermal contact conductance is calculated from the inverse of thermal contact conductance as:

$$TC_{contact} = \frac{1}{TR_{contact}} \tag{3.11}$$

The thermal contact conductance and electrical contact conductance values for 2.5 mm and 13.6 mm connectors are given in Appendix 3.

It is to be noted that by defining the thermal contact conductance and electrical contact conductance input calculated from the electrical contact conductance and pressure relationship for silver coating and the thermal conductivity and electrical resistivity of silver, the effect of the silver coating in the simulation is indirectly taken into account. Otherwise, given the size of the connector, including the surface coating in the simulation is found to be computationally expensive and the solution is difficult to converge.

## 3.2 Results of parametric structural optimization

Some parts of this chapter have been published in the paper “Parametric optimization of connectors by means of coupled simulation” [187] in the proceedings of ‘8. Symposium Connectors – Elektrische und optische Verbindungstechnik, Lemgo, Germany, 2021’.

### 3.2.1 Experimental results - reference connectors

#### 3.2.1.1 Contact force

The contact force is measured using the procedure discussed in (3.1.4.1). Using the force, deflection and stiffness relationship as given by equation (2.28) the stiffness of spring segments in respective connectors is obtained.

Table 3.6 shows the contact force at maximum deflection and corresponding spring stiffness measured in both the reference connectors. The difference in the smallest and largest contact force measured in 2.5 mm and 13.6 mm connectors is 0.01 N and 0.6 N respectively. The measured average contact force and average individual spring stiffness in 2.5 mm connector is 0.925 N and 16.815 N/mm. In 13.6 mm connector, the average contact force and average individual spring stiffness from experiment are 26.7 N and 66.75 N/mm respectively.

Table 3.6: Contact force and stiffness of single spring segments in 2.5 mm and 13.6 mm connectors from experiment

| Test nr. | **2.5 mm connector** | | | **13.6 mm connector** | | |
|---|---|---|---|---|---|---|
| | Deflection (mm) | Contact force (N) | Spring stiffness (N/mm) | Deflection (mm) | Contact force (N) | Spring stiffness (N/mm) |
| 1 | 0.055 | 0.93 | 16.91 | 0.4 | 27 | 67.5 |
| 2 | | 0.92 | 16.72 | | 26.4 | 66 |
| Average | | 0.925 | 16.815 | | 26.7 | 66.75 |

#### 3.2.1.2 Contact area

The contact area of the individual spring segments is measured by the procedure discussed in section 3.1.4.2. As mentioned in the procedure, the experimentally determined value of contact area cannot be assured to be precise, since it makes use of the wear scars developed by relative motion between receptacle and pin. The dimensions of the actual contact zone can vary strongly from the dimensions of the wear scars used for determining contact area. The results of the major and minor axes of the wear scars in 2.5 mm and 13.6 mm connector and contact area calculated using equation (3.5) are shown in Table 3.7. It can be seen that there is a considerable deviation in the measured length of the axes formed by the wear scars. Such a deviation can be

attributed to coarse measurement method as well as to the manufacturing process. The contact zone formed by all the spring segments with the pin can vary due to the tolerances in manufacturing process due to which the contact area formed by one spring segment can differ significantly from another.

Table 3.7: Experimentally measured contact area in 2.5 mm and 13.6 mm connectors

| Test nr. | **2.5 mm connector** | | | **13.6 mm connector** | | |
|---|---|---|---|---|---|---|
| | Major axis (mm) | Minor axis (mm) | Contact area ($mm^2$) | Major axis (mm) | Minor axis (mm) | Contact area ($mm^2$) |
| 1 | 0.213 | 0.080 | 0.0134 | 1.22 | 0.214 | 0.205 |
| 2 | 0.255 | 0.072 | 0.0144 | 1.1 | 0.2 | 0.173 |
| 3 | 0.267 | 0.077 | 0.0161 | 1.37 | 0.184 | 0.198 |
| Average | 0.245 | 0.076 | 0.0146 | 1.23 | 0.2 | 0.192 |

### 3.2.2 Structural optimization of 13.6 mm connector

#### 3.2.2.1 Structural simulation results of 13.6 mm reference connector

The structural simulation of single spring element of 13.6 mm reference connector model results in a contact area of 0.084 mm² and contact force of 23.275 N. Therefore, for entire connector with 8 spring segments, the total contact area is 0.672 mm² and total contact force is 186.2 N.

Fig. 3.15 shows the simulated equivalent stress distribution across receptacle. The maximum stress equal to 352.42 MPa, which is slightly greater than the yield limit of 350 MPa, is observed at the root of receptacle which was also the case observed in the investigations by [24] [34]. The maximum stress in the connector occurs at the root of receptacle and in the contact zone. The plastic deformation at the root of the receptacle can result in the stress relaxation in connector. Since, the maximum stress is localized to a very small region, the connector can function safely. The overall contact pressure calculated from contact force and contact area is 277 MPa.

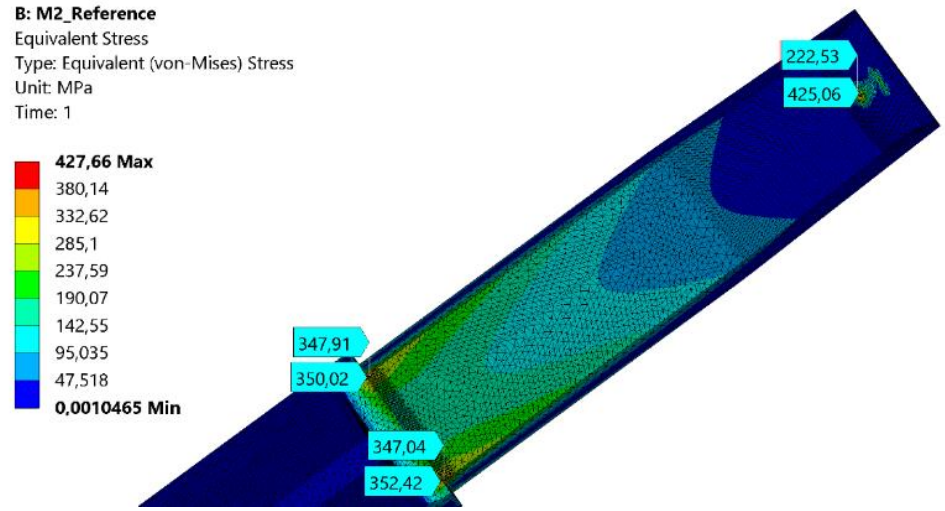


Fig. 3.15: Equivalent stress distribution in 13.6 mm reference connector

### 3.2.2.2 Influence of individual design parameters

The results discussed in this section correspond to the structural simulations performed with the models derived through variation of individual parameters within the pre-defined range and step size by keeping the remaining parameters the same as that in the reference connector as highlighted in Table 3.2 of section 3.1.2. Also the illustrated results correspond to the contact area and contact force obtained with simulation of single spring element.

#### 3.2.2.2.1 Influence of outer diameter *D1*

The results of the variation of the outer diameter *D1* on the contact force and contact area are illustrated in Fig. 3.16. It can be seen that the smaller outer diameter of receptacle spring results in the larger contact area. For the values of *D1* greater than the value of *D1* in reference connector which is equal to 17.2 mm, the influence on contact area significantly reduces. The smaller *D1* values tend to result in relatively straighter spring segment thereby resulting in lower contact force. The higher *D1* values result in the highly curved spring element causing the contact force to increase.

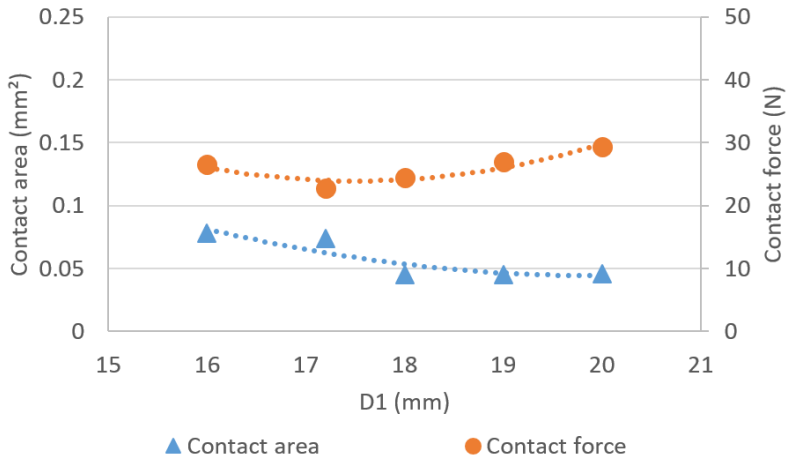


Fig. 3.16: Influence of outer diameter *D1* on contact area and contact force

#### 3.2.2.2.2 Influence of spring thickness *t1*

As seen from Fig. 3.17, the spring thickness *t1* has positive correlation with contact area and contact force. For a constant outer diameter, the increasing *t1* values tend to result in straighter spring segments thereby increasing the contact area. After a certain value, the influence of *t1* on increase of contact area decreases. This can be due to interaction with other design parameters. The spring thickness *t1* has a very significant effect on the contact force. The contact force increases almost linearly as the spring becomes thicker.

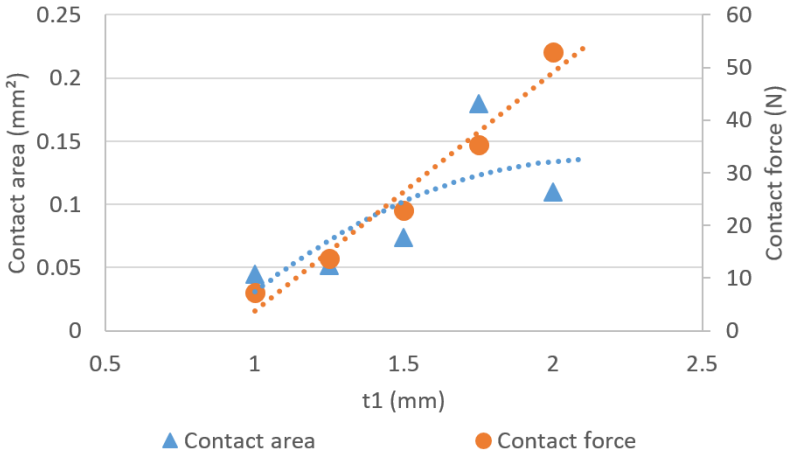


Fig. 3.17: Influence of spring thickness *t1* on contact area and contact force

3.2.2.2.3 Influence of total spring length *L1*

Fig. 3.18 shows the individual effect of the total length of spring segment *L1* on contact force and contact area. It has relatively smaller effect on the contact area. However, the influence on contact force is significant. With the increasing *L1*, the contact force shows a strong decrease. The decrease is due to the reducing stiffness caused by the increasing length *L1* of the spring segment while the cross sectional dimensions remain constant.

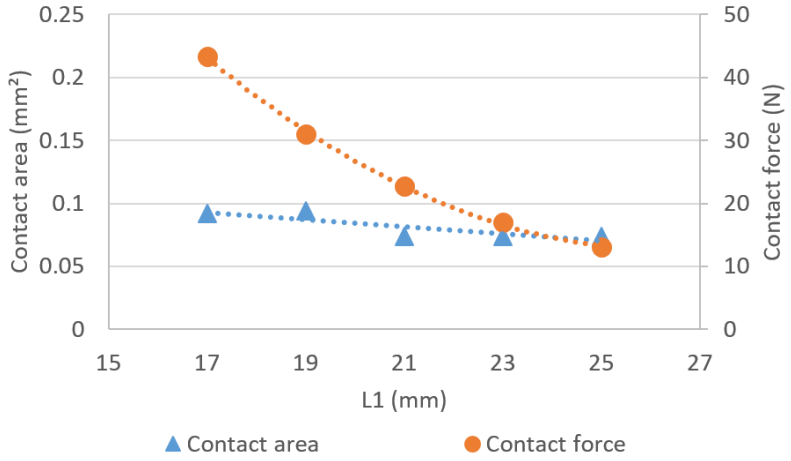


Fig. 3.18: Influence of total spring length *L1* on contact area and contact force

3.2.2.2.4 Influence of length of bended portion of spring L2

As seen from Fig. 3.19, the individual influence of length of the bended portion of the spring element *L2* on the contact area as well as contact force is insignificant. However, it can be visualized that *L2* in combination with *L1* could influence the curvature of the spring thereby influencing the contact force and contact area.

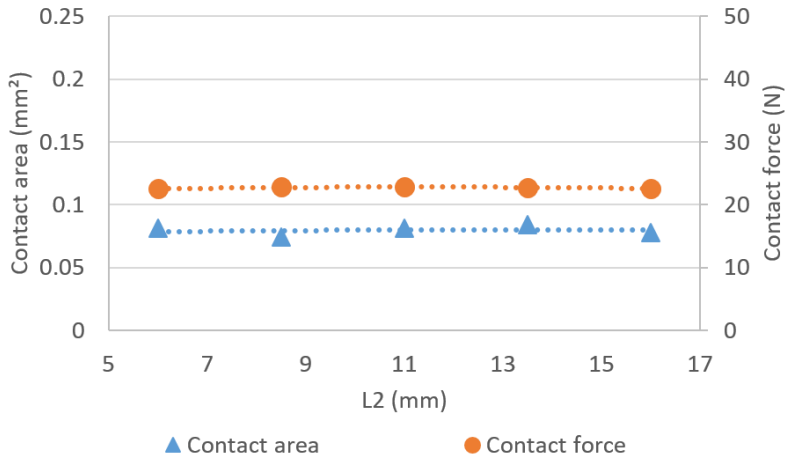


Fig. 3.19: Influence of length of bended portion of spring *L2* on contact area and contact force

3.2.2.2.5 Influence of contact radius *R*

Fig. 3.20 highlights the influence of contact radius *R* on the contact area and contact force. The contact radius *R* is directly proportional to the contact force and contact area. However, the increase in the contact area is significantly greater in comparison to the contact force, which is ideal for an electrical connector.

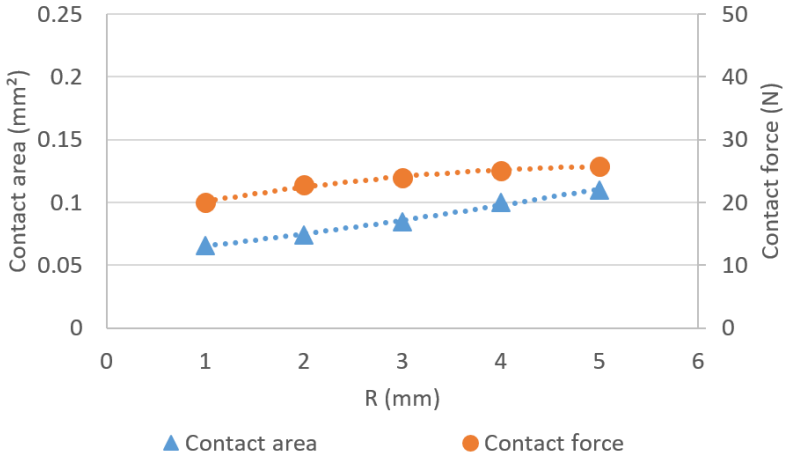


Fig. 3.20: Influence of contact radius *R* on contact area and contact force

3.2.2.2.6 Influence of number of spring elements *N*

Fig. 3.21 shows the influence of number of spring elements in the receptacle on the contact area and contact force. For given constant values of other parameters, the influence of N on contact area is very small whereas the influence on contact force is very significant. The highest contact area for individual spring is obtained in reference connector when *N*=8. Thereafter, the contact area decreases slightly. Similarly, the contact force reduces significantly up to a certain number

of spring elements after which the reduction is relatively slower. However considering the total contact area i.e. sum of contact areas for all the spring elements in receptacle, the higher number of spring elements *N* are ideal for an electric connector.

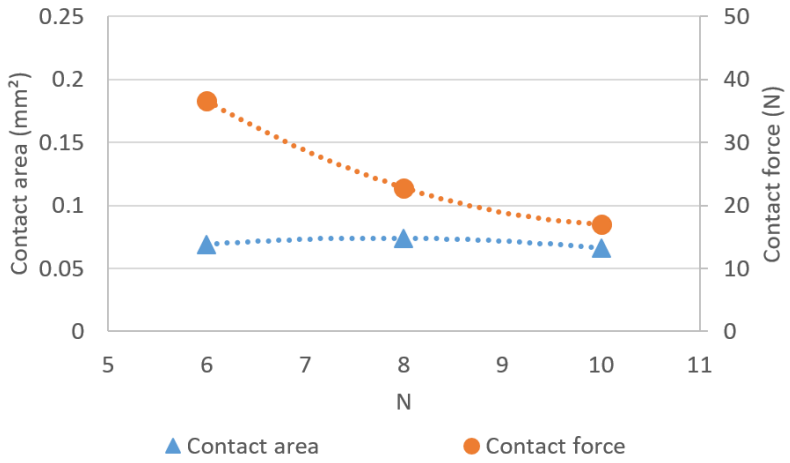


Fig. 3.21: Influence of number of spring elements *N* on contact area and contact force

### 3.2.2.2.7 Correlation coefficient for individual parameters

Table 3.8 highlights the correlation coefficient values of individual geometric parameters with the output parameters contact area and contact force. It can be seen that *R, D1, L1* and *t1* have significant influence on the contact area. The contact force is mainly influenced by *t1, N, L1* and *R*. The selection of the four most influential parameters has to be done for the detailed analysis using two level full factorial DoE. The parameters *t1, L1* and *R* have significant influence on contact area as well as contact force. However, as positive individual effect of higher *N* on contact force and contact area is clearer in comparison to the *D1*, *D1* is chosen as fourth most influential parameter for analysis of interaction effect and obtaining an optimal connector design in subsequent steps.

Table 3.8: Correlation coefficient of individual design parameters with contact force and contact area

| | **D1** | **t1** | **L1** | **L2** | **R** | **N** |
|---|---|---|---|---|---|---|
| **Contact force** | 0.59 | 0.98 | -0.98 | 0.12 | 0.96 | -0.97 |
| **Contact area** | -0.86 | 0.74 | -0.85 | 0.17 | 1.00 | -0.37 |

3.2.2.3 Results based on two level full factorial DoE

Based on the observations from the investigation of individual parameter influence as discussed in section 3.2.2.2, *D1*, *t1*, *L1* and *R* are selected for further analysis using two level full factorial DoE. The upper and lower levels of *D1*, *t1*, *L1* and *R* used for modelling are given in Table 3.2. This results in $2^4 = 16$ models. *N* and *L2* are kept constant as in reference model at 8 and 8.5 mm respectively. The models *M_L1* to *M_L16* obtained from two level full factorial DoE with their corresponding parameter values are shown in Table 10.1 in Appendix 1. The term *L* in model name indicates large connector. The model *Ref_L* refers to 13.6 mm reference connector.

The total contact force and total contact area in the models *M_L1* up to *M_L16* from $2^4$ DoE and reference model *Ref_L* are shown in Fig. 3.22. An ideal connector should have maximum possible contact area with smaller contact force. The models *M_L5*, *M_L9* and *M_L16* have comparatively larger contact areas in comparison to other models but with very high total contact force ranging from 1000 N to 1160 N. Such high forces are not practical from application point of view. The total contact force of reference connector is 186 N. Therefore, the aim is to have the total contact force which is smaller if possible or at least in the range closer to the total contact force in reference connector. The model *M_L7*, indicated in green oval shape, has 11 % smaller total contact area and 38 % smaller total contact force as compared to the reference connector. Therefore, a significant improvement is achieved in model *M_L7* with respect to contact force as compared with the reference connector with relatively smaller reduction in contact area. However, the contact area plays a significant role in miniaturization of connectors. Therefore, further possibilities of optimization have to be investigated.

The statistical models of the contact area $F_A$ and contact force $F_K$ obtained by performing stepwise regression on contact area and contact force results of single spring segments of *M_L1* to *M_L16* models using model based calibration toolbox in Matlab software are given as:

$$F_A = -0.159 - 0.0136 \cdot D1 - 0.0177 \cdot L1 + 0.0109 \cdot R + 0.0306 \cdot t1 \tag{3.12}$$

$$F_K = 75.14 + 1.92 \cdot D1 - 14.93 \cdot L1 + 1.26 \cdot R + 24.41 \cdot t1 \tag{3.13}$$

From the respective coefficients of the parameters in statistical model from multiple regression, the significance of the parameter on contact area and contact force can be determined. It can be seen that, *L1* and *D1* have negative correlation while *R* and *t1* have positive correlation with contact area. The spring element thickness *t1* has highest influence indicated by coefficient value of 0.0306 on contact area followed by *L1*, *D1* and *R*. On the other hand, *t1* also has the highest and most important influence on the contact force highlighted by its coefficient of 24.41. *L1* has second highest influence on contact force and has negative correlation with coefficient of -14.93. The influence of *D1* and *R* on contact force is comparatively smaller.

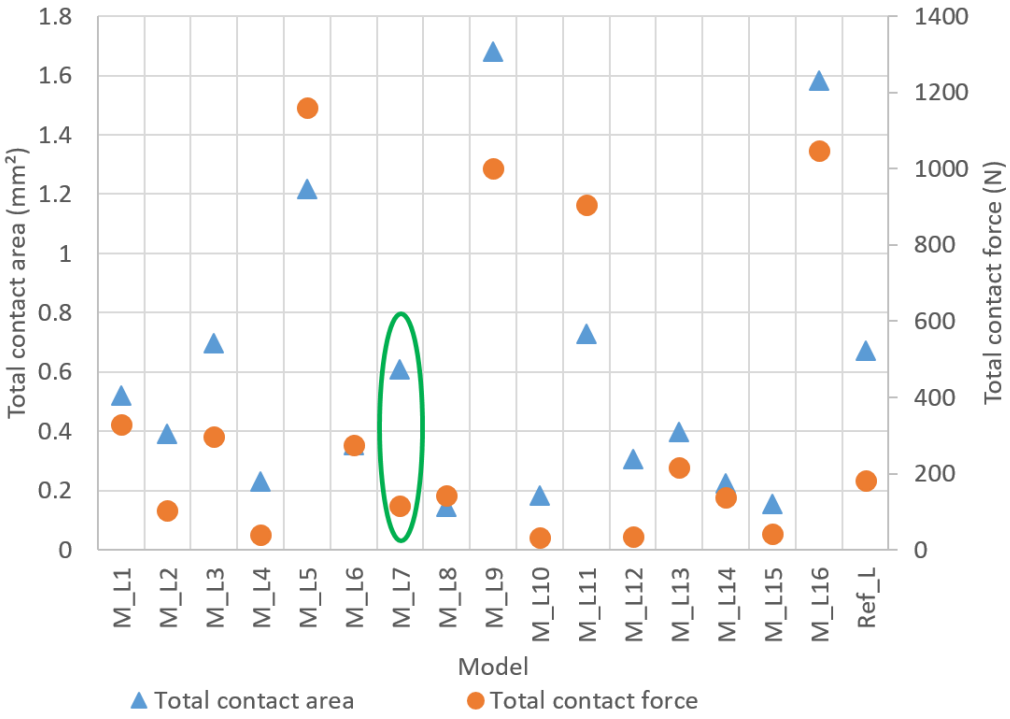


Fig. 3.22: Total contact area and total contact force in models from full factorial DoE and reference model

**Surface response plots**

The surface response plots based on the stepwise regression are plotted to study the interaction effects between design parameters under consideration. Fig. 3.23 shows the surface response plot for *D1* and *L1* interaction w.r.t. contact force and contact area respectively. The contact force increases with decrease in *L1* for a given *D1*. *D1* has a very small effect on contact force. The combination of smaller *D1* and shorter *L1* results in larger contact areas.

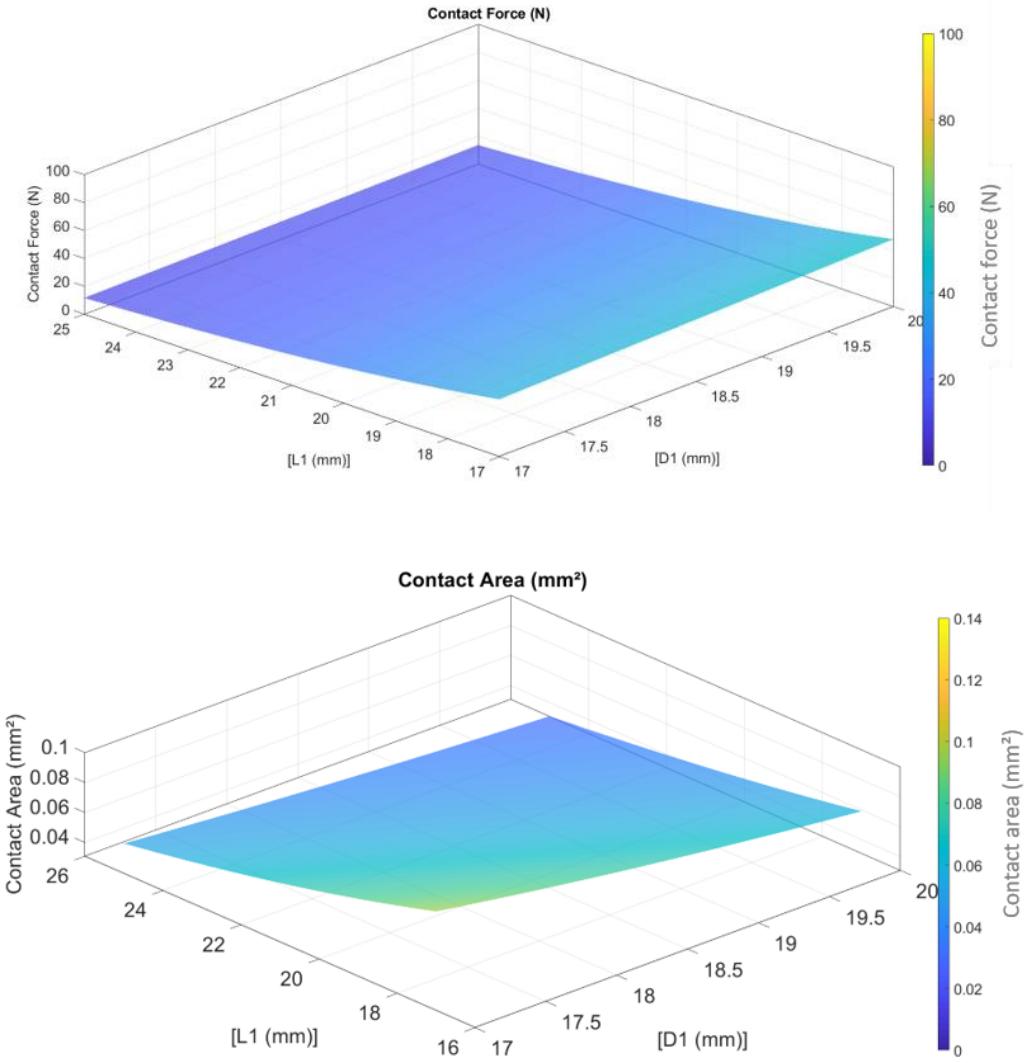


Fig. 3.23: Interaction effect of *D1* and *L1* on contact force (top) and contact area (bottom)

Fig. 3.24 shows the influence of *D1* and *R* on contact area and contact force. The interaction of *D1* and *R* has insignificant effect on contact force. On the other hand, larger contact areas are obtained with lower *D1* and greater *R* values which would result in reduced curvature of spring segment with other parameters held constant.

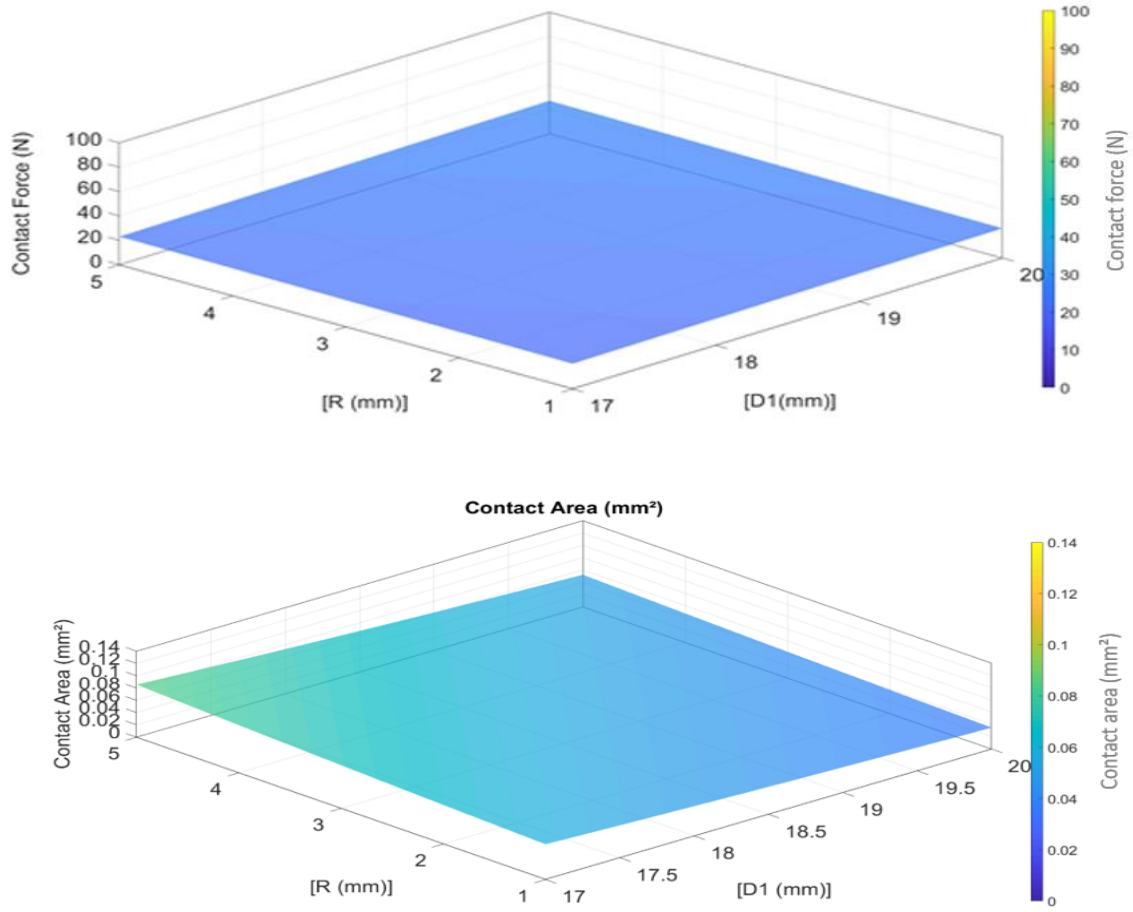


Fig. 3.24: Interaction effect of *D1* and *R* on contact force (top) and contact area (bottom)

Fig. 3.25 shows the interaction effect of *D1* and *t1* on contact force and contact area. The interaction effect on contact area is more pronounced. The lower *D1* and moderate *t1* results in intermediate contact area. The larger *t1* and smaller *D1* combination results in largest contact areas. However, with increase in *t1*, the contact force increases significantly in comparison to the variation in *D1*. The higher *D1* values result in further increase in curvature of spring segment due to which highest contact force is observed for the combination of largest *t1* and *D1*.

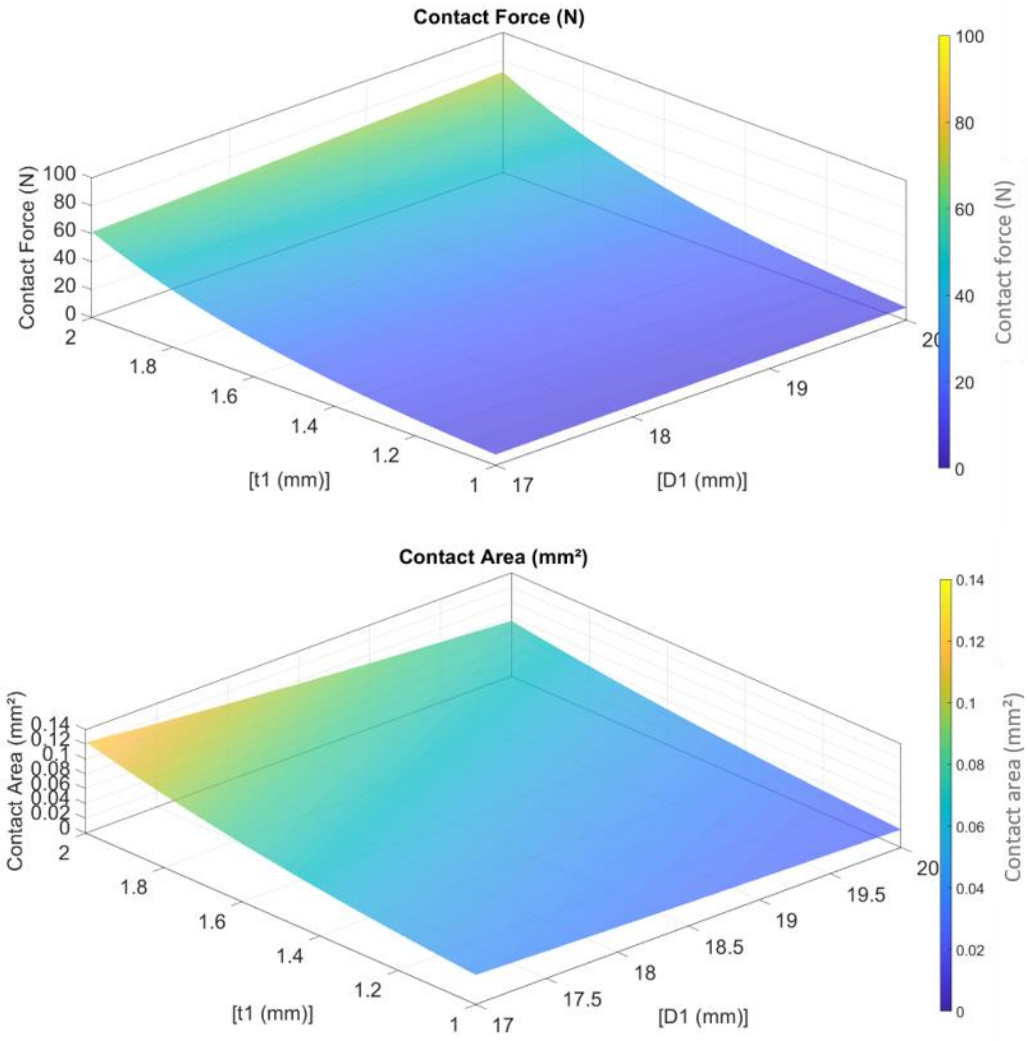


Fig. 3.25: Interaction effect of *D1* and *t1* on contact force (top) and contact area (bottom)

Fig. 3.26 shows the influence of *L1* and *R* on contact force and contact area. It can be seen that the contact radius has insignificant effect on the contact force. Irrespective of the values of *R*, the contact force decreases almost linearly with increase in *L1*. The reduction in L1 cause the increase in stiffness of spring causing the increase in contact force. The lower *L1* and moderate to high *R* values result in larger contact areas.

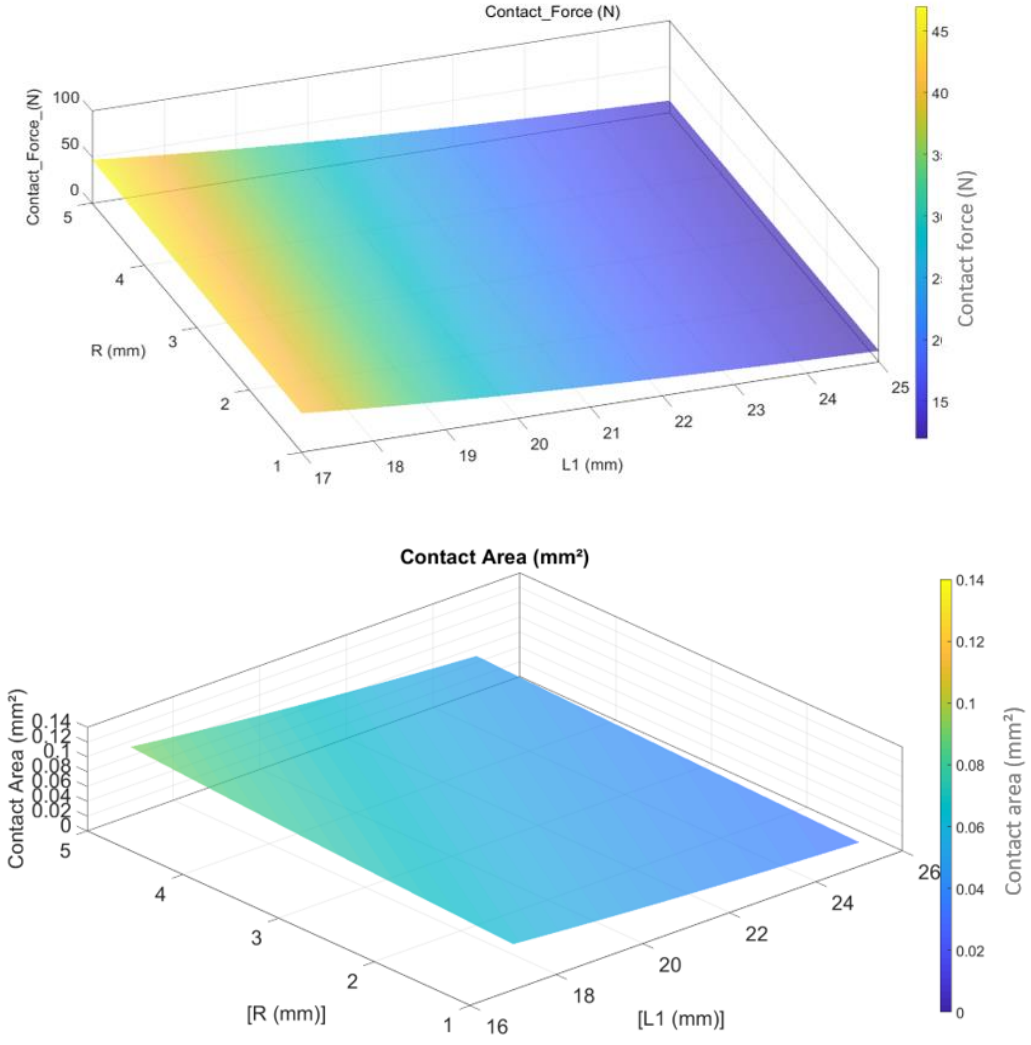


Fig. 3.26: Interaction effect of *L1* and *R* on contact force (top) and contact area (bottom)

From the surface response plots illustrating the interaction between *L1* and *t1* on contact area and contact force in Fig. 3.27, it can be seen that the lower *L1* and higher *t1* values result in larger contact areas and significantly larger contact forces. Also the interaction effect of *L1* and *t1* combination on contact force as well as on contact area appears to be highly significant. The lower *L1* and moderate *t1* combination results in optimal size of contact area. However, the contact forces are also considerably high with this combination.

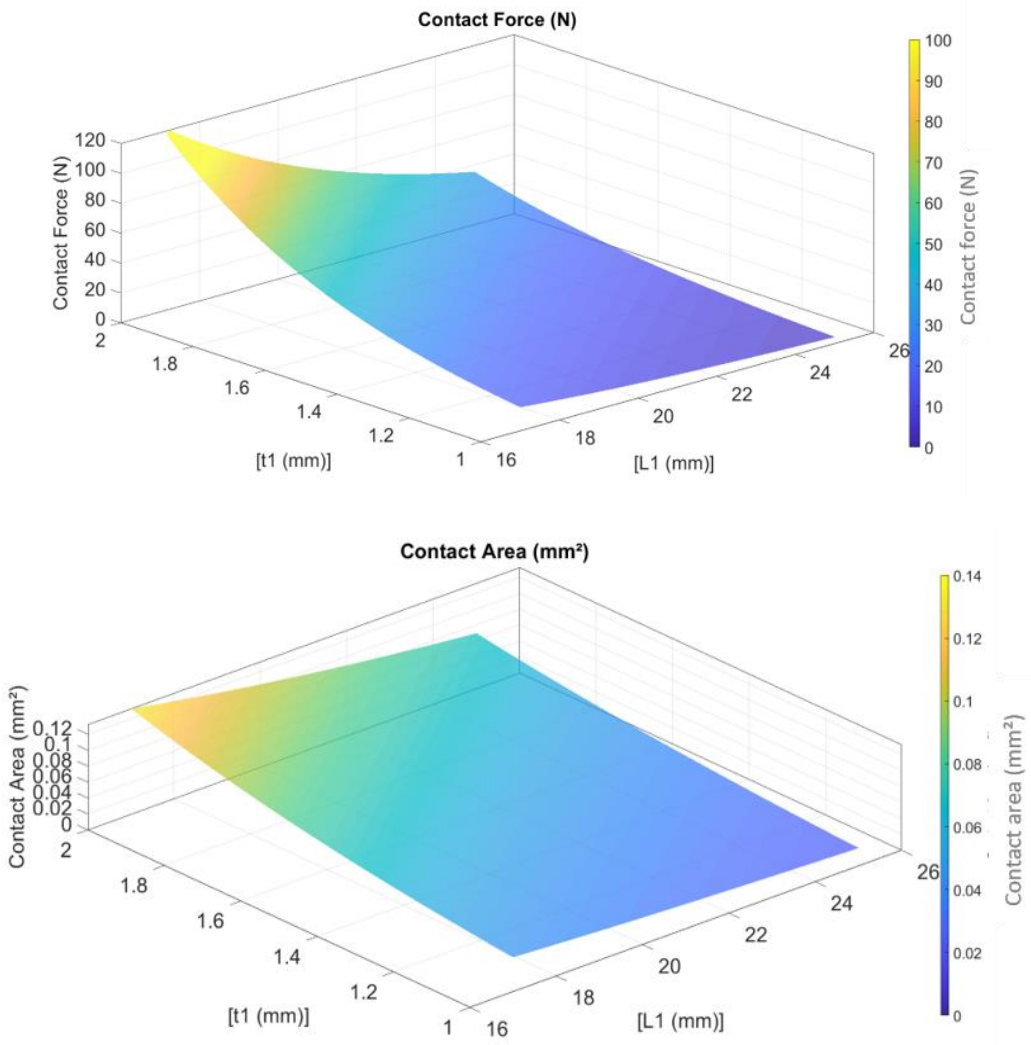


Fig. 3.27: Interaction effect of *t1* and *L1* on contact force (top) and contact area (bottom)

Fig. 3.28 shows the influence of *t1* and *R* on the contact area and contact force. The contact force increases with increase in *t1* and comparatively remains unaffected by variation in *R*. The larger *R* and *t1* values results in larger contact areas. For a given spring thickness *t1*, the increase in *R* results in increase in contact area without significantly affecting the contact force.

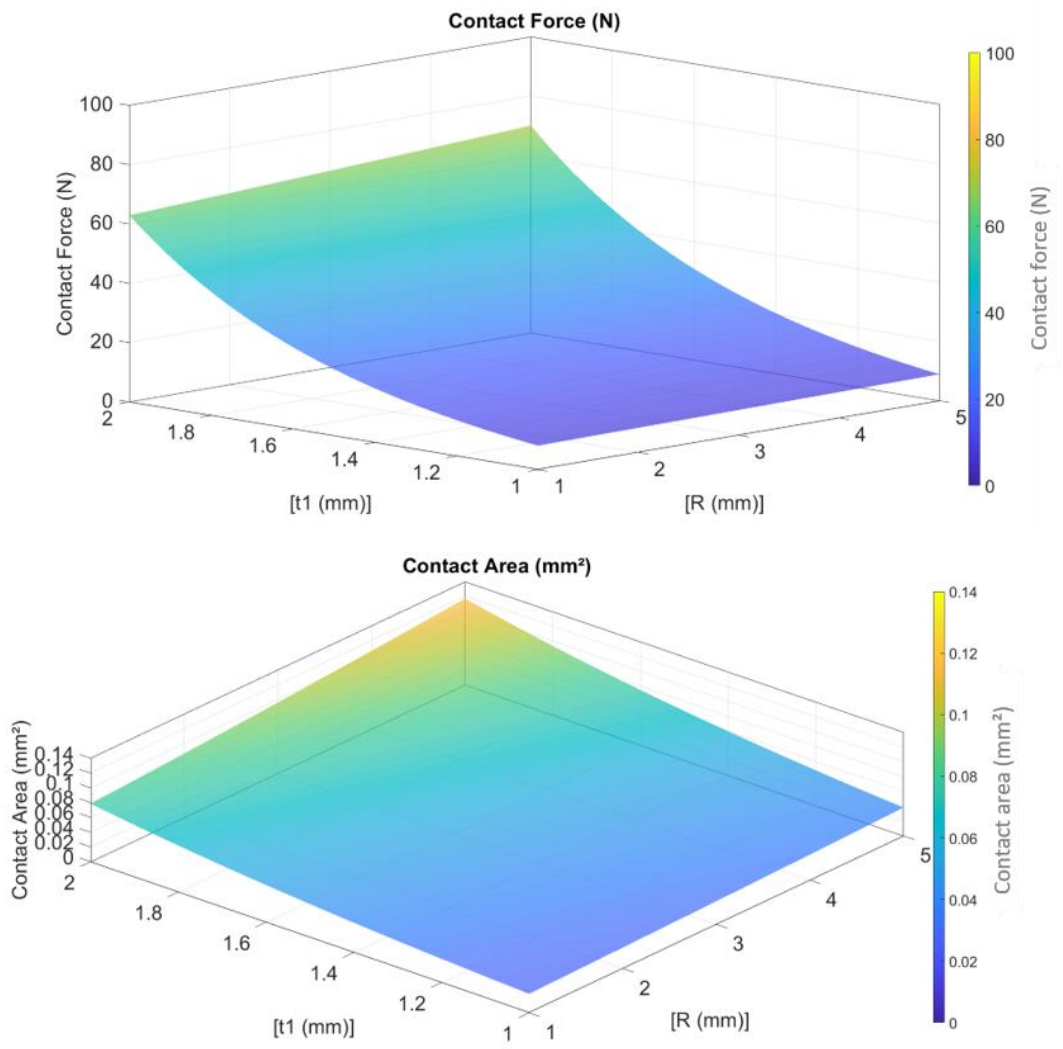


Fig. 3.28: Interaction effect of *t1* and *R* on contact force (top) and contact area (bottom)

### 3.2.2.4 Discussion on influence of individual parameters and their interactions

Based on the investigations of individual parameter influence and statistical model and surface response plots from two level full factorial DoE, in order to achieve the reduction in contact force, *t1* should be reduced. The increase in *L1* also results in lower contact forces along with some reduction in the contact area. As *L1* decreases with *L2* being constant, the curvature of the spring segment increases thereby influencing the contact area. Therefore, optimum values of *t1* and *L1* are vital from optimization point of view. The outer diameter *D1* tends to show smaller influence on contact force and considerable effect on contact area in combination with other parameters. The contact radius *R* can be increased to achieve larger contact areas with comparatively minor changes in contact force. Therefore, for verifying the further possibility of optimization, the contact radius *R* is kept constant at 2.5 mm and the length of bended portion of spring *L2* is taken into consideration for optimization in next step where the models are constructed based on the experiment designed using Taguchi L8 design. This decision is based

on the fact that the variation in *L2* could influence the contact force and contact area by influencing the curvature of the spring segment in combination with other parameters. Also, the length of the spring segment is important from miniaturization point of view.

#### 3.2.2.5 Results based on Taguchi L8 DoE

The experiment designed using Taguchi L8 design with four parameters *t1, D1, L1* and *L2* results in eight connector models. The value of *R* is kept constant at 2.5 mm and the number of spring segments *N* at 8. The eight different models of receptacle *MT2_L1* to *MT2_L8* based on Taguchi L8 design along with their respective parameter values are given in Table 10.2 in Appendix 1. Based on the learnings of the results from analysis of influence of individual parameters as well as two level full factorial DoE, the upper and lower limits of parameters are modified. The changes in minimum and maximum values of parameters in full factorial DoE and Taguchi L8 can be visualized from Table 3.9. Also the corresponding values of parameters in reference connector are given. The larger values of *L2* than that of reference connector are selected since the further reduction in *L2* would result in almost straighter spring segments which would not be favorable from contact force point of view.

Table 3.9: Modifications in the ranges of parameter values used in 2 level full factorial DoE and 2 level Taguchi DoE

| | **D1 (mm)** | **t1 (mm)** | **L1 (mm)** | **R (mm)** | **L2 (mm)** | **N** |
|---|---|---|---|---|---|---|
| Full factorial DoE | 17 to 20 | 1 to 2 | 17 to 25 | 1 to 5 | 8.5 | 8 |
| Taguchi L8 | 17 to 19 | 0.8 to 1.5 | 15 to 20 | 2.5 | 10 to 14 | 8 |
| Reference | 17.2 | 1.5 | 21 | 2 | 8.5 | 8 |

The results of the total contact area and total contact force obtained from the models using Taguchi L8 DoE are highlighted in Fig. 3.29. The model *MT2_L7* highlighted in green oval curve results in approximately 41 % larger total contact area as compared to the reference connector which is a significant increase. Also, the value of the total contact force is comparable with the magnitude of total contact force in reference connector. The increase in total contact force in *MT2_L7* connector is 12.5 % in comparison to the reference connector *Ref_L*. The total reduction of approximately 4 % in receptacle mass is obtained with *MT2_L7* connector design as compared to reference model. The results of optimized model *MT2_L7* and reference connector are highlighted in Table 3.10.

Table 3.10: Comparison of structural results of reference and optimized (MT2_L7) 13.6 mm connector models

| **Model** | **t1 in mm** | **L1 in mm** | **L2 in mm** | **D1 in mm** | **R in mm** | **Total contact force in N** | **Total contact area in mm²** | **Receptacle mass in g** |
|---|---|---|---|---|---|---|---|---|
| Reference | 1.5 | 21 | 8.5 | 17.2 | 2 | 186.208 | 0.672 | 74.048 |
| MT2_L7 | 1.5 | 20 | 10 | 17 | 2.5 | 209.544 | 0.944 | 71.136 |

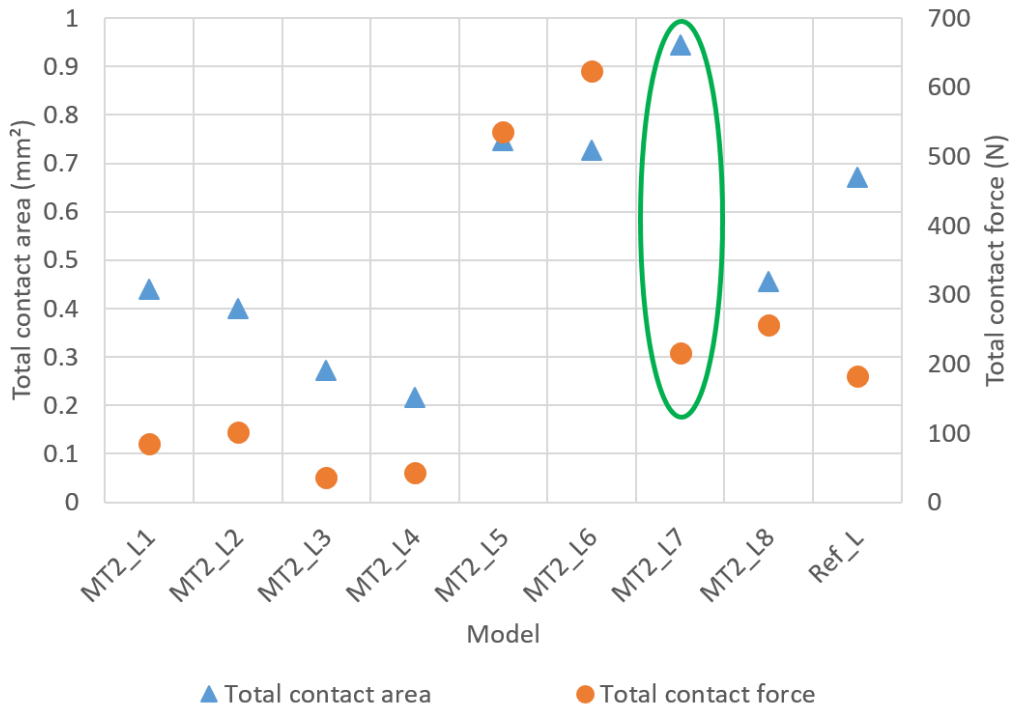


Fig. 3.29: Total contact area and total contact force in models from 2 level Taguchi L8 DoE and reference model

Also, the stress distribution in the optimized connector is improved as compared to the reference connector as shown in Fig. 3.30. The maximum equivalent stress observed at the root of the spring element is 348.29 MPa which is smaller than the yield stress of 350 MPa. The reference connector showed a maximum equivalent stress of 352 MPa at the root of spring element (Fig. 3.15). Also, the pressure in the contact zone calculated from the simulated contact force and contact area is 222 MPa which is smaller than the pressure of 277 MPa in reference connector. This would result in reduced wear in *MT2_L7* connector when compared to the wear in reference connector with same surface conditions.

The statistical models obtained from stepwise regression analysis for contact area $F_A$ and contact force $F_K$ results of the models from Taguchi L8 design are given as:

$$F_A = -0.063 - 0.008 \cdot D1 - 0.014 \cdot L1 \; - \; 0.01 \cdot L2 \; + \; 0.025 \cdot t1 \tag{3.14}$$

$$F_K = 29.62 + 2.38 \cdot D1 - 12.42 \cdot L1 + 9.08 \cdot L2 + 21.37 \cdot t1 - 0.9 \cdot D1 \cdot L1 + 1.62 \; \cdot D1 \cdot t1 \tag{3.15}$$

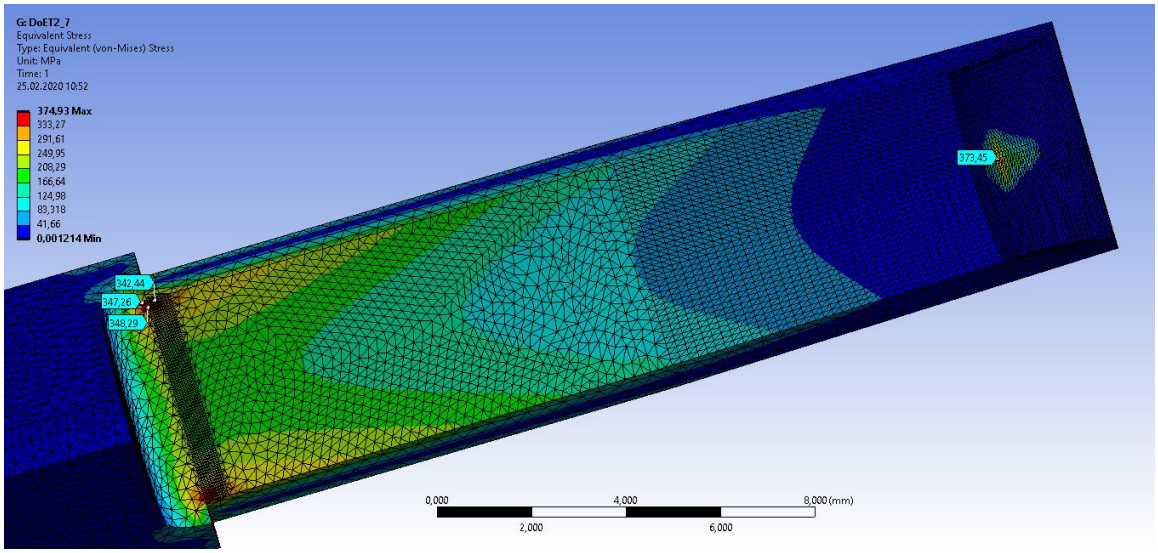


Fig. 3.30: Equivalent stress distribution in optimized model *MT2_L7*

The statistical models correspond to the contact force and contact area of single segment of receptacle. Based on the coefficients of design variables, it can be seen that the contact force is mainly influenced by the thickness of the spring segment *t1*, which has a positive coefficient of 21.37 followed by the total length of spring element *L1* with a negative coefficient of 12.42. *L2* also shows considerable effect on the contact force with a positive coefficient of 9.08. The outer diameter *D1* has smaller individual effect on contact force. The interactions between parameters also have very small influence on contact force. Similar to the contact force, thickness of spring element *t1* followed by its total length *L1* has the highest influence on the contact area. The length of the bended portion of spring element *L2* and outer diameter *D1* have a moderate effect on contact area. With the model derived for contact area $F_A$ the reduction in *D1*, *L1* and *L2* and increase in *t1* result in increase in contact area.

### 3.2.3 Structural optimization of 2.5 mm connector

3.2.3.1 Structural simulation of 2.5 mm reference connector

The structural FEM analysis of 2.5 mm reference connector having 6 spring elements results in a total contact area of 0.0193 mm² and total contact force of 6.85 N i.e. the contact area and contact force in single spring segment being 0.0032 mm² and 1.14 N. The total contact area and total contact force are obtained by multiplying the respective contact area and contact force values of single spring element used in simulation model with the total number of spring elements in the receptacle. Fig. 3.31 represents the stress distribution across receptacle. The maximum equivalent stress near the root of the receptacle is 271MPa, which is considerably lower than the yield stress limit of 350MPa. The contact pressure calculated from the resulting contact area and the contact force from single spring segment is 355 MPa.

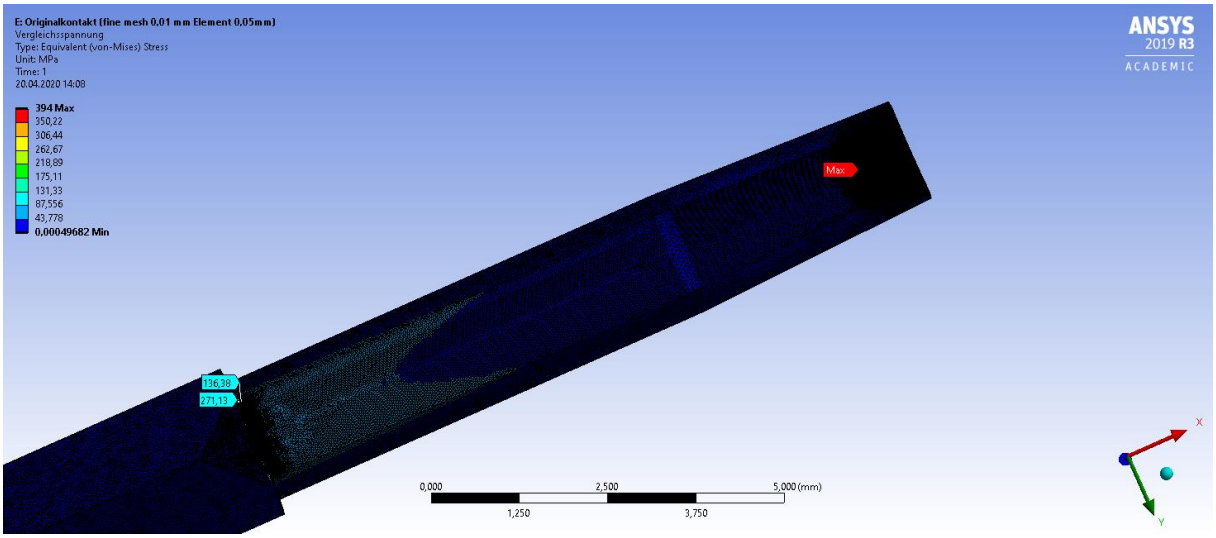


Fig. 3.31: Equivalent stress distribution in 2.5 mm reference connector

3.2.3.2 Results based on Taguchi L9 DoE

The parameters selected for the structural optimization of the 2.5 mm connector are based on the conclusions drawn from the investigations of 13.6 mm connector as discussed in section 3.2.2. Therefore, outer diameter *D1*, total length of the spring element *L1*, length of bended portion of the spring element *L2* and thickness of spring element *t1* are chosen for structural optimization of 2.5 mm connector. The value of contact radius *R* and the number of spring elements *N* is retained same as that in the reference connector i.e. $R$ = 1 mm and $N$ = 6. As against in the case of 13.6 mm connector, where 2 levels of parameters were used in optimization process, the optimization in 2.6 mm connector is performed with 3 levels of

parameters using Taguchi L9 design. The upper, middle and lower levels of parameters are given in Table 3.4.

The nine different models *M_S1 to M_S9* obtained from Taguchi L9 design along with their respective parameter values are given in Table 10.3 in Appendix 1. The model *Ref_S* indicates the reference model. The results of the total contact area and total contact force obtained from the models using Taguchi L9 DoE are highlighted in Fig. 3.32. The model *MS_5* indicated in green oval curve, results in approximately 2.4 times larger total contact area as compared to the reference connector which is a significant increase. The total contact force in *M_S5* is 84 % of the total contact force in reference connector. Also the model *M_S5* model is 16 % lighter than the reference connector. Therefore, a significant improvement in contact area, contact force and size are obtained with *M_S5* model. Apart from *M_S5*, *M_S1* also results in improved contact area and slightly reduced contact force in comparison to the reference connector. The results of optimized model *M_S5* and reference connector are highlighted in Table 3.11.

Table 3.11: Comparison of structural results of reference and optimized (*M_S5*) 2.5 mm connector models

| **Model** | **t1 (mm)** | **L1 (mm)** | **L2 (mm)** | **D1 (mm)** | **R (mm)** | **Total contact force (N)** | **Total contact area (mm²)** | **Receptacle mass (g)** |
|---|---|---|---|---|---|---|---|---|
| Reference | 0.75 | 10.20 | 3.60 | 4.50 | 1 | 6.85 | 0.019 | 1.21 |
| M_S5 | 0.75 | 10.20 | 4.20 | 4.0 | 1 | 5.76 | 0.046 | 1.02 |

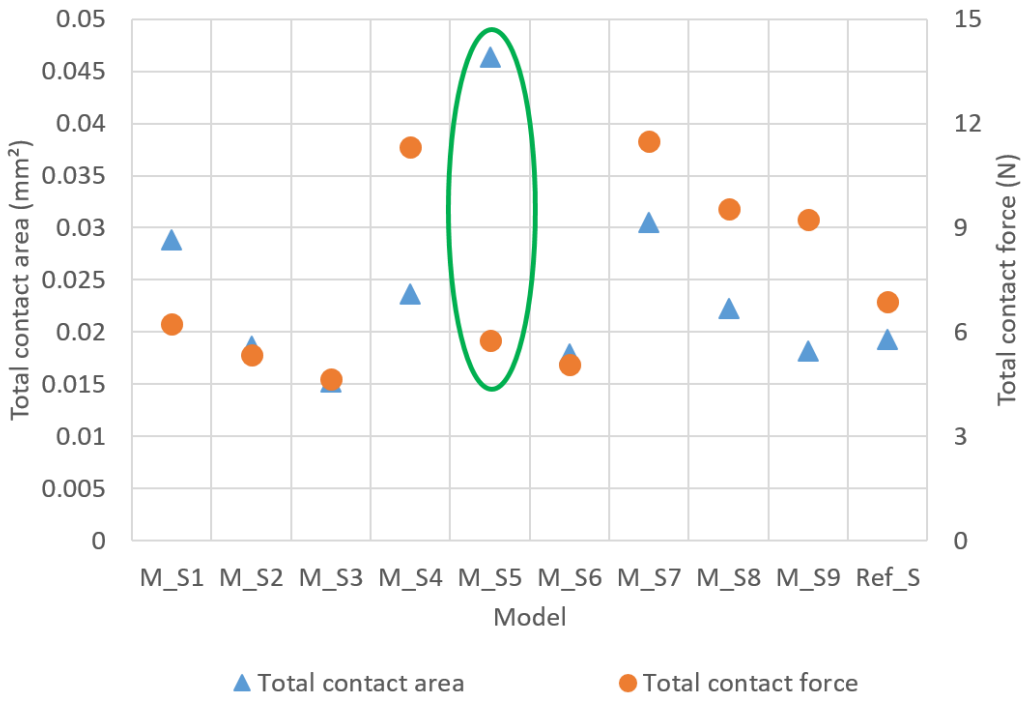


Fig. 3.32: Total contact area and total contact force in models from 2 level Taguchi L8 DoE and reference model

The statistical models obtained from stepwise regression analysis of simulated contact area $F_A$ and contact force $F_K$ results of the models from Taguchi L9 design are given as:

$$F_A = 0.004 - 0.0009 \cdot D1 + 0.0002 \cdot L1 + 0.0018 \cdot L2 + 0.0002 \cdot t1 + 0.0022 \cdot D1 \cdot t1 \quad (3.16)$$

$$F_K = 1.27 + 0.215 \cdot D1 - 0.28 \cdot L1 + 0.126 \cdot L2 + 0.42 \cdot t1 - 0.14 \cdot D1 \cdot L1 + 0.20 \cdot D1 \cdot L2 + 0.2 \cdot L1 \cdot t1 \quad (3.17)$$

Similar to the 13.6 mm connector, the statistical models in this case also correspond to the contact force and contact area of single segment of receptacle. The individual influence and correlation of the parameters on contact force is similar to that in the case of 13.6 mm connector. However, the interaction effects of some of the parameters on contact force are more pronounced in case of 2.5 mm connector which could be due to the inclusion of additional level of parameters for experiments. Based on the coefficients of design variables, it can be seen that the contact force is mainly influenced by the thickness of the receptacle segment *t1*, which has a positive coefficient of 0.42 followed by the total length of spring element *L1* with a negative coefficient of 0.28. The outer diameter *D1* has considerable individual effect on contact force followed by *L2*. *D1* in combination with *L1* and *L2* respectively and interaction of *L1* with *t1* have considerable effect on the contact force.

The thickness of spring element *t1* and total length *L1* have the highest individual influence on the contact area followed by *L2* and *D1*. The interaction effect between *D1* and *t1* has the most significant effect on the contact area. This can be visualized from the fact that the combination of the outer diameter *D1* and thickness *t1* have huge impact on the curvature of the spring thereby significantly affecting the contact area. When compared to 13.6 mm connector, the correlation of the individual parameters with respect to contact area differs significantly from those observed in case of 2.5 mm connector. *L1* and *L2* exhibit negative correlation with contact area in 13.6 mm connector as against the positive correlation observed in the case of 2.5 mm connector. Also, the interaction between *D1* and *t1* is most significant influence on contact area in 2.5 mm connector whereas this interaction is not included in the contact area model for 13.6 mm connector (equation (3.14)). This could be due to the 3 levels of parameters employed in analysis of 2.5 mm connector thereby adding additional information to statistical model as against the 2 levels of parameters used in 13.6 mm connector. Also, the parameter selection for defining the model in stepwise regression which is done manually could influence the models. In spite of these differences, considerable improvements are achieved in the structurally optimized models of 2.5 mm as well as 13.6 mm connectors. However, from this discussion it can be seen that while optimizing the contact area in connector, the chosen DoE methodology could play a significant role. Based on the levels of improvements achieved in case of 2.5 mm

and 13.6 mm connectors, the selection of 3 levels of parameters for DoE appears to be favorable from structural optimization point of view.

### 3.2.4 Discussion on parametric structural optimization approach

A systematic procedure for the parametric structural optimization of round electrical connector with the application of CAD, FEM and statistical analysis tools is laid down. The initial detailed analysis is performed using a large sized 13.6 mm connector model as a reference. The structural optimization is achieved by optimizing the spring segment of the receptacle while keeping the pin design constant. The different geometrical parameters in spring segment which could influence the contact area and contact force are identified. The individual influence of the design parameters is investigated through structural simulations. Based on the observations of individual influence, four most influential parameters namely thickness *t1*, total length of spring segment *L1*, outer diameter of receptacle *D1* and contact radius *R* are selected for further investigation using two level full factorial DoE. The structural simulation of resulting models from two level full factorial DoE enables the statistical modelling of contact area and contact force with respect to design parameters and the response surface plots help to understand the interaction between variables on the contact area and contact force. According to statistical model from two level full factorial experiment, *t1* and *L1* have most significant influence on both contact force as well as contact area. In contact area model, considerable influence of *D1* and *R* is also seen. However, the contact force obtained with the models was mostly larger than the permissible limit due to which the design parameter limits are altered and new models based on two level Taguchi *L8* design of experiment are generated to enable faster analysis. Also, *R* is kept constant and new variable *L2* i.e. length of bended portion of spring element is included. Form the statistical models of contact force and contact area, it is seen that *t1* and *L1* have significant influence on the contact force and contact area as in case of two level full factorial design. Also interaction between the *D1-L1* and *D1-t1* is found to improve the model quality of contact force. The interaction effects are not found to be significant for contact area and the statistical model consists of all the individual effects. One of the models *MT2_L7* from Taguchi L8 design resulted in an optimal combination of contact area and contact force in which contact area is significantly improved and contact force is in the comparable range as in reference connector. This would be considered for investigating thermal-electric performance in next step.

The process is repeated for a smaller 2.5 mm connector to validate the applicability of the proposed approach for different sizes. As against two levels of parameters used in 13.6 mm connector, the models are designed using three level Taguchi L9 design of experiment. The individual influences of the design parameters are similar to that observed in 13.6 mm connector while *D1-L2, t1-L1* interaction for contact force and *D1-t1* interaction for contact area are found to improve the statistical models. Out of nine different receptacle designs, two are found to be better than the reference connector. The design *M_S5* with the highest contact area and lowest contact force would be considered for thermal-electric simulation in next step.

The aim of achieving an optimal combination of contact area and contact force is successfully achieved and the influence of different design parameters and design of experiments on the optimization process are understood. Three levels of parameter in design of experiment could be seen to be effective in comparison to two parameter levels. Also, the Taguchi design of experiments can be reliably used in the optimization process.

### 3.2.5 Summary of the structural optimization

In this section, the procedure for the structural optimization of the round electrical connector through variations in the receptacle spring segment and while keeping the pin design unchanged has been introduced. A detailed investigation is conducted using a large 13.6 mm round connector and in the process a connector design having improved contact area and comparable contact force as that of reference connector is obtained. The procedure of parametric structural optimization is then validated through a smaller connector of 2.5 mm size. The observations such as individual effects and interaction effects of geometric parameters in 13.6 mm connector are in good agreement with the observations in 2.5 mm connector. The influence of interaction effects is dominant when three parameter levels are used in experiments. Overall, the proposed approach appears to be effective and transferable to different sizes of connectors.

## 3.3 Results of thermal and electric performance optimization

Some parts of this chapter have been published in the paper “Parametric optimization of connectors by means of coupled simulation” [187] in the proceedings of ‘8. Symposium Connectors – Elektrische und optische Verbindungstechnik, Lemgo, Germany 2021’.

### 3.3.1 Thermal and electrical optimization of 13.6 mm connector

#### 3.3.1.1 13.6 mm reference connector

The temperature rise and electrical resistance of the connector are the parameters used for evaluating the thermal and electrical behavior of the connector. The measurements show that the temperature rise in connector against the input current shows a parabolic behavior due to the joule heating. A similar trend is observed in [200]. The cable heating contributes mainly to the temperature rise in connector [28]. Further increase in connector temperature occurs due to the joule heating resulting from bulk resistance of the receptacle and pin and contact resistance between them and at crimp where they are connected to the cable. Therefore, the connector temperature in majority of the cases is higher than the cable temperature. This causes the heat flow from the connector to the cable resulting in the increased cable temperature near the connector. This temperature decays with distance away from the connector and becomes constant after a certain length where the connector heating no longer affects the cable temperature. The bigger the cable size, smaller is the temperature rise in cable for the given current, cable material and length owing to the increased cross sectional area and reduced electrical resistance [194]. This constant temperature in the cable for a given current load is measured by passing current through the cable without connector.

The joule heating results of cable and connector are illustrated in Fig. 3.33. The measured joule heating in cable is recorded at the middle portion of the cable without connector while the measured joule heating in the connector represents the measured temperature rise at the receptacle surface near the contact region. It is observed that for 100 A current, the temperature rise in cable is 5.85 K and in connector is 8.04 K, indicating a temperature rise of 2.19 K due to joule heating in connector. Thus, the cable contributes to approximately 73 % temperature rise in the connector with respect to the ambient temperature.

Similarly, the temperature rise in cable at 75 A is approximately 75 % of the temperature rise in connector. The maximum temperature rise is measured on the receptacle ($\Delta T_{receptacle}$) near the contact where the highest joule heating occurs in the contact zone as shown in Table 3.12. The difference between $\Delta T_{crimp\_receptacle}$ and $\Delta T_{cable}$ gives an estimation of the effect of connector on the cable heating. The simulated temperature rise curve highlighted by green color and

measured temperature rise curve colored in blue show similar pattern (Fig. 3.33). For a current input of 75 A and 100 A, temperature difference of 0.29 K (7 %) and 0.34 K (4.22 %) is observed between measured and simulated results.

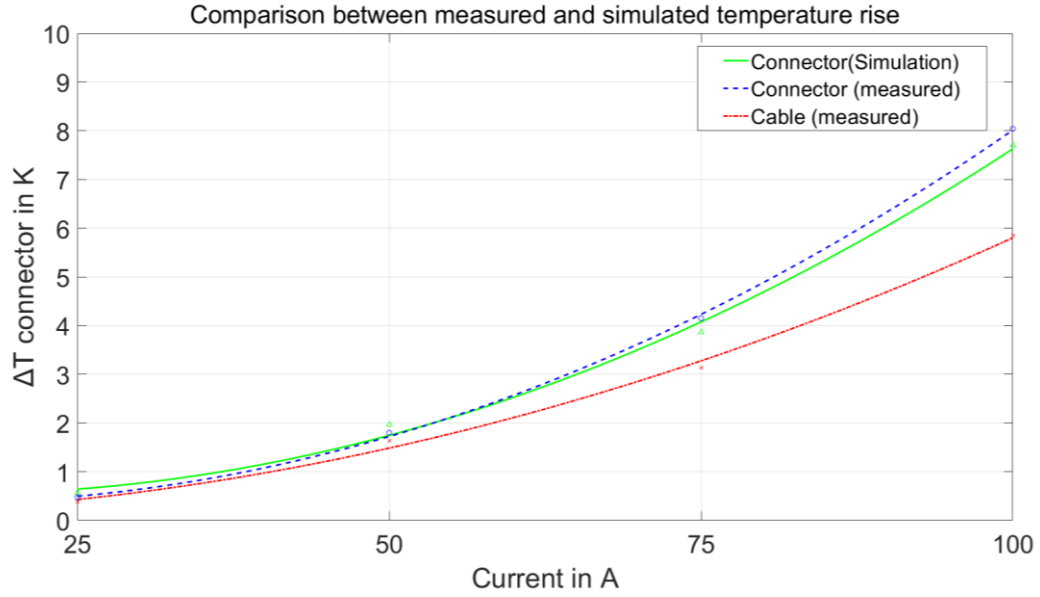


Fig. 3.33: Joule heating results in 95 mm² cable and 13.6 mm reference connector

Table 3.12: Measured joule heating in 95 mm² cable and 13.6 mm reference connector

| **Current (A)** | **$\Delta T_{crimp\_receptacle}$ (K)** | **$\Delta T_{receptacle}$ (K)** | **$\Delta T_{pin}$ (K)** | **$\Delta T_{crimp\_pin}$ (K)** | **$\Delta T_{cable}$ (K)** |
|---|---|---|---|---|---|
| 100 | 7.25 | 8.04 | 7.77 | 7.22 | 5.85 |

Fig. 3.34 shows the temperature distribution across the 13.6 mm reference connector for 100 A current. It can be seen that the highest temperature occurs in the area where the receptacle and pin contact as observed in the measurements. The temperature in the front portion of the receptacle where the cross-section is thinner is comparatively higher than the rear parts of the connector. This is due to the increased electrical resistance and current density due to the smaller cross-section in turn resulting in higher joule heating in front portion of the receptacle.

The electrical resistance of the connector is calculated from the measured and simulated voltage drop across the connector for the given current input. Fig. 3.35 shows the simulated electrical resistance increase in 13.6 mm reference connector with respect to the current from 25 A to 100 A along with the measured electrical resistance at 0.1 A. The electrical resistance measured at 0.1 A of current is approximately 60 µΩ. The limitations of the equipment available in-house allowed the measurement of the electrical resistance to be conducted with a maximum input current of 0.1 A. For the increase in current from 25 A to 100 A, the simulated electrical resistance increases from 57.7 µΩ to 58.4 µΩ. Given the size of the 13.6 mm connector, the joule heating increase and hence the electrical resistance increase is relatively smaller for the

considered current range. Fig. 3.36 illustrates the simulated voltage drop across the reference connector for current input of 100 A.

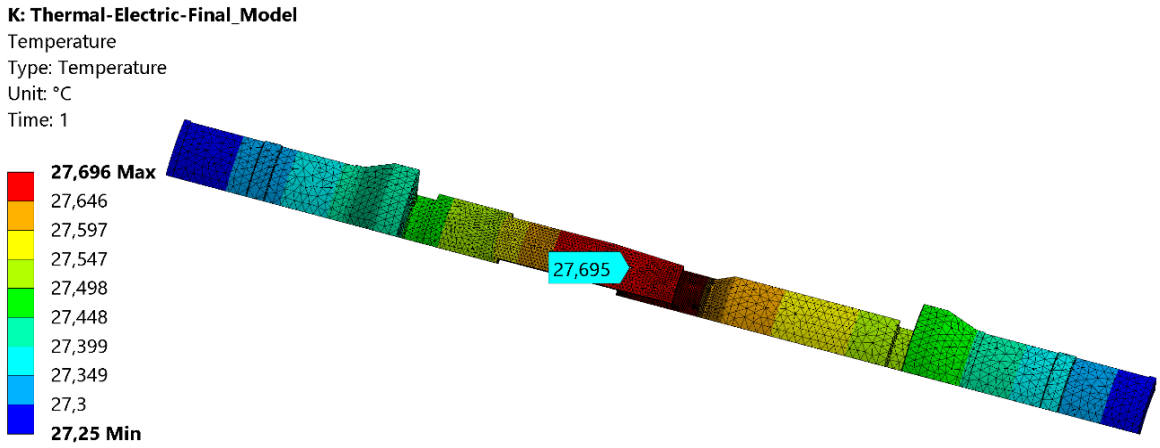


Fig. 3.34: Simulated temperature distribution across 13.6 mm reference connector at 100 A

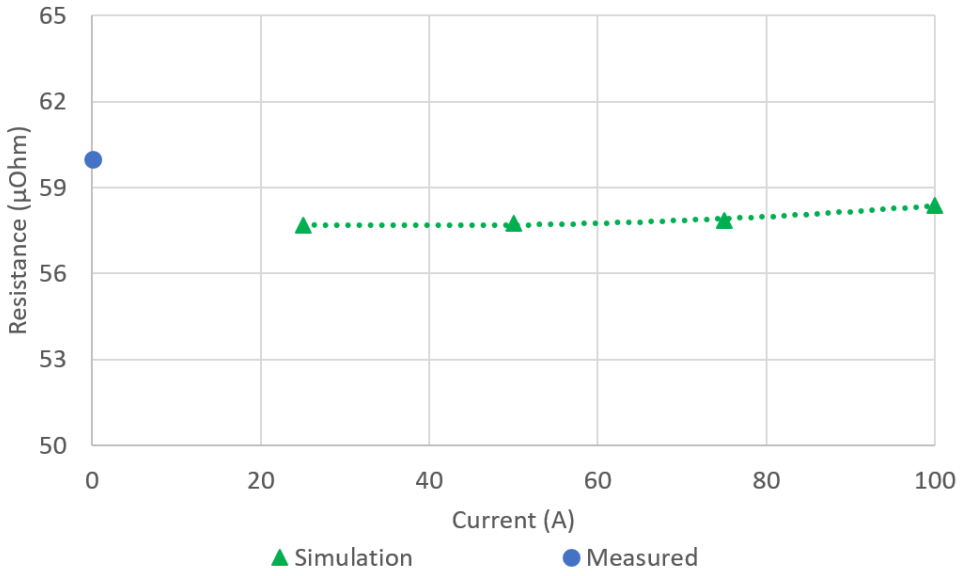


Fig. 3.35: Measured and simulated electrical resistance in 13.6 mm reference

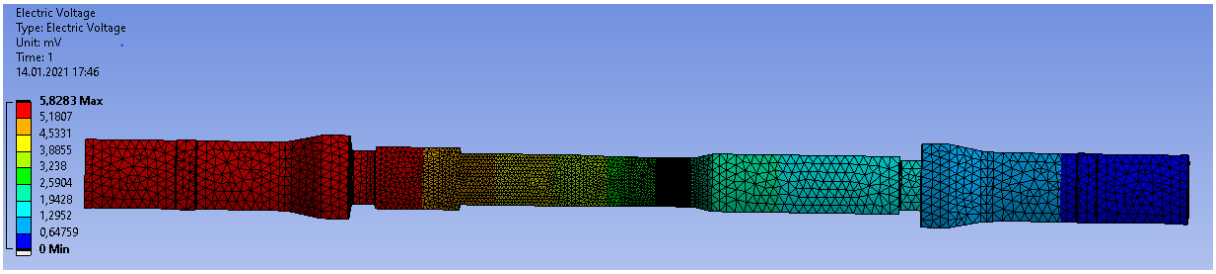


Fig. 3.36: Simulated potential difference across 13.6 mm reference connector at 100 A

### 3.3.1.2 Comparison between connector heating and electrical resistance of 13.6 mm reference and optimized model

Table 3.13 shows the comparison of temperature rise and electrical resistance of reference and structurally optimized connector *MT2_L7*. The optimized connector is 3 % lighter in mass than the reference connector. The temperature rise in optimized connector is almost the same as that in the reference connector with a minor difference of 0.03 K for a current input of 100 A. The temperature distribution across the optimized connector at 100 A is shown in Fig. 3.37. The electrical resistance is reduced by 2.19 µΩ in optimized connector. The total electrical resistance and size of the connector are one of the parameters significantly affecting the joule heating in the connector. The total electrical resistance comprises of the bulk and contact resistances of which the bulk resistance constitutes a significant proportion. The larger size connector will have smaller bulk resistance. Therefore, the temperature rise in reference connector due to bulk resistance is smaller in comparison to the temperature rise due to bulk resistance in optimized connector. However, the larger contact area in optimized connector, which is 40.5 % larger than the reference connector, leads to considerable reduction in electrical resistance near the contact zone.

Table 3.13: Thermal-electric simulation results of 13.6 mm reference and optimized *MT2_L7* connector

| **Model** | **Receptacle mass in g** | **Current in A** | **$\Delta T_{receptacle}$ in K** | **$\Delta V_{connector}$ in mV** | **$R_{connector}$ in µΩ** |
|---|---|---|---|---|---|
| Reference | 74.048 | 100 | 7.69 | 5.828 | 58.28 |
| MT2_L7 | 71.136 | 100 | 7.66 | 5.609 | 56.09 |

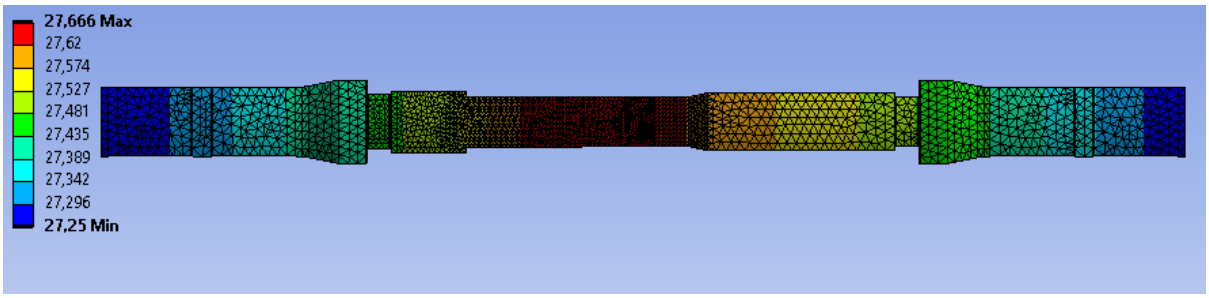


Fig. 3.37: Simulated temperature distribution across 13.6 mm optimized connector MT2_L7 at 100 A

Fig. 3.38 shows the voltage drop near the contact zone in the original and optimized connector for a current of 100 A. The voltage drop in optimized connector is approximately 13 % smaller as compared to the reference connector. This results in the reduced total resistance in optimized connector in spite of the comparatively smaller size. In addition, the temperature rise in optimized connector when compared to the reference connector is not increased, as the contribution of joule heating at contact surface to the total joule heating due to larger contact area and hence reduced current density, is decreased. From the comparison of the results, it can

be seen that the design of the reference connector is close to the optimized state based on the parametric models derived from the two level Taguchi L8 design of experiments.

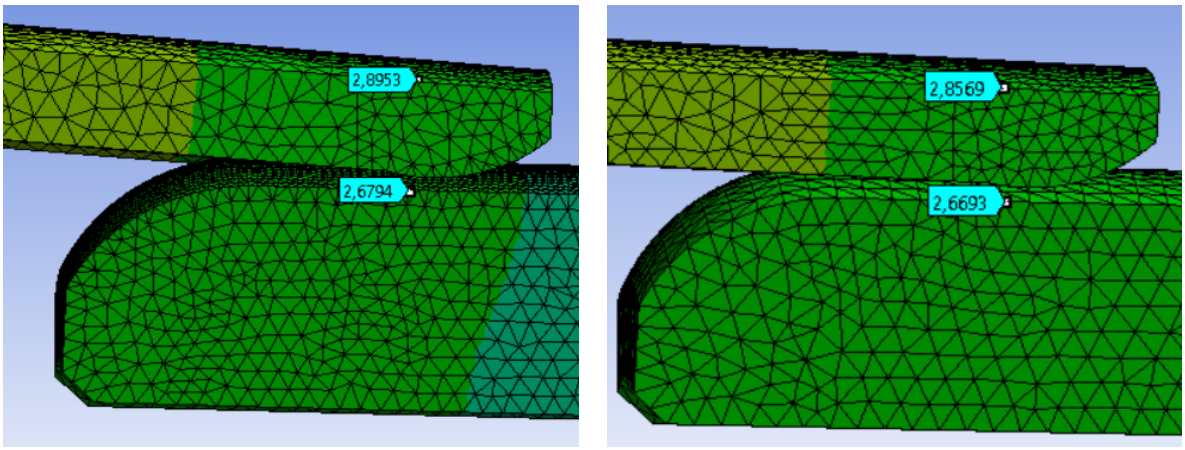


Fig. 3.38: Potential difference near contact region in 13.6 mm reference connector (left) and optimized MT2_L7 connector (right)

### 3.3.2 Thermal and electrical optimization of 2.5 mm connector

3.3.2.1 2.5 mm reference connector

The measured joule heating in cable without connector $\Delta T_{cable}$, at crimp-cable interface $\Delta T_{crimp\_receptacle}$ and near contact zone in receptacle $\Delta T_{receptacle}$ is shown in Table 3.14. Also the joule heating on the pin surface $\Delta T_{pin}$ and at crimp of pin $\Delta T_{crimp\_pin}$ is given. At the current input of 30 A, the measured joule heating in cable without connector is 35.30 K whereas the joule heating measured near the contact zone on the receptacle surface is 39.45 K. Therefore, cable contributes around 89.4 % of the total joule heating in connector. It is to be noted that the contribution of the cable to the joule heating could be affected by the selection of cable size. In this case, the cable is relatively larger i.e. 2.5 mm² for the given 2.5 mm connector.

Table 3.14: Measured joule heating in 2.5 mm² cable and 2.5 mm reference connector

| **Current (A)** | **$\Delta T_{crimp\_receptacle}$ (K)** | **$\Delta T_{receptacle}$ (K)** | **$\Delta T_{pin}$ (K)** | **$\Delta T_{crimp\_pin}$ (K)** | **$\Delta T_{cable}$ (K)** |
|---|---|---|---|---|---|
| 30 | 39.42 | 39.45 | 38.67 | 38.74 | 35.30 |

The results of the measured joule heating in 2.5 mm² cable without connector along with the measured and simulated joule heating results from coupled thermal-electric simulation of reference connector with respect to the current input of 5 A up to 30 A are illustrated in Fig. 3.39. The simulated joule heating results are shown for two different surface emissivity values namely with e=0.02 corresponding to polished silver surface which is the ideal case and e=0.97 corresponding to the polypropylene tape used for fixing the thermocouples to connector surface which covered the entire surface thereby representing the actual case. The measured joule heating in cable without connector is shown by red dotted curve and the blue dotted curve shows the measured joule heating in reference connector. The orange dashed curve and gray continuous curve highlight the simulated joule heating with respect to emissivity values of 0.02 and 0.97 respectively. It can be seen that the gray curve which takes into account the influence of polypropylene tape almost overlaps with the measured joule heating in connector. At the current input of 30 A, the temperature difference of 0.16 K and 0.85 K is calculated between the measured and simulated temperature rise with emissivity of 0.97 and 0.02 respectively. An example of the simulated temperature distribution across the reference connector is illustrated in Fig. 3.40.

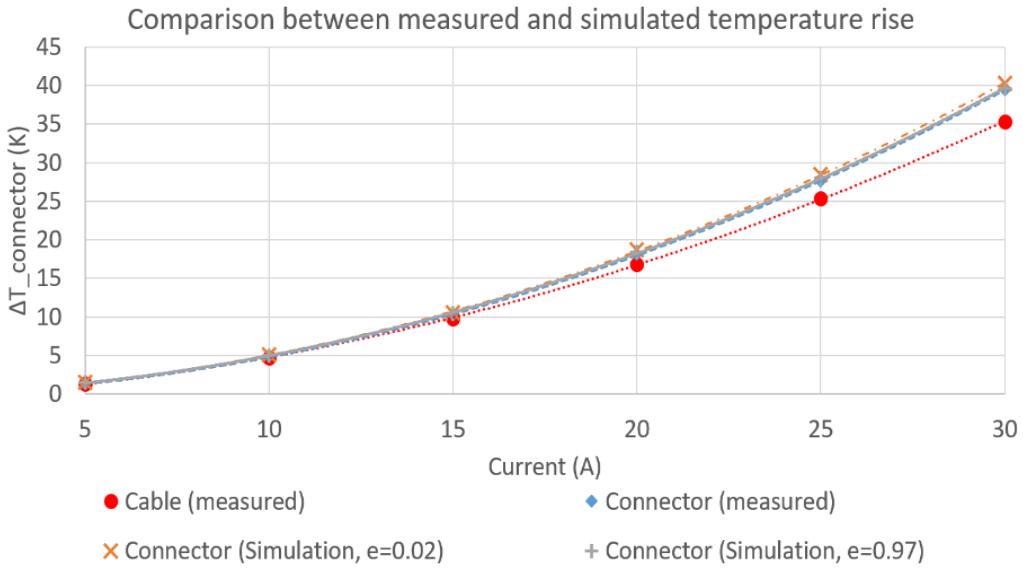


Fig. 3.39: Joule heating results in 2.5 mm² cable and 2.5 mm reference connector

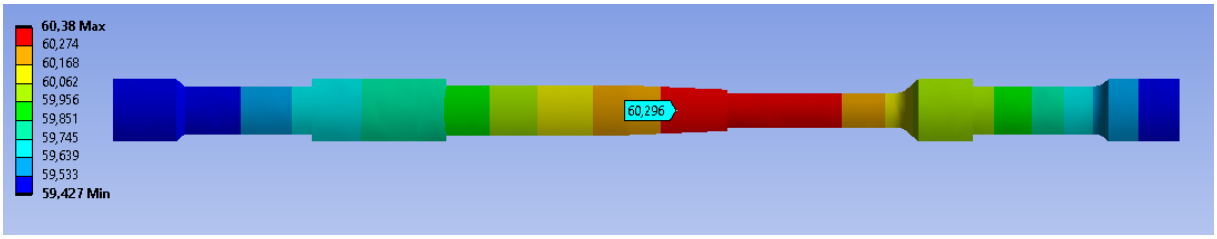


Fig. 3.40: Simulated temperature distribution across 2.5 mm reference connector at 30 A

Fig. 3.42 shows the simulated electrical resistance increase in 2.5 mm reference connector with respect to the current along with the measured electrical resistance at 0.1 A. The electrical resistance measured at 0.1 A of current is 303 μΩ. The simulation results show an increase in the electrical resistance from 318 μΩ to 342 μΩ for the increase in the current input from 5 A to 30 A. An example of the simulated voltage drop at 30 A current across reference connector is illustrated in Fig. 3.41.

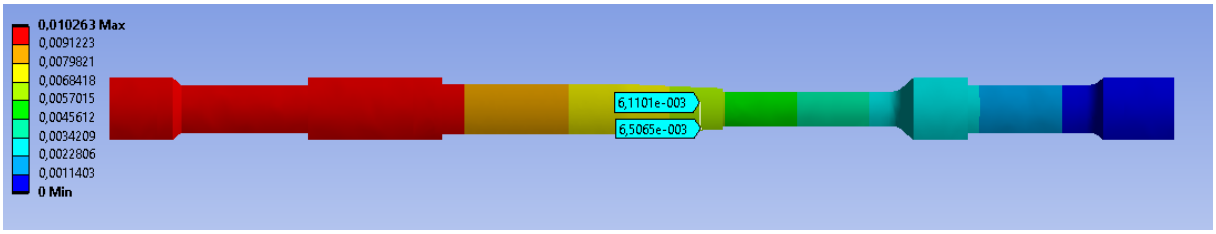


Fig. 3.41: Simulated potential difference across 2.5 mm reference connector at 0.1 A

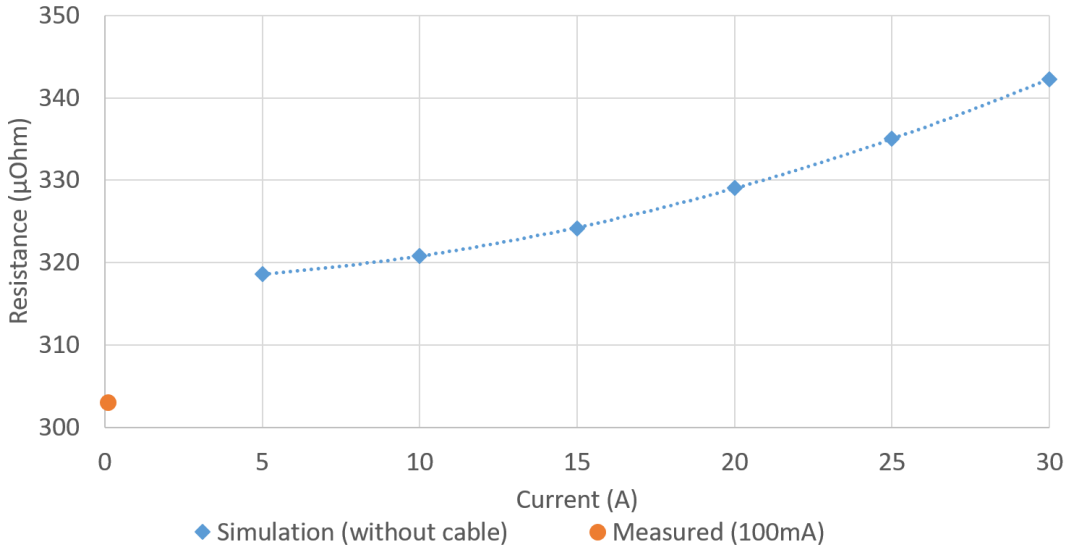


Fig. 3.42: Measured and simulated electrical resistance in 2.5 mm reference connector

### 3.3.2.2 Comparison between connector heating and electrical resistance of 2.5 mm reference and optimized model

Table 3.15 shows the comparison of temperature rise and electrical resistance of reference and structurally optimized connector *M_S5*. The optimized connector is 15.7 % lighter and hence smaller than the reference connector. At a current input of 30 A, the temperature rise and total electrical resistance in optimized connector are 0.28 K i.e. 0.7 % and 15.1 µΩ i.e. 4.2 % higher than the reference connector respectively. The temperature distribution across the optimized connector at 30 A is shown in Fig. 3.43.

On the other hand, due to the larger contact area, the voltage drop near the contact region of optimized model is 22 % smaller in comparison to the reference model, thereby leading to considerable decrease in the electrical contact resistance. The voltage drop near the contact zone of the 2.5 mm reference connector and optimized connector M_S5 is shown in Fig. 3.44. Therefore, the optimized model which is 15.7 % smaller shows a negligible increase in joule heating and small increase in total electrical resistance as compared to the reference model.

Table 3.15: Thermal-electric simulation results of 2.5 mm reference and optimized M_S5 connector

| **Model** | **Receptacle mass (g)** | **Current (A)** | **$\Delta T_{receptacle}$ (K)** | **$\Delta V_{connector}$ (mV)** | **$R_{connector}$ (µΩ)** |
|---|---|---|---|---|---|
| Reference | 1.21 | 30 | 40.38 | 0.3964 | 342.1 |
| M_S5 | 1.02 | 30 | 40.66 | 0.3091 | 357.2 |

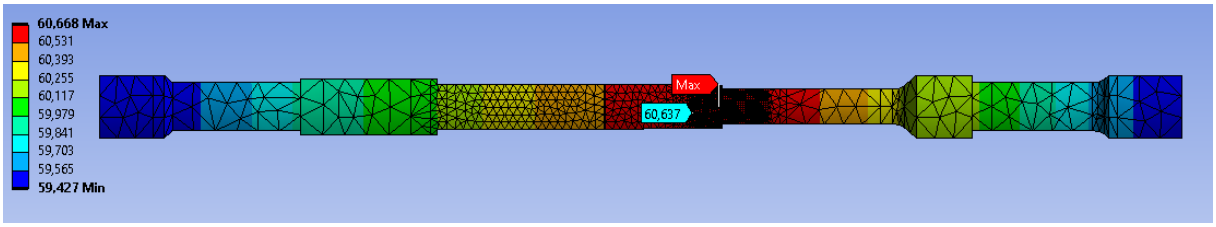


Fig. 3.43: Simulated temperature distribution across optimized 2.5 connector *M_S5* at 30 A

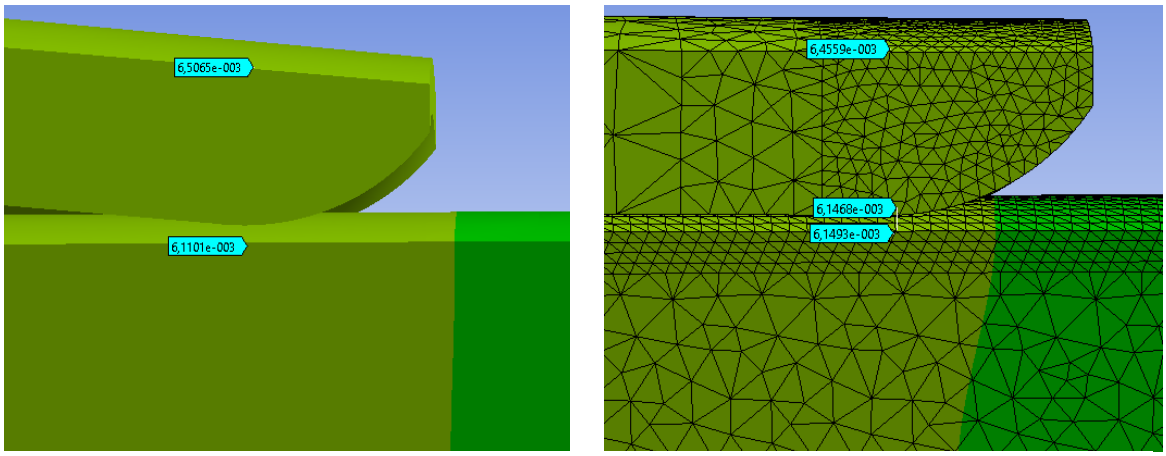


Fig. 3.44: Potential difference near contact region in 2.5 mm reference connector (left) and optimized *M_S5* connector (meshed, right)

### 3.3.3 Symmetry verification in thermal-electric simulation

The symmetry verification for validating the use of single spring segment for thermal-electric performance of connector is performed using 13.6 mm reference connector. The current flow in the connector can be considered to be flowing across the parallel circuit. Therefore, the current input in the model is equal to the total current in the complete connector divided by eight. Also, the electrical resistance for single element i.e. $1/8^{th}$ of the connector, is calculated by dividing the voltage drop between connector ends with the input current. This resistance when divided by 8 gives the electric resistance of entire connector. The temperature rise in the connector is calculate by subtracting the maximum temperature on the surface of receptacle near contact zone by 20 °C. According to thermal-electric analogy, the temperature rise in the model is analogous to the voltage drop. The voltage drop across one segment of connector is equal to the voltage drop in the complete connector. Thus from the analogy, the temperature distribution in the complete connector is similar to the temperature distribution in the simulated segment. These assumptions have been validated from the symmetry verification by comparing the results of $1/8^{th}$ (single spring segment) and quarter ($1/4^{th}$ i.e. 2 spring segments) connector models respectively (Table 3.16). The figures of simulated joule heating and voltage drop in $1/8^{th}$ and quarter connector models are given in Appendix 4.

Table 3.16: Symmetry verification results

| **Model** | **Voltage (mV)** | **Current in A** | **Resistance in model (mΩ)** | **Resistance in connector (8 elements) in mΩ** | **Max. Temperature in °C** |
|---|---|---|---|---|---|
| Quarter | 2.5921 | 10 | 0.25921 | 0.0648 | 20.108 |
| One-eighth | 2.5921 | 5 | 0.51842 | 0.0648 | 20.108 |

### 3.3.4 Summary of thermal-electric performance analysis

The proposed coupled structural-thermal-electric simulation model gives a precise prediction of the joule heating and electrical resistance in 13.6 mm as well as 2.5 mm reference connectors. The symmetry of the connector is exploited effectively using thermal-electrical analogy and the reliable results are obtained. The measured joule heating and electrical resistance are in good agreement with the simulation results. The 13.6 mm reference connector design has reached its optimal phase since the optimized connector yields relatively smaller reductions in the joule heating, electrical resistance and size. There is considerable scope of improvement in 2.5 mm connector as indicated by optimized model which results in significant improvement in connector volume with almost similar joule heating and total electrical resistance as compared to reference model. A considerable improvement is observed in the contact resistance near the contact zone in both the optimized connector models due to larger contact areas.

# 4 Real contact area – Influence of surface roughness and contact force

Some parts of this chapter have been published in the paper “Influence of surface roughness on contact behaviour” [203] in the proceedings of ‘9. Symposium Connectors – Elektrische und optische Verbindungstechnik, Lemgo, Germany 2023’.

## 4.1 Procedure of real contact area determination and validation

### 4.1.1 Sample preparation:

The sphere-plane contact combination is used in the analysis. The contact partners are punched from a 0.3 mm thick bronze sheet. The radius of spherical part is 4.5 mm and width of flat part is 3 mm as shown in Fig. 4.1 (a). The samples are coated with 0.8 µm gold layer by galvanizing process. Due to the inertness of gold, the real contact area can be considered as the electrically effective contact area. The coating thickness is measured using X-ray fluorescence spectroscopy (XRF) from Helmut Fischer GmbH. Before coating, the roughness of base material i.e. bronze is altered using silicon carbide grained polish papers in order to obtain coarse surface finishing. Grade P280 is used for rough surface finish while polishing is done using the polishing wheel with multifunctional Dremel 4000 tool. These processed samples are then used for galvanic coating process. Fig. 4.1 (b) shows the example of the flat sample with smooth and rough surface finishing. The roughness parameters of these samples are measured using 3D confocal microscope µsurf explorer from NanoFocus AG.

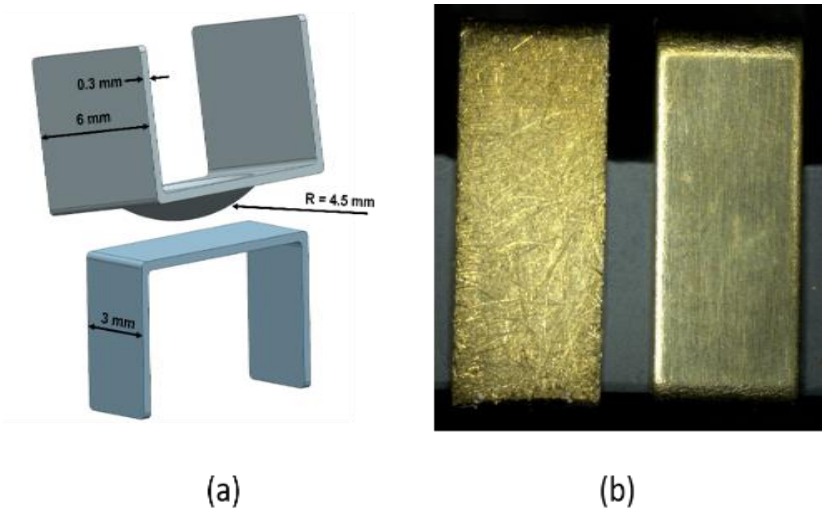


Fig. 4.1: (a) Contact geometry, (b) Rough sample (left) and Polished sample (right)

### 4.1.2 Roughness profile determination:

The surface roughness profile determination is important in order to simplify the surface roughness for simulation purpose. The surface profile is determined with the procedure similar to the one described in [18]. The core roughness $R_K$ and average groove width $R_{SM}$ are the roughness parameters described in DIN EN ISO 4287 which are used to model the surface roughness in this work. Their values are obtained directly from the 3D confocal microscope µsurf explorer from NanoFocus AG. The roughness of a surface can be assumed to be constituted from number of groove shaped structures. The average groove width $R_{SM}$ is obtained by averaging the individual groove widths $X_{Si}$ over the sampling length $l_r$ as shown in Fig. 4.2 [204]:

$$R_{SM} = \frac{1}{n}\sum_{i=1}^{n} X_{Si} \tag{4.1}$$

where $X_{Si}$ is the individual width of groove $i$ = 1,2,3…$n$.

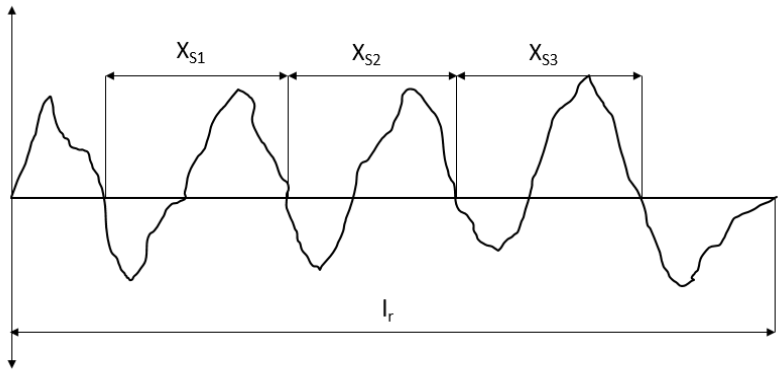


Fig. 4.2: Average groove width ($R_{SM}$)

The bearing area curve also known as Abbott-Firestone curve, is defined by the surface roughness parameters such as core roughness $R_K$, reduced peak height $R_{PK}$ and reduced valley depth $R_{VK}$ [204]. The method of derivation of these roughness parameters is described in Appendix 6. The core roughness $R_K$ is the main parameter for bearing the load since the peaks of the roughness asperities are usually demolished in the initial phase of the contact and the valleys of the roughness are not involved in bearing the load. It is to be noted that for a given bearing area curve, the core roughness $R_K$ is a variable quantity and depends on the selection of the material ratio interval of the surface roughness. The material ratios are selected based on the application. Since this work focuses on the surface roughness deformation for different loads, higher material ratio i.e. 90 % is selected by cutting the bearing area curve at 5 % and 95 % material ratios which is similar to the case in [18]. In this way, it is considered that the

peaks and valleys constitute material ratio of only 5 % each. The bearing area curve of one such flat contacts used in this work is shown in Fig. 4.3. It has a $R_K$ of 4.3 µm

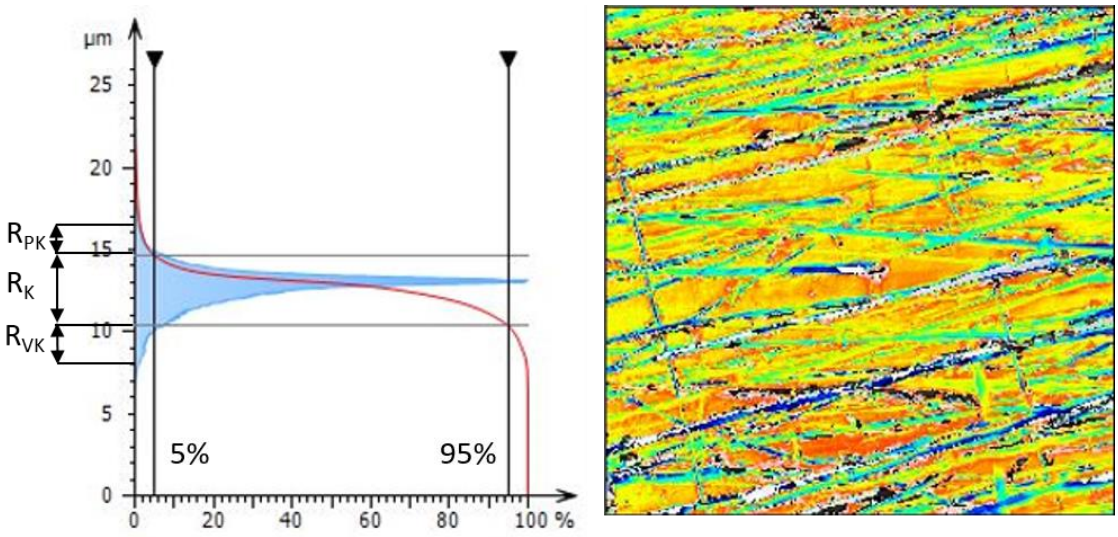


Fig. 4.3: Bearing area curve (left), surface topography image from confocal microscopy

The average values of $R_K$ and $R_{SM}$ used for modelling rough and polished surfaces are shown in Table 4.1. Also, the corresponding reduced peak height $R_{PK}$, reduced valley depth $R_{VK}$, average roughness $R_a$ and mean roughness depth $R_z$ values are given.

Table 4.1: Roughness parameters and values measured for polished and rough surfaces

| **Surface** | **Polished (µm)** | | | **Rough (µm)** | | |
|---|---|---|---|---|---|---|
| **Roughness parameter** | **Average** | **Min** | **Max** | **Average** | **Min** | **Max** |
| $R_a$ | 0.023 | 0.01 | 0.034 | 0.31 | 0.21 | 0.40 |
| $R_z$ | 0.10 | 0.084 | 0.115 | 1.39 | 0.97 | 1.72 |
| $R_K$ | 0.80 | 0.70 | 1.05 | 4.50 | 2.80 | 5.20 |
| $R_{PK}$ | 0.10 | 0.07 | 0.15 | 0.9 | 0.70 | 1.15 |
| $R_{VK}$ | 0.13 | 0.11 | 0.16 | 1.53 | 1.26 | 1.80 |
| $R_{SM}$ | 12 | 11.2 | 14.1 | 20 | 17.7 | 24 |

It is to be noted that in order to eliminate the effect of extreme tips of surface asperities peak having extremely small cross sections and playing no role in carrying the load since they get eliminated under very small load such as in the range of few millinewtons, material ratio of 3 % under bearing area curve is considered to measure $R_{PK}$. This is important for logical comparison of the actual surface roughness of rough and polished surfaces with contact surface deformation obtained from simulation which uses only core roughness $R_K$ effect under relatively higher contact forces in the range of 1 N to 5 N.

### 4.1.3 Contact resistance under normal load

The prepared samples are then subjected to continuously increasing contact force and the contact resistance is measured. The test set up to measure the contact resistance as a function of contact force is shown in Fig. 4.4. The flat part is clamped to the fixed lower contact holder and sphere part is clamped on the upper contact holder forming sphere on flat contact combination. The contact force is applied gradually through downward displacement of the upper clamp at 0.5 µm/s by using stepper motor from Nanotec Electronic GmbH & Co.KG. The contact force applied is in the range of 0 N to 5 N. After the 5 N force is reached, the displacement direction is reversed and the contacting partners are separated. The contact resistance is simultaneously measured along with the contact force using four-point resistance measurement method with a current input of 10 mA.

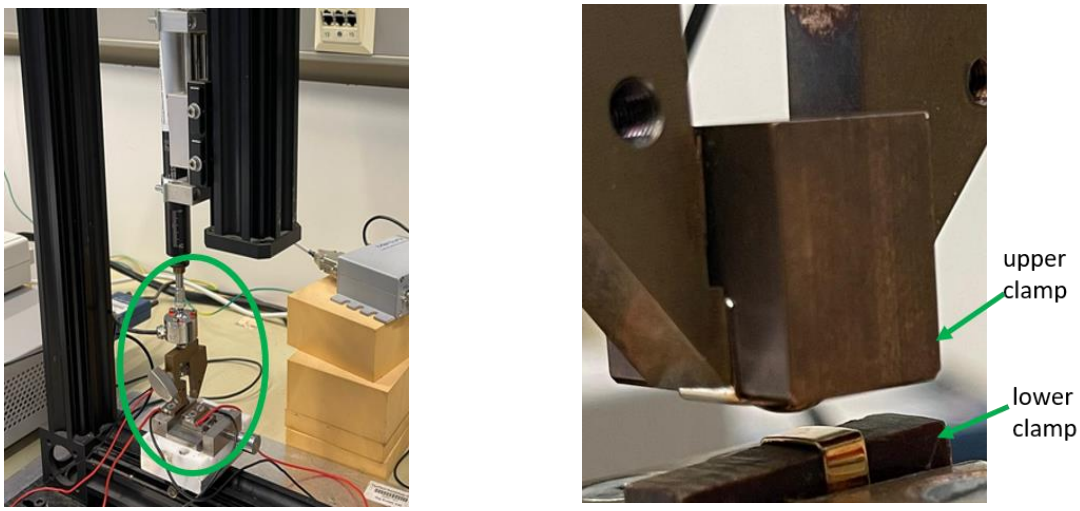


Fig. 4.4: Apparatus for contact resistance and force measurement (left), magnified image of clamp for contact mounting (right)

### 4.1.4 Finite element simulation model

The contact deformation under normal contact load is simulated using Abaqus/CAE finite element analysis software and the real contact area of given roughness under the given load is the obtained as an output. The simulation model is based on the model proposed in [18] for determination of the surface wear in silver coated electrical contacts. The following simplifications are done to the roughness profile:

- The surface roughness is modeled as triangular shaped rib structures based on the slope of the bearing area curve, Fig. 4.3 and [18].
- The spherical surface is modeled as smooth surface
- The rough profile is created on the top of flat surface where the contact occurs.

An example of the sphere-flat assembly model with meshing used for simulation of contact deformation is shown in Fig. 4.5. Taking the symmetry of the geometry into consideration, the quarter model is used for simulation in order to improve computational efficiency and results by using smaller mesh sizes. The meshing is performed using C3D8R 8 node linear brick element with reduced integration and hourglass control. The geometry is partitioned enabling the use of finer element sizes in the contact zone and comparatively larger elements in the redundant regions. The mesh size of 0.3 µm is used in the contact zone.

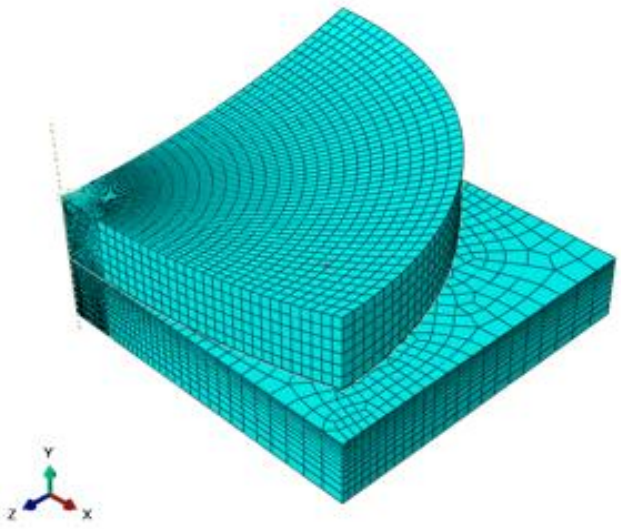


Fig. 4.5: Sphere-flat contact model for simulation

The base material is 0.3 mm thick bronze in both sphere and flat parts. On the base material, 0.8µm thick gold layer is constructed using electroplating process. The material behavior used is ideal elastic-plastic. The material properties of bronze and gold are shown in Table 4.2 [205] [206] [207].

Table 4.2: Material properties of bronze and gold [205] [206] [207]

| **Material Property:** | **Bronze** | **Gold** |
|---|---|---|
| Young's modulus (GPa) | 118 | 77.2 |
| Poisson's ratio | 0.34 | 0.42 |
| Density (g/cm³) | 8.85 | 19.32 |

The roughness on the gold surface in flat part is modelled in the form of triangular ribs with height equal to core roughness $R_K$ and width equal to average groove width $R_{SM}$ as illustrated in Fig. 4.6.

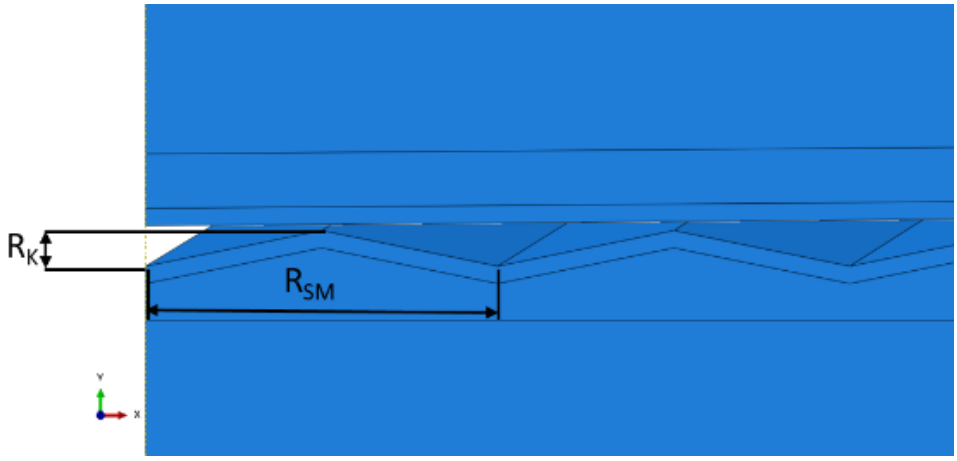


Fig. 4.6: Roughness profile modelled based on $R_k$ and $R_{SM}$

The boundary conditions applied in the model are shown in Fig. 4.7. The lower surface of the flat part is fixed. The symmetrical surfaces are assigned respective symmetry constraints. The upper surface of the sphere is kinetically coupled to the reference point *RP-1* defined on the tip of the vertical edge of sphere portion. The force is applied on the reference point along the negative Y direction. Since the quarter model is used, one fourth of the actual contact force is defined as an input. For example, to simulate the effect of 1 N contact force, a force of 0.25 N is defined as force input. The simulations are performed for three levels of contact force viz. 1 N, 3 N and 5 N.

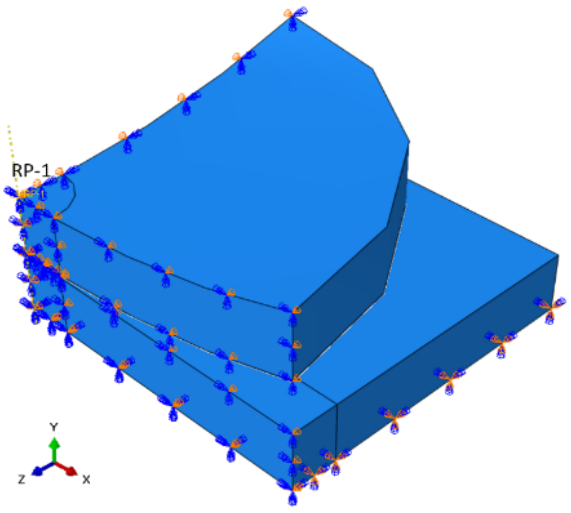


Fig. 4.7: Boundary conditions applied in simulation

The contact behavior is defined using tangential and normal contact behaviors. The contact interaction type is defined as general explicit contact with included surface pairs as 'all with self'. The spherical contact surface is defined as first surface and the upper gold surface of the flat part with roughness is defined as second surface. The simulation type used is explicit dynamic. The total area in contact '*CAREA*' is defined for the upper rough surface domain in

history output request section which gives the real contact of the surface at the end of the simulation.

## 4.2 Results of influence of contact force and surface roughness on real contact area

### 4.2.1 Contact resistance from experiment

Fig. 4.8 shows the measured contact resistance development in the rough and polished surfaces of contacts with gold coating. It can be seen that the rough surface has higher electrical resistance in comparison to the polished surface which is as expected due to relatively smaller real contact area resulting from bigger roughness asperities in rough surfaces. Initially, at the smaller contact forces, the contact resistance difference between polished and rough contacts is considerable. As the contact force increases, the contact resistance curves start to converge. In rough surface, approximately from the force of 4 N onwards, the reduction in the contact resistance decreases greatly and the contact resistance approaches stability. Similarly, the contact resistance in polished surface almost stabilizes after 2 N force. The spread of confidence interval at 95 % confidence level of measured contact resistance from the force of 1 N onwards is very small in polished contact. In rough contacts, the spread is initially considerably larger and decreases with increasing force. From the force of 2 N onwards, the spread of measured resistance stabilizes.

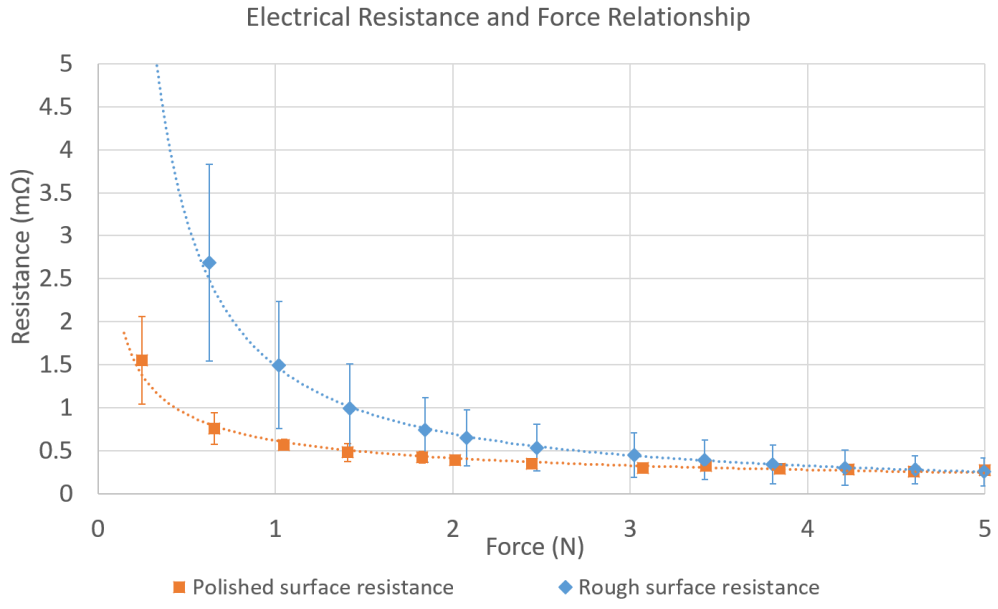


Fig. 4.8: Measured contact resistance development with force in rough and polished contacts

### 4.2.2 Simulated contact area

Fig. 4.9 shows an example of the simulated rough surface deformation. The simulations are performed with ideal elastic plastic material properties. The results of the contact areas of the rough and polished surfaces obtained from simulation are compared with the nominal contact area calculated for smooth sphere-plane combination with gold using Hertz contact theory with elastic material properties.

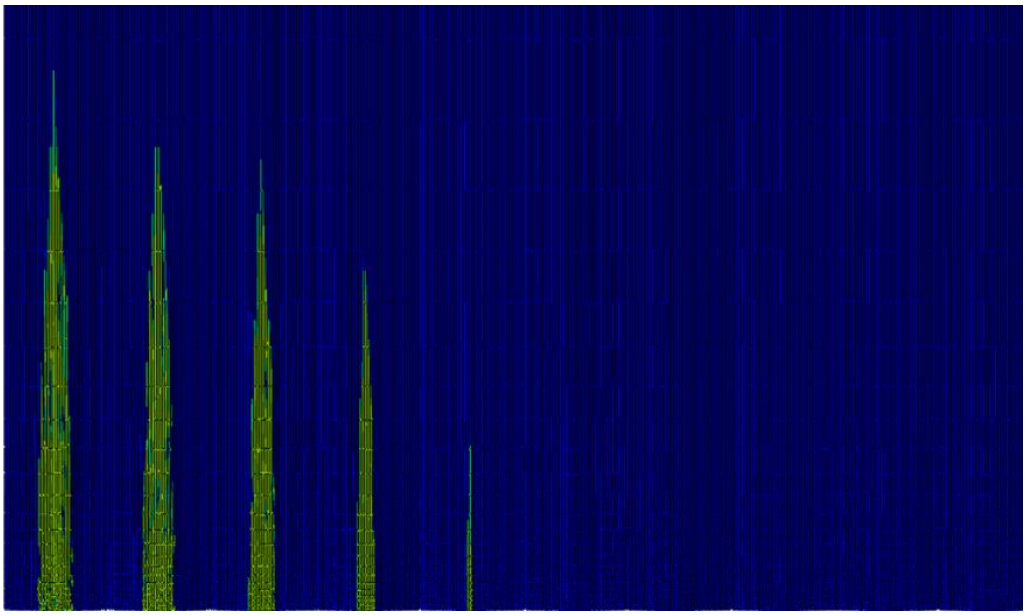

Fig. 4.9: Real contact area formed by rough surface deformation in simulation

Fig. 4.10 shows the relationship between the ratio of real contact area to nominal contact area and the contact force. In the rough surface, real contact area is considerably smaller in comparison to the polished surface. The ratio of real to nominal contact area in the rough surface increases from 0.34 to 0.47 for the corresponding rise in contact force from 1 N to 5 N. On the other hand, this ratio increases from 0.48 to 0.61 in case of polished surface. Thus, the real contact area in relatively smooth surfaces is closer to the nominal contact area for the given contact force.

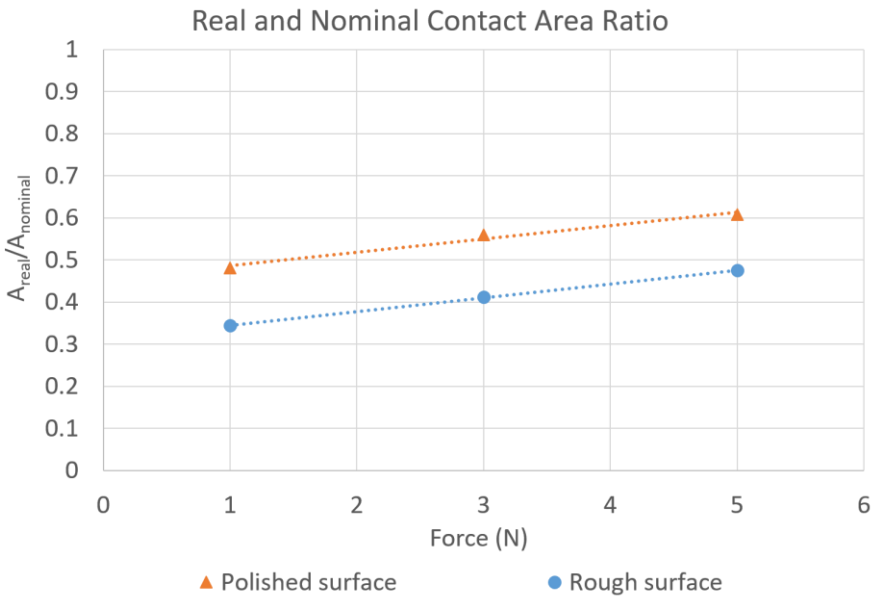


Fig. 4.10: Real (from simulation) and nominal contact area (from Hertz contact) ratio development with force

### 4.2.3 Contact resistance and contact area correlation

In order to verify the simulation results of estimated real contact area using simplified roughness profile, the contact resistance is calculated using Holm's equation for circular constriction resistance as given by equation (2.12) with the electrical resistivity of gold equal to 2.4E- 08 Ω - m. The real contact area obtained from the deformation of the triangular rib shaped roughness profiles in simulation $A_{real}$ is equated to the circular area and the effective contact radius $a$ is calculated as:

$$a = \sqrt{A_{real}/\pi} \tag{4.2}$$

Fig. 4.11 shows the values of measured contact resistance, effective contact radius and calculated contact resistance using effective contact radius values with respect to contact force. It can be seen that the contact radius rises according to power law within the simulated force range of 1 N to 5 N whereas the contact resistance decreases as per power law with the increasing force. The inverse relationship between contact resistance and effective contact radius calculated form real contact area is clearly visible. The calculated contact resistance in contact with polished surface is in good agreement with the measured contact resistance values. In the contact with rough surface, the calculated contact resistance values for 3 N and 5 N force lie within the confidence interval of measured contact resistance values and are in good agreement with the measured values. However, at the contact force of 1 N, the calculated

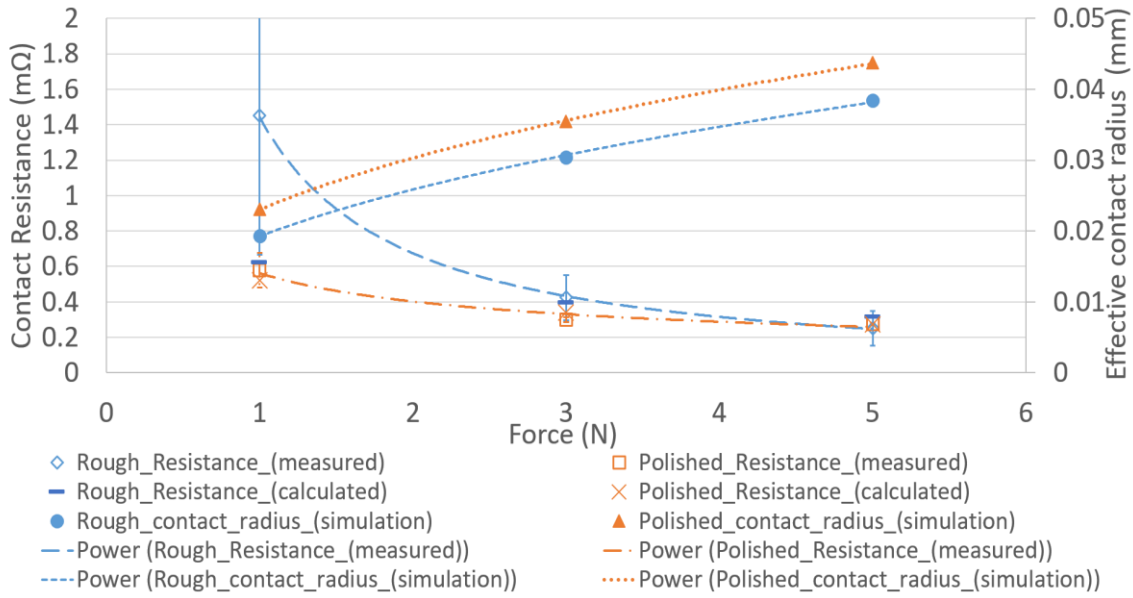


Fig. 4.11: Electrical resistance and contact area development as a function of force

contact resistance value is 0.62 mΩ which is approximately 6 % below the lower limit of confidence interval of measured resistance of 0.66 mΩ.

The reason for this variation in measured and calculated resistance can be understood from Fig. 4.12. The surface topography of the polished surface shows far fewer asperities and also the maximum height of the asperities, approximately around 0.8 µm, is considerably smaller in comparison to the maximum height of asperities in rough surface which is approximately between 4 µm and 4.5 µm for the surface roughness of the sample shown in Fig. 4.12. Also, the randomness in the height distribution of asperities across the measured surface is high in rough surface which can be seen from the presence of greenish colored zones having smaller heights around 2 µm in between reddish colored zones with asperity heights around 4 µm representing bigger asperities. Against this, the height distribution of surface asperities is more uniform in smooth surface as can be seen from continuous patches of same color. Also, the difference in the heights between the higher reddish colored asperities with heights around 0.8 µm and the medium ranged greenish colored asperities with heights around 0.4 µm is considerably smaller in comparison to the rough surface. Due to such a phenomenon, there exists a possibility that the actual rough surface deformation at 1 N force results in a smaller real contact area as the large number of asperities hold the load by undergoing smaller deformation in comparison to the deformation of the simplified roughness profile applied in simulation. Only after the load greater than 1 N, the asperities in actual rough surface deform adequately and give results in agreement with the simulated values. This can be validated from the comparison of the respective contact surface displacements i.e. asperity deformation of the rough and polished surfaces obtained from the simulation given in Table 4.3 with their reduced peak height $R_{PK}$ values given in Table 4.1.

Table 4.3: Simulated surface asperity deformation in polished and rough surface

| **Force (N)** | **Contact surface deformation (µm)** | |
|---|---|---|
| | **Polished** | **Rough** |
| 1 | 0.58 | 1.05 |
| 3 | 0.78 | 1.4 |
| 5 | 0.9 | 1.65 |

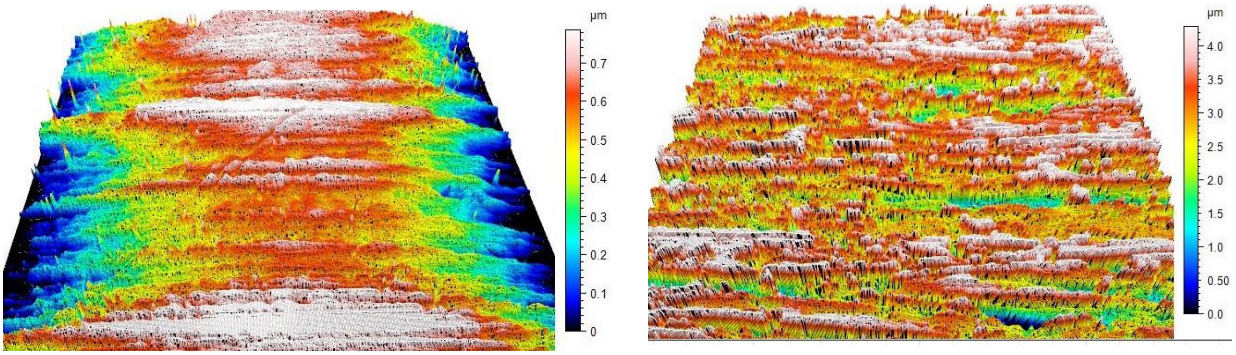


Fig. 4.12: Surface topography images from confocal microscopy: polished surface (left) and rough surface (right)

The $R_{PK}$ values for the polished and rough surfaces are 0.1 µm and 0.9 µm respectively as given in Table 4.1. It can be seen that the contact surface displacement in polished surface is considerably greater than the $R_{PK}$ value even at the smallest simulated force of 1 N indicating that the peaks of surface asperities have very less influence and core roughness $R_K$ is effectively carrying the load as is the case in simulation also. However, in the rough surface, maximum contact displacement at 1 N force is 1.05 µm which is close to the measured reduced peak height $R_{PK}$ of 0.9 µm. This suggests that the majority of the applied force of 1 N is consumed for the deformation of the peak of surface asperities and the contribution of core roughness $R_K$ is smaller in bearing the load. Therefore, in actual surface deformation, the smaller effective contact area could be formed majorly by the deformation of material represented by reduced peak height $R_{PK}$ resulting in higher measured contact resistance at 1 N force without or with very small portion of the core roughness coming into play. Against this, the contact area in simulation is obtained by the deformation of core roughness $R_K$ resulting in larger contact area and hence smaller contact resistance at 1 N force. However, at larger forces of 3 N and 5 N, the closer measured and calculated values of contact resistance suggest minimal influence of peak of surface asperities in rough surfaces.

### 4.2.4 Summary of the surface roughness influence on electrical contact resistance

The electrical resistance and force relationship as a function of rough and polished contact zones in bronze contacts with gold coating is determined both experimentally and with simulation. The sphere on flat contact geometry combination is used in this work. A significant influence of surface roughness can be observed both in experiments and numerical simulation at low contact force. This influence declines markedly with the increasing contact force.

The simulations are performed to obtain real contact area through surface roughness deformation of flat part under different contact forces. The measured and calculated contact resistances are found to be in good agreement at all simulated contact forces in contacts with polished surface. In the contacts with rough surface, the calculated contact resistance at force of 3 N and 5 N is closer to the respective measured values. At lower force of 1 N, the calculated contact resistance is slightly outside the confidence interval bounds of measured contact resistance which can be due to the difference in the deformation of simplified roughness profile in simulation and the actual deformation occurring in presence of bigger roughness peaks. The simulation at low contact force can be further improved by using a more precise selection of material ratio in bearing area curve to model surface roughness.

# 5 State of health and reliability prognosis

Some parts of this chapter have been published in the papers “State of Health of Connectors – Early Indicators” [208] in the proceedings of ‘IEEE 67th Holm Conference on Electrical Contacts (HLM), 2022’ and ‘Prediction of failure in time (FIT) of electrical connectors with short term tests’ [5] in journal of Microelectronics Reliability, Vol. 138, 2022.

## 5.1 Procedure of state of health and reliability prognosis

### 5.1.1 Accelerated life test and data

5.1.1.1 Connector samples and materials

The data of more than 80 lifetime test results corresponding to different acceleration levels and more than 20 different connector types and approximately 4000 contacts forms the basis of this study. As this study aims at development of a general statistical procedure for the reliability prognosis using the initial part of the test data applicable to all kinds of electrical connectors irrespective of their design and loading conditions, the design details of the connectors are not discussed here. The applicability of the proposed approach across different connector designs and acceleration levels in this study has been illustrated using 5 different connectors named as Connector T1, Connector T2, Connector T3, Connector T4 and Connector T5. The data has been selected such that it consists of the connectors having low reliability where all the contacts fail during test, medium reliability where some parts of the tested contacts fail and high reliability where no failure occurs during complete test duration. In this way, the validity of the proposed approach for different reliability levels can be proven.

5.1.1.2 Accelerated life time test procedure

The connectors in this study are subjected to cyclic thermal stresses in laboratory conditions in accordance to EN 60068-2-14 test standards [62]. Two levels of temperature are used in any given test. The lower temperature limit is -40 °C in all the tests whereas the upper limit is either of 140 °C, 150 °C or 160 °C based on the intended acceleration level for the given test. The temperature transition between the upper and lower temperature limits is gradual with ramp up and ramp down duration of 2 h. The temperature is held constant at upper and lower limits for 3 h each. In this way the duration of one cycle is equal to 10 h.

A total of 48 to 50 contacts of each connector type are mounted on a test board and placed in the temperature chamber. Such a sample size is adequate for analysis since smaller sample size could reduce the accuracy of prognosis whereas the bigger sample size could increase the cost and effort [60].

The contact resistance of each contact is measured using the four-point method using a Keithley 3706 A Switch system/Multimeter. The current input to the contacts is 10 mA. Three contact resistance readings at the interval of 20 s each are recorded at 2/3rd of the dwell period at upper and lower temperature limits of each cycle. Since the individual cycle duration is 10 h, three readings every 10 h are recorded at the given constant temperature phase of thermal cycle. In this way, at each temperature extremes of a given cycle, 150 contact resistance readings are available for the set of 50 contacts in a connector at the given point of time during the test.

#### 5.1.1.3 Failure criteria and termination of test

The electrical resistance is the criterion for measuring the connector degradation. The electrical resistance of a contact rises very fast after its collapse [65]. Based on the design or the field of application, the failure criteria could vary. There are different failure criteria defined in different standards for electrical connectors [62] [209]. In this work, the failure criteria defined is 300 mΩ in accordance with [62]. Therefore, the contact is termed as failed when the first reading of contact resistance $\geq$ 300 mΩ is recorded. Once the given contact in a connector fails, it is bypassed and the resistance of that contact is further not recorded.

The criteria for the termination of tests is not defined, given the fact that the contact failure is highly random even for the same type of connector and acceleration level. In practice, for the reliable prediction of the CLT with the Weibull distribution, which corresponds to the time to 63.2 % of contacts failures, there should be an adequate number of failures occurring during the test. From the number of previous in-house reliability analysis of electrical connectors, it has been observed that for the reliable estimation of the CLT using the Weibull distribution, the time to failure data of 10 % to 20 % failed contacts is needed. The connectors with lower reliability have large number of failures in shorter duration of time. On the other hand, the connectors with high reliability need a longer test duration for adequate number of failures to take place. Also, the failures depend on the acceleration level of the test [58] [210]. The tests are conducted until at least 30 % to 50 % contact failures occur and the failure time data is plotted in order to determine the CLT through extrapolation using the Weibull probability plot with the procedure defined in [61] [211]. An example of one such CLT estimation using the Weibull probability plot is shown in Appendix 5. The Weibull FIT rate is then determined using the procedure defined in section 2.7.3.2. For the connectors with very high reliability or low acceleration levels, no failure or very small number of failures might occur even after running the tests for couple of years. In such cases, the tests are terminated without failures and the reliability is predicted using Chi-square distribution as discussed in section 2.7.3.3. In this work, the failure data collected from the tests mainly corresponds to type 1 censoring where the tests

are run for the specific duration and the time to failure data of failed contacts is recorded [212, p. 467]. In the case of connectors with low reliability, complete data of time to failure of all the contacts is obtained as such contacts mostly fail completely or undergo a very large number of failures before the predetermined test duration.

### 5.1.2 Prognosis Method

It is to be noted that the time data used for representation of the results in this study is scaled from the runtime in test to equivalent runtime in field with operating temperature range of 20 °C to 80 °C using Norris-Landsberg model given in section 2.7.2.3.

#### 5.1.2.1 Contact degradation and surge point

The mean ($\mu$) and standard deviation ($\sigma$) of the contact resistance of 48 to 50 samples of contacts of a given connector type recorded at each measurement time during the thermal cycling tests is calculated. In the initial phase of the test when the connectors are in healthy state, the contact resistance of all the contacts and hence the mean contact resistance is expected to remain stable. Also the standard deviation of the measured contact resistance is expected to be negligible. The mean contact resistance and the standard deviation should increase as contacts degrade with the test progression. In this work, for initial analysis, four sigma level is used as a measure of the scatter of electrical resistance from the mean using the following formula:

$$R_{upper\_spread}(t)=\mu(t)+2\cdot\sigma(t) \tag{5.1}$$

where $R_{upper\_spread}(t)$ is the upper spread from the mean of electrical resistance at time $t$, $\mu(t)$ is mean of the contact resistance of all samples measured at time $t$ and $\sigma(t)$ is the standard deviation of the mean of contact resistance of all samples measured at time $t$.

From a technical point of view, the spread of contact resistances scattered above the mean value are of interest, since these lead to faster failure and represent the worst case. Hence, only the scatter above the mean values i.e. the upper spread is taken into account. The standard normal variate of 2 representing 4 sigma level is used since the interval $\mu(t)+2\cdot\sigma(t)$ describes 95.44 % of the observations under any normal distribution [182, p. 37]. It is to be noted that the possibility of the analysis with an upper spread using 6 sigma, i.e. $\mu(t)+3\cdot\sigma(t)$ was tried as well. However, it did not yield effective results and hence was not considered further.

The graph of the mean contact resistance, upper spread and number of contact failures against the time is plotted is shown in Fig. 5.1. The mean and upper spread of contact resistance are shown by blue and orange colored points respectively. The number of contact failures are highlighted in red. As expected, the mean and the upper spread of the contact resistance values are stable and almost overlap during the initial phase of the test when the contacts are in healthy

condition. After a certain time, the mean and upper spread start rising suddenly and the contact failures also start to occur. As seen from the figure, there exists a certain time period during the test when the mean and scatter of contact resistance suddenly surges. This point is termed as a surge point in this study.

The upper spread of contact resistance rises from few milliohms before the surge point to higher magnitudes of resistance values after the surge point. The surge point thus indicates the first anomaly in the connector system and indicates the upcoming contact failures in near future. The surge point is usually followed by the first failure. From Fig. 5.1, it can be seen that the time to surge point for the given connector is around 930 days from the commencement of operation. Fig. 5.2 shows the magnified image of the contact resistance development around the surge point indicated in Fig. 5.1. It can be observed that the upper spread of contact resistance at surge is around 75 mΩ which is one-fourth of the failure criterion of 300 mΩ. Since the contact resistance after a certain degree of degradation rises suddenly, it can be observed that the first failure in the given connector in Fig. 5.1 occurs around the 1148$^{th}$ day.

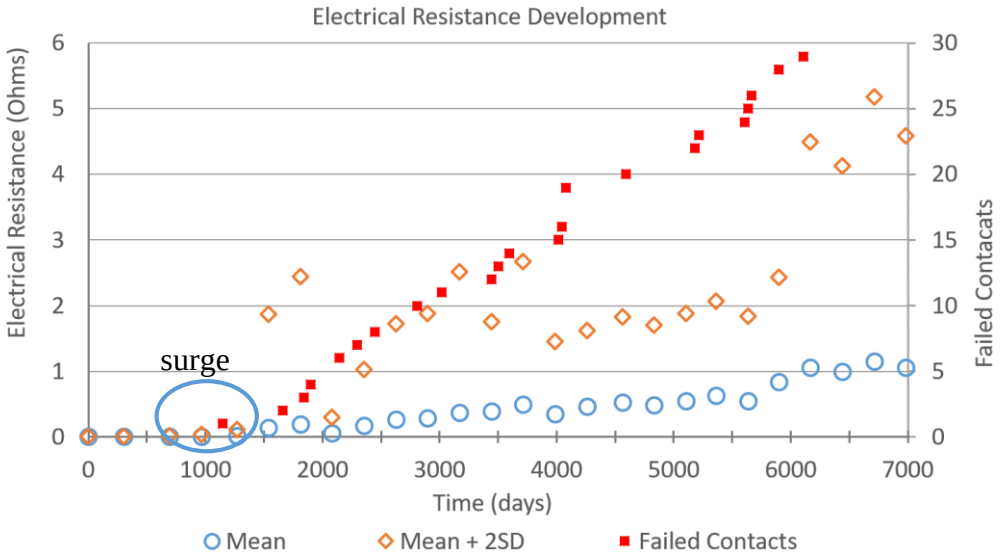


Fig. 5.1: Contact resistance and failure development

In this work, the data recorded up to the surge point, i.e. shortly before the occurrence of the first failure, forms the basis of statistical procedure for forecasting the connector performance in the longer run. Also, time to surge is used as a state of health indicator of the connector in this work. The connectors having higher reliability are expected to have longer time to surge in comparison to the connectors with lower reliability. In highly reliable connector designs, the contact resistance can be expected to remain stable throughout the test without occurrence of remarkable surge in the resistance.

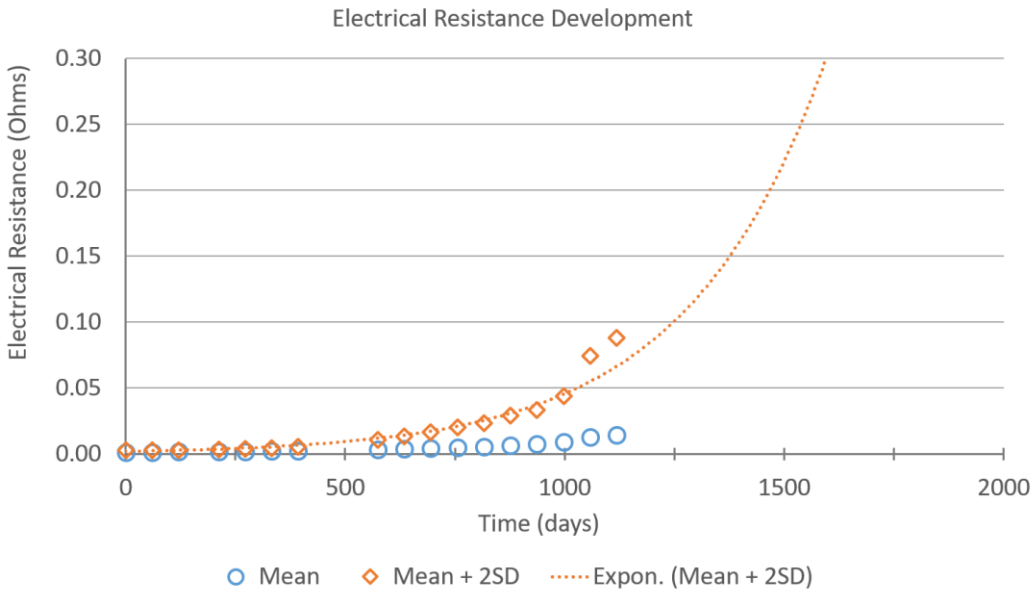


Fig. 5.2: Surge and contact resistance development

### 5.1.2.2 Extrapolation of degradation path

The $R_{upper\_spread}$ values at the surge point are below the failure criterion of 300 mΩ since the contact has not completely failed by the time to surge as seen in Fig. 5.2. In order to determine the time to failure using the upper scatter $R_{upper\_spread}$, the $R_{upper\_spread}$ data from the time to surge is required to be extrapolated till the failure criteria of 300 mΩ since only the data till the surge point is used in the reliability prognosis procedure. It can been seen that the upper spread of contact resistance rises strongly after the surge.

In order to determine the equation for extrapolating the $R_{upper\_spread}$ up to the failure criterion, linear, polynomial and exponential curves are fitted to the $R_{upper\_spread}$ data until the surge point and extrapolated, and the best fit is determined through the coefficient of determination $R^2$. As seen in Fig. 5.3, with respect to $R^2$ values, the exponential function best fits the data, followed by the polynomial curve and linear curve, respectively. The contact resistance degradation paths in different studies also indicate similar trend where the resistance is stable in the initial phase of the test and rises almost exponentially in later phases [63] [65] [75]. Therefore, the degradation paths and hence the upper spread of contact resistance data are extrapolated using an exponential function for both the distribution based as well as percentiles based methods in this study in order to determine the time to failure.

### 5.1.2.3 Determination of quotient *q*

In this work, the quotient $q$ is introduced which serves as an indicator of the contact's degradation or state of health with respect to the test duration. It is defined as the ratio of the

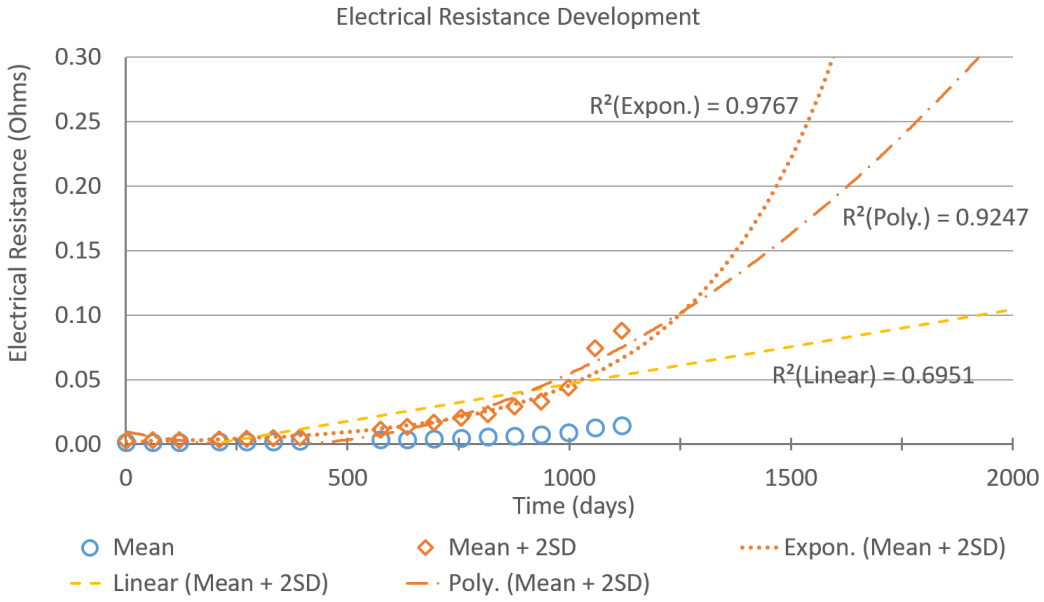


Fig. 5.3: Extrapolation of upper spread of resistance with different curve fittings

upper spread of contact resistance $R_{upper\_spread}$ at the given time to the mean contact resistance at the start of the test $\mu_{initial}$ and is given as:

$$q(t) = \frac{R_{upper\_spread}(t)}{\mu_{initial}} \tag{5.2}$$

Thus the initial contact resistance is used as a reference for measuring the extent of degradation. Since $\mu_{initial}$ is constant, $q$ is directly proportional to $R_{upper\_spread}$. The quotient $q$ can be determined at any given duration irrespective of the surge point. The value of the quotient $q$ shortly before the surge point is used as an indicator to compare the performance of different electrical connectors. It is used as a state of health indicator as the life of connectors progresses and is used to classify the connectors as highly stable, stable and unstable. The highly stable connectors have very high reliability followed by stable and unstable connectors respectively. The highly stable connectors will have smaller $q$ values and vice-versa. The analysis of different connectors have shown the $q$ value ranging from 4 to 50 shortly before respective surge points. The connectors undergoing no failures have shown to have $q < 2$. In this study, the CLT of different connectors is initially prognosed with respect to the $q$ value at the surge i.e. using the data until shortly before the occurrence of first failure. Further, in order to investigate the feasibility of lifetime prediction without the occurrence of first failure i.e. surge, the $q$ value is used as a basis for data selection. For this purpose, an additional analysis is conducted to investigate the influence on prognosis results obtained by using the data selected with respect to various $q$ values before the surge.

### 5.1.3 Characteristic lifetime and FIT rate determination

#### 5.1.3.1 Contact resistance and failure probabilities correlation

In order to determine the CLT of the connectors, the parametric and non-parametric procedures are applied and the results are compared with the measured CLT using the Weibull distribution. The parametric method is based on the standard normal distribution and generalized extreme value (GEV) distribution and applies mean and standard deviation of the contact resistance of the sample population for prognosis. On the other hand, the non-parametric method is a distribution free method based on the percentiles of the measured contact resistance of the sample population.

In electrical connectors, the variation in reliability is reflected by the variation in the degradation [75]. Considering this factor, the contact resistance development in connectors is correlated to the failure probabilities in this work as highlighted in Fig. 1.8 and Table 5.1. For example, the 90 percentiles of contact resistance represent 10 % failure probability which indicates that the $90^{th}$ to $100^{th}$ percentiles of the actual measured contact resistance in case of distribution free method and the 10 % area on the right side under the probability distribution curve correspond to 10 % failure probability. The $37^{th}$ percentile corresponds to the characteristic life time (CLT).

Table 5.1: Failure probabilities and contact resistance percentiles

| **Failure Probability** | **Contact Resistance Percentile** |
|---|---|
| 2% | 98 |
| 10% | 90 |
| 20% | 80 |
| 40% | 60 |
| 45% | 55 |
| CLT | 37 |

#### 5.1.3.2 Probability Distribution based prognosis method

For the CLT prognosis using parametric procedure, the upper spread of the contact resistance till the surge point is calculated using the standard score of the given distribution denoted by *c*, for the different failure probabilities viz. 2 %, 10 %, 20 %, 40 % and 45 % in this work. This upper spread of the contact resistance *S* corresponding to given failure probability *p* and time *t* is calculated as:

$$S(p,t)=\mu(t)+c\cdot\sigma(t) \tag{5.3}$$

For a probability distribution fitted to contact resistance data, the higher contact resistance values lying towards the upper tail represent the degradation and hence failed connectors. These *c* scores are obtained using the inverse of the standard normal distribution and the inverse of the negatively skewed GEV distribution function. The *c* score values for the normal and GEV distribution are given in Table 5.2.

Table 5.2: *c* sores for standard normal and GEV distribution

| **Failure probability (p)** | **Normal distribution** | **GEV distribution** |
|---|---|---|
| 2 % | 2.053 | 1.3641 |
| 10 % | 1.281 | 0.834 |
| 20 % | 0.841 | 0.4759 |
| 40 % | 0.253 | -0.0874 |
| 45 % | 0.125 | -0.225 |

As discussed in the section 2.7.4.2, the GEV distribution can be positively skewed as well as negatively skewed. The *c* scores in case of GEV distribution used in this study correspond to the negatively skewed generalized extreme value distribution with the shape and location parameter equal to 0 and scale parameter equal to 1 which is equivalent to the standard extreme value distribution having negative skewness. It is to be noted that other scores obtained using different shape parameter values of the generalized extreme value distribution were also tried for the prognosis of CLT, which however lead to very large deviations from the expected results. Hence their results are not discussed here.

For the prognosis using probability distributions, firstly, the *c* scores values are determined and the upper spread of resistance *S(p)* based on respective failure probability are calculated until the surge point using the equation (5.3). The *S(p)* data for respective failure probabilities is then plotted against the test duration and extrapolated until the failure criterion of 300 mΩ using the exponential function as discussed in section 5.1.2.2. Fig. 5.4 illustrates one such plot of upper spread of the contact resistance for 2 %, 10 %, 20 %, 40 % and 45 % failure probabilities plotted with respect to time and extrapolated up to the failure criterion of 300 mΩ.

The exponential function fitted to the upper spread of resistance for respective failure probability in terms of test time *t* is of the form:

$$S(t,p)=a \cdot e^{k \cdot t} \tag{5.4}$$

where, *S(t,p)* is the upper spread of contact resistance as a function of failure probability and test duration *t* and *a* and *k* are the coefficients of the exponential fit.

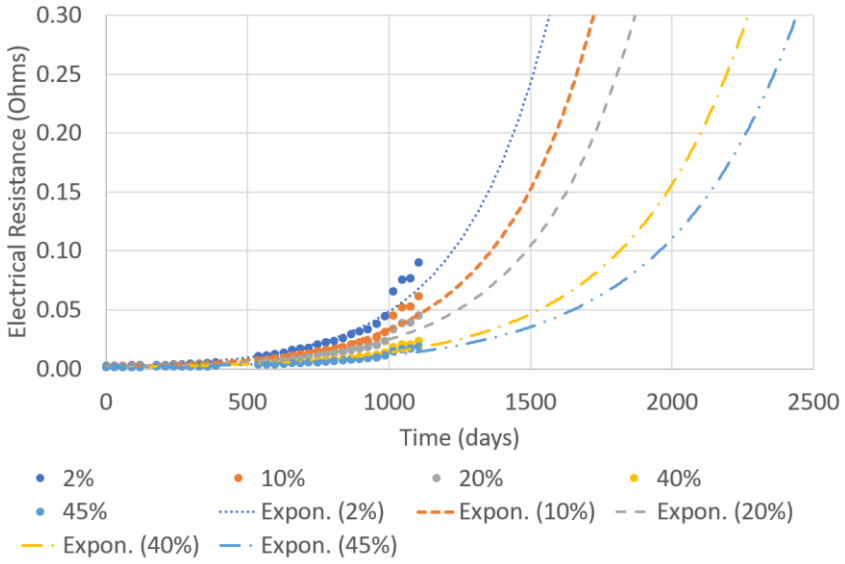


Fig. 5.4: Extrapolated contact resistance for failure probabilities with c-scores of distribution

The coefficient *k* can also be used as a state of health indicator. The connectors having extremely small values of *k* have longer time to failure and hence higher reliability and vice versa. In the equation of exponential function, when *S(t,p)* is replaced with failure criteria of contact $R_{failure}$, equal to 300 mΩ in this study, the time to failure of respective failure probability is calculated as:

$$t(R_{failure}, p) = \frac{1}{k} \cdot \ln(\frac{R_{failure}}{a}) \tag{5.5}$$

After the time to failure for 2 %, 10 %, 20 %, 40 % and 45 % failure probabilities is calculated using equation (5.5), the graph of failure probability against the logarithm of time to failure is plotted and logarithmically extrapolated up to the failure probability of 63.2 % in order to obtain the CLT as illustrated in Fig. 5.5, which is then used for calculating the FIT rate based on the Weibull distribution as discussed in section 2.7.3.2. The logarithmic function fitted to the failure probability against the logarithm of the test time is of the following form:

$$F(p,t) = m \cdot \ln(t) - n \tag{5.6}$$

where *F(p,t)* is the failure probability as a function of time *t* and *m* and *n* are the coefficients of logarithmic fit. By substituting *F(p,t)* = 63.2 %, the CLT is calculated by:

$$CLT = \exp(\frac{0.632 + n}{m}) \tag{5.7}$$

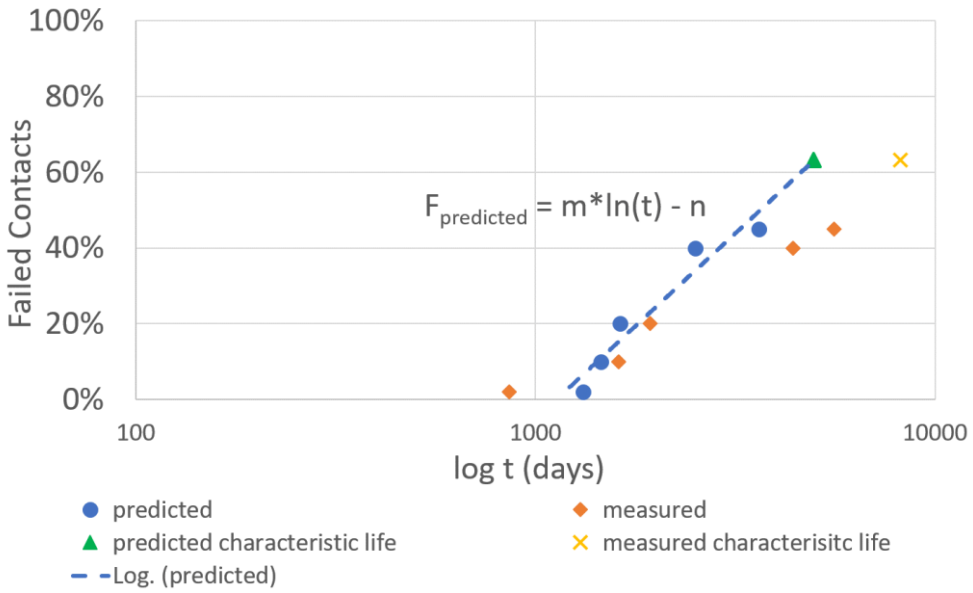


Fig. 5.5: Extrapolation of predicted time to failure data till CLT

5.1.3.3 Non-parametric precentiles based prognosis method

Similarly, for the distribution free method, the 98$^{th}$, 90$^{th}$, 80$^{th}$, 60$^{th}$ and 55$^{th}$ percentiles of the contact resistances, which correspond to the 2 %, 10 %, 20 %, 40 % and 45 % failure probabilities as shown in Table 5.1, are obtained at each measured data set of contact resistance until surge point using the quantile function in Matlab. Also, the data of contact resistance corresponding to 37$^{th}$ percentile which represents the CLT is calculated so as to check the possibility of direct estimation of lifetime. This is a distribution free method and does not apply mean, standard deviation and scores of a selected distribution as in the case of the prognosis using probability distributions. However, the procedure of CLT prognosis using the non-parametric procedure is identical to that of the parametric procedure with the only difference being that the upper spread of the contact resistance *S(p)* for respective failure probability at each measurement time calculated using equation (5.3) is replaced with the percentiles of measured contact resistance corresponding to the respective failure probability.

The extrapolation of the respective percentiles of contact resistance till the failure criteria is done using an exponential fit as shown Fig. 5.6 and the time to failure for a given failure probability is calculated using equation (5.5). After the time to failure for 2 %, 10 %, 20 %, 40 % and 45 % failure probabilities is determined, the graph of failure probabilities is plotted against the logarithmic scale of the test duration similar to that shown in Fig. 5.5. The predicted time to failure is then extrapolated to the 63.2 % failure probability to determine CLT. It was observed that the linear extrapolation yielded a better CLT prediction in comparison to the logarithmic extrapolation used in the distribution based procedure. The linear function fitted to the failure probability against the test time is of the following form:

$$F(p,t) = x \cdot \mathrm{t} - y \tag{5.8}$$

By substituting *F(p, t)* with 63.2 %, the CLT is calculated as:

$$CLT = \frac{0.632 + y}{x} \tag{5.9}$$

The CLT calculation method by linearly extrapolating the failure probabilities in this way is denoted as the indirect method in this work. On the other hand, the CLT calculation method through the exponential extrapolation of the 37$^{th}$ percentile of contact resistance using equation (5.5) is denoted as direct method. Also, the FIT rates based on Weibull are calculated after the CLT determination as discussed in section 2.7.3.2.

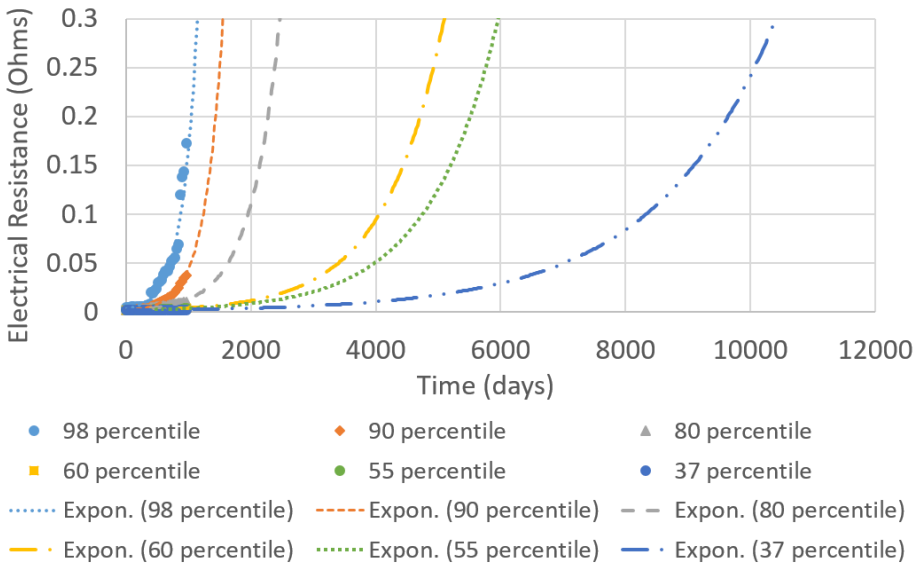


Fig. 5.6: Extrapolated contact resistance for failure probabilities with percentiles

## 5.2 Results of state of health and reliability prognosis

Some parts of this chapter have been published in the papers “State of Health of Connectors – Early Indicators” [208] in the proceedings of ‘IEEE 67th Holm Conference on Electrical Contacts (HLM), 2022’ and ‘Prediction of failure in time (FIT) of electrical connectors with short term tests’ [5] in journal of Microelectronics Reliability, Vol. 138, 2022

### 5.2.1 Variations in contact resistance distribution with time

For the extrapolatory data analysis, distribution fittings are done to the contact resistance data set with respect to time. As the contact resistance increases with degradation, the distribution of the resistance data is also expected to change. One such example of connector T4 is highlighted in Fig. 5.7. It can be seen that on day 1, the standard normal, generalized extreme value (GEV) and inverse Gaussian distributions provide a good fit to the measured contact resistance data. Also, the data appears to be normally distributed and the maximum resistance is around 1.6 mΩ. With increasing time, the connectors degrade to varying extents and degradation in some of the connectors is very high in comparison to others. It can be seen on day 20, the some of the contacts are heavily degraded in comparison to others and the maximum measured resistance is around 30 mΩ. However, the maximum contact resistance corresponding to around 0.98 cumulative probability is around 5 mΩ with only one connector recording the resistance of 30 mΩ. This connector acts as an outlier and affects the distribution fitting and also represents the upcoming failure. Under such circumstances, the GEV distribution provides a better fitting as it properly predicts the outlier amongst the tested distributions.

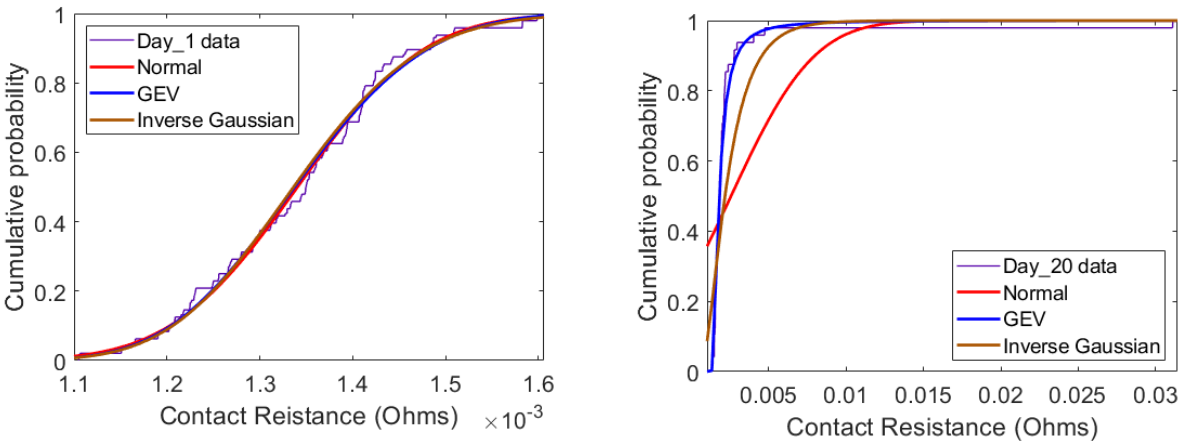


Fig. 5.7: CDF plots comparing different distributions fitted to contact resistance data after day 1(left) and day 20 (right) in connector T4

The quality of the distribution fitting is determined using the log likelihood and the Kolmogorov Smirnov (KS) goodness-of-fit test as shown in Table 5.3. Analogous to connector T4, the distribution fitting results of the second connector T2 have been also highlighted. The significance level of 5 % is used. For a given distribution, a *p* value greater than 0.05 means the data can be modelled more precisely using that distribution. It can be seen that on day 1, all the tested distributions fit well to the data as indicated by the p-value. However, after few days, as the contact degrades, the GEV distribution appears to be suitable for modelling the contact resistance data with outliers representing the heavily degraded contacts.

Table 5.3: Log likelihood and Kolmogorov-Smirnov goodness of fit test results of distribution fitting to contact resistance data set at different test durations

| Connector | Duration | Distribution | Log likelihood | p-value |
|---|---|---|---|---|
| T4 | Day 1 | Normal | 1112.2 | 0.97 |
| | | Inverse Gaussian | 1112.3 | 0.93 |
| | | GEV | 1112.6 | 0.93 |
| | Day 20 | Normal | 583 | 6.8E-11 |
| | | Inverse Gaussian | 780 | 3.33E-08 |
| | | GEV | 896 | 0.31 |
| T2 | Day 1 | Normal | 1207 | 0.34 |
| | | Inverse Gaussian | 1210 | 0.51 |
| | | GEV | 1213 | 0.94 |
| | Day 7 | Normal | 376 | 1.8E-09 |
| | | Inverse Gaussian | 641 | 9.1E-03 |
| | | GEV | 677 | 0.42 |

### 5.2.2 Contact resistance development and surge

The time data shown in the results is comparable to the test duration which is obtained by converting the test duration in ALT to field duration with operating temperature range of 20 °C to 80 °C using the acceleration factor calculated using Norris-Landsberg model as discussed in section 2.7.2.3. The mean $\mu$ and upper spread of the measured contact resistance calculated by mean plus twice the standard deviation (*Mean + 2SD*) at the given time are expected to be stable initially when the connectors are relatively new and in healthy condition. With the increasing degradation of the connectors with progressing time, the standard deviation in the measured resistance is expected to increase along with the mean resistance. The surge in the upper spread is also expected to be followed by the first failure since the contact resistance in electrical connectors rises suddenly after the contact zone is completely degraded.

### 5.2.2.1 Connector T1

Fig. 5.8(a) shows the contact resistance and failure pattern development in connector T1. The mean and upper spread is stable initially with no failure occurring before this period. Thereafter, at around 1100 days of operation, a sudden surge in the upper spread is observed after which the first failure takes place. Fig. 5.8(b) illustrates the contact resistance development till surge point. It can be seen that approximately after 700 days of operation, the upper spread starts deviating markedly from the mean resistance indicating that the damage of the contact zone through failure mechanisms has started influencing the contact resistance and hence connector performance. This deviation could be due to one or more connectors in operation. Around 1,100 days sudden increase in the contact resistance is observed indicating the wear through or complete oxidation of the contact zone in the near future. Connector T1 shows a total of 29 failures within 6,000 days of operation. The value of quotient *q* at surge in connector T1 is equal to 46.

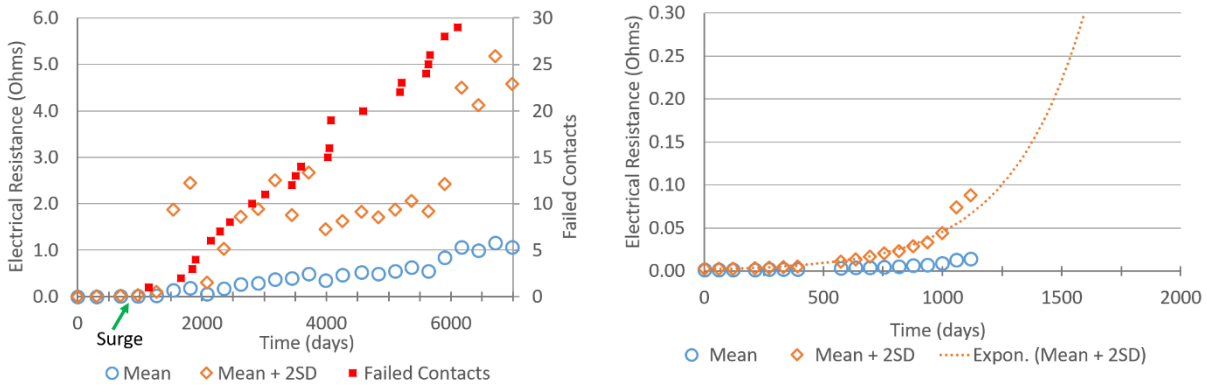


Fig. 5.8: Connector T1: (a) Contact resistance and failure pattern development (left); (b) Upper spread at surge (right)

### 5.2.2.2 Connector T2

Fig. 5.9(a) shows the contact resistance and failure pattern development in connector T2. The surge in the upper spread of contact resistance approximately occurs after 800 days. As seen from Fig. 5.9(b), the mean and upper spread are stable till around 500 days after which they show marked increase. Roughly after 800 days, the upper spread increases suddenly. The first failure is observed at 900 days. A total of 34 contacts indicated by red colored squares in Fig. 5.9(a) failed within 10,000 days of operation. The *q* value at surge in connector T2 is equal to 50.

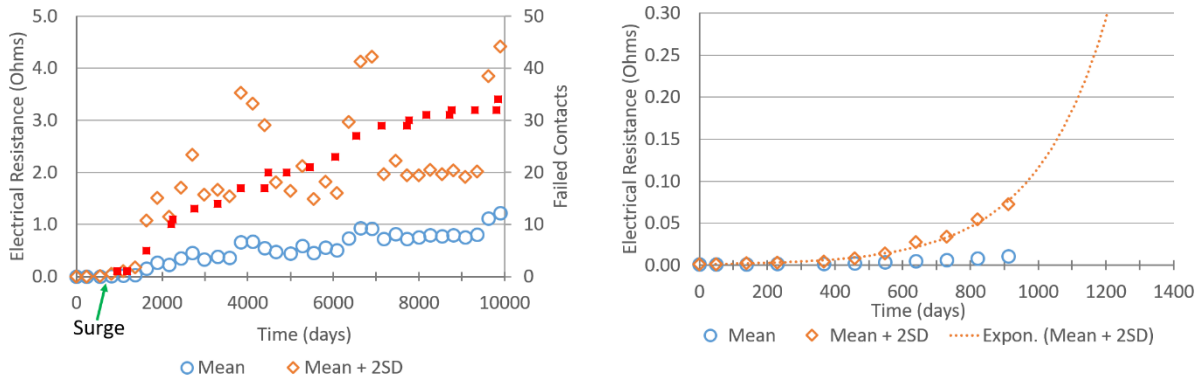


Fig. 5.9: Connector T2: (a) Contact resistance and failure pattern development (left); (b) Upper spread at surge (right)

5.2.2.3 Connector T3

The contact resistance and failure development in connector T3 is highlighted in Fig. 5.10(a). In this connector, a considerably longer time is recorded between 1st and succeeding failures. This reflects the extent of randomness in the failure patterns in electrical connectors. The first failure is recorded at 1027th day while the second failure occurs at 9000th day. Another 9 contacts fail in following 9000 days. As seen in Fig. 5.10(b), the contact resistance is stable for majority of the portion and just around 1,000 days, sudden surge is observed in upper spread. This is opposite to the situation in connectors T1 and T2 where the increase in upper spread was relatively gradual before the surge point. The *q* value at surge is equal to 8.5 indicating a comparatively stable connector in comparison to T1 and T2.

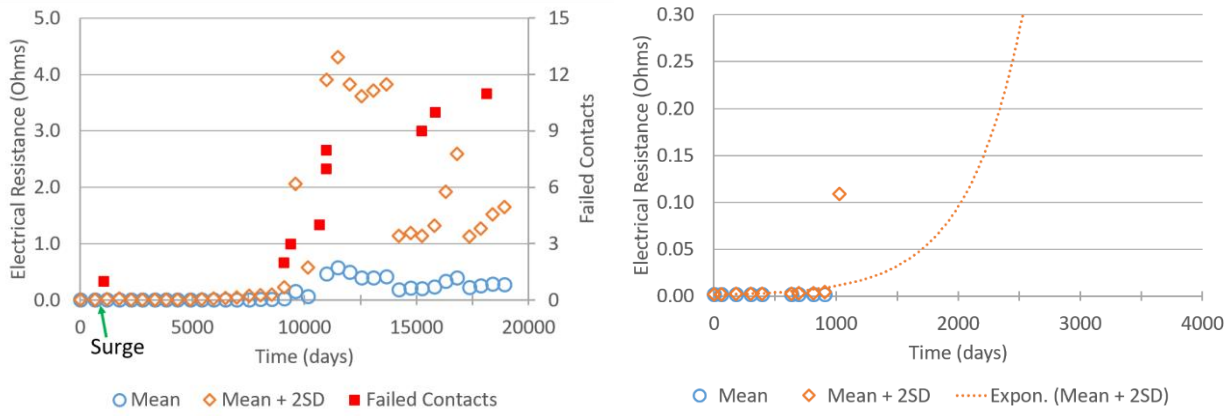


Fig. 5.10: Connector T3: (a) Contact resistance and failure pattern development (left); (b) Upper spread at surge (right)

### 5.2.2.4 Connector T4

Fig. 5.11(a) shows contact resistance and failure development in connector T4. The first failure occurs around 4,480 days. A total of 8 failures occur till time period of 10,500 days. As seen in Fig. 5.11(b), the mean and upper spread of resistance are stable till around 2,000 days after which the upper spread starts to increase markedly. The upper spread tends to surge around 4,260 days. The *q* value calculated at surge is equal to 40. In spite of the higher *q* value at surge, based on the number of failures, connector T4 appears to be more reliable than the connectors T1 and T2

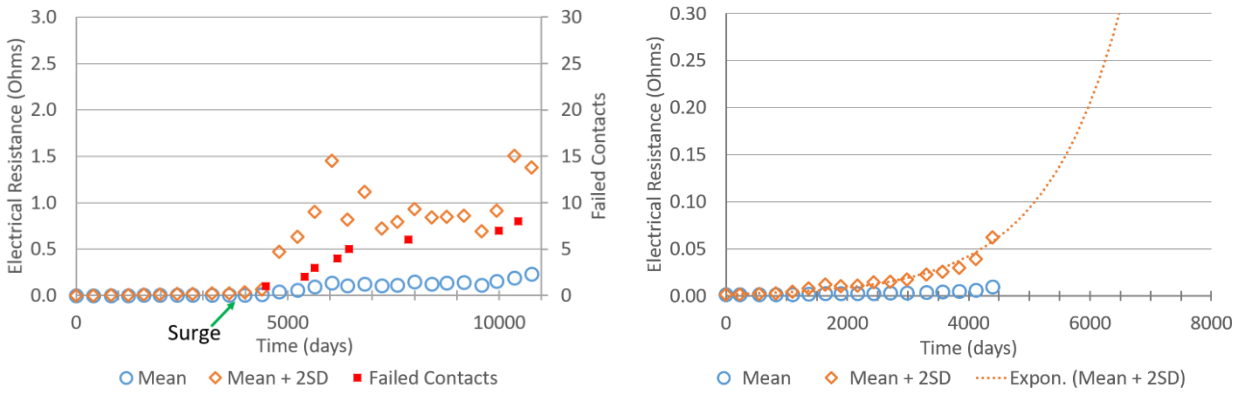


Fig. 5.11: Connector T4: (a) Contact resistance and failure pattern development (left); (b) Upper spread at surge (right)

### 5.2.2.5 Connector T5

Fig. 5.12(a) shows the contact resistance development in the connector T5 till 40,000 days of operation. This is a very highly stable connector and no failures are recorded during entire test period. The contact resistance is stable throughout as indicated by the mean and upper spread.

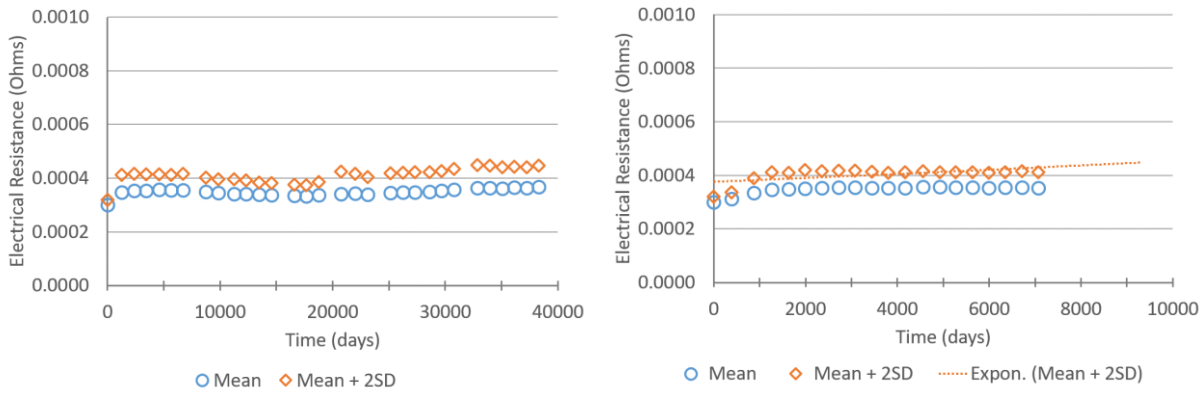


Fig. 5.12: Connector T5: (a) Contact resistance development with no failures (left); (b) Upper spread with no surge (right)

There is no surge occurring in T5 and the mean and standard deviation fluctuate between 0.3 mΩ and 0.45 mΩ which is almost unchanged over entire operation duration as seen in Fig. 5.12(a). The *q* value throughout remains below 2. In this study, data till 7200 days is used for the prognosis in T5.

5.2.2.6 Time to surge and *q* values overview in connectors T1 to T5

The time to surge and *q* values for the connectors T1 to T5 are highlighted in Table 5.4. The development of *q* values with respect to operation duration is illustrated in Fig. 5.13. The *q* values shortly before the surge varies across a wide range in the observed connectors. The *q* values are connector specific and hence cannot be used for comparison between different connectors.

Table 5.4: Time to surge and q values at surge in connectors T1 to T5

| **Connector** | **Time to surge (days)** | **q-value** |
|---|---|---|
| T1 | 1100 | 46 |
| T2 | 850 | 50 |
| T3 | 985 | 8.5 |
| T4 | 4260 | 40 |
| T5 | No surge (7200 days) | < 2 |

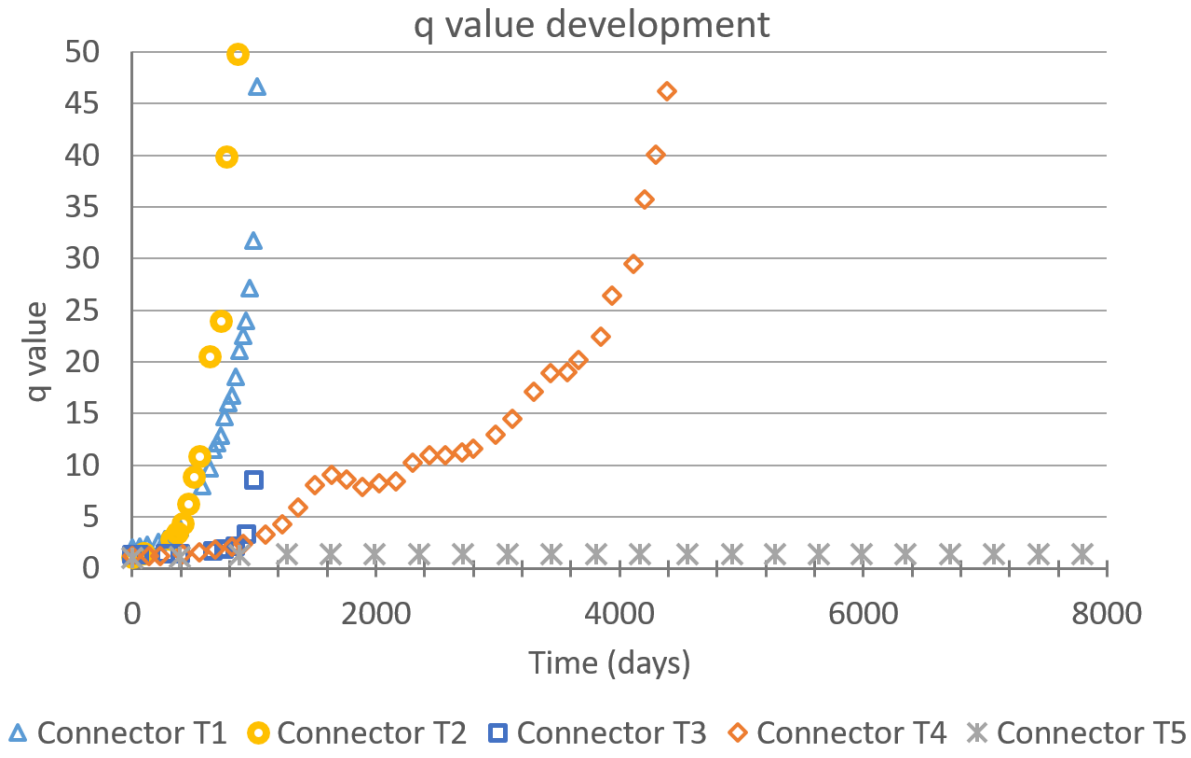


Fig. 5.13: Development of q values with time in connectors T1 to T5

### 5.2.3 CLT and time to failure prognosis using data up to surge

In this section, the results of the exponential extrapolation of the contact resistance data i.e. the time to failures corresponding to respective failure probabilities using the upper spread of contact resistance calculated from the standard normal distribution and the negatively skewed generalized extreme value (GEV) distribution as well as through distribution free method using percentiles as discussed in sections 5.1.3.2 and 5.1.3.3 are highlighted. The time to failure for the given failure probability from the exponential fit are calculated using equation (5.5). Also, the characteristic lifetime (CLT) obtained using the logarithmic extrapolation of time to 2 %, 10 %, 20 %, 40 % and 45% failure probabilities in case of distribution based method calculated using equation (5.7) and linear extrapolation of time to failure of similar failure probabilities in case of percentiles based method calculated using equation (5.9) are given. The directly calculated CLT using exponential extrapolation of $37^{th}$ percentile of the contact resistance is also compared with the measured CLT and indirectly calculated CLT by logarithmic and linear extrapolation of 2 %, 10 %, 20 %, 40 % and 45% failure probabilities in distribution based and percentile based methods respectively. The data shortly before the surge in resistance of the respective connectors is used for extrapolation and prognosis of the CLT.

#### 5.2.3.1 Connector T1

The exponential extrapolation of the contact resistance in connector T1 using *c*-scores of the standard normal distribution, GEV distribution and percentiles of the contact resistance along with the results of the given time to failures and CLT are shown in Fig. 5.14. The time to failures for 2 %, 10 %, 20 %, 40 % and 45 % failure probabilities obtained by exponential extrapolation of the contact resistance corresponding to given distributions and percentiles are given in Table 5.5. The CLT corresponds to 63.2 % failure probability. Fig. 5.15 represents the magnification of the extrapolation curves during the initial part of the operation. The time to failure trends predicted using GEV distribution and percentiles are in good agreement with the measured time to failure of the respective failure probabilities amongst which the values predicted using percentiles are in closer proximity with measured values. It can be seen that the CLT predicted by linear extrapolation of failure times obtained by percentiles method is almost close to the measured CLT with a difference of 0.1 %. The CLT predicted directly using $37^{th}$ percentile of measured contact resistance is 40.1 % greater than the measured CLT. In case of distribution based method, the GEV distribution results in the better approximation of CLT in comparison to the standard normal distribution. The CLT obtained using distributions are on safer side as compared to the CLT predicted directly using $37^{th}$ percentile. Given the unpredictability in the failures of electrical contacts, the CLTs determined using all the methods can be considered to be adequately precise for reliability estimation.

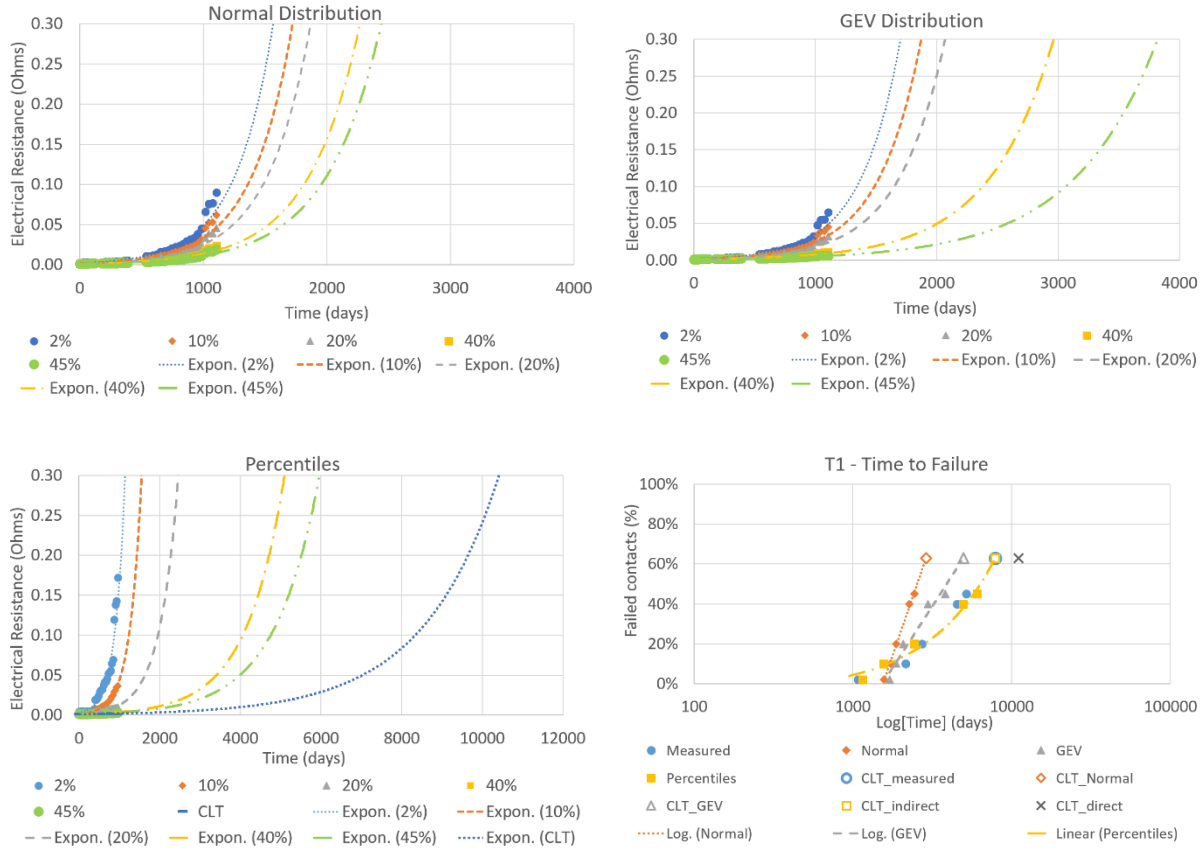


Fig. 5.14: Connector T1: Extrapolation of contact resistance from surge till failure and CLT extrapolation - (a) Normal distribution based (top left), (b) GEV distribution based (top right), (c) Percentiles based (bottom left), (d) extrapolation of time to failure and CLT (bottom right)

Table 5.5: Connector T1: Predicted time to failure for different failure probabilities from distribution based method and percentiles (indirect: linear extrapolation; direct: 37th percentile) based method and difference w.r.t. measured time to failure

| **Failure probability** | **Measured (days)** | **Predicted time to failure (days)** | | | | **Difference (%)** | | | |
|---|---|---|---|---|---|---|---|---|---|
| | | **Distribution** | | **Percentiles** | | **Distribution** | | **Percentiles** | |
| | | **Normal** | **GEV** | **Indirect** | **Direct** | **Normal** | **GEV** | **Indirect** | **Direct** |
| 2% | 1075 | 1566 | 1702 | 1149 | | +45.7 | +58.3 | +6.9 | |
| 10% | 2150 | 1723 | 1873 | 1555 | | -19.8 | -12.9 | -27.7 | |
| 20% | 2723 | 1870 | 2068 | 2440 | - | -31.3 | -24.0 | -10.4 | - |
| 40% | 4515 | 2269 | 2963 | 4947 | | -49.7 | -34.4 | +9.6 | |
| 45% | 5160 | 2440 | 3819 | 6046 | | -52.7 | -26.0 | +17.2 | |
| CLT | 7883 | 2895 | 4980 | 7893 | 11043 | -63.3 | -36.8 | +0.1 | +40.1 |

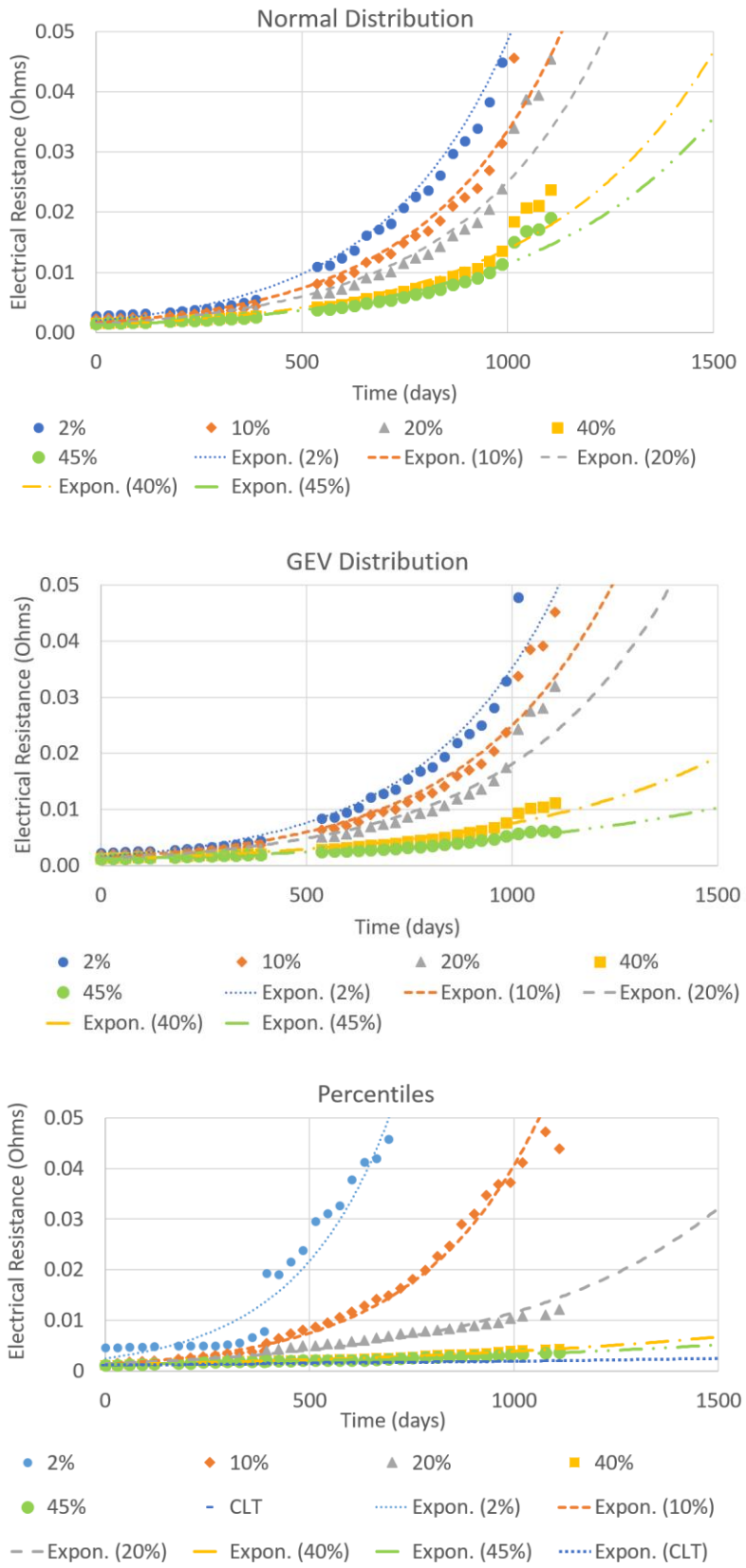


Fig. 5.15: Connector T1: Magnification of the extrapolation of different failure probabilities during initial part of operation using (a)Normal distribution (top), (b) GEV distribution (center), (c) Percentiles (bottom)

### 5.2.3.2 Connector T2

The exponential extrapolation of the upper spread of the contact resistance in connector T2 calculated using *c*-scores of the standard normal distribution and the GEV distribution as well as that of the percentiles of the measured contact resistance corresponding to given failure probabilities are highlighted in Fig. 5.16. The magnification of the extrapolation curves during the initial part of the operation are highlighted in Fig. 10.6 in Appendix 7. Table 5.6 shows the time to failure of the respective failure probabilities calculated from the exponential fit as well as the CLT determined using respective methods. Similar to T1, the time to failure values predicted using the percentiles method are in closer proximity with the measured values than the GEV distribution. All the methods predict the CLT on the safer side, with the directly predicted CLT by exponential extrapolation of the 37$^{th}$ percentile giving 14.3 % lower estimation than the measured CLT. Also the CLT predicted indirectly through application of *c*-scores of standard normal distribution, GEV distribution and percentiles of contact resistance is 70.8 %, 39.1 % and 31.1 % respectively lower than the measured CLT. Given the high degree of randomness in the degradation and failure patterns of electrical connectors, these predictions can be considered to be adequately precise for the determination of reliability.

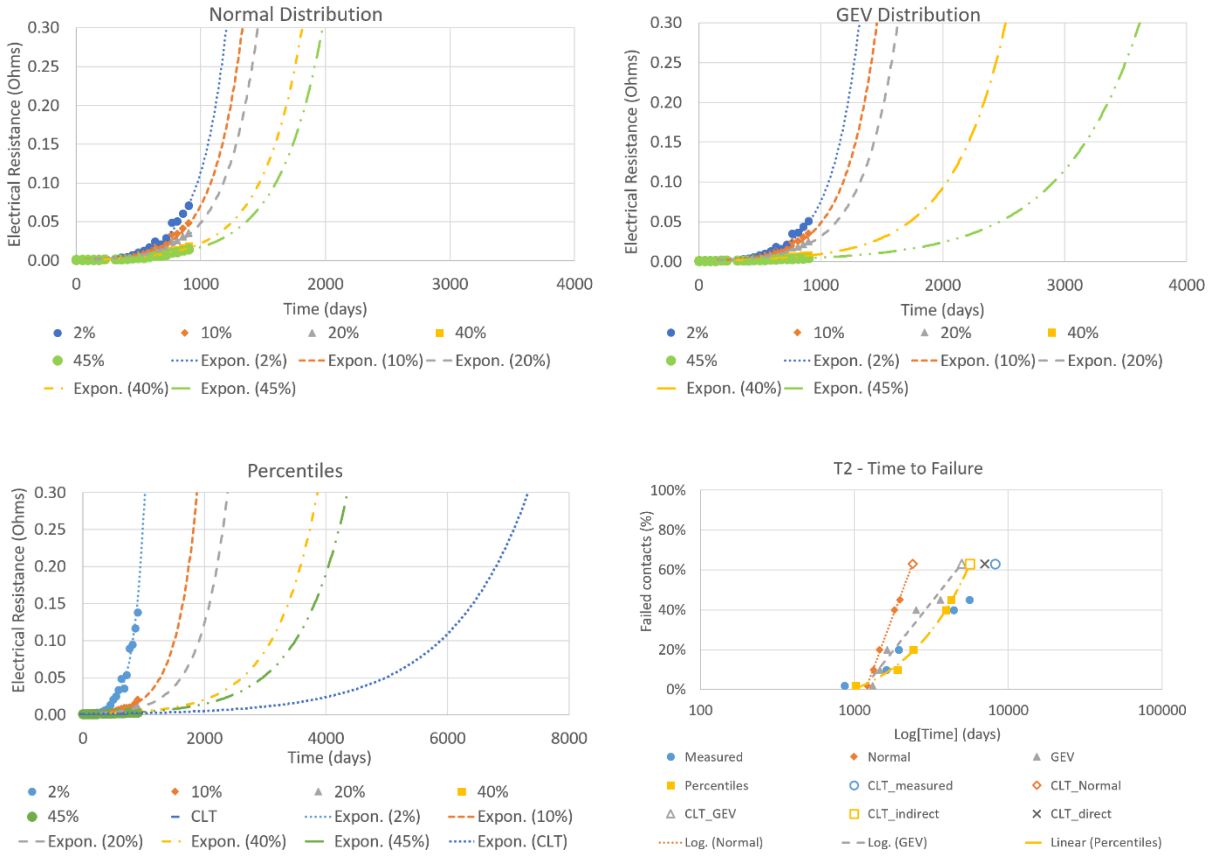


Fig. 5.16: Connector T2: Extrapolation of contact resistance from surge till failure and CLT extrapolation - (a) Normal distribution based (top left), (b) GEV distribution based (top right), (c) Percentiles based (bottom left), (d) extrapolation of time to failure and CLT (bottom right)

Table 5.6: Connector T2: Predicted time to failure for different failure probabilities from distribution based method and percentiles (indirect: linear extrapolation; direct: 37th percentile) based method and difference w.r.t. measured time to failure

| **Failure probability** | **Measured (days)** | **Predicted time to failure (days)** | | | | **Difference (%)** | | | |
|---|---|---|---|---|---|---|---|---|---|
| | | **Distribution** | | **Percentiles** | | **Distribution** | | **Percentiles** | |
| | | **Normal** | **GEV** | **Indirect** | **Direct** | **Normal** | **GEV** | **Indirect** | **Direct** |
| 2% | 861 | 1205 | 1316 | 1020 | | +39.9 | +52.8 | +18.4 | |
| 10% | 1615 | 1333 | 1460 | 1904 | | -17.4 | -9.6 | +17.9 | |
| 20% | 1938 | 1457 | 1632 | 2401 | | -24.8 | -15.8 | +23.9 | |
| 40% | 4414 | 1813 | 2516 | 3944 | | -58.9 | -43.0 | -10.7 | |
| 45% | 5598 | 1976 | 3617 | 4247 | | -64.7 | -35.4 | -24.1 | |
| CLT | 8182 | 2386 | 4982 | 5635 | 7011 | -70.8 | -39.1 | -31.1 | -14.3 |

### 5.2.3.3 Connector T3

Fig. 5.17 shows the exponential extrapolation of the upper spread of contact resistance for given failure probabilities with respect to standard normal distribution, GEV distribution and corresponding percentiles of the contact resistance. Also, the corresponding time to given failure probabilities and CLT thus predicted are illustrated. The magnification of the extrapolation curves during the initial part of the operation are highlighted in Fig. 10.7 in Appendix 7. Table 5.7 gives an overview of the predicted time to failure for given failure probabilities and CLT for respective prognosis methods. It can be seen that exponentially extrapolated curves for 40 % and 45 % failure probabilities overlap in percentile based method. Also, the spacing between the first failure i.e. 2 % failure probability and 10 % failures is larger in percentile based method. This behavior reflects the actual failure pattern as seen in Fig. 5.10 where the time to failure between first and succeeding failures is considerably large. Whereas, in the case of method with probability distributions, the spacing between the exponentially extrapolated failure probabilities is predictable due to the generalization of upper spread of resistance made possible by *c*-scores of respective failure probabilities.

The CLT predicted by GEV distribution is almost close to the measured CLT with a difference of 1.6 %. The CLT predicted by extrapolation of time to failures calculated using standard normal distribution and indirectly with percentiles is approximately 67 % and 30 % lower than the measured CLT. The CLT predicted directly using $37^{th}$ percentiles of contact resistance is 41.7 % lower than the measured CLT. Therefore, the prognosis of the CLT in case of connector T3 using all the proposed methods are adequately reliable for the reliability estimation.

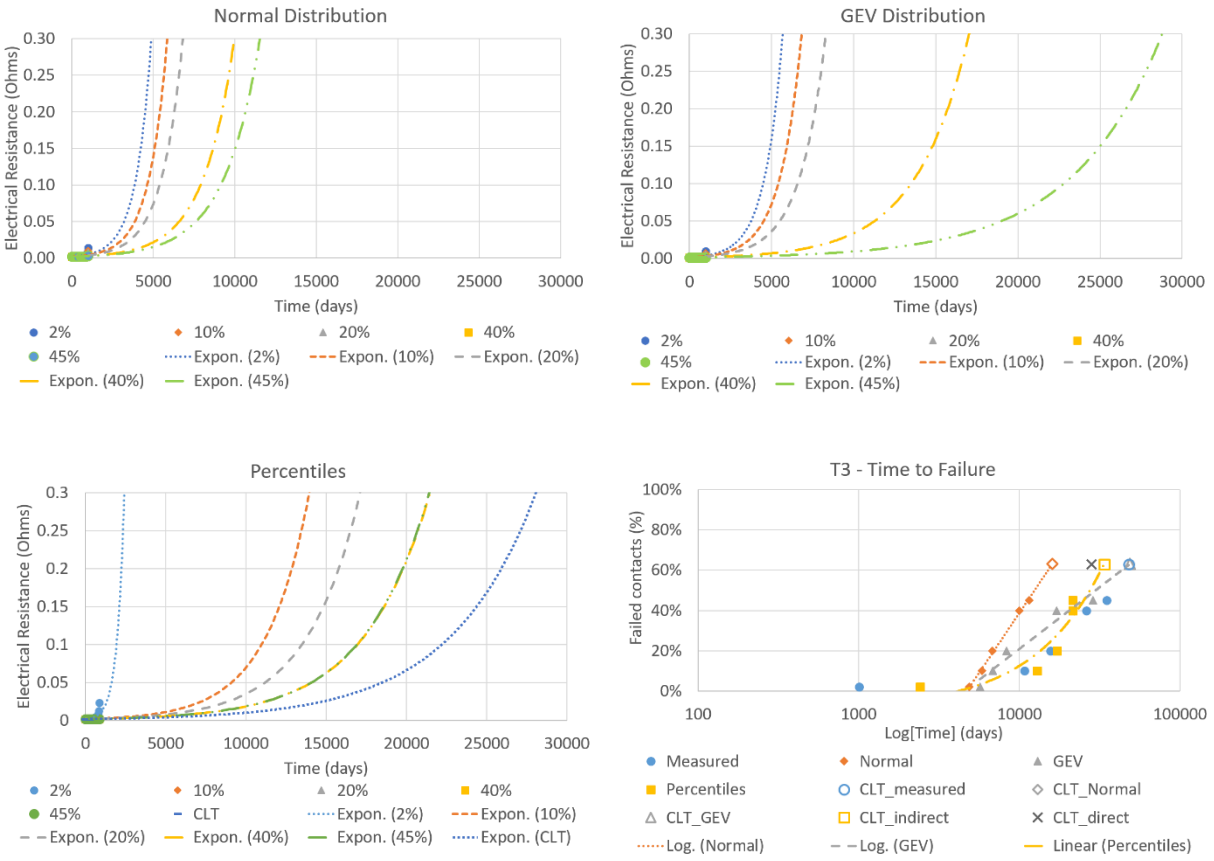


Fig. 5.17: Connector T3: Extrapolation of contact resistance from surge till failure and CLT extrapolation - (a) Normal distribution based (top left), (b) GEV distribution based (top right), (c) Percentiles based (bottom left), (d) extrapolation of time to failure and CLT (bottom right)

Table 5.7: Connector T3: Predicted time to failure for different failure probabilities from distribution based method and percentiles (indirect: linear extrapolation; direct: 37th percentile) based method and difference w.r.t. measured time to failure

| **Failure probability** | **Measured (days)** | **Predicted time to failure (days)** | | | | **Difference (%)** | | | |
|---|---|---|---|---|---|---|---|---|---|
| | | **Distribution** | | **Percentiles** | | **Distribution** | | **Percentiles** | |
| | | **Normal** | **GEV** | **Indirect** | **Direct** | **Normal** | **GEV** | **Indirect** | **Direct** |
| 2% | 1003 | 4878 | 5676 | 2416 | | +386 | +466 | +141 | |
| 10% | 10749 | 5853 | 6829 | 12933 | | -45.5 | -36.5 | +20.3 | |
| 20% | 15622 | 6806 | 8305 | 17118 | | -56.4 | -46.8 | +9.6 | |
| 40% | 26084 | 9973 | 17035 | 21464 | | -61.8 | -34.7 | -17.7 | |
| 45% | 35042 | 11539 | 28792 | 21430 | | -67.1 | -17.8 | -38.8 | |
| CLT | 48156 | 16058 | 48918 | 33685 | 28077 | -66.7 | +1.6 | -30.0 | -41.7 |

### 5.2.3.4 Connector T4

The exponential extrapolation of the upper spread of the contact resistance using the standard normal distribution, GEV distribution and percentiles of contact resistance along with the respective time to failure for different failure probabilities and CLT in connector T4 are illustrated in Fig. 5.18. The magnification of the extrapolation curves during the initial part of the operation are highlighted in Fig. 10.8 in Appendix 7. Table 5.8 compares the measured time to failure and CLT against the time to failure and CLT prognosed using respective distribution and percentile based methods. The time to failures determined using the percentile based method are greater than the corresponding measured time to failures in all cases. Also, in case of percentile based method, the CLT obtained indirectly through linear extrapolation and directly through 37$^{th}$ percentile are 22.7 % and 31.2 % respectively greater than the measured CLT. The GEV distribution provides best estimation of CLT in comparison to others with the difference in the prognosed and measured values being 17.2 %. Also, the prediction is on safer side. The standard normal distribution results in 77.8 % lower CLT than the measured value. Similar to connectors T1, T2 and T3, the prognosis obtained for T4 is also well precised and can be applied for reliability estimation.

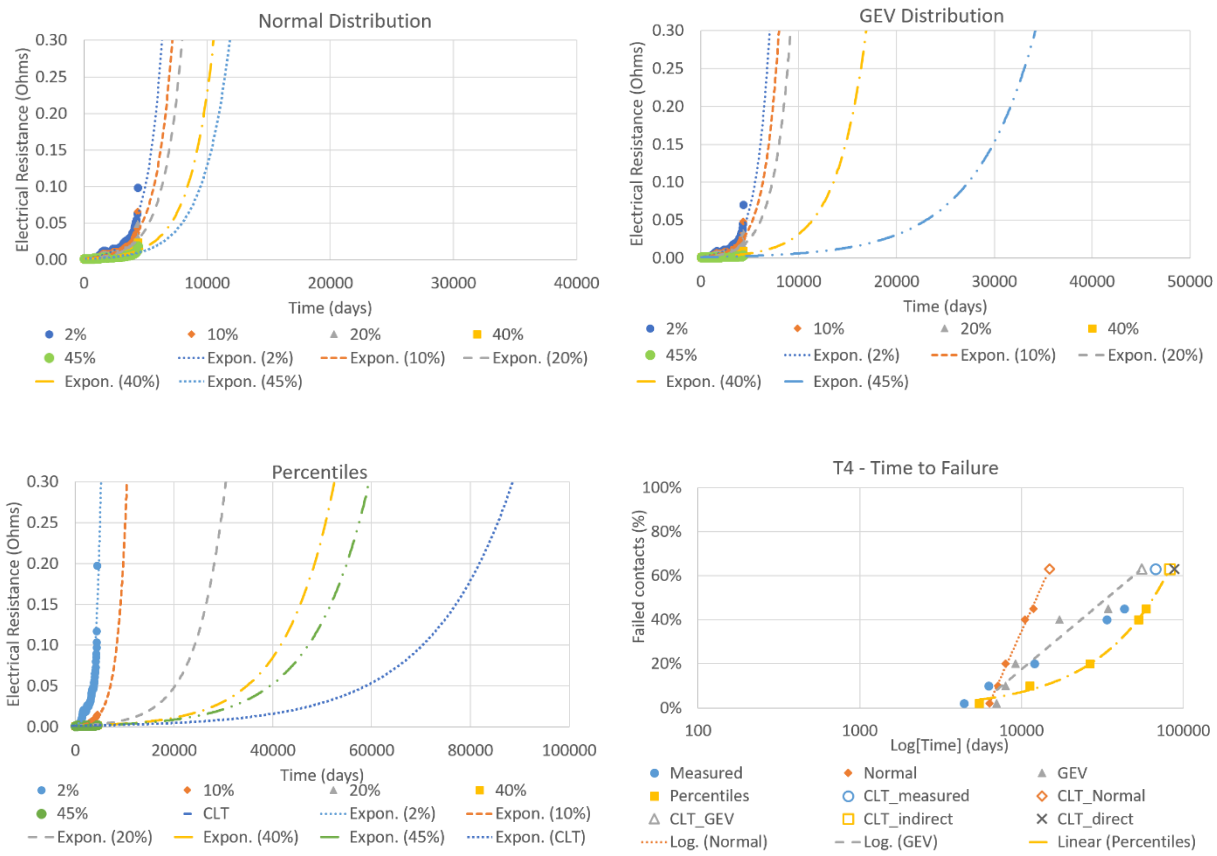


Fig. 5.18: Connector T4: Extrapolation of contact resistance from surge till failure and CLT extrapolation - (a) Normal distribution based (top left), (b) GEV distribution based (top right), (c) Percentiles based (bottom left), (d) extrapolation of time to failure and CLT (bottom right)

Table 5.8: Connector T4: Predicted time to failure for different failure probabilities from distribution based method and percentiles (indirect: linear extrapolation; direct: 37th percentile) based method and difference w.r.t. measured time to failure

| **Failure probability** | **Measured (days)** | **Predicted time to failure (days)** | | | | **Difference (%)** | | | |
|---|---|---|---|---|---|---|---|---|---|
| | | **Distribution** | | **Percentiles** | | **Distribution** | | **Percentiles** | |
| | | **Normal** | **GEV** | **Indirect** | **Direct** | **Normal** | **GEV** | **Indirect** | **Direct** |
| 2% | 4414 | 6335 | 7024 | 5461 | | +43.5 | +59.1 | +23.7 | |
| 10% | 6244 | 7178 | 7988 | 11217 | | +15.0 | +27.9 | +79.6 | |
| 20% | 12058 | 7966 | 9184 | 26492 | | -33.9 | -23.8 | +119.7 | |
| 40% | 33698 | 10528 | 17211 | 52983 | | -68.8 | -48.9 | +57.2 | |
| 45% | 43064 | 11831 | 34254 | 58870 | | -72.5 | -20.5 | +36.7 | |
| CLT | 67288 | 14942 | 55706 | 82556 | 88305 | -77.8 | -17.2 | +22.7 | +31.2 |

### 5.2.3.5 Connector T5

The exponential extrapolation of the upper spread of contact resistance derived from standard normal distribution and GEV distribution along with the exponential extrapolation of the respective percentiles of measured contact resistance are represented in Fig. 5.19. Also, the plot of the time to failure for different failure probabilities along with CLT predicted using distribution and distribution free methods are illustrated. The magnification of the extrapolation curves during the initial part of the operation are highlighted in Fig. 10.9 in Appendix 7. The time to failure predicted for different failure probabilities along with CLT are given in Table 5.9. The connector T5 is a highly stable connector and has no recorded failure during test. Therefore, the CLT obtained from prognosis cannot be validated through comparison with measured CLT. Instead, the CLT is calculated indirectly using Chi-square FIT, equation (2.78). Firstly Chi-square FIT rate is determined with respect to the complete test duration which is then substituted for FIT rate value in Weibull Fit rate in equation (2.76). This results in a CLT of approximately 900,000 days. To be on safer side, the target value to be achieved is set as 750,000 days. It can be seen that, the measured CLT and CLT prognosed using different methods are in close proximity with each other. The maximum difference between measured and prognosed CLT is -17 % observed in standard normal distribution, followed by direct percentile, indirect percentile and GEV distribution. This indicates that the CLT thus prognosed could be reliable and can be applied for estimation of connector's performance. This assumption is validated using the failure in time (FIT) rate discussed in section 5.2.4.

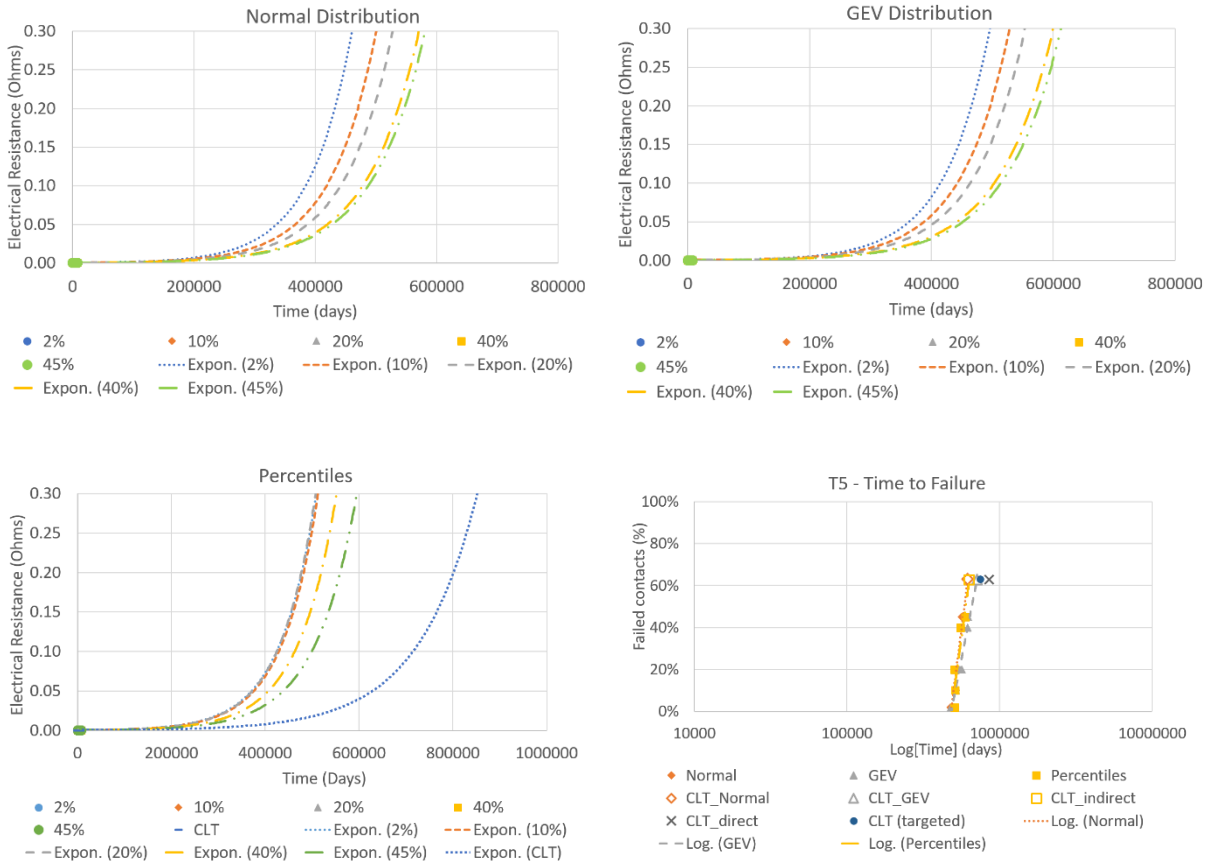


Fig. 5.19: Connector T5: Extrapolation of contact resistance from surge till failure and CLT extrapolation - (a) Normal distribution based (top left), (b) GEV distribution based (top right), (c) Percentiles based (bottom left), (d) extrapolation of time to failure (bottom right)

Table 5.9: Connector T5: Predicted time to failure for different failure probabilities from distribution based method and percentiles (indirect: linear extrapolation; direct: 37th percentile) based method

| **Failure proba-bility** | **Predicted with $\chi^2$ FIT (days)** | **Predicted time to failure (days)** | | | | **Difference (%)** | | | |
|---|---|---|---|---|---|---|---|---|---|
| | | **Distribution** | | **Percentiles** | | **Distribution** | | **Percentiles** | |
| | | **Normal** | **GEV** | **Indirect** | **Direct** | **Normal** | **GEV** | **Indirect** | **Direct** |
| 2% | No failures, targeted CLT = 750000 | 475592 | 478818 | 507638 | | | | | |
| 10% | | 516070 | 518417 | 511693 | | | | | |
| 20% | | 518417 | 563758 | 506808 | | | | | |
| 40% | | 565216 | 618764 | 553122 | | | | | |
| 45% | | 565955 | 619866 | 597477 | | | | | |
| CLT | | 619301 | 712033 | 628203 | 854042 | -17.4 | -5.1 | -16.2 | +13.9 |

### 5.2.4 Discussion on using data till surge for reliability prognosed with respect to failure in time (FIT) rate

The CLT predicted using the standard normal distribution, GEV distribution and the percentiles of measured contact resistance are used for calculation of the Weibull FIT rate using equation (2.76). It is to be noted that the CLT results discussed here correspond to CLT in field ($t_{CL\_field}$). The predicted FIT rates thus calculated using Weibull are then compared with the Weibull FIT rate calculated using the measured CLT. In case of connector T5, where the measured CLT is not available, the calculation of actual Weibull FIT rate is therefore not possible. Therefore, the FIT rate using Chi-square method is determined for connector T5 using the procedure discussed in section 2.7.3.3 and compared with the prognosed Weibull FIT rate. Table 5.10 highlights the measured and predicted CLT for all connectors which are used for determining the Weibull FIT rate. Also the time to surge, up to which the data is used for prognosis of CLT is given.

Table 5.10: Predicted CLT from distribution based method and percentiles (direct: linear extrapolation; indirect: 37th percentile) based method and difference w.r.t. measured CLT in connectors T1 to T5 and data till time to surge applied for prognosis

| **Conne-ctor** | **Time to surge (days)** | **Measured CLT (days)** | **Predicted CLT (days)** | | | | **Difference w.r.t. measured (%)** | | | |
|---|---|---|---|---|---|---|---|---|---|---|
| | | | **Distribution** | | **Percentiles** | | **Distribution** | | **Percentiles** | |
| | | | **Normal** | **GEV** | **Indirect** | **Direct** | **Normal** | **GEV** | **Indirect** | **Direct** |
| T1 | 1100 | 7883 | 2895 | 4980 | 7893 | 11043 | -63.3 | -36.8 | +0.1 | +40.1 |
| T2 | 850 | 8182 | 2386 | 4982 | 5635 | 7011 | -70.8 | -39.1 | -31.1 | -14.3 |
| T3 | 985 | 48155 | 16058 | 48918 | 33685 | 28077 | -66.7 | +1.6 | -30 | -41.7 |
| T4 | 4260 | 67287 | 14942 | 55706 | 82556 | 88305 | -77.8 | -17.2 | +22.7 | -31.2 |
| T5 | No surge (Data till: 7200) | No failures (Targeted CLT = 750000) | 619301 | 712033 | 628203 | 854042 | -17.4 | -5.1 | -16.2 | +13.9 |

The measured and prognosed FIT rates are given in Table 5.11. It can be seen that both the distribution based method as well as distribution free method using percentiles can be dependably applied for the prognosis of electrical connector reliability. As there is a very high degree of randomness involved in reliability of electrical connectors, the FIT rate prognosed using the proposed statistical method can be considered to be adequately precise. Amongst standard normal distribution and negatively skewed GEV distribution, the GEV distribution provides best estimation in all the cases. In case of percentiles based method, the indirect prognosis achieved using the extrapolation of various failure probabilities till CLT as well as the direct prognosis achieved using exponential extrapolation of $37^{th}$ percentile are precise and reliable. In comparison to the standard normal distribution, the prognosis obtained using GEV distribution is in better agreement with the measurements as well as with prognosis using

percentiles. Also it can be seen from the time to surge and CLT comparison in Table 5.10, that in less stable connectors such as T1 and T2, time required for prognosis can be brought down by up to 85 % to 90 %. The less stable connectors also fail quickly in tests. In connectors with medium stability such as T3 and T4, the time required for reliability estimation can be reduced up to 94 % to 98 %. In case of highly stable connectors such as T5, which require extremely long time to undergo failures, the data up to 7200 days was used and the reliable prognosis up to 750,000 days was achieved.

Table 5.11: Predicted FIT rate from distribution based method and percentiles (direct: linear extrapolation; indirect: 37th percentile) based method and ratio with. measured FIT rate in connectors T1 to T5

| **Connector** | **Measured FIT** | **Predicted FIT** | | | | **Ratio of measured and predicted FIT** | | | |
|---|---|---|---|---|---|---|---|---|---|
| | | **Distribution** | | **Percentiles** | | **Distribution** | | **Percentiles** | |
| | | **Normal** | **GEV** | **Indirect** | **Direct** | **Normal** | **GEV** | **Indirect** | **Direct** |
| T1 | 5286 | 14393 | 8367 | 5279 | 3773 | 0.37 | 0.63 | 1.00 | 1.40 |
| T2 | 5092 | 17463 | 8363 | 7394 | 5943 | 0.29 | 0.61 | 0.69 | 0.86 |
| T3 | 865 | 2595 | 852 | 1237 | 1484 | 0.33 | 1.02 | 0.70 | 0.58 |
| T4 | 619 | 2789 | 748 | 505 | 472 | 0.22 | 0.83 | 1.23 | 1.31 |
| T5 | 47 | 67 | 59 | 66 | 49 | 0.69 | 0.79 | 0.70 | 0.95 |

The FIT rate estimated with the standard normal distribution is on a safer side in all the connectors though the difference with measured reliability is considerably larger. In case of GEV distribution, the prognosed reliability is closer to the measured values and either on lower side or approximately equal to the measured values. The FIT rates estimated using percentile method could be seen on the upper as well as lower side of the respective measured FIT rates.

Therefore it can be seen that the proposed statistical procedures using distribution based methods as well as percentiles based methods can be efficiently applied for the lifetime and state of health prognosis of electrical connectors. Also, in case of sophisticated systems, the system health can be prognosed and managed through the prognosis of the state of health of the installed electrical connectors. The computation effort in all the methods is considerably low. In terms of magnitude, the results obtained through all the methods are comparable with each other. Hence, it can be recommended to use two or more methods simultaneously in order to validate and obtain dependable prognosis. In cases where system safety is an utmost priority, it can be recommened to consider the prognosis obtained through standard normal distribution since its predictions are on conservative side in all connectors. For prognosis with least computation effort, the percentiles method based on direct extrapolation of $37^{th}$ percentile of contact resistance can be reliably applied. In case of distribution based methods, the failure pattern is significantly influenced by the *c*-scores of the given probability distribution. The percentiles based method is entirely the function of measured contact resistances and is independent of the external parameters such as *c*-scores in case of distribution based methods.

### 5.2.5 Influence on CLT prognosis with quotient q based data selection

In the above section 5.2.3, the prognosis is performed using the data up to shortly before the surge, after which the first failure follows. Selecting the data up to shortly before the surge for the prognosis also provides a basis for comparison of the effectiveness of the proposed method in different connector types irrespective of their design and operating loads. The unstable connectors i.e. less reliable connectors such as T1 and T2 reach the surge point faster in comparison to the connectors with intermediate stability such as T3 and T4 as seen in section 5.2.2. In case of very highly stable connectors like that of T5, the surge point does not occur during the entire operation. As against the surge point which can only be identified if the sudden increase in upper spread of electrical resistance takes place, the quotient $q$ is available throughout the duration of operation. Like surge point, quotient $q$ is also an important state of health indicator and could be effectively used for prognosis of CLT and FIT rate in electrical connectors.

For this purpose, the effect of the data selected based on the $q$ value on the reliability prognosis is investigated. Through this, an attempt is made to further shorten the short term duration required for the prognosis of long term performance, thereby eliminating the need of occurrence of even first failure for reliable prognosis. The selection of an appropriate duration for the reliable CLT prognosis can be done using $q$ value. The quotient $q$ is calculated using equation (5.2). The quotient $q$ which is ratio of upper spread of resistance to the average initial resistance, is a time dependent quantity and increases with increase in performance degradation. Since, the average initial resistance is constant, the development trend of quotient $q$ is similar to the upper spread of resistance i.e. mean plus twice the standard deviation at a given time. The development of $q$ values in the connectors T1 to T5 is illustrated in Fig. 5.13. Here, the graphical results illustrating the $q$ value influence on CLT are highlighted for standard normal distribution, GEV distribution and percentile based method.

#### 5.2.5.1 Connector T1

In connector T1, the surge occurs around 1100 days and the corresponding value of $q$ at surge is equal to 46. The increase in the upper spread of resistance till the surge point in T1 is gradual as highlighted in Fig. 5.8. Fig. 5.20 highlights the time to failure and CLT in T1 prognosed using standard normal distribution, GEV distribution and percentiles with respect to the data corresponding to the various q values such as $q$ = 46, 24, 10 and 4 respectively. It can be seen that in all the cases, the CLT prognosed for all the q values lie in close proximity to one another. Also the time to failure curves for all $q$ values except for $q$ = 4, are very close to one another thereby giving closer predictions for various failure probabilities. Table 5.12 highlights the prognosed CLT using standard normal distribution, GEV distribution and percentiles based method and the corresponding differences with the measured CLT. The standard normal

distribution gives the best estimation for $q$ = 4 with least difference of 44 % in comparison to measured CLT.

In case of GEV distribution, the best estimation is obtained for $q$ = 10 followed by $q$ = 24. However, all the estimated CLTs are in close range with difference between the highest and the lowest prognosed CLT with respect to measured CLT being 9.3 %. In percentiles based method, the CLT obtained indirectly by extrapolation of different failure probabilities as in distribution based method, is almost similar to that of measured CLT for almost all the $q$ values except for $q$=4 where the prognosed CLT is 34.6 % lower than measured CLT. The CLT prognosed directly through exponential extrapolation of 37$^{th}$ percentile of resistance, are around 25 % to 40 % higher than the measured CLT except for $q$ = 10 where the estimated CLT is almost similar to the measured CLT. Therefore, in case of connector T1, no particular $q$ value can be identified to give best estimation for all the methods. However, the prognosed CLT for all the $q$ values can be considered to be acceptable given the extent of randomness in the degradation of electrical connectors.

Table 5.12: Connector T1: Influence of $q$ on predicted CLT from distribution based method and percentiles (direct: linear extrapolation; indirect: 37th percentile) based method and difference w.r.t. measured CLT

| **q** | **Data duration (days)** | **Meas-ured (days)** | **Predicted (days)** | | | | **Difference (%)** | | | |
|---|---|---|---|---|---|---|---|---|---|---|
| | | | **Distribution** | | **Percentile** | | **Distribution** | | **Percentile** | |
| | | | **Normal** | **GEV** | **In-direct** | **Direct** | **Normal** | **GEV** | **In-direct** | **Direct** |
| 46 (surge) | 1100 | 7883 | 2895 | 4980 | 7893 | 11043 | -63.3 | -36.8 | +0.1 | +40.1 |
| 24 | 925 | | 3259 | 5450 | 7904 | 9856 | -58.7 | -30.9 | +0.3 | +25.0 |
| 10 | 627 | | 3757 | 5692 | 7688 | 7859 | -52.3 | -27.8 | -2.5 | -0.3 |
| 4 | 388 | | 4400 | 4959 | 5158 | 10859 | -44.2 | -37.1 | -34.6 | +37.8 |

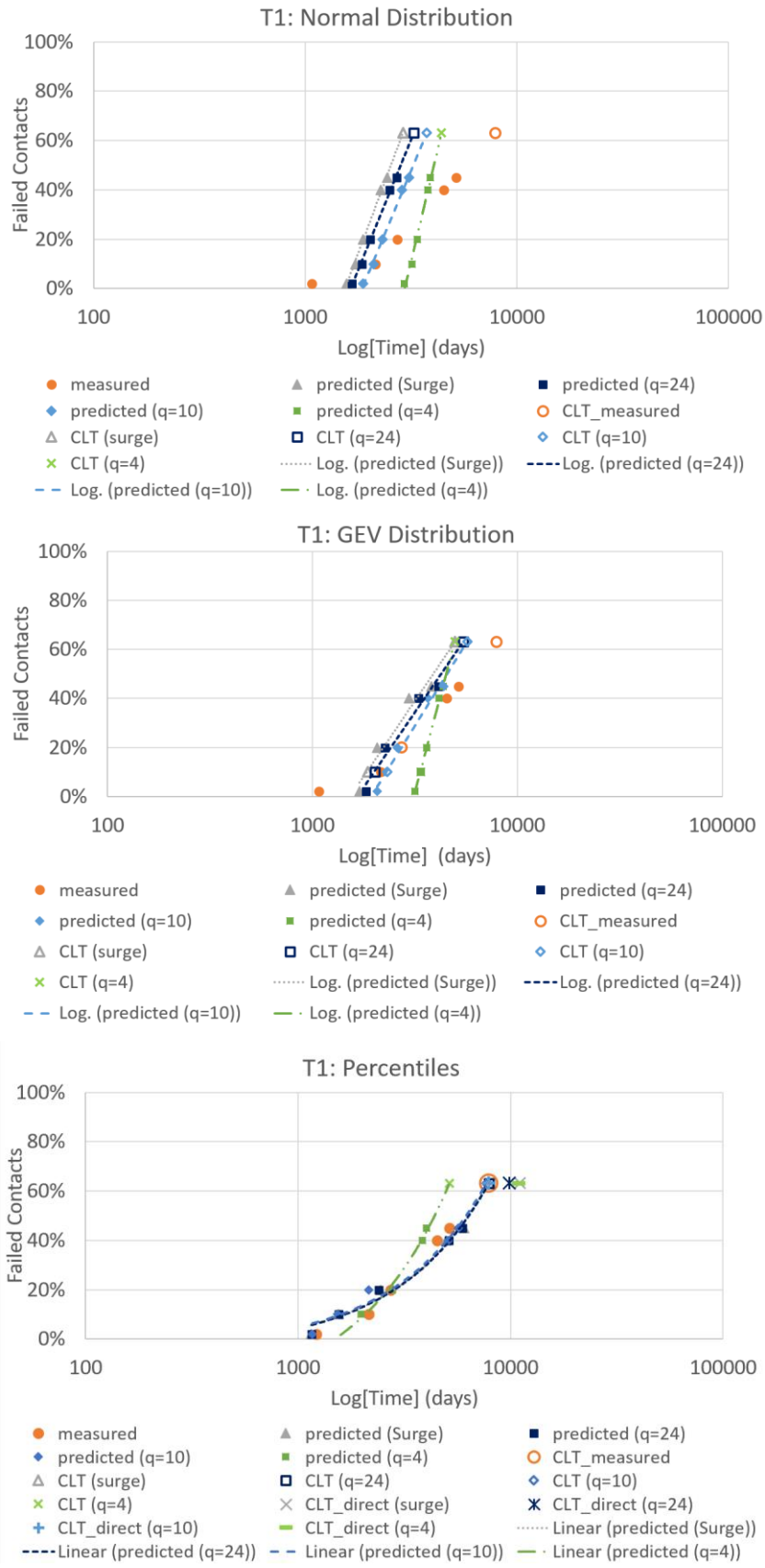


Fig. 5.20: Connector T1: Time to failure and CLT prognosis based on different *q* values using (a)Normal distribution (top), (b) GEV distribution (center), (c) Percentiles (bottom)

5.2.5.2 Connector T2

In connector T2, the value of *q* at surge occurring around 850 days is equal to 50. Fig. 5.21 shows the prognosed time to failures and CLTs obtained using normal and GEV distributions and percentile based method for different *q* values along with the measured values. The CLTs prognosed using different *q* values and their comparison with measured CLT are highlighted in Table 5.13. The time to failure curves for various *q* values follow similar trend with best estimation of CLT obtained with $q = 4$ in almost all the cases followed by estimation with $q = 11$. The CLTs obtained through directly extrapolating the $37^{th}$ percentile gives the best estimation in all the cases with minimum and maximum difference with respect to measured CLT being 14.3 % and 0.8 % respectively. Also, the CLTs measured indirectly using percentiles method are in closer proximity to each other with the difference between maximum and minimum difference in comparison to measured CLT being 10.1 %.

Table 5.13: Connector T2: Influence of *q* on predicted CLT from distribution based method and percentiles (direct: linear extrapolation; indirect: 37th percentile) based method and difference w.r.t. measured CLT

| **q** | **Data duration (days)** | **Meas-ured (days)** | **Predicted (days)** | | | | **Difference (%)** | | | |
|---|---|---|---|---|---|---|---|---|---|---|
| | | | **Distribution** | | **Percentile** | | **Distribution** | | **Percentile** | |
| | | | **Normal** | **GEV** | **In-direct** | **Direct** | **Nor-mal** | **GEV** | **Indirect** | **Dir-ect** |
| 50 (surge) | 850 | 8182 | 2386 | 4982 | 5635 | 7011 | -70.8 | -39.1 | -31.1 | -14.3 |
| 24 | 721 | | 2775 | 5277 | 5423 | 7725 | -66.1 | -35.5 | -33.7 | -5.6 |
| 11 | 541 | | 3469 | 6508 | 5853 | 8155 | -57.6 | -20.5 | -28.5 | -0.3 |
| 4 | 407 | | 4534 | 6958 | 6254 | 8251 | -44.6 | -15.0 | -23.6 | +0.8 |

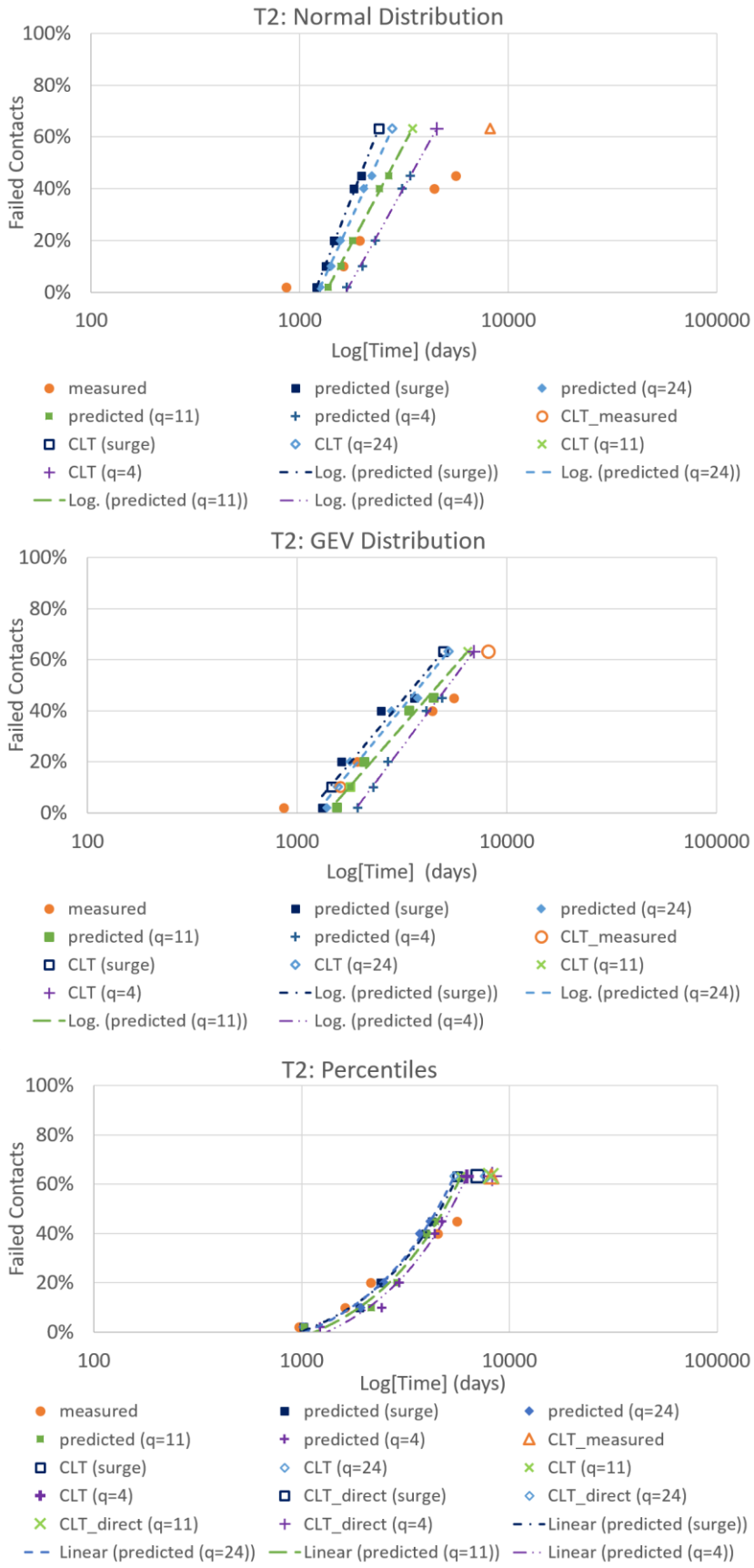


Fig. 5.21: Connector T2: Time to failure and CLT prognosis based on different q values using (a)Normal distribution (top), (b) GEV distribution (center), (c) Percentiles (bottom)

### 5.2.5.3 Connector T3

The development in the upper spread of the contact resistance in connector T3 is given in Fig. 5.10. It is a relatively stable connector and the value of $q$ at surge is 8.5 occurring around 985 days. Also the duration between first and second failure was observed to be very high in comparison to interval between remaining successive failures. The time to given failure probabilities and the CLTs estimated using different $q$ values with standard normal distribution, GEV distribution and percentile based method are shown in Fig. 5.22. The time to failure curve trends in percentile based method are in close proximity in percentile based method than in the distribution based method. Table 5.14 shows the estimated CLT using different $q$ values and their comparison with measured CLT. The CLT predicted using the data till surge gives the best estimation of CLT in all the cases except for the standard normal distribution. Also the CLTs estimated using the standard normal distribution and the direct and indirect percentile based method are on conservative side and closer to each other, with the difference between the difference between highest and lowest predicted CLTs with respect to measured CLT being within 10 %.

Table 5.14: Connector T3: Influence of $q$ on predicted CLT from distribution based method and percentiles (direct: linear extrapolation; indirect: 37th percentile) based method and difference w.r.t. measured CLT

| **q** | **Data duration (days)** | **Meas-ured (days)** | **Predicted (days)** | | | | **Difference (%)** | | | |
|---|---|---|---|---|---|---|---|---|---|---|
| | | | **Distribution** | | **Percentile** | | **Distribution** | | **Percentile** | |
| | | | **Normal** | **GEV** | **Indirect** | **Direct** | **Normal** | **GEV** | **Indirect** | **Direct** |
| 8.5 (surge) | 985 | 48156 | 16058 | 48918 | 33685 | 28077 | -66.7 | +1.6 | -30.1 | -41.7 |
| 5 | 955 | | 19547 | 34522 | 32058 | 23722 | -59.4 | -28.3 | -33.4 | -50.7 |
| 2 | 806 | | 20820 | 24309 | 28506 | 24128 | -56.8 | -49.5 | -40.8 | -49.9 |

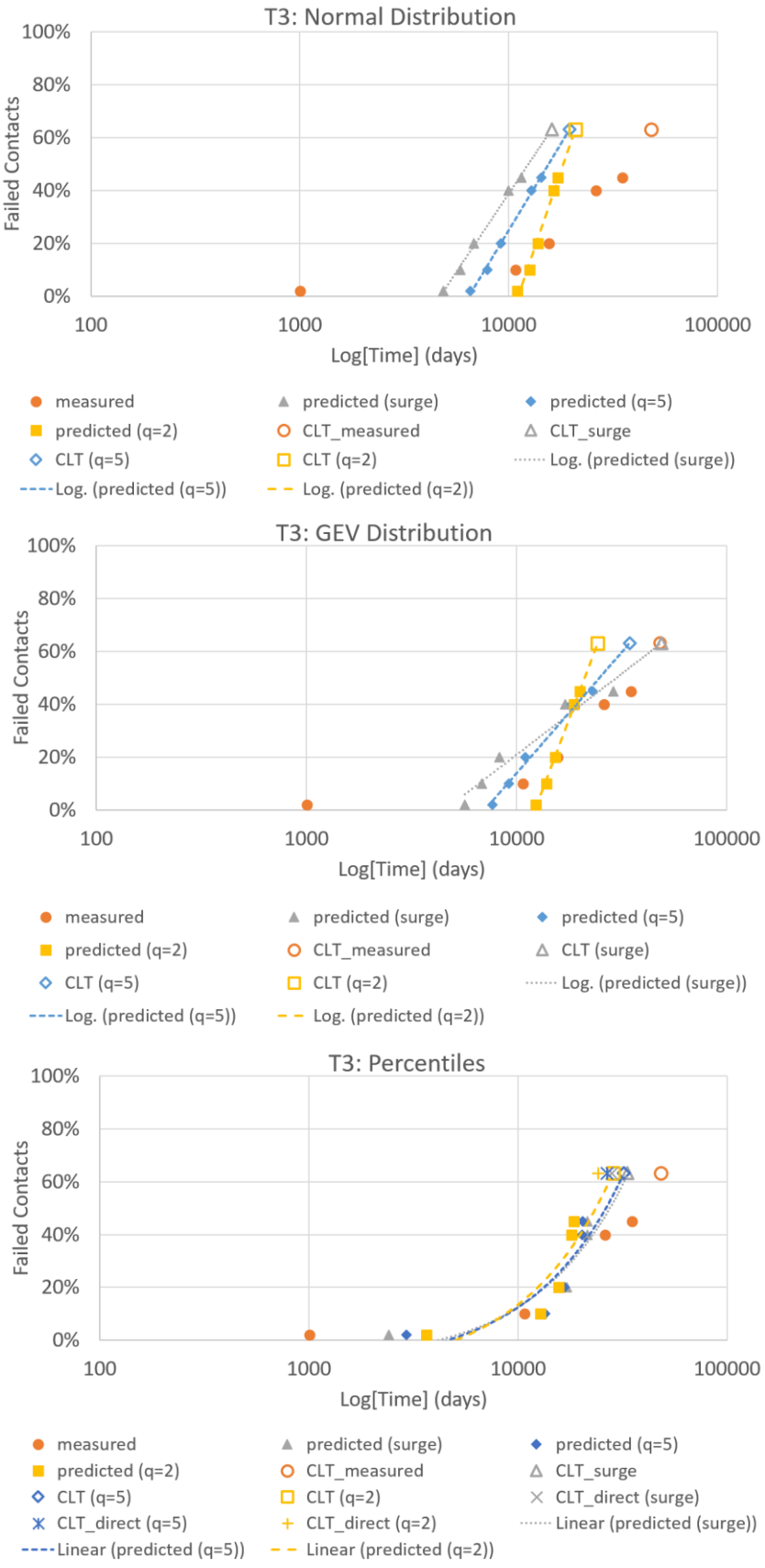


Fig. 5.22: Connector T3: Time to failure and CLT prognosis based on different *q* values using (a)Normal distribution (top), (b) GEV distribution (center), (c) Percentiles (bottom)

#### 5.2.5.4 Connector T4

The development in the failure pattern and the upper spread of the contact resistance in connector T4 is given in Fig. 5.11. It is also a stable connector with surge occurring around 4260 days of operation and *q* value at surge being equal to 40. Fig. 5.23 illustrates the development in time to failure for different failure probabilities and the CLT prognosed using standard normal distribution, GEV distribution and percentile based method. The CLTs prognosed using standard normal distribution, GEV distribution and percentile based methods along with their comparison with measured CLT are given in Table 5.15. The indirect percentile based method gives better prediction of CLT for all *q* values with the maximum difference from measured CLT being below 24 % followed by direct percentile method and standard normal distribution where the maximum difference in comparison to the measured CLT is approximately 45 % and 78 % respectively. The GEV distribution also gives better estimation of CLT except for the *q* value of 10.

Table 5.15: Connector T4: Influence of *q* on predicted CLT from distribution based method and percentiles (direct: linear extrapolation; indirect: 37th percentile) based method and difference w.r.t. measured CLT

| **q** | **Data duration** | **Measured (days)** | **Predicted (days)** | | | | **Difference (%)** | | | |
|---|---|---|---|---|---|---|---|---|---|---|
| | | | **Distribution** | | **Percentile** | | **Distribution** | | **Percentile** | |
| | | | **Normal** | **GEV** | **Indirect** | **Direct** | **Normal** | **GEV** | **Indirect** | **Direct** |
| 40 (surge) | 4260 | 67288 | 14942 | 55706 | 82556 | 88305 | -77.8 | -17.2 | +22.7 | +31.2 |
| 20 | 3633 | | 16977 | 94225 | 70192 | 70814 | -74.8 | +40.0 | +4.3 | +5.2 |
| 10 | 2287 | | 16248 | 244300 | 56087 | 46946 | -75.9 | +263.1 | -16.6 | -30.2 |
| 5 | 1300 | | 19662 | 82900 | 51340 | 37189 | -70.8 | +23.2 | -23.7 | -44.7 |

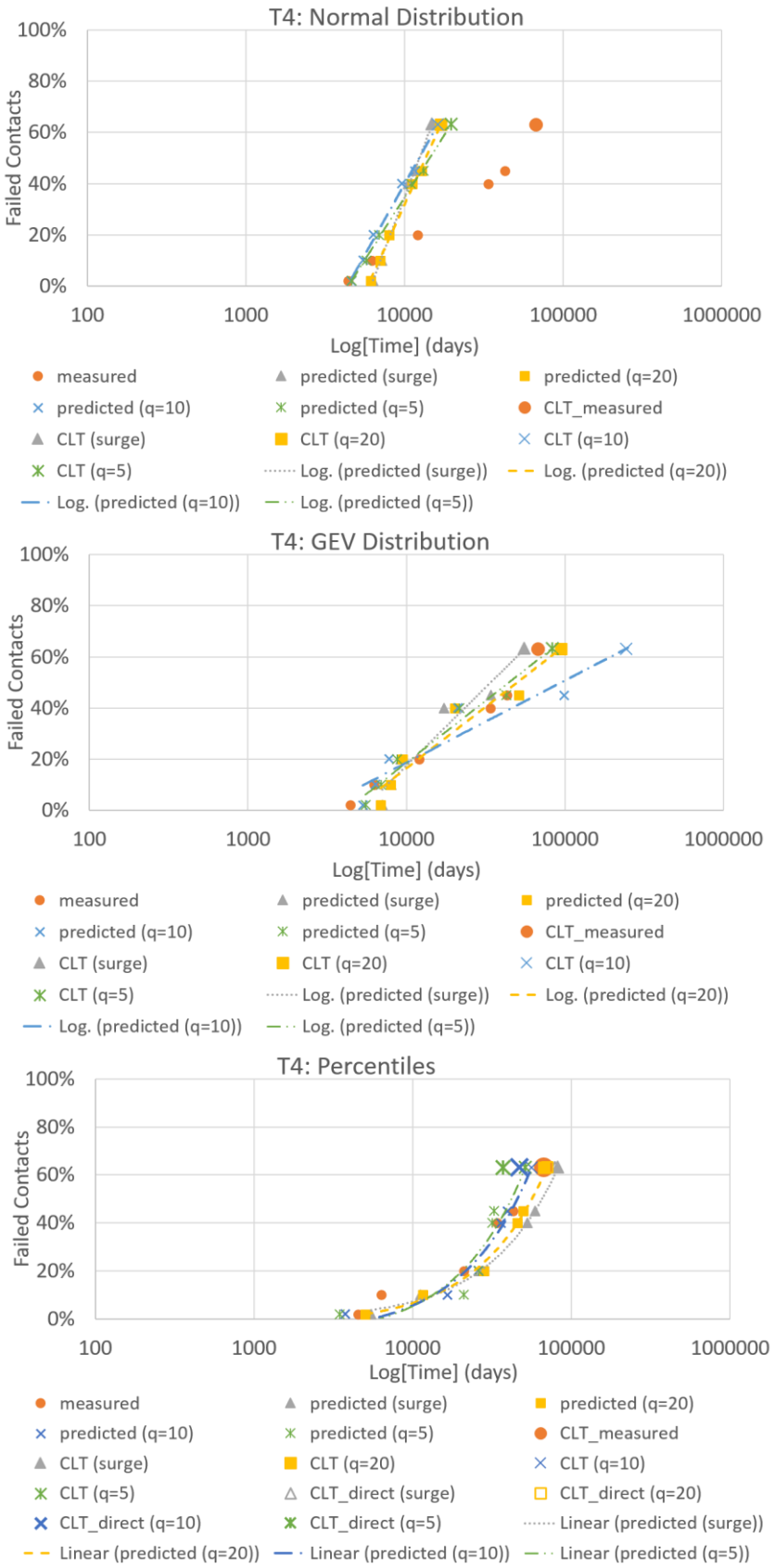


Fig. 5.23: Connector T4: Time to failure and CLT prognosis based on different q values using (a)Normal distribution (top), (b) GEV distribution (center), (c) Percentiles (bottom)

5.2.5.5 Connector T5

The connector T5 is a highly stable connector with no surge and failure occurring during the operation. The *q* value remains nearly constant, Fig. 5.13. Therefore, the data selection is in this case is done with respect to number of days of operation instead of *q* values. Fig. 5.24 shows the time to failure for given failure probabilities and CLTs prognosed for data with different durations using standard normal distribution, GEV distribution and percentiles based method. It can be seen that the time to failure curves and CLTs prognosed have considerable spacing between them. The spacing decreases with increase in the data duration used for analysis.

Table 5.16 highlights the prognosed CLTs using data up to different time durations using standard normal distribution, GEV distribution and percentiles based methods. Since no failures occur during the test, the CLT is predicted using the Chi-square FIT procedure as given in section 2.7.3.3. The predicted CLTs with Chi-square FIT for respective durations are about 2 to 8 times smaller than the prognosed CLTs using distributions and percentiles. The predicted CLT with Chi-square FIT increases with increase in the operation duration. Therefore, for appropriate comparison with the prognosis, the targeted CLT of 750,000 days calculated from Chi-square FIT with respect to the total operation duration of 43,000 days is used. The CLT prognosed using 7200 days of data is in good agreement with the targeted CLT of 750,000 days as derived from Chi-square FIT rate. The prognosis obtained using 5400 days of data is also acceptable since it is on safer side than CLT obtained with 7200 days of data. Therefore, it would be advisable to use the data of the above 5000 days for the prognosis in case of connector T5. The CLT prognosed using 7200 days is around 6 to 9 times larger than the CLT prognosed using 1800 days.

Table 5.16: Connector T5: Influence of data from different durations on predicted CLT from distribution based method and percentiles (direct: linear extrapolation; indirect: 37th percentile) based method and difference w.r.t. targeted CLT from Chi-square FIT rate

| **q** | **Data duration** | **Predicted with $\chi^2$ FIT (days)** | **Predicted (days)** | | | | **Difference (%)** | | | |
|---|---|---|---|---|---|---|---|---|---|---|
| | | | **Distribution** | | **Percentile** | | **Distribution** | | **Percentile** | |
| | | | **Normal** | **GEV** | **Indirect** | **Direct** | **Normal** | **GEV** | **Indirect** | **Direct** |
| 1.32 | 9000 | 186729 | 1145673 | 979716 | -ve slope | 1451790 | 52.8 | 30.6 | - | 93.6 |
| 1.36 | 7200 | 149385 | 619301 | 712033 | 628203 | 854042 | -17.4 | -5.1 | -16.2 | 13.9 |
| 1.37 | 5400 | 112037 | 388528 | 401630 | 445704 | 503224 | -48.2 | -46.4 | -40.6 | -32.9 |
| 1.37 | 3600 | 74691 | 201775 | 225854 | 288900 | 236747 | -73.1 | -69.9 | -61.5 | -68.4 |
| 1.39 | 1800 | 37345 | 84836 | 96133 | 103120 | 89681 | -88.7 | -87.2 | -86.3 | -88.0 |
| Targeted CLT of 750000 days based on Chi-square FIT for complete operation duration of 43000 days | | | | | | | | | | |

With the increase in the data duration used for prognosis, it can be seen that the slope of the succeeding time to failure curves tend to increase. The time to failure curve for 9000 days in case of GEV distribution is nearly vertical. Moreover, the time to failure curve for 9000 days obtained by indirect method results in a negative slope due to 2 % failure having larger time to failure than the following higher failure probabilities.

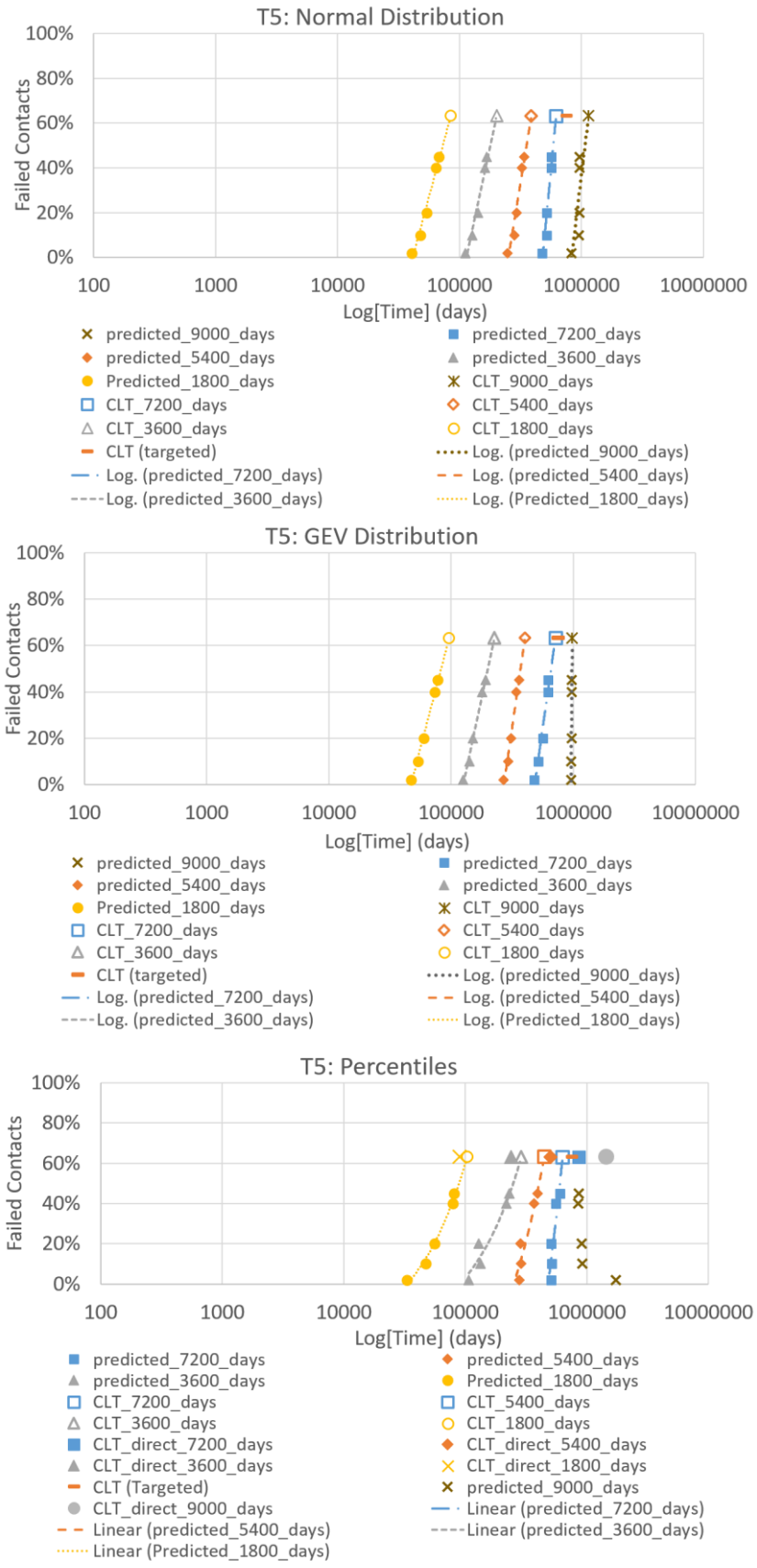


Fig. 5.24: Connector T5: Time to failure and CLT prognosis based on different test duration using (a)Normal distribution (top), (b) GEV distribution (center), (c) Percentiles (bottom)

The reason for the occurrence of negative slope for prognosis with 9000 days of data can be understood from the development of the upper spread of resistance in connector T5 shown in Fig. 5.12. Compared to the failure criterion of 300 mΩ, the change in the upper spread is extremely small. For 40000 days of operation, the upper spread increases from around 0.3 mΩ to 0.45 mΩ which is almost negligible. Also, within the given smaller range of contact resistance values, the increase in the upper spread is not gradual as observed in other connectors. The upper spread of resistance shows a sudden increase during the initial 1000 days of operation after which it remains nearly stable until 7000 days. The upper spread then gradually decreases until 15000 days of operation followed by a stable phase upto 18000 days. Though these fluctuations in the upper spread of resistance are very small i.e. within the range of 0.15 mΩ and can be considered as almost unchanged, from the data fitting and extrapolation point of view, such minor fluctuations in the upper spread development can have very high significance for prognosis as observed in this case. The influence of such minor fluctuations in contact resistance values can be clearly observed in the indirect method using percentiles of the measured contact resistances, where the exponential extrapolation of the 9000 days of data results in larger lifetime for 2 % failure probability in comparison to succeeding failure probabilities. The $98^{th}$ percentiles of the contact resistance values show decreasing trend after 7000 days. This results in a lower slope of the exponential fit for 9000 days represented by coefficient *k* in equation (5.4) and hence higher time to failure as prognosed using exponential exrtrapolation as shown in Fig. 10.13 in Appendix 9. On the other hand, the higher failure probabilities such as those corresponding to $90^{th}$ and $60^{th}$ percentiles of measured contact resistances show almost stable or slightly increasing trend and hence larger slopes of exponential fit resulting in shorter prognosed time to failures in comparison to $98^{th}$ percentile, Fig. 10.14 and Fig. 10.15 (Appendix 9). Hence, special care has to be taken when dealing with such a data and the targeted CLT should be used as a reference for deciding on the suitable data for prognosis.

### 5.2.6 Discussion on influence of quotient q on reliability prognosis with respect to failure in time (FIT) rate

Table 5.17 shows the Weibull FIT rate estimated using the prognosed CLTs for connectors T1 to T5 with respect to the various quotient *q* values along with the comparison with measured FIT rate. It is to be noted that since no failure occurred in T5, the measured FIT rate corresponds to the Chi-square FIT rate for connector T5 which is then compared with the prognosed Weibull FIT rate. The FIT rates estimated with respect to various *q* values in connector T1, T2, T3 and T4 can be taken as to be precise enough considering the randomness in the extent of degradation and failures in electrical connectors with the only exception being the FIT rate prognosed in connector T4 using GEV distribution for *q* value of 10. In connector T5, the prognosis using the data from 5400 days and 7200 days improved the estimated FIT rate. However, the pattern of development of upper spread of resistance which was not gradually increasing as in the case of connectors T1 to T4, played an important role in the estimation of reliability in T5. Also, the data of 9000 days could not be applied for indirect percentile method since it had a negatively sloped time to failure curve and the predicted FIT rate for other methods was observed to be on upper side.

Therefore, it can be seen that in the case of connectors where the upper spread of resistance shows a continuous increase at least till the first failure, the selection of the data for the prognosis can be made on the basis of *q* value as small as 2 to 5 and the need to wait till occurrence of surge in upper spread of resistance in order to reliably predict the long term performance can be further eliminated. However, it is advisable to compare the prognosis results for 2 to 3 different *q* values so that the forecasted results could be confirmed as precise and reliable. Also, the reliability prognosed with standard normal distribution tends to be mostly on the safer side. The prognosis with GEV distribution, direct and indirect percentile methods estimate the reliability on lower as well as higher side. Hence, when the prognosis is to be made with data corresponding to very small values of *q*, the use of standard normal distribution could be recommended. In this way, the short term operation duration can be further shortened for the long term performance prognosis. In case of highly stable connectors such as T5, it is advisable to consider the upper spread of resistance development at much magnified level and preferably use the data that is stable for considerably longer duration so that reliable prognosis can be obtained. Another recommendation would be to run the tests till about $1/100^{th}$ duration of the targeted CLT when q values are not increasing and the data has to be chosen based on the test duration.

Table 5.17: Influence of *q* value on predicted FIT rate from distribution based method and percentiles (direct: linear extrapolation; indirect: 37th percentile) based method and ratio w.r.t. measured FIT rate

| Conn-ector | q | Data duration | Meas-ured FIT | Predicted FIT | | | | Ratio of measured and predicted FIT | | | |
|---|---|---|---|---|---|---|---|---|---|---|---|
| | | | | Distribution | | Percentile | | Distribution | | Percentile | |
| | | | | Normal | GEV | Indirect | Direct | Normal | GEV | Indirect | Direct |
| T1 | 46 (surge) | 1100 | 5286 | 14393 | 8367 | 5279 | 3773 | 0.37 | 0.63 | 1.00 | 1.40 |
| | 24 | 925 | | 12785 | 7645 | 5272 | 4228 | 0.41 | 0.69 | 1.00 | 1.25 |
| | 10 | 627 | | 11090 | 7320 | 5420 | 5302 | 0.48 | 0.72 | 0.98 | 1.00 |
| | 4 | 388 | | 9470 | 8402 | 8078 | 3837 | 0.56 | 0.63 | 0.65 | 1.38 |
| T2 | 50 (surge) | 850 | 5092 | 17463 | 8363 | 7394 | 5943 | 0.29 | 0.61 | 0.69 | 0.86 |
| | 24 | 721 | | 15015 | 7896 | 7683 | 5394 | 0.34 | 0.64 | 0.66 | 0.94 |
| | 11 | 541 | | 12011 | 6402 | 7119 | 5109 | 0.42 | 0.80 | 0.72 | 1.00 |
| | 4 | 407 | | 9190 | 5988 | 6662 | 5050 | 0.55 | 0.85 | 0.76 | 1.01 |
| T3 | 8.5 (surge) | 985 | 865 | 2595 | 852 | 1237 | 1484 | 0.33 | 1.02 | 0.70 | 0.58 |
| | 5 | 955 | | 2132 | 1207 | 1300 | 1756 | 0.41 | 0.72 | 0.67 | 0.49 |
| | 2 | 806 | | 2001 | 1714 | 1462 | 1727 | 0.43 | 0.50 | 0.59 | 0.50 |
| T4 | 40 | 4260 | 619 | 2789 | 748 | 505 | 472 | 0.22 | 0.83 | 1.23 | 1.31 |
| | 20 | 3633 | | 2454 | 442 | 594 | 588 | 0.25 | 1.40 | 1.04 | 1.05 |
| | 10 | 2287 | | 2564 | 171 | 743 | 888 | 0.24 | 3.63 | 0.83 | 0.70 |
| | 5 | 1300 | | 2119 | 503 | 812 | 1120 | 0.29 | 1.23 | 0.76 | 0.55 |
| T5 | 1.32 | 9000 | 47 | 36 | 43 | - | 29 | 1.28 | 1.1 | - | 1.62 |
| | 1.36 | 7200 | | 67 | 59 | 66 | 49 | 0.69 | 0.79 | 0.70 | 0.95 |
| | 1.37 | 5400 | | 107 | 104 | 93 | 83 | 0.43 | 0.45 | 0.50 | 0.56 |
| | 1.37 | 3600 | | 207 | 184 | 144 | 176 | 0.23 | 0.25 | 0.32 | 0.26 |
| | 1.39 | 1800 | | 491 | 433 | 404 | 465 | 0.09 | 0.11 | 0.12 | 0.10 |

### 5.2.7 Summary of state of health and reliability prognosis

A comprehensive and feasible data driven statistical approach for prognosis of connector reliability in long term through the use of short term performance data is introduced. The state of health indicators such as time to surge and *q*-value are vital for the prognosis and understanding the stability of connector. The analysis shows that the electrical contact resistance development can be reliably linked to the failure probability in order to predict the time to failures and CLT. The time for estimation of connector reliability can be reduced from 85 % to 98 % depending on the stability of connector. The distribution based method using the *c*-scores of standard normal distribution and negatively skewed GEV distribution effectively predict the CLT. The CLT estimated by GEV distribution is closer to the measured CLT in majority of the cases though the CLT prognosed by standard normal distribution is mostly on the conservative side thereby making it more reliable given the randomness in the performance of connectors. The CLT is also reliably predicted using the percentiles of the measured contact resistance. The indirect method applying the linear extrapolation of time to failure data till CLT

can be considered to be more reliable than the direct method which predicts the CLT through exponential extrapolation of $37^{th}$ percentiles of measured contact resistance.

In the connectors where the contact resistance shows continuously upward trend, the CLT can be reliably prognosed with data corresponding to $q$ values of 2 to 5 thereby achieving further reduction in the time needed to estimate the reliability. The proposed method enables the CLT prediction in the case of highly stable connectors which do not fail during the entire operation and where the $q$ value remains almost constant with minor fluctuations. However, targeted CLT calculated using Chi-square method should be taken as reference while selecting the data for the prognosis in such connectors. The proposed approach can be helpful in significant saving of time and resources needed for the reliability prognosis. This approach can be used in the management of health of critical and complex systems through monitoring the state of health and estimating remaining useful life of electrical connectors installed in them.

# 6 Conclusion and Outlook

The aim of this thesis is to develop a parametric and statistical approach for design of electrical connectors having an optimal combination of structural, tribological, thermal and electrical performance as well as a method to significantly scale down the time required for the reliability estimation in accelerated life tests of electrical connectors subjected to thermal cycling. During this process, a feasible stepwise approach for design and testing of electrical connectors has been introduced. The approach corresponding to each of the considered aspects of design and testing of electrical connectors is developed with an intention to minimize the time, cost and effort.

In the first phase, the parametric study to investigate the influence of geometrical parameters on the structural performance of an electrical connector is conducted. The contact area and contact force are treated to be the output parameters of interest. Also, the equivalent stresses in the connector are taken into account while achieving an optimal combination of contact area and contact force in the design. The idea of aiming for an ideal combination of maximum contact area and permissible contact force in design is based on the fact that such a combination results in reduced contact resistance and joule heating alongside improving the lifetime through tribological performance in the contact zone. A round 13.6 mm electrical connector has been used as a reference model for optimization. The contact force, contact area, total electrical resistance and joule heating measurements are performed on the reference model to determine its structural and thermal-electric performance. These results are then validated through FEM simulations. The simulation results are observed to be in good agreement with the experiments.

The dimensions of the spring segment are varied to generate different receptacle models using a design of experiment method while keeping the pin geometry same as that in the reference connector. Also, the generation of the different CAD models through parametric CAD modeling procedures enables modifications in the reference designs to generate new models in very short time. The connector symmetry is exploited during structural simulations to reduce the computational effort and save significant amount of time needed for analyzing the individual and interaction influence of the geometrical parameters on structural performance. The statistical models of contact area and contact force defining their relationships with geometrical parameters are obtained through multiple regression analysis. The surface response plots give an idea of the individual and interaction effects of the various geometrical parameters.

Amongst the different geometrical parameters considered in the optimization, the thickness *t1* and total length *L1* of the spring segment are found to be most significant followed by the outer diameter *D1* and contact radius *R* at the tip of spring segment. In the two level full factorial

DoE, the contact force and contact area models are obtained using individual influences only. In Taguchi L8 DoE, the contact area modelled is influenced mainly by the individual effects of parameters whereas the contact force is observed to be influenced by the interaction of the outer diameter *D1* with thickness *t1* and *L1* in addition to the individual influences. The contact radius *R* significantly influences the contact area and has a relatively smaller influence on the contact force. Also, its interaction effect on contact force with other parameters is not significant. In such a scenario, when a parameter's tendency is clear, it can be held constant at a given value and another parameter such as *L2* which can be imagined to influence the spring curvature and hence contact force and contact area in combination with other parameters can be included in analysis. This consideration proves to be true as *L2* shows to have significant influence on contact area and contact force models. For a given connector, a larger possible contact radius *R* is suggested. The optimized 13.6 mm connector model results in 41 % larger contact area and 4 % reduction in receptacle volume when compared to the reference model. The coupled thermal-electric analysis of optimized 13.6 mm connector results in 13 % lower electrical contact resistance in contact zone and 3.75 % lower total electrical resistance in comparison to the reference model. The results show that the 13.6 mm reference connector design is already closer to its optimized state.

To validate the transferability of the design optimization approach used for 13.6 mm connector to other connector sizes, a smaller 2.5 mm connector is used. The contact force, contact area, joule heating and total electrical resistance are measured experimentally which are then validated using FEM simulation as in the case of 13.6 mm connector. For 2.5 mm connector, instead of two levels of parameters, the models are generated using three levels of parameters with Taguchi L9 DoE. The interaction terms are more dominant in the statistical models of contact area and contact force when three levels of parameters are considered. The optimized 2.5 mm model has 16 % less contact force and 2.4 times larger contact area than the reference model. Also, 16 % reduction in volume is obtained. The joule heating in the optimized 2.5 mm model is almost similar to that of the reference model. Also, 22 % lower electrical resistance near the contact zone is observed. The total electrical resistance in the optimized model is 4.4 % higher than in the reference model. Given the amount of reduction achieved in the size of receptacle, this can be considered to be a good trade off.

A coupled structural-thermal-electric simulation model exploiting the geometrical symmetry allows the analysis to be reliably performed using single spring segment thereby saving significant time and resources. The simulated joule heating shows very good agreement with the measured joule heating in both the reference connectors. The convective heat transfer coefficients calculated with free convection yield precise results. The selection of emissivity values accounting for radiation heat transfer in simulation is vital for improving the joule heating estimation. The coupled structural-thermal-electric simulation models thus applied in this work give precise estimations of the connector performance.

In this way, a systematic approach of firstly structurally optimizing the connector design through structural simulation of the models generated with DoE and multiple regression analysis of the structural simulation results followed by performing coupled structural-thermal-electric simulation on the optimized model proves to be an effective method in the design phase of electrical connectors.

The tribological aspects in an electrical connector system are vital from the contact resistance point of view. The surface roughness and topography directly influence the real contact area formed when two bodies contact under the given contact force and contacting conditions. Looking at the importance of determining the real contact area in order to estimate contact resistance, structural simulations are performed using FEM and real contact areas are determined. The bronze sphere-flat contact geometry with gold coating and two categories of surfaces, namely rough and polished, are used for analysis. The contact resistance at various contact force values is measured in the respective contact samples.

The surface roughness in the simulation is simplified in the form of triangular rib structures through the measured core roughness $R_K$ derived from bearing area curve and the average groove width $R_{SM}$ of surface roughness. The structural simulation of such a simplified roughness model is computationally very efficient and yields reliable estimation of real contact area. The simulated contact area under given contacting conditions and force is used to determine the contact resistance by Holm's equation. This contact resistance calculated by Holm's equation using real contact area is in very good agreement with the measured contact resistance in the polished contacts at all the contact forces and in case of rough contacts at contact forces of 3 N and 5 N. In case of rough contacts, at the lower contact force of 1 N, the calculated contact resistance is slightly outside the confidence level limits of the measured contact resistance. This could be resulting from the difference in the deformation of asperities in actual rough surface and the simplified roughness profile. The selection of material ratio in the bearing area curve has significant influence on the results for rough surface at lower forces. The estimation of the real contact area at higher roughness and lower contact force combination can be improved with much precise selection of the material ratio while determining the core roughness $R_K$ for modelling the roughness.

The proposed approach for estimation of real contact area can be very useful while determining the contact resistance in an electrical connector during the design phase itself. An ideal contacting condition i.e. suitable surface roughness, coating materials, contact force, etc. can be integrated in the connector after the optimal model is identified, with a view to further improve the performance of the connector. Also, the proposed approach eliminates the convergence issues encountered while using the roughness models developed by extracting the point cloud of actual roughness or statistically generated rough surfaces.

To overcome the issue of very long test durations required for determining the reliability of newly designed electrical connectors in accelerated lifetime tests (ALT) under thermal loads, a

data driven statistical process is introduced which can be applied to all the connectors irrespective of their design. Through the proposed approach, the long term performance of the connector is reliably estimated using the short term test data and the results are validated through comparison with measured lifetime. The state of health parameters such as time to surge, surge point and quotient *q* defining the condition of electrical connectors are introduced. The approach aims at determining the characteristic lifetime (CLT) which is then employed to determine the failure in time (FIT) rate of connectors from the Weibull distribution at given stress levels. The test durations from the accelerated tests conditions are converted to an equivalent operating time scale in field conditions using the suitable acceleration factor calculated from Norris-Landzberg model. The resulting time scales from field conditions are used for representing the prognosis results.

A strong correlation between the contact resistance development and contact failures are observed which is then exploited for the prognosis of connector lifetime. A reliable lifetime prognosis is achieved by correlating the percentiles of contact resistance with the failure probabilities. The methods based on probability distributions and percentiles of measured contact resistance are devised for prognosis of CLT using the short term contact resistance data.

In the first step, the contact resistance data until the surge point is used for the prognosis. The distribution based method as well as percentile based method give an adequately precise estimation of the CLT in all the connectors considered in this work. The upper spread of the contact resistance and the percentiles of the measured contact resistance can be exponentially extrapolated until the failure criteria to determine the time to failure for given failure probability. In case of distribution based methods, the predicted time to failure data is logarithmically extrapolated to get CLT. The CLT prognosis obtained by negatively skewed generalized extreme value distribution is in better agreement with the measured CLT values when compared with the CLT prognosis with standard normal distribution. The CLT obtained using the linear extrapolation of time to failures from the percentiles of measured contact resistance is also in good agreement with the measured CLT. The CLT prognosed using the exponential extrapolation of $37^{th}$ percentile of contact resistance gives adequately precise prediction of CLT and is the shortest method of CLT prognosis.

However, it is advisable to use an indirect method as the failure pattern in the given connector can be understood and the possibility of error in the prediction can be avoided. Even though, the CLT estimated by the standard normal distribution has highest deviation from the measured CLT, the prognosis is always on the safer side and hence can be employed reliably. Through this method, the time required for reliability estimation can be brought down by around 85 % in connectors which have low reliability and fail relatively faster during operation. In connectors with intermediate stability which require longer time to fail, the proposed method enables up to 95 % reduction in time required for reliable prognosis. In case of highly stable connectors which do not fail by the end of the test duration, the proposed method can be applied for such contacts also and CLT can be predicted which would be otherwise not possible with

Weibull distribution. For validation of prognosis results in connectors with no failures, the FIT rate based on Chi-square distribution is used in combination with Weibull FIT rate.

The highly stable connectors have $q < 2$. For the majority of the connectors which show surge in contact resistance, the $q$ values shortly before the surge point range between 4 and 50. The scope of further possibility of reduction in the time needed for reliability estimation is tested with respect to $q$ values. The data with respect to different $q$ values from surge till $q$ values of 2 to 5 depending on the stability of connector are tested. It is observed that the further reduction in time for reliable prognosis of CLT is possible. The data corresponding to the $q$ values as low as 2 to 5 gives good estimation of CLT thereby greatly reducing the time needed for reliability estimation. However, it is advisable to calculate the CLT at different $q$ values and compare the failure pattern trends in order to confirm the results.

The contact resistance development pattern plays an important role in prognosis based on $q$ values. When the contact resistance development trend continuously moves in upward direction, the data corresponding to lower $q$ values can be reliably used for CLT prognosis. However, in the case of highly stable connectors where the contact resistance fluctuates within a very small range and is as good as treated to be constant, data selection based on $q$ values is not possible. In such a case, the targeted CLT is determined using Chi-square and Weibull FIT rates along with the suitable acceleration factor. The prognosis is to be performed with data corresponding to different durations. When the prognosis with data corresponding to a number of test durations continuously predict approximately similar CLT values and are in good agreement with targeted CLT, then the prognosis is to be considered to be reliable. The tests in cases with no failures and constant $q$ values are recommended to be run till a duration of at least $1/100^{th}$ of the targeted CLT.

The proposed statistical process for reliability prognosis is thus not influenced by the failure mechanisms and the detailed knowledge of the connector system is not required for its implementation. Through this method, the remaining useful life of the connectors and future performance can be predicted. The state of health parameters such as $q$ value can be employed to monitor the connector performance in the sophisticated systems where large number of connectors are installed and hence monitor the system health. Based on the developments in the contact resistance, preventive measures can be taken well in advance.

**Outlook**

The proposed structural optimization procedure applied for round connectors in this work can be used for the other types of connectors such as flat ones. From the point of view of thermal-electrical performance, it would be interesting to include the influence of connector casing in the simulation along with performing transient analysis. It would be also interesting to modify the triangular rib shaped simplified roughness using core roughness and average groove width further in such a way that the modelled surface consists of pyramidal shaped asperities and

perform multi-physics analysis investigating the roughness influence on thermal and electrical performance such as contact spot heating and current density distribution. The state of health and lifetime prognosis method could be tested in the accelerated lifetime tests with other kinds of environmental stresses such as humidity, dust and saline conditions.

# 7 List of figures

# 8 List of tables

# 9 References


[1] C. Tamm, "Connectors - the weak link in the chain!," in *2011 IEEE PES 12th International Conference on Transmission and Distribution Construction, Operation and Live-Line Maintenance (ESMO); pp. 1-10; DOI: 10.1109/TDCLLM.2011.6042224*, Providence, RI, USA, 2011.

[2] U. Lindemann, Handbuch Produktentwicklung, München: Carl Hanser Verlag, 2016.

[3] A. Raeburn, "Product development process: The 6 stages (with examples)," Asana, Inc., 01 10 2022. [Online]. Available: https://asana.com/resources/product-development-process. [Accessed 15 01 2023].

[4] J. Feldhausen and B. Gebhardt, Product Lifecycle Management für die Praxis - Ein leitfaden zur modularen Einführung, Umsetzung und Anwendung, Springer-Verlag Berlin Heidelberg; ISBN: 978-3-540-34009-6, 2008.

[5] J. Song, A. Shukla and R. Probst, "Prediction of failure in time (FIT) of electrical connectors with short term tests," *Microelectronics Reliability*, vol. 138; DOI: https://doi.org/10.1016/j.microrel.2022.114684, 2022.

[6] P. Slade, Electrical Contacts: Principles and Applications, Second Edition, Boca Raton, FL: CRC Press; DOI: https://doi.org/10.1201/b15640, 2014.

[7] E. Bock and J. Whitley, "Fretting Corrosion in Electrical Contacts," in *20th Annual Holm Seminar on Electrical Contacts-1974*, Harrisburg, Penna, 1974.

[8] P. van Dijk, "Critical Aspects of Electrical Connector Contacts," in *Proc. 21st ICEC; pp. 161-168;*, 2002.

[9] S. Timsit, "Electrical contact resistance: properties of stationary interfaces," in *Electrical Contacts - 1998. Proceedings of the Forty-Fourth IEEE Holm Conference on Electrical Contacts; pp. 1-19; DOI: 10.1109/HOLM.1998.722422*, Arlington, VA, USA, 1998.

[10] M. Antler, "Survey of Contact Fretting in Electrical Connectors," *IEEE Transactions on Components, Hybrids, and Manufacturing Technology*, vol. 8, no. 1, pp. 87-104; DOI: 10.1109/TCHMT.1985.1136462, 1985.

[11] G. Kulwanoski, M. Gaynes, A. Smith and B. Darrow, "Electrical contact failure mechanisms relevant to electronic packages," in *Electrical Contacts - 1991 Proceedings of the Thirty-Seventh IEEE HOLM Conference on Electrical Contacts; pp. 184-192; DOI: 10.1109/HOLM.1991.170823*, Chicago, USA, 1991.

[12] D. Hilmert, H. Yuan and J. Song, "The Analysis of Failure Mechanisms of Electrical Connectors in Long-term Use Field Vehicles," in *2022 IEEE 67th Holm Conference on Electrical Contacts (HLM); pp. 1-8; DOI: 10.1109/HLM54538.2022.9969820*, Tampa, FL, USA, 2022.

[13] Å. K. Rudolphi and S. Jacobson, "Stationary loading, fretting and sliding of silver coated copper contacts — influence of corrosion films and corrosive atmosphere," *Tribology International,* vol. 30, no. 3, pp. 165-175; DOI: https://doi.org/10.1016/S0301-679X(96)00031-X, 1997.

[14] J. Song, H. Yuan and V. Schinow, "Fretting corrosion behavior of electrical contacts with tin coating in atmosphere and vacuum," *Wear,* Vols. 426-427, no. Part B, pp. 1439-1445; DOI: https://doi.org/10.1016/j.wear.2018.11.024, 2019.

[15] H. Yuan, J. Song, C. Koch, E. Silbernagel and V. Schinow, "Tribological properties and fretting performance of gold, silver and tin coatings," in *Proceedings of XXX International Conference on Surface Modification Technologies (SMT30)*, Milan, Italy, 2016.

[16] X. Guan, N. Shu, K. Bing, Q. Yan, L. Zipin, L. Hongtao and W. Xiaowen, "Multi-Physics Calculation and Contact Degradation Mechanism Evolution of GIB Connector Under Daily Cyclic Loading," *IEEE Transactions on Magnetics,* vol. 52, no. 3, pp. 1-4; DOI: 10.1109/TMAG.2015.2488626, 2016.

[17] S. Sawada, K. Shimizu, S. Shimada and Y. Hattori, "Prediction of Electrical Contact Resistance of Tin-Plated and Silver-Plated Terminals," *SEI Technical Review,* vol. 71, pp. 37-43, 2010.

[18] H. Yuan, J. Song and V. Schinow, "Simulation Methodology for Prediction of the Wear on Silver-Coated Electrical Contacts With a Sphere/Flat Configuration," *IEEE Transactions on Components, Packaging and Manufacturing Technology,* vol. 8, no. 3, pp. 364-374; DOI: 10.1109/TCPMT.2017.2776748;, 2018.

[19] A. Lee, A. Mao and M. Mamrick, "Fretting corrosion of tin at elevated temperatures," in *Electrical Contacts, 1988., Proceedings of the Thirty Fourth Meeting of the IEEE Holm Conference on Electrical Contacts; pp. 87-91; DOI: 10.1109/HOLM.1988.16101,* San Francisco, CA, USA, 1988.

[20] R. Mroczkowski, "Concerning reliability modeling of connectors," in *Electrical Contacts - 1998. Proceedings of the Forty-Fourth IEEE Holm Conference on Electrical Contacts; pp. 57-68; DOI: 10.1109/HOLM.1998.722428*, Arlington, VA, USA, 1998.

[21] Z. Zeng, Z. Zhou, X. Li, M. Tang and P. Bei, "Numerical modeling and optimization on micro-D electrical connector," *International Journal of Numerical Modelling: Electronic Networks, Devices and Fields,* vol. 31, no. 1, e2256; DOI: https://doi.org/10.1002/jnm.2256, 2017.

[22] K. Duan, F. Zhu, Y. Li, K. Tang, S. Liu and Y. Chen, "Contact resistance investigation of electrical connector with different shrink range," in *2014 15th International Conference on Electronic Packaging Technology, IEEE; pp. 1146-1149; DOI: 10.1109/ICEPT.2014.6922846*, Chengdu, China, 2014.

[23] Y. Zhou, J. Yang and X. Yin, "Analysis and improvement of a wire harness terminal connector with insufficient locking force," in *7th International Conference on Reliability of Electrical Products and Electrical Contacts*, Suzhou, China, 2019.

[24] Y. Li, F. Zhu, Y. Chen, K. Duan, K. Tang and S. Liu, "Analysis of insertion force of electric connector based on FEM," in *Proceedings of the 21th International Symposium on the Physical and Failure Analysis of Integrated Circuits (IPFA); pp. 195-198; DOI: 10.1109/IPFA.2014.6898160*, Marina Bay Sands, Singapore, 2014.

[25] F. Loos, H.-D. Ließ and K. Dvorsky, "Simulation methods for heat transfer processes in mechanical and electrical connections," in *2011 1st International Electric Drives Production Conference; pp. 214-220; DOI: 10.1109/EDPC.2011.6085573*, Nuremberg, Germany, 2011.

[26] S. Angadi, R. L. Jackson, V. Pujar and M. R. Tushar, "A Comprehensive Review of the Finite Element Modeling of Electrical Connectors Including Their Contacts," *IEEE Transactions on Components, Packaging and Manufacturing Technology*, vol. 10, no. 5, pp. 836-844; DOI: 10.1109/TCPMT.2020.2982207, May 2020.

[27] J. R. Polchow, S. V. Angadi, R. L. Jackson, G. T. Flowers, S.-y. Choe, B.-Y. Lee and L. Zhong, "A Multi-Physics Finite Element Analysis of Round Pin High Power Connectors," in *2010 Proceedings of the 56th IEEE Holm Conference on Electrical Contacts; pp. 1-9; DOI: 10.1109/HOLM.2010.5619567*, Charleston, SC, USA, 2010.

[28] S. V. Angadi, S. Jackson, S. -Y. Choe, G. T. Flowers, B. -Y. Lee and L. Zhong, "A Multi-Physics Finite Element Model of a 35A Automotive Connector Including Multiscale Rough Surface Contact," in *2010 Proceedings of the 56th IEEE Holm Conference on Electrical Contacts, pp. 1-11; DOI: 10.1109/TCHMT.1985.1136462*, Charleston, SC, USA, 2010.

[29] Luo Yanyan et al., "The finite element analysis on the stress field of contacts for electrical connectors," in *Proceedings 2013 International Conference on Mechatronic Sciences, Electric Engineering and Computer (MEC); pp. 3317-3320; DOI: 10.1109/MEC.2013.6885589*, Shengyang, 2013.

[30] A. Beloufa, "The Effect of Cable Section on the Variation of Power Automotive Connector Temperature," *IEEE Transactions on Components, Packaging and Manufacturing Technology*, vol. 9, no. 6, pp. 1020-1028; doi: 10.1109/TCPMT.2019.2914894, 2019.

[31] A. Beloufa, "Influence of Shapes, Contact Forces and High Copper Alloys on the Contact Resistance and Temperature," in *Proceedings of the 2nd WSEAS*

*International Conference on Engineering Mechanics, Structures and Engineering Geology (EMESEG '09)*, Rodos, 2009.

[32] G. Shao, Q. Dong, J. Hong, S. Wang, J. Qiu and C. Liu, "Finite Element Analysis of Mechanical and Electric Properties of Electric Connector in Electric Vehicle," in *2012 Sixth International Conference on Electromagnetic Field Problems and Applications; pp. 1-4; DOI: 10.1109/ICEF.2012.6310275*, Dalian, China, 2012.

[33] X. Guan, J. Qin, N. Shu and H. Peng, "Studies on Contact Degradation Process and Failure Mechanism of GIB Plug-In Connector," *IEEE Transactions on Components, Packaging and Manufacturing Technology,* vol. 9, no. 9, pp. 1776-1784; DOI: 10.1109/TCPMT.2019.2930415, 2019.

[34] H. Essone-Obame, L. Cretinon, R. El Abdi, N. Benjemaa and E. Carvou, "Spring Stiffness Investigations for Long Lifetime Connectors," in *2009 Proceedings of the 55th IEEE Holm Conference on Electrical Contacts; pp. 214-219; DOI: 10.1109/HOLM.2009.5284398*, Vancouver, BC, Canada, 2009.

[35] N. Benjemaa and R. El Abdi, "Study of contact resistance for high copper alloys under indentation and insertion forces," *International journal of systems applications, engineering and development,* vol. 2, no. 2, pp. 75-82, 2008.

[36] M. Blauth, "Parametrisierte Modelle zur konstruktiven Auslegung optimierter elektrischer Steckverbinderkontakte," TU Ilmenau, Dissertation; ISBN: 978-3-86360-155-3;, 2017.

[37] H. Yuan, J. Song and V. Shinow, "The Influence of Roughness on the Wear and Fretting Behavior of Silver Coated Electrical Contacts," in *Proceedings of the 28th International Conference on Electric Contacts (ICEC2016); pp. 93-98;*, Edinburgh, 2016.

[38] H. Liu and J. W. McBride, "A Finite-Element-Based Contact Resistance Model for Rough Surfaces: Applied to a Bilayered Au/MWCNT Composite," *IEEE Transactions on Components, Packaging and Manufacturing Technology,* vol. 8, no. 6, pp. 919-926; DOI: 10.1109/TCPMT.2017.2782723, 2018.

[39] P. Lindholm, "Numerical Study of Asperity Distribution in an Electrical Contact," in *2011 IEEE 57th Holm Conference on Electrical Contacts (Holm); pp. 1-5; DOI: 10.1109/HOLM.2011.6034796*, Minneapolis, MN, USA, 2011.

[40] K. Wachman, E. Saputra, R. Ismail, J. Jamari and A. Bayuseno, "Analysis of the Contact Area of Smooth and Rough Surfaces in Contact with Sphere Indenter Using Finite Element Method," *MATEC Web of Conferences,* vol. 58; p. 04007; DOI: 10.1051/matecconf/20165804007, 2016.

[41] B. Persson, "Contact mechanics for randomly rough surfaces," *Surface Science Reports*, vol. 61, no. 4, pp. 201-227, DOI: https://doi.org/10.1016/j.surfrep.2006.04.001, 2006.

[42] J. Greenwood and J. Willianson, "Contact of Nominally Flat Surfaces," *Proceedings of the Royal Society of London. Series A, Mathematical and Physical Sciences*, vol. 295, no. 1442, pp. 300-319; DOI: https://doi.org/10.1098/rspa.1966.0242, 1966.

[43] O. Korchevnik, R. Goltsberg, Y. Kligerman and I. Etsion, "Electrical Resistance Model of a Bilayer-Coated Spherical Contact," *IEEE Transactions on Components, Packaging and Manufacturing Technology,* vol. 8, no. 9, pp. 1614-1620; DOI: 10.1109/TCPMT.2018.2854755, 2018.

[44] C. Gao, H. Proudhon and M. Liu, "Three-dimensional finite element analysis of shallow indentation of rough strain-hardening surface," *Friction,* vol. 7(6), pp. 587-602; ISSN 2223-7690, 2019.

[45] R. Jackson, M. Down, H. Liu and J. Mcbride, "A comparison of the predictions of a multiscale model and optical real area of contact measurements," in *2014 IEEE 60th Holm Conference on Electrical Contacts (Holm); pp. 1-8; DOI: 10.1109/HOLM.2014.7031026*, New Orleans, USA, 2014.

[46] W. Shujuan, H. Fang, S. Bonan and Z. Guofu, "Method for calculation of contact resistance and finite element simulation of contact temperature rise based on rough surface contact model," in *26th International Conference on Electrical Contacts (ICEC 2012); pp. 317-321; DOI: 10.1049/cp.2012.0668*, Beijing, China, 2012.

[47] J. McBride, K. Cross and H. Liu, "Determination of contact resistance from a finite element analysis of a rough surface using the peak summit density method," in *ICEC2022 Sapporo - 31st International Conference on Electrical Contacts*, Hokkaido, Japan, 2022.

[48] A. Megalingam and M. Mayuram, "Effect of surface parameters on finite element method based deterministic Gaussian rough surface," *Proceedings of the Institution of Mechanical Engineers, Part J: Journal of Engineering Tribology*, vol. 228, no. 12; DOI: https://doi.org/10.1177/1350650114539300, 2014.

[49] L. Kogut and K. Komvopoulos, "Electrical contact resistance theory for conductive rough surfaces," *Journal of Applied Physics*, vol. 94, no. 5, pp. 3153-3162; DOI: https://doi.org/10.1063/1.1592628, 2003.

[50] F. Maaboudallah, M. Najah and N. Atalla, "A Review on the Contact Mechanics Modeling of Rough Surfaces in the Elastic Regime: Fundamentals, Theories, and Numerical Implementations," in *Tribology of Machine Elements - Fundamentals and Applications*, London, United Kingdom, IntechOpen; DOI: 10.5772/intechopen.102358, 2022.

[51] C. Zhang and W. Ren, "Modelling of 3D Surface Morphologies for Predicting the Mechanical Contact Behaviors and Associated Electrical Contact Resistance," *Tribology Letters*, Vols. 69, Article 20; DOI: https://doi.org/10.1007/s11249-020-01392-9, 2021.

[52] W. Wilson, S. Angadi and R. Jackson, "Electrical Contact Resistance Considering Multi-Scale Roughness," in *2008 Proceedings of the 54th IEEE Holm Conference on Electrical Contacts; pp. 190-197; DOI: 10.1109/HOLM.2008.ECP.43*, Orlando, FL, USA, 2008.

[53] Y. Wen, J. Tang, W. Zhou, L. Li and C. Zhu, "New analytical model of elastic-plastic contact for three-dimensional rough surfaces considering interaction of asperities," *Friction*, vol. 10, pp. 217-231; DOI: https://doi.org/10.1007/s40544-020-0419-7, 2022.

[54] A. Sohouli, A. Goudarzi and R. Alashti, "Finite element analysis of elastic-plastic contact mechanic considering the effect of contact geometry and material properties," *Journal of Surface Engineered Materials and Advanced Technology*, vol. 1, no. 3, pp. 125-129, 2011.

[55] J. A. Greenwood, "Constriction Resistance and the Real Area of Contact," *Brit. J. Appl. Phys*, vol. 17, no. 12; DOI: 10.1088/0508-3443/17/12/310, pp. 1621-1632, 1966.

[56] H. Yuan, J. Song and V. Schinow, "Fretting corrosion of tin coated electrical contacts: The influence of normal force, coating thickness and geometry of sample configuration," in *2016 IEEE 62nd Holm Conference on Electrical Contacts (Holm); pp. 33-38; DOI: 10.1109/HOLM.2016.7780003*, Clearwater Beach, FL, USA, 2016.

[57] T. Dell, "The RAS Implications of DIMM Connector Failure Rates in Large, Highly Available Server Systems," in *Electrical Contacts - 2007 Proceedings of the 53rd IEEE Holm Conference on Electrical Contacts; pp. 256-261; DOI: 10.1109/HOLM.2007.4318226*, Pittsburgh, PA, USA, 2007.

[58] J. Song, H. Yuan and C. Koch, "Accelerated Testing of Electromechanical Connectors Considering Thermal and Mechanical Loads," in *2018 IEEE Holm Conference on Electrical Contacts; pp. 467-474; DOI: 10.1109/HOLM.2018.8611653*, Albuquerque, NM, USA, 2018.

[59] D. F. Frost and K. F. Poole, "A Method for Predicting VLSI-Device Reliability Using Series Models for Failure Mechanisms," *IEEE Transactions on Reliability*, vol. 36, no. 2, pp. 234-242; DOI: 10.1109/TR.1987.5222353, 1987.

[60] N.A., *How to measure lifetime for Robustness Validation - step by step*, Frankfurt am Main, Germany: Robustness Validation Forum ZVEI - German Electrical and Electronic Manufacturers Association e.V., 2012.

[61] N.A., Das Lebensdauernetz - Leitfaden zur grafischen Bestimmung von Zuverlässigkeitskenssgrößen der Weibull- Verteilung (DGQ*Band 17-26), Frankfurt am Main: Deutsche Gesellschaft für Qualität e. V., 1995.

[62] N.A., *Technischer Leitfaden - TLF 0214, Validierung von Automotive-Niedervolt-Steckverbindern, ZVEI,* Frankfurt am Main: ZVEI, 2021.

[63] H. Wang and T. Xu, "Reliability assessment of degradation product based on accelerated factor," in *2013 International Conference on Quality, Reliability, Risk, Maintenance, and Safety Engineering (QR2MSE); pp. 1147-1151; DOI: 10.1109/QR2MSE.2013.6625770*, Chengdu, China, 2013.

[64] W. Nelson, Accelerated testing: statistical models, test plans and data analysis, 2nd edition, Hoboken: John Wiley & Sons, Inc., 2004.

[65] Á. Gómez-Pau, J.-R. Riba and M. Moreno-Eguila, "Time Series RUL Estimation of Medium Voltage Connectors to Ease Predictive Maintenance Plans," *Applied Sciences 2020,* vol. 10, no. 24; DOI: https://doi.org/10.3390/app10249041, 2020.

[66] J. Sikorska, M. Hodkiewicz and L. Ma, "Prognostic modelling options for remaining useful life estimation by industry," *Mechanical Systems and Signal Processing,* vol. 25, no. 5, pp. 1803-1836; DOI: https://doi.org/10.1016/j.ymssp.2010.11.018, 2011.

[67] M. Pecht and R. Jaai, "A prognostics and health management roadmap for information and electronics-rich systems," *Microelectronics Reliability,* vol. 50, pp. 317-323, 2010.

[68] J. Yu, "State-of-Health Monitoring and Prediction of Lithium-Ion Battery Using Probabilistic Indication and State-Space Model," *IEEE Transactions on Instrumentation and Measurement,* vol. 64, no. 11, pp. 2937-2949; DOI: 10.1109/TIM.2015.2444237, 2015.

[69] Y. Zhao, E. Zio and G. Fu, "Remaining storage life prediction for an electromagnetic relay by a particle filtering-based method," *Microelectronics Reliability,* vol. 79, pp. 221-230; DOI: https://doi.org/10.1016/j.microrel.2017.03.026, 2017.

[70] A. Mavinkurve, L. Goumans, G. O'Halloran, R. Rongen and M.-L. Farrugia, "Copper wire interconnect reliability evaluation using in-situ High Temperature Storage Life (HTSL) tests," *Microelectronics Reliability,* vol. 54, no. 9-10, pp. 1661-1665; DOI: https://doi.org/10.1016/j.microrel.2014.07.026, 2014.

[71] Z. Yang, S. Li, C. Chen, H. Mei and Y. Liu, "Reliability prediction of rotary encoder based on multivariate accelerated degradation modeling," *Measurement,* Vols. 152, 107395; DOI: https://doi.org/10.1016/j.measurement.2019.107395, 2020.

[72] J. Martínez, J. Riba and M. Moreno-Eguilaz, "State of Health Prediction of Power Connectors by Analyzing the Degradation Trajectory of the Electrical Resistance,"

*Electronics 2021,* Vols. 10(12), 1409; DOI: https://doi.org/10.3390/electronics10121409 , 2021.

[73] M. Braunovic, V. Izmailov and M. V. Novoselova, "A model for life time evaluation of closed electrical contacts," in *Proceedings of the Fifty-First IEEE Holm Conference on Electrical Contacts; pp. 217-223; DOI: 10.1109/HOLM.2005.1518247*, Chicago, IL, USA, 2005.

[74] B. Sun, L. Yu, Z. Wang, Y. Ren, Q. Feng, D. Yang, M. Lu and X. Chen, "Remaining useful life prediction of aviation circular electrical connectors using vibration-induced physical model and particle filtering method," *Microelectronics Reliability,* vol. 92, pp. 114-122; DOI: https://doi.org/10.1016/j.microrel.2018.11.015, 2019.

[75] Y. Ren, Q. Feng, T. Ye and B. Sun, "A Novel Model of Reliability Assessment for Circular Electrical Connectors," *IEEE Transactions on Components, Packaging and Manufacturing Technology,* vol. 5, no. 6, pp. 755-761; doi: 10.1109/TCPMT.2015.2419222, 2015.

[76] J. Song, H. Yuan, A. Shukla and C. Koch, "Correlation of Connector Contact Failures in Accelerated Testing and in Long-term Use Field Vehicles," in *2019 IEEE Holm Conference on Electrical Contacts; pp. 296-302; DOI: 10.1109/HOLM.2019.8923844*, Milwaukee, WI, USA, 2019.

[77] E. Vinaricky, A. Keil and W. Merl, Elektrische Kontakte, Werkstoffe und Anwendungen: Grundlagen, Technologien, Prufverfahren, Berlin: Springer-Verlag; ISBN 978-3-642-62698-2, 2002.

[78] D. Weinhandl, "WHY IS COPPER THE BEST CHOICE FOR ELECTRICAL CONNECTORS?," Mead Metals, Inc., 11 2021. [Online]. Available: https://www.meadmetals.com/blog/copper-electrical-connectors-conductivity. [Accessed 15 01 2022].

[79] V. Behrens and R. Paulsen, Elektrische Kontakte: Werkstoffe, Gestaltungen und Anwendungen in der Nachrichten-, Automobil- und Energietechnik, 3. Auflage, Renningen: Expert Verlag, ISBN 978-3-8169-2292-6, 2010.

[80] M. Antler, "Tribology of metal coatings for electrical contacts," *Thin Solid Films,* vol. 84, no. 3, pp. 245-256, 1981.

[81] J. Williamson, "The micro-world of the contact spot," in *Proceedings of the Holm Conference on Electrical Contacts, pp 1-10,* Chicago, 1981.

[82] Z. X. Yao, L. M. Yin, L. P. Zhang and J. Zhou, "The effect of coating thickness and external force on the growth of tin whisker," in *2014 15th International Conference on Electronic Packaging Technology; pp. 100-1103; DOI: 10.1109/ICEPT.2014.6922836*, Chengdu, 2014.

[83] J. Song, C. Koch and L. Wang, "Correlation between Wear Resistance and Lifetime of Electrical Contacts," *Advances in Tribology*, vol. 12; DOI: https://doi.org/10.1155/2012/893145, 2012.

[84] M. Antler, "Electrical Effects of Fretting Connector Contact Materials: A Review," *Wear*, vol. 106, no. 1-3, pp. 5-33, 1985.

[85] S. Kyeong and M. G. Pecht, Electrical Connectors - Design, Manufacture, Test and Selection, West Sussex, UK: John Wiley & Sons Ltd.; ISBN 9781119679806, 2021.

[86] M. Antler, "Fretting of electrical contacts: An investigation of palladium mated to other materials," *Wear*, vol. 81, no. 1, pp. 159-173, 1982.

[87] M. Antler, "Fretting Corrosion of Solder-Coated Electrical Contacts," *IEEE Transactions on Components, Hybrids, and Manufacturing Technology*, vol. 7, no. 1, pp. 129-138; DOI: 10.1109/TCHMT.1984.1136330, 1984.

[88] E. Bock, "Mateability of tin to gold, palladium, and silver," in *40th Conference Proceedings on Electronic Components and Technology; pp. 840-844; DOI: 10.1109/ECTC.1990.122287*, Las Vegas, USA, 1990.

[89] N.A., "Surface Coating of Copper Alloy Strip for Electrical Connector Applications," Materion Brush Performance Alloys, 2011. [Online]. Available: https://materion.com/-/media/files/alloy/tech-briefs/at0017-0311---tech-briefs---surface-coating-of-copper-alloy-strip.pdf. [Accessed 08 08 2022].

[90] G. P. Gololobov, V. S. Gurov, S. M. Karabanov, D. V. Suvorov and V. Slivkin, "Multilayer nanosized galvanic coatings of electrical contacts of durable magnetically operated switches," in *2014 IEEE 9th Nanotechnology Materials and Devices Conference (NMDC); pp. 108-111; DOI: 10.1109/NMDC.2014.6997434*, Aci Castello, Italy, 2014.

[91] L. Rip, S. Satapathy and K.-T. Hsieh, "Effect of geometry change on the current density distribution in C-shaped armatures," *IEEE Transactions on Magnetics*, vol. 39, no. 1, pp. 72-75; DOI: 10.1109/TMAG.2002.805906, 2003.

[92] N.A., "Coefficients of Linear Thermal Expansion - Linear Thermal Expansion Coefficient Values for Metals and Alloys," Instrumentation & Control, [Online]. Available: https://instrumentationandcontrol.net/thermal-expansion-coefficient-table.html. [Accessed 12 08 2022].

[93] N.A., "Pure Metal Resistivity Data," Ness Engineering, Inc, [Online]. Available: http://www.nessengr.com/technical-data/resistivity/. [Accessed 12 08 2022].

[94] S. Mossouess, N. Benjemâa, E. Carvou, R. E. Abdi, L. Benmamas and L. Doublet, "Fretting corrosion in power contacts: Electrical and thermal analysis," in *2014 IEEE 60th Holm Conference on Electrical Contacts (Holm); pp. 1-5; DOI: 10.1109/HOLM.2014.7031058*, New Orleans, USA, 2014.

[95] S. C. Lee and N. Ren, "Behavior of Elastic-Plastic Rough Surface Contacts as Affected by Surface Topography, Load, and Material Hardness," *Tribology Transactions,* vol. 39, no. 1, pp. 67-74; DOI: https://doi.org/10.1080/10402009608983503, 1996.

[96] M. Braunovic, V. Konchits and N. Myshkin, Electrical Contacts - Fundamentals, Applications and Technology, Boca Raton, Florida: CRC Press; ISBN-10: 1-57444-727-0, 2007.

[97] S. N. Kharin, M. M. Sarsengeldin, S. Kassabek and T. Nauryz, "The Model of Melting and Welding of Closed Electrical Contacts with Softening Contact Zone," in *2018 IEEE Holm Conference on Electrical Contacts; pp. 38-42; DOI: 10.1109/HOLM.2018.8611754*, Albuquerque, NM, USA, 2018.

[98] C. Maul and J. W. McBride, "A model to describe intermittency phenomena in electrical connectors," in *Proceedings of the Forty-Eighth IEEE Holm Conference on Electrical Contacts; pp. 165-174; doi: 10.1109/HOLM.2002.1040838*, Orlando, USA, 2002.

[99] T. Kondo, H. Nakata, J. Sekikawa, Y. Kubota, K. Hayakawa and T. Nakamura, "An analysis of relationship between contact resistance and fracture of oxide film for connector contacts using finite element method," in *2014 IEEE 60th Holm Conference on Electrical Contacts (Holm); pp. 1-6; DOI: 10.1109/HOLM.2014.7031025*, New Orleans, USA, 2014.

[100] R. Tzeneva and Y. Slavtchev, "Electric field distribution in bolted busbar assemblies with longitudinal slots," in *In Proceedings of the 10th WSEAS international conference on Instrumentation, measurement, circuits and systems (IMCAS'11); pp. 60-64*, Venice, Italy, 2011.

[101] H. Seehase, "A reliability model for connector contacts," *IEEE Transactions on Reliability*, vol. 40, no. 5, pp. 513 - 523; DOI: 10.1109/24.106766, 1991.

[102] R. Holm, Electric Contacts 4th Edition, Berlin: Springer-Verlag, 1967.

[103] H. Aichi and N. Tahara, "Analysis on the constriction resistance of the electric contact by the contact model using electrolyte bath," in *Proc. 20th Int Conf Elect Cont*, Nagoya, Japan, 1994.

[104] M. Nakamura, "Constriction resistance of conducting spots by the boundary element method," *IEEE Transactions on Components, Hybrids, and Manufacturing Technology,* vol. 16, no. 3, pp. 339-343; DOI: 10.1109/33.232062, 1993.

[105] D. Keller, "Electric Contact Phenomena in Ultra Clean and Specifically Contaminated Systems," *IEEE Transactions on Parts, Hybrids, and Packaging*, vol. 8, no. 1, pp. 4-15; DOI: 10.1109/TPHP.1972.1136550, 1972.

[106] P. Barkan and E. J. Tuohy, "A Contact Resistance Theory for Rough Hemispherical Silver Contacts in Air and in Vacuum," *IEEE Transactions on Power Apparatus and Systems,* vol. 84, no. 12, pp. 1132-1143; DOI: 10.1109/TPAS.1965.4766148, 1965.

[107] Y. Nabeta, Y. Saitoh, S. Sawada, Y. Hattori and T. Tamai, "Growth Law of the Oxide Film Formed on the Tin Plated Contact Surface and Its Contact Resistance Characteristic," in *2009 Proceedings of the 55th IEEE Holm Conference on Electrical Contacts; pp. 176-181; DOI: 10.1109/HOLM.2009.5284404*, Vancouver, Canada, 2009.

[108] W. Abbott, "The Effects of Substrate on the Contact Resistance of Tarnish Films," *IEEE Transactions on Parts, Materials and Packaging,* vol. 7, no. 1, pp. 6-10; DOI: 10.1109/TPMP.1971.1136442, 1971.

[109] C. Wang and J. Schipper, "A numerical-analytical approach to determining the real contact area of rough surface contact," *Tribology - Materials, Surfaces & Interfaces*, vol. 14, no. 3, pp. 166-176, 2020.

[110] I. Nistal-González, A. Bettray and K. Maulwurf, "Thermal calculation using a 3D-EM solver and thermal-electrical analogy," in *2012 6th European Conference on Antennas and Propagation (EUCAP); pp. 1-4; DOI: 10.1109/EuCAP.2012.6206535*, Prague, Czech Republic, 2012.

[111] F. Kohlrausch, "Über den stationären Temperaturzustand eines elektrisch geheizten Leiter," *Annalen der Physik,* vol. 306, no. 1, pp. 132-158; DOI: https://doi.org/10.1002/andp.19003060107, 1900.

[112] B. D. Jensen, K. Huang, L. L. -W. Chow and K. Kurabayashi, "Low-force contact heating and softening using micromechanical switches in diffusive-ballistic electron-transport transition," *Applied Physics Letters,* Vols. 86, 023507; DOI: https://doi.org/10.1063/1.1850191, 2005.

[113] R. S. Timsit, "Electrical conduction through small contact spots," in *Proceedings of the 50th IEEE Holm Conference on Electrical Contacts and the 22nd International Conference on Electrical Contacts Electrical Contacts, 2004; pp. 184-191; DOI: 10.1109/HOLM.2004.1353116*, Seattle, USA, 2004.

[114] X. Zhou, Q. J. Wang and Y. Chung, "Contact Melting Voltage," in *Encyclopedia of Tribology*, Springer, Boston, MA, 2013, pp. 481-483.

[115] R. El Abdi and N. Benjemaa, "Study of contact resistance for high copper alloys under indentation and insertion forces," *International Journal of Systems Applications, Engineering & Development,* vol. 2, no. 2, pp. 75-82, 2008.

[116] N. Zini, M. de Rooij, M. Fadafan, M. Bazr Afshan Fadafan, N. Ismail and D. Schipper, "Extending the Double-Hertz Model to Allow Modeling of an Adhesive

Elliptical Contact," *Tribology Letters,* Vols. 66, 30; DOI: https://doi.org/10.1007/s11249-017-0976-8, 2018.

[117] S. Fouvry, P. Jedrzejczyk and P. Chalandon, "Introduction of an exponential formulation to quantify the electrical endurance of micro-contacts enduring fretting wear: Application to Sn, Ag and Au coatings," *Wear,* vol. 271, no. 9-10, pp. 1524-1534; DOI: https://doi.org/10.1016/j.wear.2011.01.058, 2011.

[118] I. Green, "An Elastic-plastic Finite Element Analysis of Two Interfering Hemispheres Sliding in Frictionless Contact," *Physical Science International Journal,* vol. 19, no. 1, pp. 1-34, 2018.

[119] V. L. Popov, M. Heß and E. Willert, Handbook of Contact Mechanics, Berlin: Springer-Verlag GmbH; ISBN 978-3-662-58708-9, 2019.

[120] X. Zhu, "Tutorial on Hertz Contact Stress - University of Arizona," 2012. [Online]. Available: https://wp.optics.arizona.edu/optomech/wp-content/uploads/sites/53/2016/10/OPTI-521-Tutorial-on-Hertz-contact-stress-Xiaoyin-Zhu.pdf. [Accessed 24 08 2022].

[121] A. Sivitski and P. Podra, "Finite element method and its usable applications in wear models design," in *9th International DAAAM Baltic Conference*, Tallinn, Estonia, 2014.

[122] F. Ossart, S. Noel, D. Alamarguy, S. Correia and P. Gendre, "Electro-mechanical modelling of multilayer contacts in electrical connectors," in *Electrical Contacts - 2007 Proceedings of the 53rd IEEE Holm Conference on Electrical Contacts; pp. 1-8; DOI: 10.1109/HOLM.2007.4318187*, Pittsburgh, PA, USA, 2007.

[123] F. Robert, "Investigation on Graphene-Coated Silver-Palladium Microelectrical Contact and Effect of Coating Thickness," *IEEE Transactions on Components, Packaging and Manufacturing Technology*, vol. 10, no. 11, pp. 1821-1828, 2020.

[124] H. Ghaednia, X. Wang, S. Saha, Y. S. A. Xu and R. L. Jackson, "A Review of Elastic–Plastic Contact Mechanics," *Applied Mechanics Review,* vol. 69, no. 6, 060804.; DOI: https://doi.org/10.1115/1.4038187, 2017.

[125] S. Cai and B. Bhushan, "A numerical three-dimensional contact model for rough, multilayered elastic/plastic solid surfaces," *Wear,* vol. 259, no. 7-12; https://doi.org/10.1016/j.wear.2005.02.014, pp. 1408-1423, 2005.

[126] M. Leidner, "Kontaktphysikalische Simulation von Schichtsystemen," Dissertation, TU Darmstadt, 2009.

[127] K. Mao, T. Bell and Y. Sun, "Effect of Sliding Friction on Contact Stresses for Multi-Layered Elastic Bodies With Rough Surfaces," *Journal of Tribology,* vol. 119, pp. 476-480; DOI: https://doi.org/10.1115/1.2833522, 1997.

[128] S. Cole and R. Sayles, "A numerical model for the contact of layered elastic bodies with real rough surfaces," *ASME Jounal of Tribology,* vol. 114, no. 2, pp. 334-340; DOI: https://doi.org/10.1115/1.2920892, 1991.

[129] J. W. McBride and H. Liu, "The Relationship between Contact Resistance and Roughness (Sq) of a Bi-layered Surface using a Finite Element Mode," in *2020 IEEE 66th Holm Conference on Electrical Contacts and Intensive Course (HLM); pp. 176-181; DOI: 10.1109/HLM49214.2020.9307833*, San Antonio, TX, USA, 2020.

[130] R. L. Jackson, W. R. Ashurst, F. G. T., S. Angadi, S. -Y. Choe and M. J. Bozack, "The Effect of Initial Connector Insertions on Electrical Contact Resistance," in *Electrical Contacts - 2007 Proceedings of the 53rd IEEE Holm Conference on Electrical Contacts; pp. 17-24; DOI: 10.1109/HOLM.2007.4318189*, Pittsburgh, USA, 2007.

[131] M. Amor, S. Belghith and S. Mezlini, "Finite Element Modeling of RMS Roughness Effect on the Contact Stiffness of Rough Surfaces," *Tribology in Industry,* vol. 38, no. 3, pp. 392-401, 2016.

[132] S. C. Lee and H. S. Cheng, "On the Relation of Load to Average Gap in the Contact Between Surfaces with Longitudinal Roughness," *Tribology Transactions,* vol. 35, no. 3, pp. 523-529; DOI: https://doi.org/10.1080/10402009208982151, 1992.

[133] T. Tamai, Y. Nabeta, S. Sawada and Y. Hattori, "Property of Tin Oxide Film Formed on Tin-Plated Connector Contacts," in *2010 Proceedings of the 56th IEEE Holm Conference on Electrical Contacts; pp. 1-8; DOI: 10.1109/HOLM.2010.5619529*, Charleston, SC, USA, 2010.

[134] T. Kondo, H. Nakata, J. Sekikawa, Y. Kubota, K. Hayakawa and T. Nakamura, "An analysis of relationship between contact resistance and fracture of oxide film for connector contacts using finite element method," in *2014 IEEE 60th Holm Conference on Electrical Contacts (Holm); pp. 1-6; DOI: 10.1109/HOLM.2014.7031025*, New Orleans, USA, 2014.

[135] D. Hyman and M. Mehregany, "Contact physics of gold microcontacts for MEMS switches," in *Electrical Contacts - 1998. Proceedings of the Forty-Fourth IEEE Holm Conference on Electrical Contacts (Cat. No.98CB36238); pp. 133-140, DOI: 10.1109/HOLM.1998.722438*, Arlington, USA, 1998.

[136] A. Elmanfalouti, R. El Abdi, M. Buisson and E. Carvou, "Deflection analysis of spring connector," in *Proceedings of the Fifty-First IEEE Holm Conference on Electrical Contacts, 2005; pp. 212-216; DOI: 10.1109/HOLM.2005.1518246*, Chicago, IL, USA, 2005.

[137] J. Ni, L. Han, J. Pan, J. Zheng, Y. Shi, Z. Cui and J. Cai, "Evolution of contact performance of industry electrical connector based on reliability accelerated testing,"

*Advances in Mechanical Engineering*, vol. 13, no. 2; DOI: https://doi.org/10.1177/1687814021998829, 2021.

[138] W. Ren, Y. Meng and T. Wang, "Preliminary Experimental Study on the Insertion and Withdrawal Characteristics of Blade and Receptacle Pair," in *2019 IEEE Holm Conference on Electrical Contacts; pp. 1-8; DOI: 10.1109/HOLM.2019.8923675*, Milwaukee, USA, 2019.

[139] R. El Abdi and N. Benjemaa, "Experimental and Analytical Studies of the Connector Insertion Phase," *IEEE Transactions on Components and Packaging Technologies*, vol. 31, no. 4, pp. 751-758; DOI: 10.1109/TCAPT.2008.2001832, 2008.

[140] L. Hong-Yang, "The characteristic research of contact insertion and separation force in connector," in *Thirty-Sixth IEEE Conference on Electrical Contacts, and the Fifteenth International Conference on Electrical Contacts; pp. 619-624; DOI: 10.1109/HOLM.1990.113068*, Montreal, Canada, 1990.

[141] J. L. Queffelec, N. Ben Jemaa, D. Travers and G. Pethieu, "Materials and contact shape studies for automobile connectors development," *IEEE Transactions on Components, Hybrids, and Manufacturing Technology*, vol. 14, no. 1, pp. 90-94; DOI: 10.1109/33.76515, 1991.

[142] A. Ilgevicius, "Analytical and numerical analysis and simulation of heat transfer in electrical conductors and fuses," Universität der Bundeswehr München - Fakultät für Elektrotechnik und Informationstechnik, Munich, 2004.

[143] H. Böhme, Mittelspannungstechnik - Schaltanlagen berechnen und entwerfen, Berlin: HUSS-MEDIEN GmbH, Verlag Technik, ISBN 3-341-01495-0, 2005.

[144] P. von Böckh and T. Wetzel, Heat Transfer - Basics and Practice, Berlin: Springer-Verlag Berlin Heidelberg; ISBN 978-3-642-19182-4, 2012.

[145] P. Stephan, "B - Grundlagen der Wärmeübertragung," in *VDI-Wärmeatlas 11th Edition*, Düsseldorf, VDI-Gesellschaft Verfahrenstechnik und Chemieingenieurwesen; ISBN 978-3-642-19980-6, 2013, pp. 19-36.

[146] J. Mottine and B. Reagor, "Investigation of Fretting Corrosion at Dissimilar Metal Interfaces in Socketed IC Device Applications," *IEEE Transactions on Components, Hybrids, and Manufacturing Technology*, vol. 7, no. 1, pp. 61-68; DOI: 10.1109/TCHMT.1984.1136332, 1984.

[147] X. Guan, L. Wu, N. Shu, H. Peng, Q. Li and Q. Shen, "Finite Element Analysis on Forces, Currents, and Magnetic Fluxes of Misaligned GIS Disconnector," *IEEE Transactions on Power Delivery*, vol. 33, no. 5, pp. 2484-2491; DOI: 10.1109/TPWRD.2018.2823753, 2018.

[148] J. Song, V. Schinow and H. Yuan, "Third bodies in electrical contacts — Wear and electrical performance," in *2017 IEEE Holm Conference on Electrical Contacts; pp. 117-124; DOI: 10.1109/HOLM.2017.8088073*, Denver, CO, USA, 2017.

[149] P. Jedrzejczyk, S. Fouvry and O. Alquier, "Quantification of the electrical contact endurance of thin platted silver coatings subjected to fretting wear: Influence of coating thickness," in *26th International Conference on Electrical Contacts (ICEC 2012); pp: 205-212; DOI: 10.1049/cp.2012.0649*, Beijing, 2012.

[150] R. Wäsche and M. Hartelt, "Fretting," in *Encyclopedia of Lubricants and Lubrication*, Springer, Berlin, Heidelberg, 2014, pp. 680-687.

[151] Y. W. Park, T. Sankara Narayanan and K. Y. Lee, "Effect of fretting amplitude and frequency on the fretting corrosion behaviour of tin plated contacts," *Surface and Coatings Technology*, vol. 201, no. 6, pp. 2181-2192, 2006.

[152] H. Yuan and J. Song, "Fretting Corrosion Behavior of Various Contact Surfaces under Diverse Operating Conditions," in *2019 IEEE Holm Conference on Electrical Contacts; pp. 19-26; DOI: 10.1109/HOLM.2019.8923871*, Milwaukee, WI, USA, 2019.

[153] J. Labbe, S. Mossouess, E. Carvou, R. El Abdi, C. Plouzeau and F. Strat, "Fretting corrosion under controlled atmospheres," 2016. [Online]. Available: https://www.researchgate.net/publication/303844073_Fretting_corrosion_under_controlled_atmospheres. [Accessed 07 09 2022].

[154] N.A., ISO26262-5, Road vehicles - functional safety, part 5: product development at the hardware level, 2016.

[155] T. Urban, "Be confident around automotive functional safety," Texas Instruments Incorporated, [Online]. Available: https://www.ti.com/lit/ml/slyp685/slyp685.pdf?ts=1687811278128&ref_url=https%253A%252F%252Fwww.google.com%252F. [Accessed 26 06 2022].

[156] N.A., "MIL-HDBK-217F, Reliability prediction of electronic equipment," 1991.

[157] N.A., "Siemens SN 29500, Reliability and quality specifications failure rates of components," 2015.

[158] J. Jones and J. Hayes, "A comparison of electronic reliability prediction methodologies," *IEEE Trans. Reliab.*, vol. 48, no. 2, pp. 127-134, 1999.

[159] J. Bowles, "A survey of reliability-prediction procedures for microelectronic devices," *IEEE Trans. Reliab.*, vol. 41, no. 1, pp. 2-12, 1992.

[160] N.A., "JESD91A, Method for developing acceleration models for electronic component failure mechanisms," 2016.

[161] W. Wang and D. Dragomir-Daescu, "Reliability quantification of induction motors-accelerated degradation testing approach," in *Annual Reliability and Maintainability*

*Symposium. 2002 Proceedings; pp. 325-331; DOI: 10.1109/RAMS.2002.981662*, Seattle, WA, USA, 2002.

[162] D. H. Collins, J. K. Freels, A. V. Huzurbazar, R. L. Warr and B. P. Weaver, "Accelerated Test Methods for Reliability Prediction," *Journal of Quality Technology,* vol. 45, no. 3, pp. 244-259; DOI: https://doi.org/10.1080/00224065.2013.11917936, 2013.

[163] M. Spahr, S. Kreitlein, R. Hass, A. Jaumann, T. Gläßel, S. Spreng and J. Franke, "Application and comparison of analytic accelerated test-models for lifetime prediction of a novel contacting method," in *2016 IEEE 62nd Holm Conference on Electrical Contacts (Holm); pp. 94-99; DOI: 10.1109/HOLM.2016.7780013*, Clearwater Beach, FL, USA, 2016.

[164] R. Fu, S.-Y. B. Choe, R. L. Jackson, G. T. Flowers, M. J. Bozack, L. Zhong and D. Kim, "Vibration-Induced Changes in the Contact Resistance of High Power Electrical Connectors for Hybrid Vehicles," *IEEE Transactions on Components, Packaging and Manufacturing Technology,* vol. 2, no. 2, pp. 185-193; DOI: 10.1109/TCPMT.2011.2170168, 2012.

[165] A. Hanif, Y. Yu, D. DeVoto and F. Khan, "A Comprehensive Review Toward the State-of-the-Art in Failure and Lifetime Predictions of Power Electronic Devices," *IEEE Transactions on Power Electronics,* vol. 34, no. 5, pp. 4729-4746; DOI: 10.1109/TPEL.2018.2860587, 2019.

[166] D. J. Klinger, "On the notion of activation energy in reliability: Arrhenius, Eyring, and thermodynamics," in *Annual Reliability and Maintainability Symposium. 1991 Proceedings; pp. 295-300; DOI: 10.1109/ARMS.1991.154451,* Orlando, FL, USA, 1991.

[167] M. Ciappa, F. Carbognani and W. Fichtner, "Lifetime prediction and design of reliability tests for high-power devices in automotive applications," *IEEE Transactions on Device and Materials Reliability,* vol. 3, no. 4, pp. 191-196; DOI: 10.1109/TDMR.2003.818148, 2003.

[168] J. Srinivasan, S. Adve, P. Bose, J. Rivers and C.-K. Hu, "Ramp: A model for reliability aware microprocessor design," IBM Research Report, RC2308 (W0312-122), Dec. 29, 2003.

[169] V. Vasudevan and X. Fan, "An acceleration model for lead-free (SAC) solder joint reliability under thermal cycling," in *2008 58th Electronic Components and Technology Conference; pp. 139-145; DOI: 10.1109/ECTC.2008.4549960,* Lake Buena Vista, FL, USA, 2008.

[170] X. Fan, G. Rasier and V. S. Vasudevan, "Effects of Dwell Time and Ramp Rate on Lead-Free Solder Joints in FCBGA Packages," in *Proceedings Electronic*

*Components and Technology, 2005. ECTC '05.; pp. 901-906; DOI: 10.1109/ECTC.2005.1441379*, Lake Buena Vista, FL, US, 2005.

[171] W. Dauksher, "A Second-Level SAC Solder-Joint Fatigue-Life Prediction Methodology," *IEEE Transactions on Device and Materials Reliability*, vol. 8, no. 1, pp. 168-173; DOI: 10.1109/TDMR.2007.912253, 2008.

[172] G. Greeff and R. Ghoshal, "8 - Production capability management," in *Practical E-Manufacturing and Supply Chain Management*, Burlington, Elsevier, 2004, pp. 214-242; ISBN: 0-7506-6272-7.

[173] D. Hirschmann, D. Tissen, S. Schroder and R. W. De Doncker, "Reliability Prediction for Inverters in Hybrid Electrical Vehicles," *IEEE Transactions on Power Electronics*, vol. 22, no. 6, pp. 2511-2517; DOI: 10.1109/TPEL.2007.909236, 2007.

[174] P. Ellerman, "Calculating Reliability using FIT & MTTF: Arrhenius HTOL Model," Microsemi Corp., [Online]. Available: https://www.microsemi.com/document-portal/doc_view/124041-calculating-reliability-using-fit-mttf-arrhenius-htol-model. [Accessed 21 11 2022].

[175] A. Bensoussan, "Microelectronic reliability models for more than moore nanotechnology products," *FACTA UNIVERSITATIS Series Electronics and Energetics* , pp. 1-25, DOI:10.2298/FUEE1701001B, 2017.

[176] D. J. Wilkins, "The Bathtub Curve and Product Failure Behavior Part One - The Bathtub Curve, Infant Mortality and Burn-in," Hottinger Bruel and Kjaer Inc., [Online]. Available: https://www.weibull.com/hotwire/issue21/hottopics21.htm. [Accessed 19 09 2022].

[177] D. J. Wilkins, "The Bathtub Curve and Product Failure Behavior Part Two - Normal Life and Wear-Out," HBM Prenscia, 12 2002. [Online]. Available: https://www.weibull.com/hotwire/issue22/hottopics22.htm. [Accessed 19 09 2022].

[178] N.A., "Chi-Squared Distribution and Reliability Demonstration Test Design," Reliability Hotwire, Issue 116, HBM Prenscia Inc., 10 2010. [Online]. Available: https://www.weibull.com/hotwire/issue116/relbasics116.htm. [Accessed 19 09 2022].

[179] H. F. Martz, "Reliability Theory," in *Encyclopedia of Physical Science and Technology (Third Edition)*, Academic Press, 2003, pp. 143-159, ISBN 9780122274107.

[180] M. Hughes, "How the Weibull Distribution Is Used in Reliability Engineering," All About Circuits, 18 04 2019. [Online]. Available: https://www.allaboutcircuits.com/technical-articles/how-the-weibull-distribution-is-used-in-reliability-engineering. [Accessed 19 09 2022].

[181] P. Barringer, "Reliability Engineering For Maintenance - Weibull Analysis," Reliabilityweb.com, [Online]. Available: https://reliabilityweb.com/articles/entry/weibull_analysis. [Accessed 19 09 2022].

[182] G. Snedecor and W. Cochran, Statistical Methods, 6th Edition, Iowa, USA: The Iowa State University Press; ISBN 0-8138-1560-6, 1967.

[183] A. Bajpai, I. Calus and J. Fairley, Statistical Methods For Engineers And Scientists, John Wiley & Sons, Ltd., 1978, ISBN: 0471996440.

[184] S. Kotz and S. Nadarajah, Extreme Value Distributions - Theory and Applications, London: Imperial College Press, ISBN 1860942245, 2000.

[185] N.A., "Generalized Extreme Value Distribution," MathWorks, 2022. [Online]. Available: https://uk.mathworks.com/help/stats/generalized-extreme-value-distribution.html. [Accessed 09 12 2022].

[186] S. Coles, An introduction to statistical modeling of extreme values, London: Springer Verlag; ISBN 1852334592, 2001.

[187] A. Shukla, T. Langer, H. Yuan, R. Probst, J. Song and S. Nolte, "Parametric optimization of connectors by means of coupled simulation," in *Elektrische und optische Verbindungstechnik 2021, Tagungsband Der VDE/VDI-GMM-Fachtagung „8. Symposium Connectors, pp. 28-43*, Lemgo, Germany, 2021.

[188] N.A., *ANSYS, Eingineering Data*, ANSYS, 2019.

[189] N.A., "Kupfer," Deutsches Kupferinstitut, [Online]. Available: https://kupfer.de/mediathek/datenblaetter/. [Accessed 07 07 2019].

[190] K. Krishnaiah and P. Shahabudeen, Applied Design of Experiments and Taguchi Methods, New Delhi: PHI Learning Pvt. Ltd.; ISBN-978-81-203-4527-0, 2012.

[191] N.A., "Model-Based Calibration Toolbox," The MathWorks, Inc., [Online]. Available: https://uk.mathworks.com/products/mbc.html. [Accessed 31 03 2020].

[192] M. Myers, "Overview of the Use of Silver in Connector Applications," Tyco Electronics, Harrisburg, PA, 2009.

[193] Y. Yoon, J. Chen, P. Lipschutz, P. Gumbley, M. Rodriguez and K. Griffin, "A Durable Electroplated Silver Contact Finish for Reusable Connectors," in *2021 IEEE 66th Holm Conference on Electrical Contacts (HLM); pp. 130-135; DOI: 10.1109/HLM51431.2021.9671134*, San Antonio, TX, USA, 2021.

[194] M. Blauth, F. Berger and J. Song, "Influence of the electrical resistance and wire size on the current carrying capacity of connectors," in *2014 IEEE 60th Holm Conference on Electrical Contacts (Holm); pp. 1-8; DOI: 10.1109/HOLM.2014.7031043*, New Orleans, LA, 2014.

[195] N.A., "3-D 10-Node Tetrahedral Structural Solid," [Online]. Available: https://www.mm.bme.hu/~gyebro/files/ans_help_v182/ans_elem/Hlp_E_SOLID187.html. [Accessed 09 08 2019].

[196] N.A., "3-D 8 Node Surface -to-Surface Contact," [Online]. Available: https://www.mm.bme.hu/~gyebro/files/ans_help_v182/ans_elem/Hlp_E_CONTA174.html. [Accessed 09 08 2019].

[197] N.A., "3-D Target Segment," [Online]. Available: https://www.mm.bme.hu/~gyebro/files/ans_help_v182/ans_elem/Hlp_E_TARGE170.html. [Accessed 09 08 2019].

[198] N.A., "3-D 10-Node Coupled-Field Solid," [Online]. Available: https://www.mm.bme.hu/~gyebro/files/ans_help_v182/ans_elem/Hlp_E_SOLID227.html. [Accessed 09 08 2019].

[199] H. Liu, D. Leray, P. Pons and S. Colin, "Finite element multi-physics modeling for ohmic contact of microswitches," in *2014 15th International Conference on Thermal, Mechanical and Mulit-Physics Simulation and Experiments in Microelectronics and Microsystems (EuroSimE); pp. 1-8; DOI: 10.1109/EuroSimE.2014.6813877*, Ghent, Belgium, 2014.

[200] R. Li, W. Yang and H. Liang, "Multi-Physics Finite Element Model of Relay Contact Resistance and Temperature Rise Considering Multi-Scale and 3D Fractal Surface," *IEEE Access,* vol. 8, pp. 122241-122250; DOI: 10.1109/ACCESS.2020.3007144, 2020.

[201] N.A., "Emissivity Coefficients common Products," The Engineering Toolbox, 2003. [Online]. Available: https://www.engineeringtoolbox.com/emissivity-coefficients-d_447.html. [Accessed 15 01 2020].

[202] M. Gatzsche, Elektrisch-thermisches Betriebs- und Langzeitverhalten hochstromtragfähiger Kontaktelemente. Dissertation, Aachen: Shaker Verlag GmbH; ISBN: 978-3-8440-4894-0, 2016.

[203] A. Shukla and J. Song, "Influence of surface roughness on electrical contact resistance," in *Elektrische und optische Verbindungstechnik 2023, Tagungsband Der VDE/VDI-GMM-Fachtagung „9. Symposium Connectors*, Lemgo, Germany, 2023.

[204] N.A., "Oberflächenkenngrößen in der Praxis," Jenoptik AG, [Online]. Available: https://www.jenoptik.de/-/media/websitedocuments/metrology/neu/parameters/rauhheit-faltblatt-de.pdf. [Accessed 20 01 2023].

[205] N.A., "Gold (Au) - Properties, Applications," AZO Materials, [Online]. Available: https://www.matweb.com/search/DataSheet.aspx?MatGUID=b9639c2f4ed84006923b2956f90cc13c. [Accessed 21 01 2023].

[206] N.A., "CuSn4," KME Germany GmbH & Co. KG, [Online]. Available: https://www.kme.com/alloyfinder/wp-content/uploads/pdf/mds_kme_540_cusn4_English.pdf. [Accessed 21 01 2023].

[207] N.A., "Bronze CuSn4," Metal Rolling Services, [Online]. Available: https://www.metal-rolling-services.com/cusn4-en. [Accessed 21 01 2023].

[208] J. Song, A. Shukla and R. Probst, "State of Health of Connectors — Early Indicators," in *2022 IEEE 67th Holm Conference on Electrical Contacts (HLM); pp. 1-7; DOI: 10.1109/HLM54538.2022.9969839*, Tampa, FL, USA, 2022.

[209] N.A., *Technische Leitfaden: Ausfallraten für Bordnetz-Komponenten im Automobil - Erwartungswerte und BedingungenTechnische Leitfaden: Ausfallraten für Bordnetz-Komponenten im Automobil - Erwartungswerte und Bedingungen, ZVEI*, Köln, 2021.

[210] Z. Yu, Z. Ren, J. Tao and X. Chen, "Accelerated Testing with Multiple Failure Modes under Several Temperature Conditions," *Mathematical Problems in Engineering, Article: 839042*, vol. 2014; DOI: https://doi.org/10.1155/2014/839042, 2014.

[211] N.A., "Reliability basics - Probability Plotting (Reliability Hotwire, Issue 8, Otober 2001)," ReliaSoft Corporation, 10 2001. [Online]. Available: https://weibull.com/hotwire/issue8/relbasics8.htm. [Accessed 05 12 2021].

[212] M. Rausand and A. Høyland, System Reliability Theory - Models, Statistical Methods, and Applications - 2nd Edition, New Jersey: John Wiley & Sons, Inc.; ISBN: 0-471-47133-X, 2004.

[213] S. Sawada, K. Shimizu, Y. Hattori, T. Tamai and K. Iida, "Analysis of Contact Resistance Behavior for Electric Contacts with Plating Layer," in *2010 Proceedings of the 56th IEEE Holm Conference on Electrical Contacts; pp. 1-8; DOI: 10.1109/HOLM.2010.5619560*, Charleston, USA, 2010.

[214] H. Yuan and J. Song, "Influence of plating pairing on the fretting behavior of electrical contacts," in *60. Tribologie-Fachtagung der Gesellschaft für Tribologie e.V.*, Göttingen, 2019.

# 10 Appendix

## Appendix 1. Models from parametric CAD modelling based on design of experiment

Table 10.1: 13.6 mm connector receptacle models from two level full factorial design of experiment

| **Model** | **D1 (mm)** | **t1 (mm)** | **L1 (mm)** | **R (mm)** |
|---|---|---|---|---|
| M_L1 | 20 | 2 | 25 | 5 |
| M_L2 | 17 | 1 | 17 | 1 |
| M_L3 | 17 | 2 | 25 | 5 |
| M_L4 | 20 | 1 | 25 | 5 |
| M_L5 | 20 | 2 | 17 | 5 |
| M_L6 | 20 | 2 | 25 | 1 |
| M_L7 | 17 | 1 | 17 | 5 |
| M_L8 | 20 | 1 | 17 | 1 |
| M_L9 | 17 | 2 | 17 | 1 |
| M_L10 | 17 | 1 | 25 | 1 |
| M_L11 | 20 | 2 | 17 | 1 |
| M_L12 | 17 | 1 | 25 | 5 |
| M_L13 | 17 | 2 | 25 | 1 |
| M_L14 | 20 | 1 | 17 | 5 |
| M_L15 | 20 | 1 | 25 | 1 |
| M_L16 | 17 | 2 | 17 | 5 |
| Ref_L (Reference) | 17.2 | 1.5 | 21 | 2 |

Table 10.2: 13.6 mm connector receptacle models from two level Taguchi L8 design of experiment

| **Model** | **D1 (mm)** | **t1 (mm)** | **L1 (mm)** | **L2 (mm)** |
|---|---|---|---|---|
| MT2_L1 | 17 | 0.8 | 15 | 10 |
| MT2_L2 | 19 | 0.8 | 15 | 10 |
| MT2_L3 | 17 | 0.8 | 20 | 14 |
| MT2_L4 | 19 | 0.8 | 20 | 14 |
| MT2_L5 | 17 | 1.5 | 15 | 14 |
| MT2_L6 | 19 | 1.5 | 15 | 14 |
| MT2_L7 | 17 | 1.5 | 20 | 10 |
| MT2_L8 | 19 | 1.5 | 20 | 10 |
| Ref_L (Reference) | 17.2 | 1.5 | 21 | 8.5 |

Table 10.3: 2.5 mm connector receptacle models from three level Taguchi L9 design of experiment

| **Model** | **D1 (mm)** | **t1 (mm)** | **L1 (mm)** | **L2 (mm)** |
|---|---|---|---|---|
| M_S1 | 4 | 0.7 | 9.2 | 3 |
| M_S2 | 4.5 | 0.7 | 10.2 | 3.6 |
| M_S3 | 5 | 0.7 | 11.2 | 4.2 |
| M_S4 | 5 | 0.75 | 9.2 | 3.6 |
| M_S5 | 4 | 0.75 | 10.2 | 4.2 |
| M_S6 | 4.5 | 0.75 | 11.2 | 3 |
| M_S7 | 4.5 | 0.8 | 9.2 | 4.2 |
| M_S8 | 5 | 0.8 | 10.2 | 3 |
| M_S9 | 4 | 0.8 | 11.2 | 3.6 |
| Ref_S | 4.5 | 0.75 | 10.2 | 3.6 |

# Appendix 2. Convection coefficient values at different cross sectional diameters along the connector axis in 2.5 mm and 13.6 mm reference connectors

Table 10.4: Properties of air at 30 °C and 70 °C surface temperature [143](pp. 88)

| $\lambda_{air}$ | $T_{connector}$ (°C) | $T_{air}$ (°C) | $T_m$ (°C) | $\beta p$ | $\mu_d$ | $\nu_k$ | $\delta$ | a | cp | Pr |
|---|---|---|---|---|---|---|---|---|---|---|
| 0.02699 | 70 | 20 | 45 | 0.00315 | 1.94E-05 | 1.75E-05 | 1.109 | 2.42E-05 | 1007 | 0.724338 |
| 0.02605 | 30 | 20 | 25 | 0.003215 | 1.85E-05 | 1.56E-05 | 1.185 | 2.14E-05 | 1007 | 0.7125 |

Table 10.5: $\alpha_{conv}$ values for 13.6 mm connector at 30 °C surface temperature and 2.5 mm connector at 70 °C

| | *d* (mm) | $l_{char}$ (m) | *Gr* | *Nu* | $\alpha_{conv}$ (W/m²K) |
|---|---|---|---|---|---|
| 13.6 mm connector | 19 | 0.029845 | 34541.05 | 6.763537 | 5.90348 |
| | 23.2 | 0.036442 | 62883.78 | 7.856419 | 5.615967 |
| | 17.2 | 0.027018 | 25624.77 | 6.277041 | 6.052216 |
| 2.5 mm connector | 4.5 | 0.007069 | 1781.848 | 3.236657 | 12.35854 |
| | 3.45 | 0.005419 | 802.9535 | 2.651866 | 13.20735 |
| | 2.5 | 0.003927 | 305.5295 | 2.082775 | 14.3148 |
| | 5 | 0.007854 | 2444.236 | 3.502796 | 12.03726 |

## Appendix 3. Calculation of Thermal Contact Conductance ($TC_{contact}$) and Electrical Contact Conductance ($EC_{contact}$)

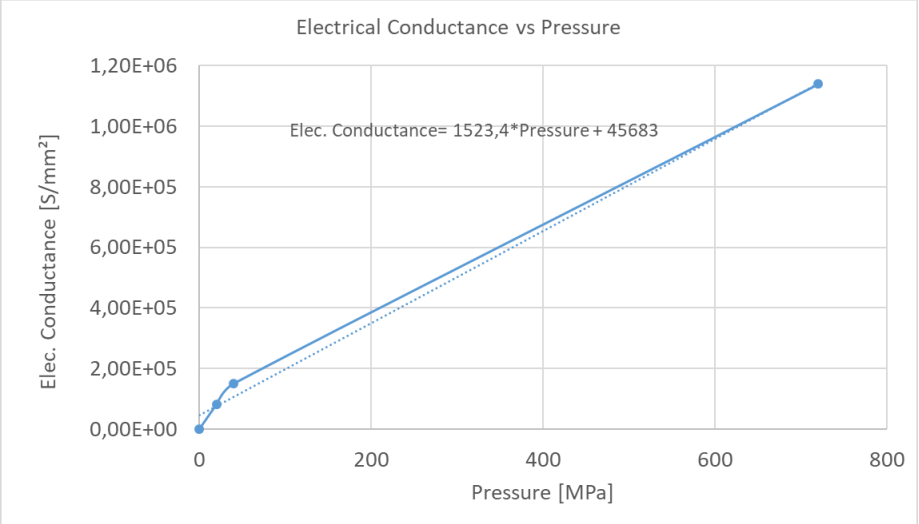


Electrical contact conductance ($EC_{contact}$) and pressure relationship

Table 10.6: Thermal Contact Conductance ($TC_{contact}$) and Electrical Contact Conductance ($EC_{contact}$)

| | 13.6mm Connector | 2.5mm Connector |
|---|---|---|
| Contact area (mm²) | 0.084 | 0.0032 |
| Contact force (N) | 23.276 | 1.143 |
| $EC_{contact}$ (S/mm²) | 4.6766E05 | 5.89536E05 |
| $TC_{contact}$ (W/mm²-K) | 3.41 | 4.298 |

## Appendix 4. Joule heating and voltage drop in simulations for symmetry verification for thermal-electric simulation

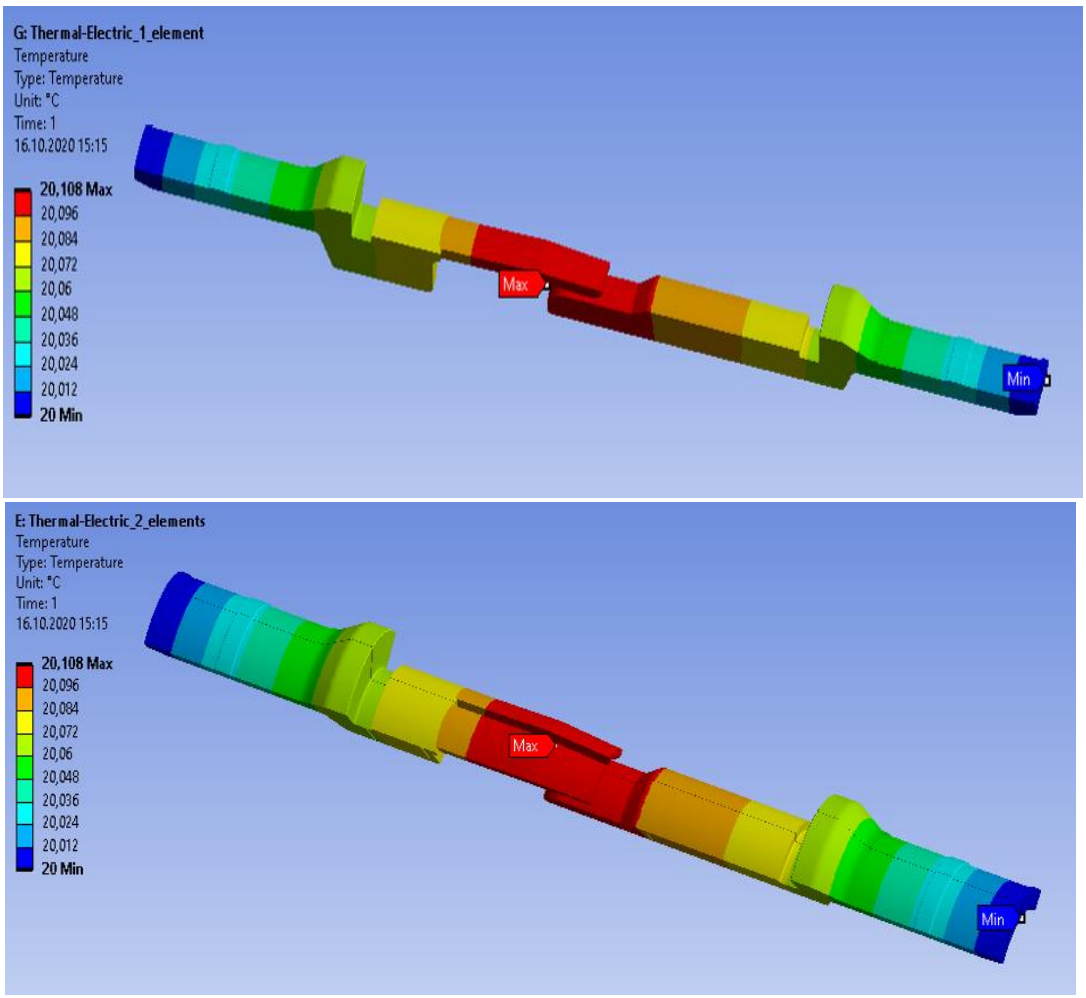


Fig. 10.1: Joule heating in 1/8th model (top) and quarter model (bottom) in 13.6 mm reference connector

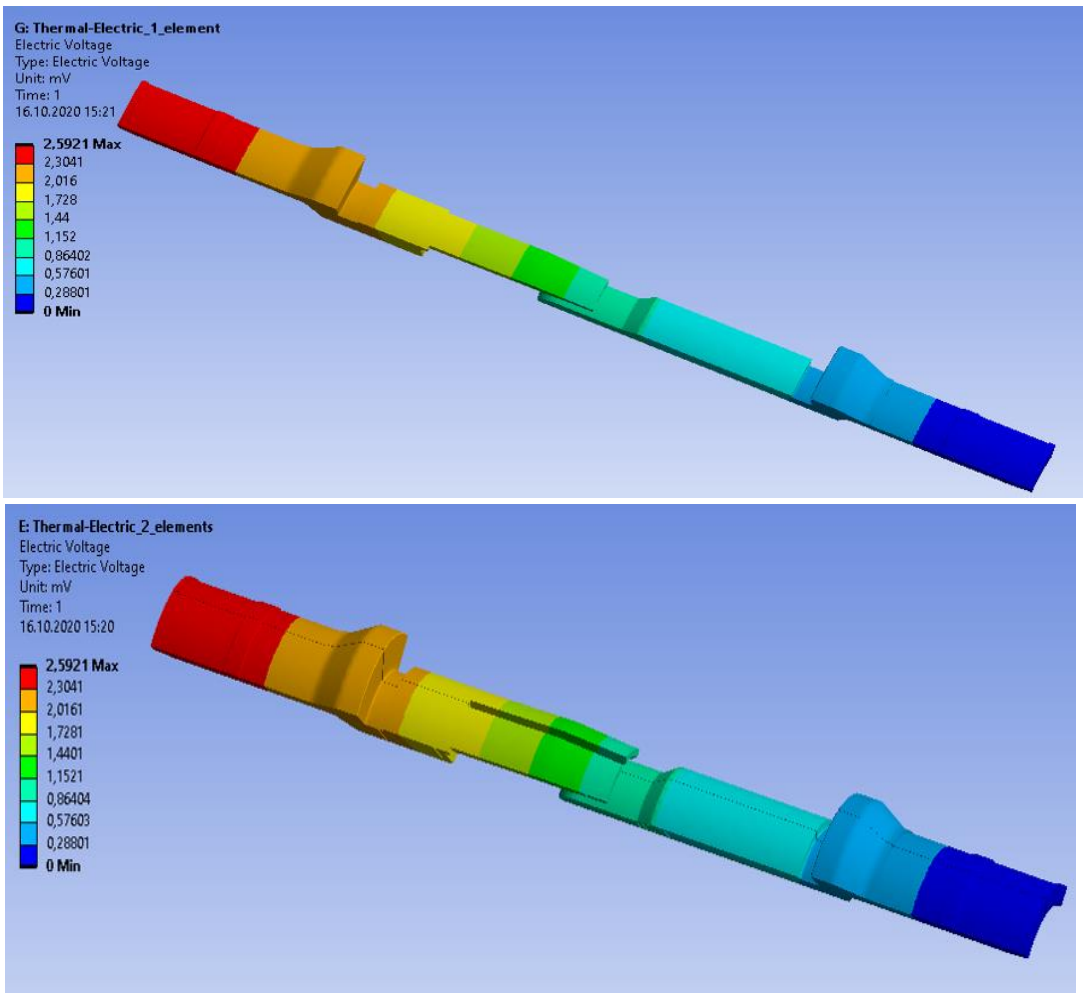


Fig. 10.2: Voltage drop in 1/8th model (top) and quarter model (bottom) in 13.6 mm reference connector

## Appendix 5. Example of Weibull probability plot for characteristic lifetime determination

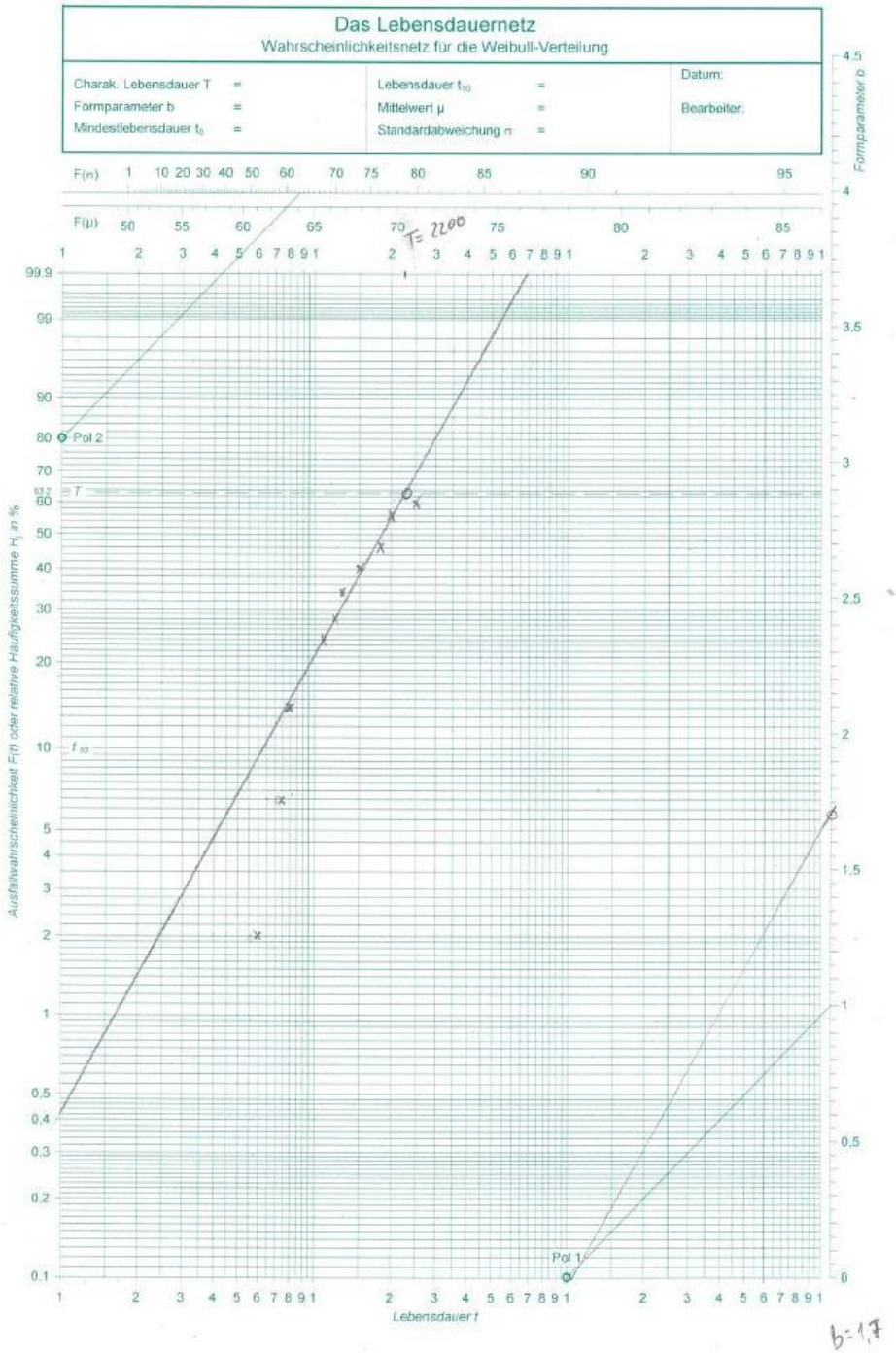

## Appendix 6. Roughness parameters and bearing area curve

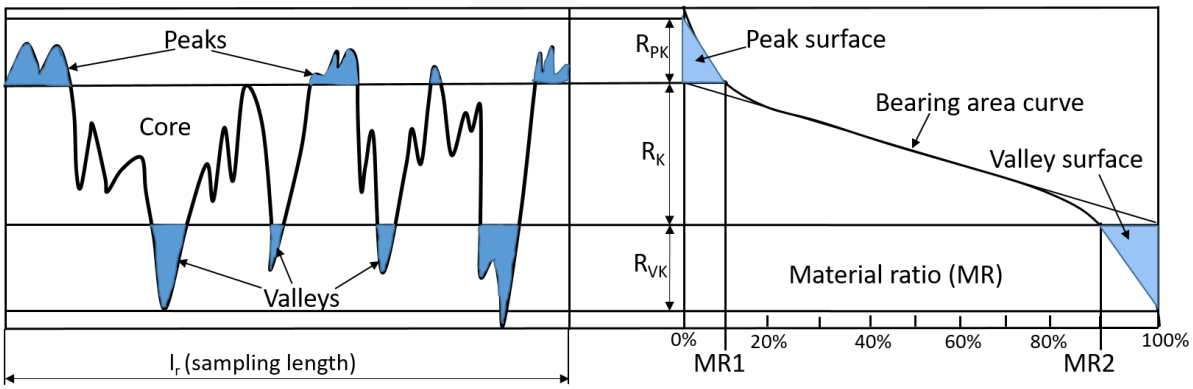


Fig. 10.3: Graphical representation of the bearing area curve consisting of material ratio and roughness parameters $R_{PK}$, $R_K$ and $R_{VK}$ [204]

Material ratio (*MR*) indicates the ratio of the total length of the material at the given height of the roughness profile to the sampling length ($l_r$) (in percentage).

*MR1* indicates the upper material ratio cutoff i.e. the upper limit of the roughness core area, Fig. 10.3. The percentage of the material allocated to the peaks in the roughness profile is decided by selection of the *MR1*. These peaks of the roughness profile correspond to the reduced peak height ($R_{PK}$) of the bearing area curve. Selection of *MR1* = 10 % means that the 10 % of the material in the sampling length $l_r$ correspond to the peaks of the roughness profile.

*MR2* indicates the lower material ratio cutoff i.e. the lower limit of the roughness core area, Fig. 10.3. The percentage of the material allocated to the valleys in the roughness profile is decided by selection of the *MR2*. These valleys of the roughness profile correspond to the reduced valley depth ($R_{VK}$) of the bearing area curve. Selection of MR2 = 90 % means that the remaining 10 % of the material in the sampling length $l_r$ correspond to the valleys of the roughness profile.

The height of the roughness profile formed by the material ratio cutoff *MR1* and *MR2* is the core roughness $R_K$, Fig. 10.3. The reduced peak height $R_{PK}$ is the average height of the peaks above the core of the roughness profile. The reduced valley depth $R_{VK}$ is the average depth of the valleys below the core of the roughness profile.

The average roughness $R_a$ is the measure of the surface deviation with respect to a mean height over a sampling length $l_r$, Fig. 10.4. It is given as [204]:

$$R_a = \frac{1}{l_r}\int_0^{l_r} |Z(x)|dx \tag{10.1}$$

The average of the five roughness depths $R_{Z1}$ to $R_{Z2}$ measured from five sampling lengths $l_{r1}$ to $l_{r5}$ gives the mean roughness depth $R_Z$ of the roughness profile, Fig. 10.5. It is given as [204]:

$$R_Z = \sum_{i=1}^{5} R_{Zi} \tag{10.2}$$

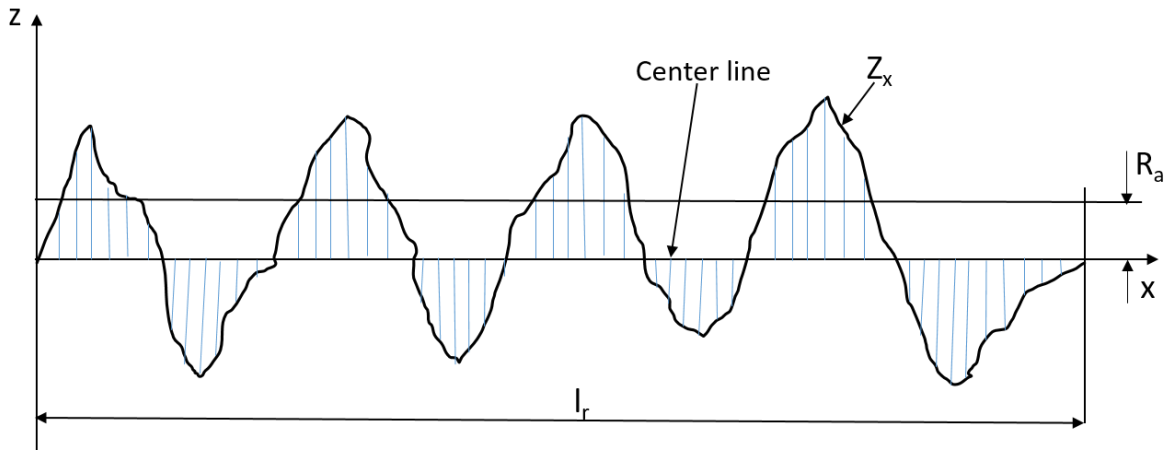


Fig. 10.4: Schematic representation of average roughness Ra [204]

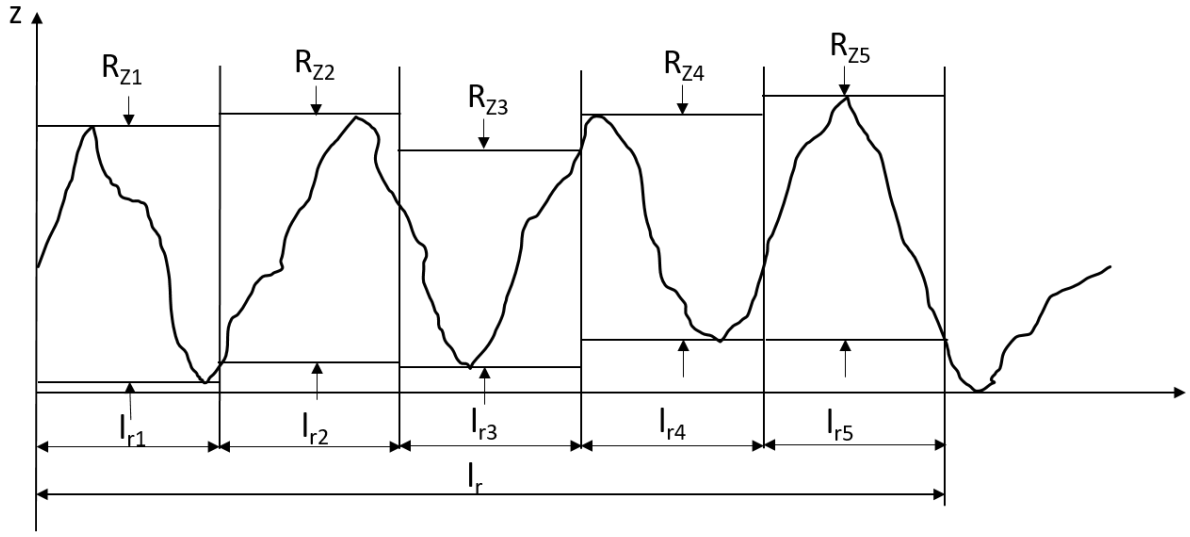


Fig. 10.5: Schematic representation of mean roughness depth Rz [204]

## Appendix 7. Magnification of the extrapolated curves during initial part of operation

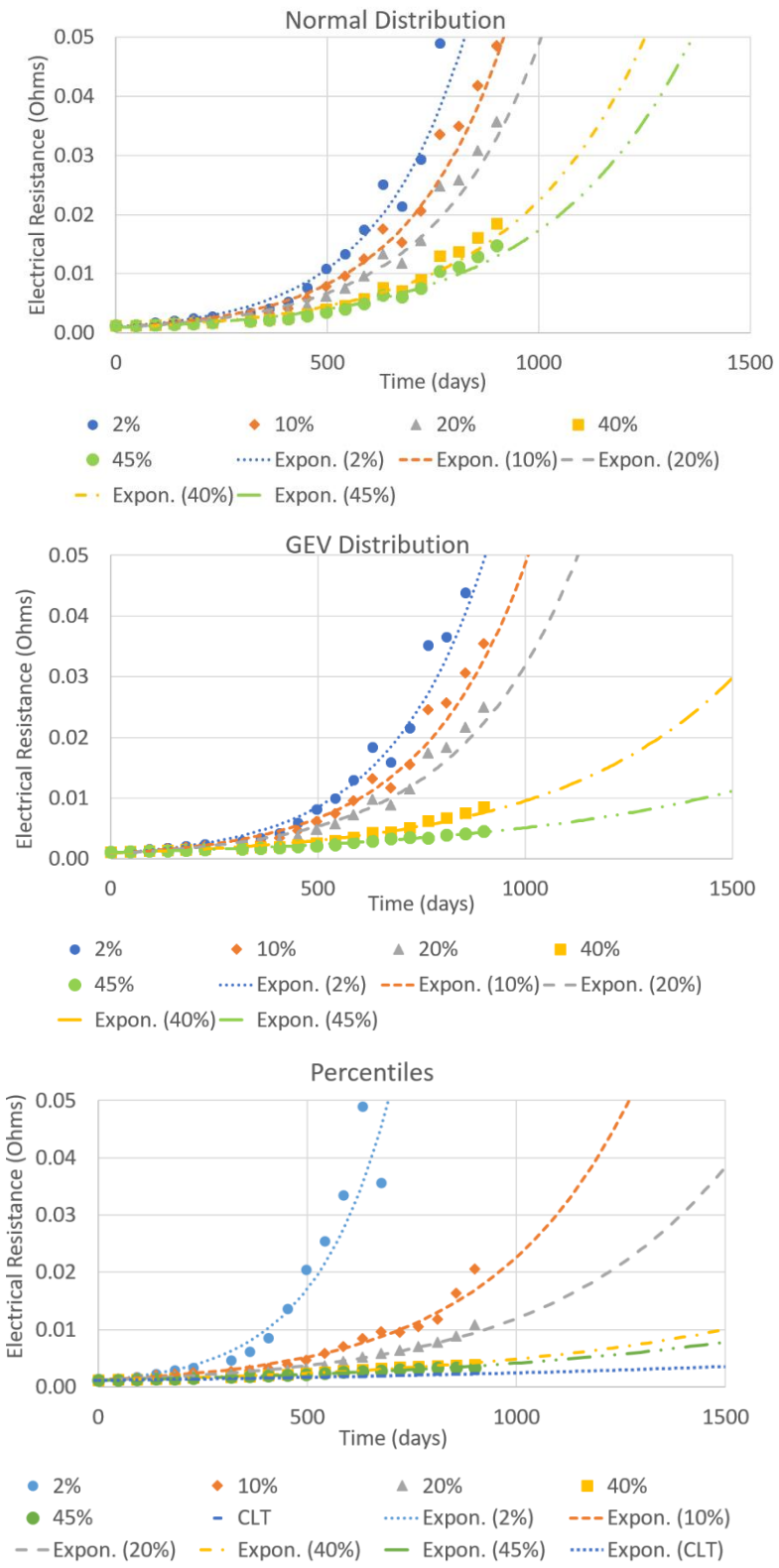


Fig. 10.6: Connector T2: Magnification of the extrapolation of different failure probabilities during initial part of operation using (a)Normal distribution (top), (b) GEV distribution (center), (c) Percentiles (bottom)

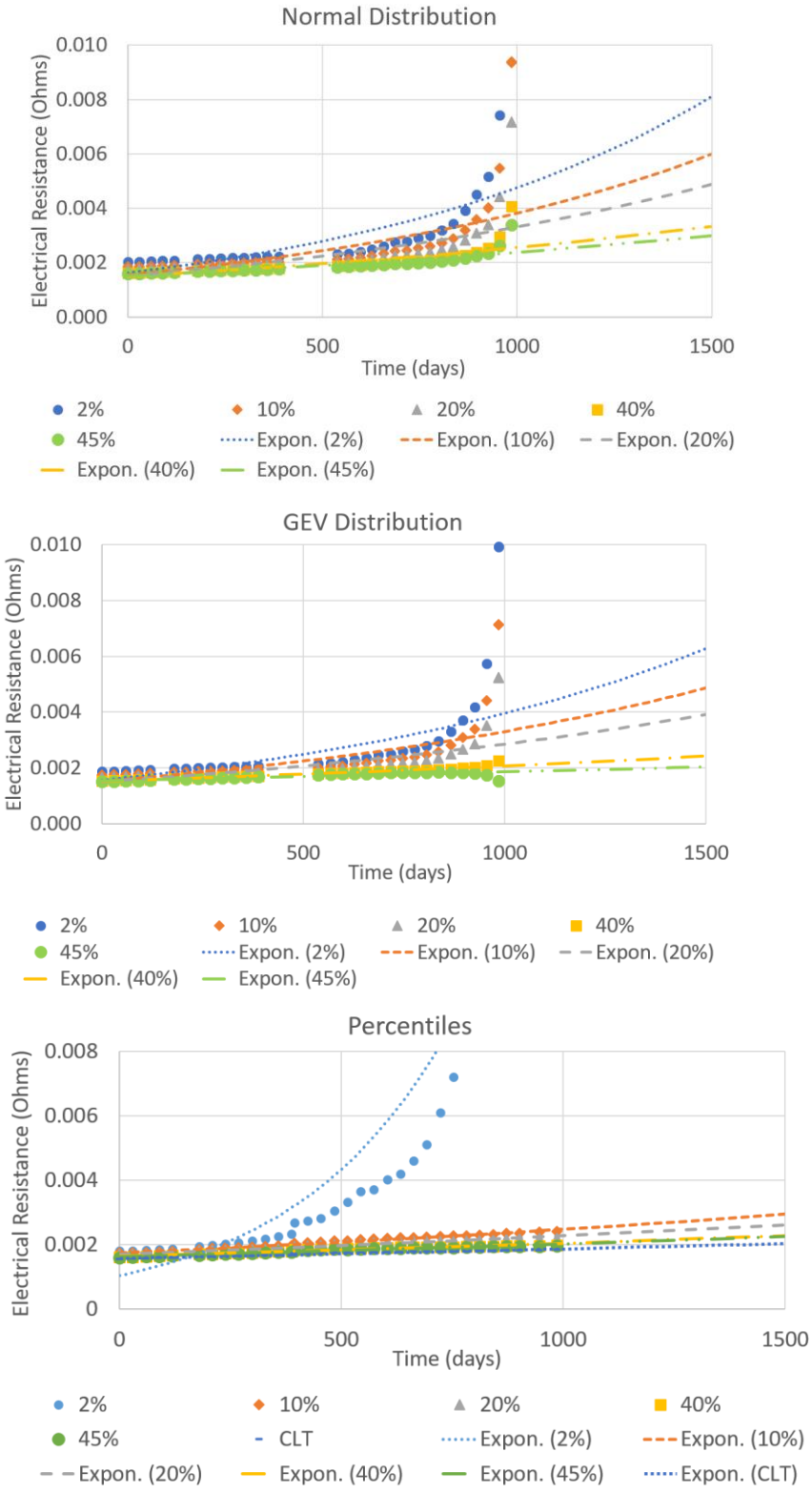


Fig. 10.7: Connector T3: Magnification of the extrapolation of different failure probabilities during initial part of operation using (a)Normal distribution (top), (b) GEV distribution (center), (c) Percentiles (bottom)

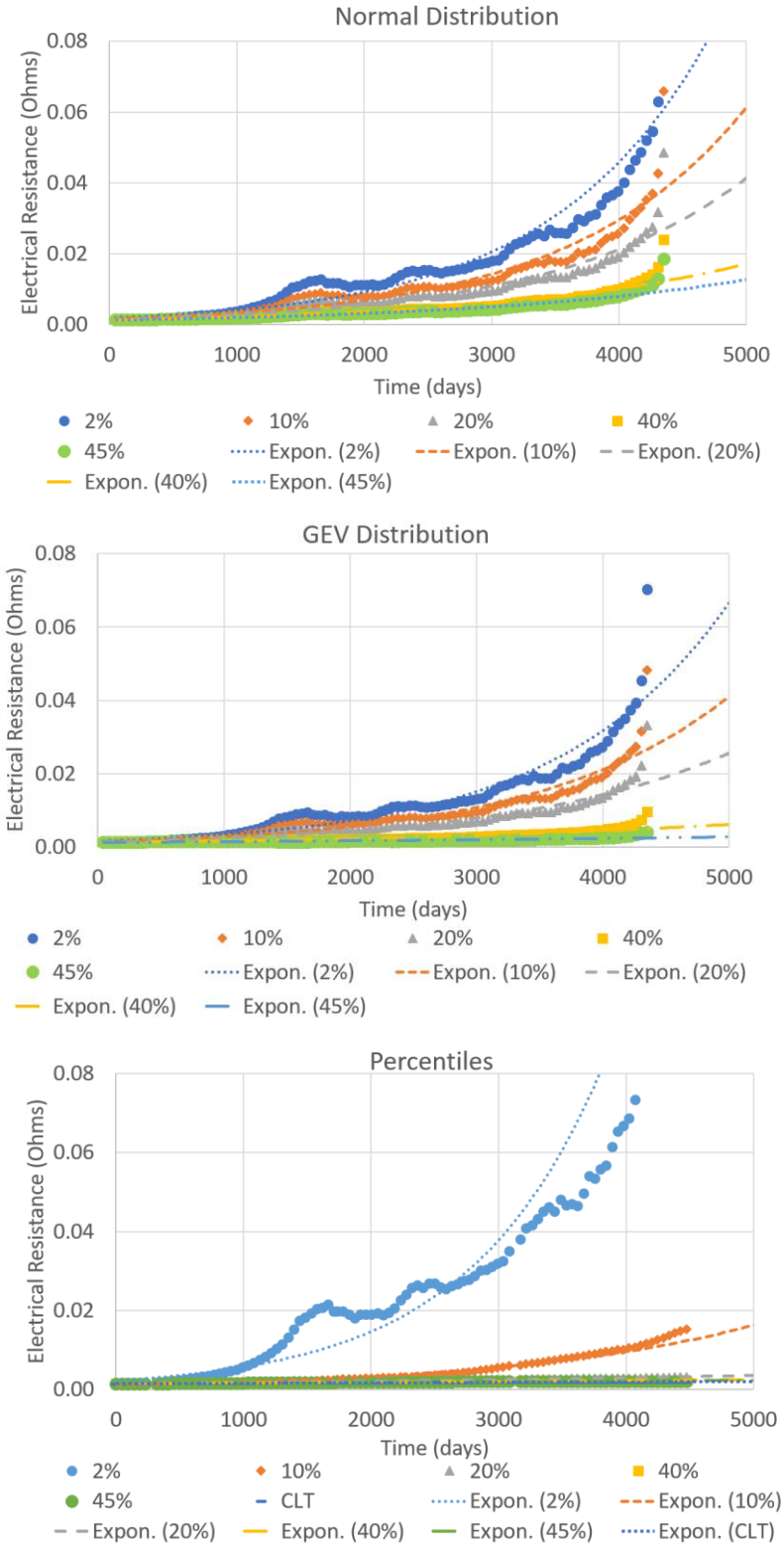


Fig. 10.8: Connector T4: Magnification of the extrapolation of different failure probabilities during initial part of operation using (a)Normal distribution (top), (b) GEV distribution (center), (c) Percentiles (bottom)

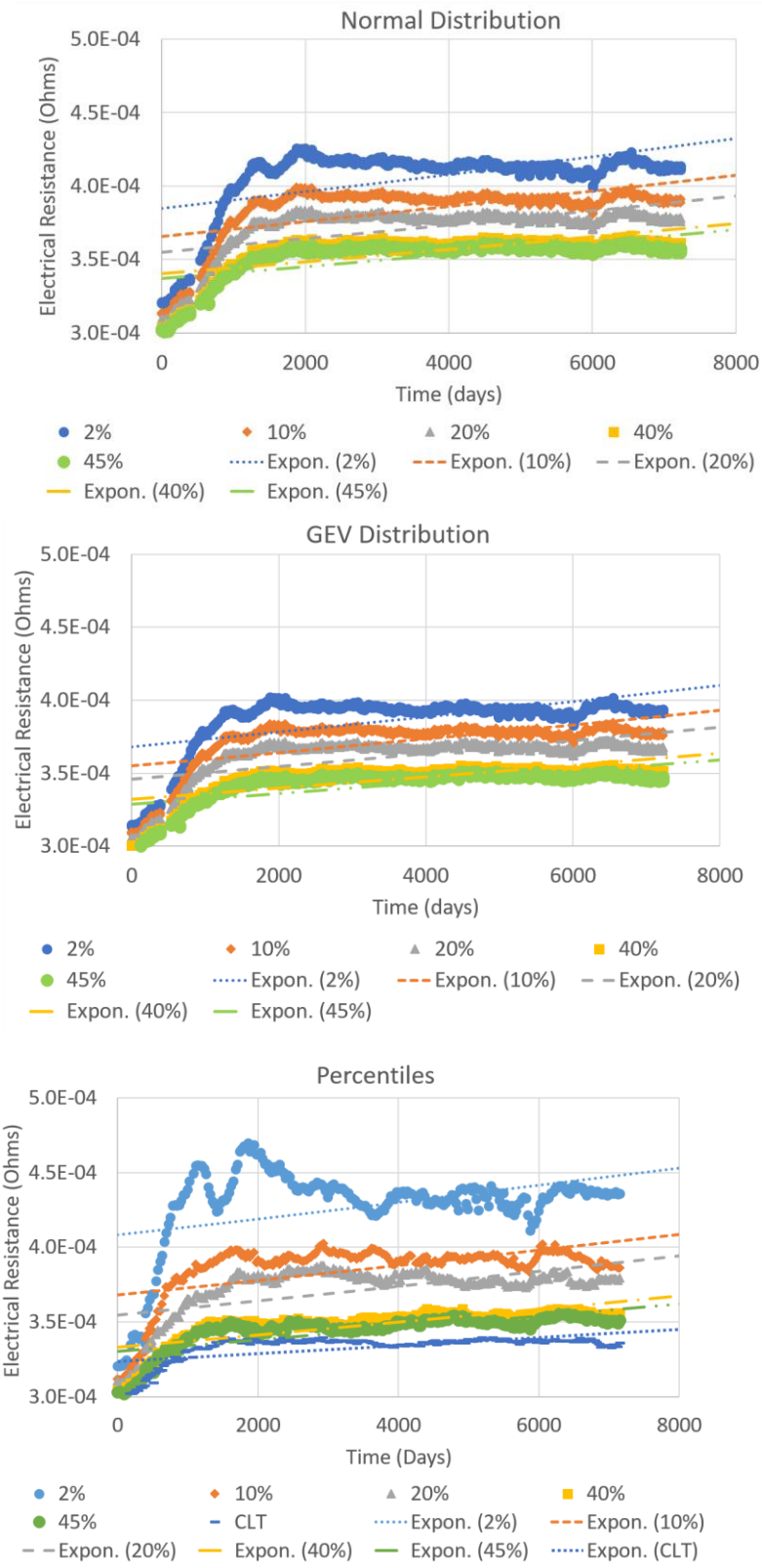


Fig. 10.9: Connector T5: Magnification of the extrapolation of different failure probabilities during initial part of operation using (a)Normal distribution (top), (b) GEV distribution (center), (c) Percentiles (bottom)

## Appendix 8. FEM contact area results verification with additional experiment

Since the method to optically determine the contact area using the procedure described in section 3.1.4.2 is not efficient due to irregular wear scars created from insertion and extraction process, an alternate method in order to validate the contact area output of the FEM simulation has been used. The goal is to obtain a comparable contact pressure as in the simulation of the original component. In the simulation of 2.5 mm reference connector, the contact area of single spring segment is 0.003 $mm^2$ and the contact force is 1.143 N resulting in the contact pressure of 381 $N/mm^2$.

For validation of simulation model with respect to contact area results, a copper sphere of 5 mm diameter coated with 0.3 µm gold is pressed on the polycarbonate plate using the tension and bending test machine. The plate is fixed on a lower clamp and the sphere is moved against the plate using the stepper motor. The wear scars formed in such a manner represent the contact point between sphere and plate as the sphere engages and disengages at the contact point and relative displacement in the lateral direction is eliminated. The diameter of such a contact point is optically measured using Keyence optical microscope. The compression force for the test used is 17 N which results in the diameter of 0.244 mm i.e. a contact area of 0.047 $mm^2$ as shown in Fig. 10.10. Therefore, the experimentally determined contact pressure in gold coated copper sphere and polycarbonate plate contact under 17 N contact force is 361 $N/mm^2$. The measurements are repeated and the contact area ranging from 0.044 $mm^2$ to 0.048 $mm^2$ are obtained. Thus the contact pressure in the experiments varies from 354 $N/mm^2$ to 386 $N/mm^2$.

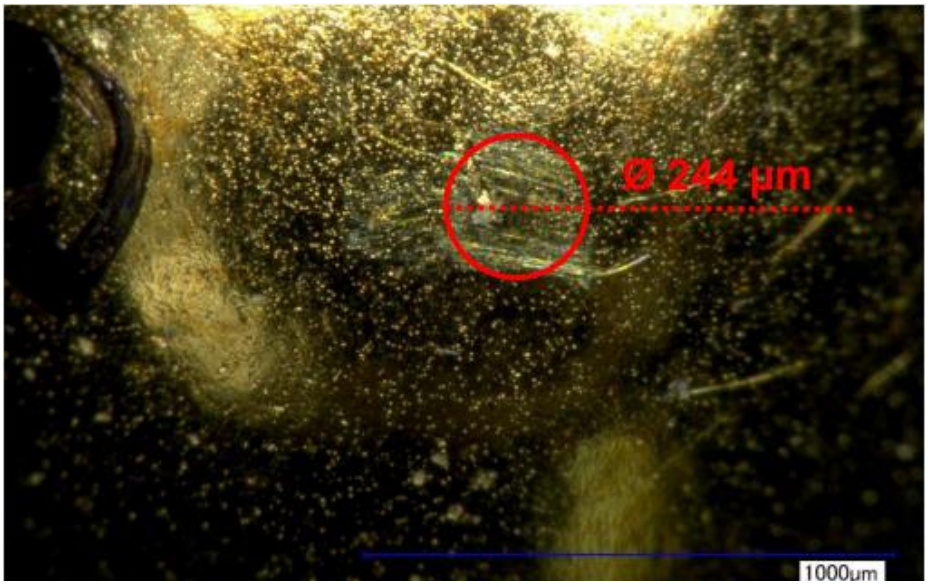


Fig. 10.10: Contact spot diameter created on gold coated copper sphere on pressing against polycarbonate plate

The experimental results based on the simplified geometry of a sphere on a plane contact combination are to be confirmed by a FEM simulation. An axisymmetric 2D simulation is carried out using the Ansys 2019 R3 simulation program. The ideal elastic-plastic material

properties are considered for simulation. The material properties for gold, copper and polycarbonate are given in Table 10.7

Table 10.7: Material properties of copper, gold and polycarbonate [188] [205]

| **Material Property:** | **Gold** | **Copper** | **Polycarbonate** |
|---|---|---|---|
| Young's modulus (GPa) | 77.2 | 8.96 | 2.3 |
| Poisson's ratio | 0.42 | 0.34 | 0.4002 |
| Density (g/cm³) | 19.32 | 8.96 | 1.13 |

The simplification of the model is made due to the symmetrical geometry of both contact partners. Fig. 10.11 shows the boundary conditions applied to two contact partners. A displacement in the X direction is constrained at the entire upper edge highlighted by A, so that the ball is only contacted vertically and cannot roll along the plate surface. Pressure is applied the upper edge highlighted by B. This has a value of 0.8658 $N/mm^2$ and is calculated from the required force of 17 N divided by the cross-sectional area of the upper edge of the sphere which is equal to 19.63 $mm^2$ where pressure is to be applied. The polycarbonate plate is fixed at the lower surface shown by C. The global mesh element size is 30 µm and the mesh element size in the contact zone is 2 µm. The resulting equivalent stress in the model is shown in Fig. 10.12.

The simulation results in contact area of 0.046 mm². When the downward force of 17 N is divided with the contact area from simulation, the contact pressure of 370 N/mm² is obtained. The results are summarized in Table 10.8. The mean value of the laboratory measurements carried out for the case of a sphere on a plane is also equal to 370 $N/mm^2$ and thus almost exactly reflects the simulation result for the same case. The agreement of these two results indicates that the simulation results are correct. It is therefore obvious that the simulation of the contact with the original dimensions also led to a correct result and consequently the laboratory measurement of the contact area on the original contact was not sufficiently accurate.

Table 10.8: Comparison of contact area validation results from experiment and simulation

| | **Contact area (mm²)** | **Contact force (N)** | **Contact pressure (N/mm²)** |
|---|---|---|---|
| Experiment | 0.044 to 0.048 | 17 | 354 to 386 |
| Simulation | 0.0046 | 17 | 370 |

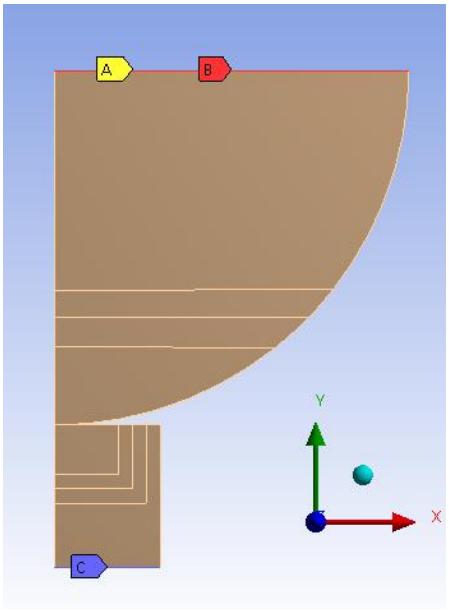


Fig. 10.11: Boundary conditions in contact area verification experiment - Copper sphere with gold coating and flat polycarbonate plate

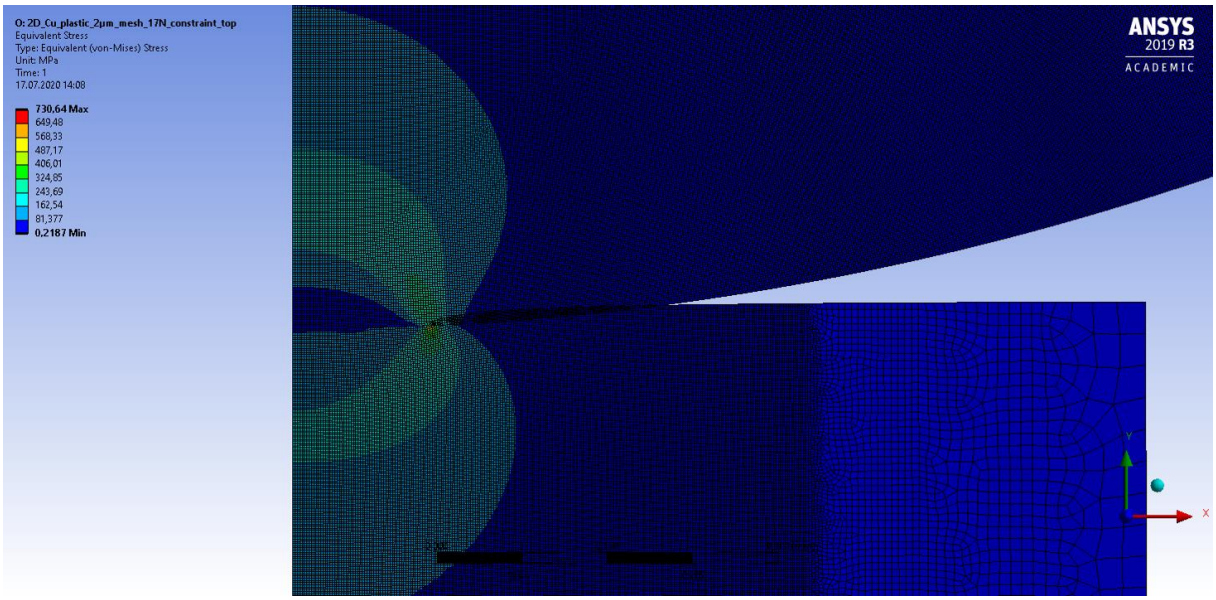


Fig. 10.12: Stress distribution in contact between gold coated copper sphere and polycarbonate plate

## Appendix 9. Exponential curve fitting to percentiles of contact resistances in connector T5

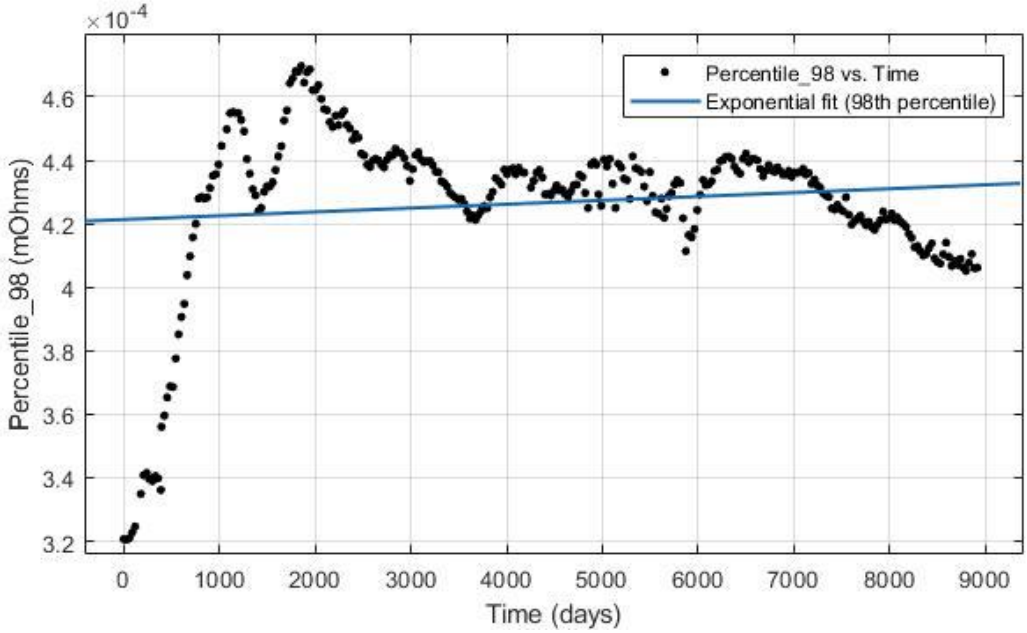


Fig. 10.13: Connector T5: 98th percentile development and exponential curve fitting (slope of exponential fit = 2.847E-06)

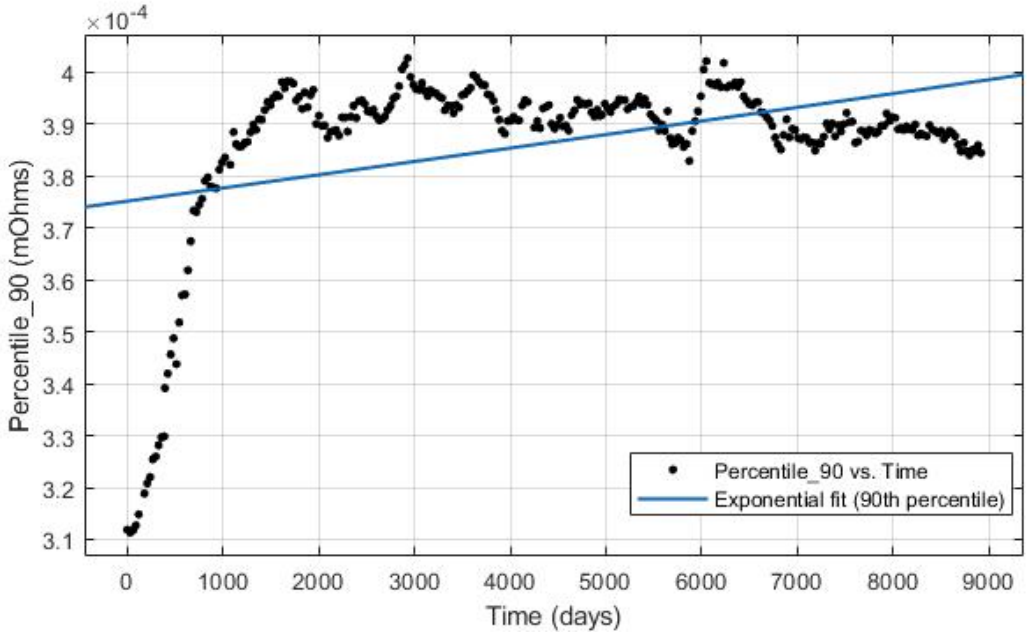


Fig. 10.14: Connector T5: 90th percentile development and exponential curve fitting (slope of exponential fit = 6.72E-06)

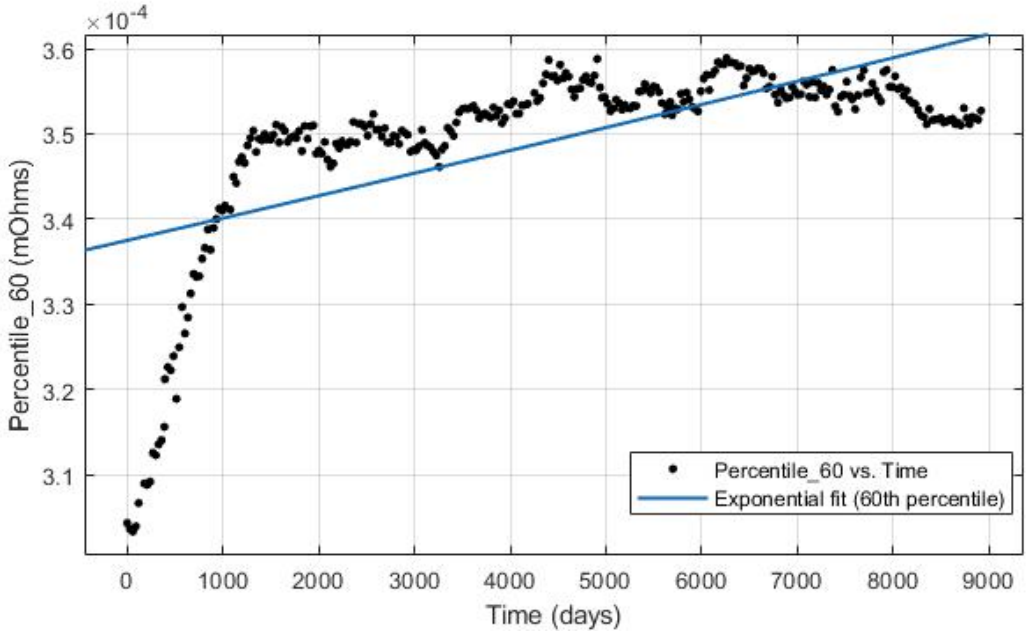


Fig. 10.15: Connector T5: 60th percentile development and exponential curve fitting (slope of exponential fit = 7.684E-04)